Theoretical Study on Finite Temperature Effect in Spin Polarization and Damping Constant of Magnetic Materials

Ivan Kurniawan

February 2023

Theoretical Study on Finite Temperature Effect in Spin Polarization and Damping Constant of Magnetic Materials

Ivan Kurniawan
Doctoral Program in Engineering Sciences
Subprogram in Materials Science and Engineering

Submitted to the
Degree Programs in Pure and Applied Sciences of the
Graduate School of Science and Technology
in Partial Fulfillment of the Requirements
for the Degree of Doctor of Philosophy in Engineering

at the
University of Tsukuba

Contents

Chapter 1: Introduction

1.1. Spintronics: Future of Data Storage Technology

In the future, spintronics is inevitably appealing to fulfill our increasing needs on information technology especially storage and memory [1]. Thanks to utilization of electron spin, spintronics is becoming more superior than conventional electronics [2]. While electronics prefer the semiconductor materials and need more energy to maintaining the devices current, spintronics effect appears in the simple metal and its combined multilayer with smaller energy to change and transfer the electron spin. As traditional electronics strongly depends on silicon semiconductor and will eventually faces its physical size limit and thermal heat dissipation issue at very small devices size, it is predicted that doubling of transistors number in an integrated circuit (IC) every 2 years observed by Moore's law will slow down and cease to apply at around 2025 [3]. That is why spintronics is promising as an alternative solution for high demand of storage, sensors, and quantum computing technology.

The history of oldest spintronics product can be traced into 1956, when IBM 350 is introduced as first hard disk drive (HDD) with areal density 2 kbit/in^2 to store around 4 MB information inside 50 magnetic disks weighted almost 1 ton. By discovery of giant magnetoresistance (GMR) in 1988 [4,5], a world record of storing capacity of 10 Gbit/in^2 achieved again by IBM nine years later, using GMR head technology as reading mechanism. The GMR effect itself is resistance change corresponds to the magnetic configuration between two ferromagnetic (FM) layer sandwiching nonmagnetic metal. In contrast to GMR, resistance change may also happen in the magnetic tunnel junction (MTJ) consisted of FM/insulator/FM which called as tunneling magnetoresistance (TMR). Despite the TMR effect is first observed at low temperature in 1975 [6], it started to attract attention when room temperature observation is reported twenty years later. In 2005, Seagate implemented TMR read head with areal density around 300 Gbit/in^2. Currently, TMR read head with areal density more than 600 Gbit/in^2 is still incorporated in the HDD, using MgO as an insulator layer.

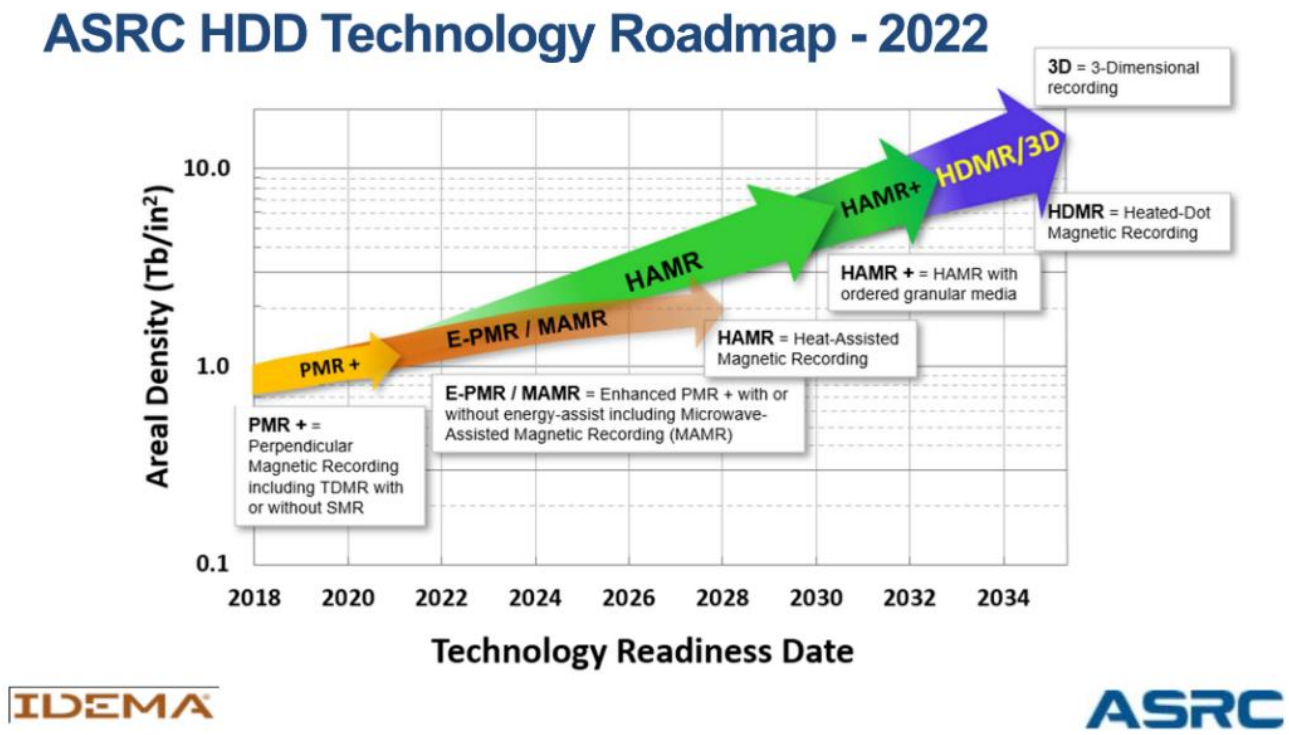

Fig 1.1. Advanced Storage Research Consortium (ASRC) roadmap for the future of HDD. Reuse with permission [7]

However, as predicted by International Data Corporation (IDC) [1], current hard drives technology is not enough to store growing worldwide data up to 163 ZB by 2025, which is ten times larger from produced data in 2017. In order to push the areal density limit, the recording technology is also significantly evolving as shown in the Fig 1.1, from the old fashioned Longitudinal Magnetic Recording (LMR) [8–15] which align the magnetic bits in-plane to the recording media, into Perpendicular Magnetic Recording (PMR) [16–24] which allow to shrink the grain size and increase the areal density with retained Signal to Noise Ratio (SNR). Alternatively, Shingled Magnetic Recording (SMR) [25–30] squeeze the magnetic track which consists of track bits closer together to achieve the higher areal density. Combining the PMR and SMR together, unfortunately we can only reach the limit around 1 Tbit/in2 due to the required field to "write" the bit magnetization will be too high, more than Slater-Pauling limit [31]. One of clever solution for this limit is Heat Assisted Magnetic Recording (HAMR) [32–37] which heat up the recording media to reduce the its coercivity as shown in the Fig 1.2(a)-(b), hence available writing field is still usable and simultaneously may enhance the areal density up to 5 Tb/in^2.

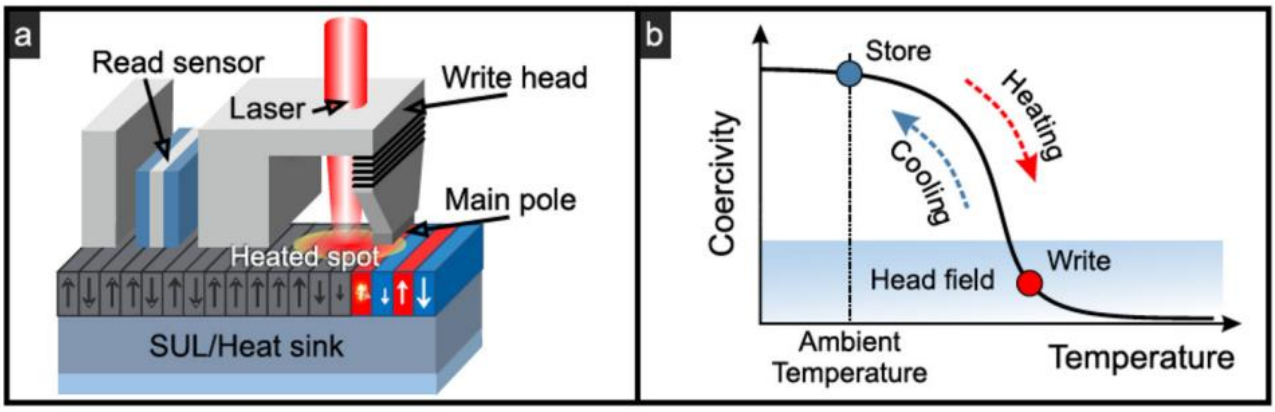

Fig 1.2. (a) Typical HAMR structure and (b) writing mechanism in HAMR. Reuse with permission [33].

In this doctoral thesis, we theoretically investigated two properties that play important role behind the GMR/TMR (reading mechanism) and HAMR (writing mechanism) of ultrahigh-density recording, which are the spin polarization *P* and damping constant α, respectively. When highly spin-polarized FM layer such as Heusler alloy is used to create magnetoresistance (MR) effect in the trilayer FM/barrier/FM, the output MR ratio is also large because it only allows one of spin to pass through the barrier. However, its large MR ratio suffers the strong reduction at finite temperature, implying the significant reduction of spin polarization of FM layer. Meanwhile in HAMR, better performance is shown via faster writing process which require the large damping constant of HAMR media not only at ambient temperature but also at near Curie temperature (T_C). Understanding the behavior of P and α at finite temperature will lead us to improve the storage technology via material selection or device design.

1.2. Magnetoresistance Effect

In the simple trilayer structure of FM/NM/FM shown in the Fig 1.3, MR effect is quantitatively defined as

$$MR\ ratio = \frac{\Delta RA}{R_P A} = \frac{R_{AP}A - R_P A}{R_P A} = \frac{R_{AP} - R_P}{R_P} \times 100\% \quad (1\text{-}1)$$

With R_{AP} and R_P are resistance when the magnetization direction between two FM layers are antiparallel and parallel, respectively. If the barrier is a nonmagnetic metal, it is called as CPP-GMR effect. While the nonmagnetic insulator is used, the TMR effect may happen.

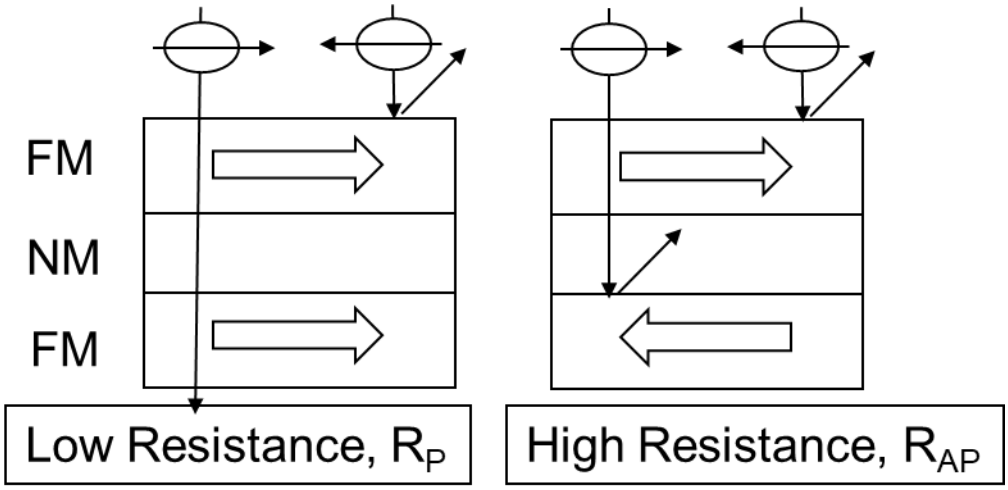

Fig 1.3. Schematic stacking structure of magnetoresistance effect in FM/NM/FM

1.2.1. Early GMR experiments

In 1988, Fert and Grunberg separately discovered that resistance change happens by applying the field on the Fe/Cr multilayers or Fe/Cr/Fe trilayer [4,5]. This effect called as current-in-plane giant magnetoresistance (CIP-GMR) because the electric current measurement is "in-plane" of the multilayer. Origin of the magnetoresistance was described as spin-dependent transmission of electrons between the metallic layers, due to the difference of magnetization orientation between ferromagnetic layers. In the [4], it is shown that without applied magnetic field, opposite direction of magnetization between adjacent Fe layer lead to the high resistance. Thus, increasing magnetic field cause the parallel alignment of Fe layers, resulting in reduction of in-plane resistance. At that time, metallic layers were grown using slow Molecular Beam Epitaxy (MBE) process.

Instead of in-plane measurement, current-perpendicular-to-plane giant magnetoresistance (CPP-GMR) reported by Pratt *et al.* [38] on Co/Ag multilayers at 4.2 K offers its attractiveness due the larger magnitude compared with its CIP counterpart even in the same sample as shown in the Fig 1.4. This is also followed by first measurement of the CPP-GMR at room temperature in the Fe/Cr and Co/Cu multilayers by Gijs *et al.* [39–41] which confirmed that CPP-GMR value is always larger than CIP-GMR for the same sample over wide temperature range. Afterwards, development of theoretical model of CPP-GMR show the possibility to further improve the MR ratio by incorporate the highly spin-polarized materials.

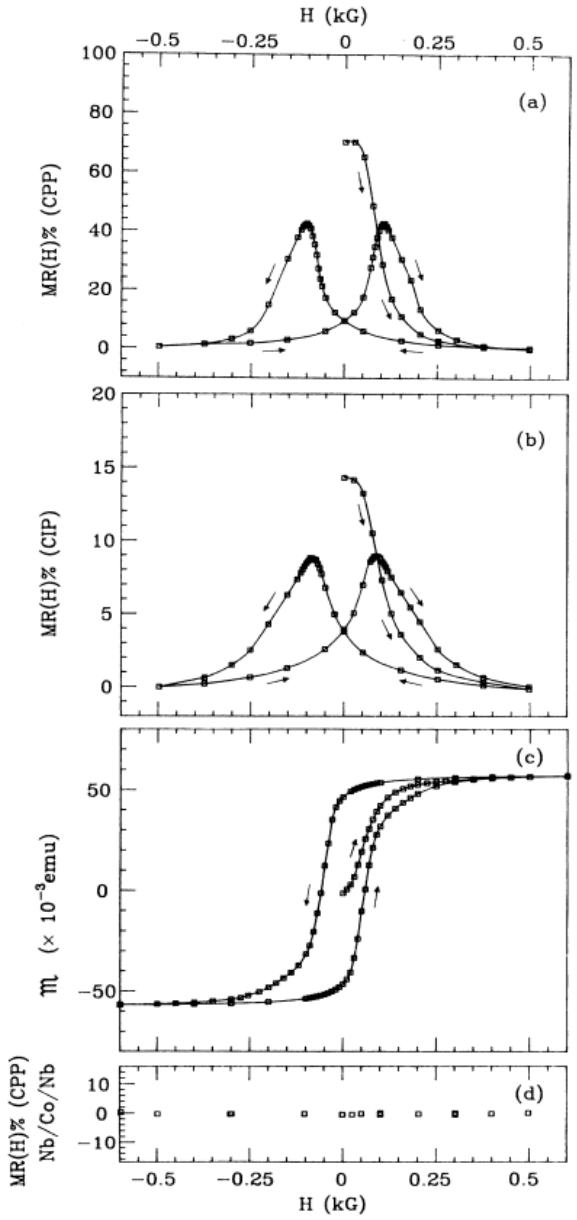

Fig 1.4. (a) CPP-MR, (b) CIP-MR, and (c) magnetization dependence on applied magnetic field of Co/Ag multilayers. (d) CPP-GMR for Nb/Co/Nb layer. Reuse with permission [38]

1.2.2. Theoretical model of CPP-GMR

When GMR started to branch into CIP and CPP geometry at 1991 [38], CPP-GMR offers more advantages and attract much interest compared than CIP-GMR. Current uniformity which is difficult in the CIP geometry may be easily realized in the CPP. There is also only one characteristic length parameter considered in CPP called as spin-diffusion length, representing the how long conduction electron diffuses before its spin moment change the direction. Therefore, analysis of CPP-GMR were carried out firstly with the simple model such as two-current series resistor (2CSR) model [42] as shown in Fig 1.5.

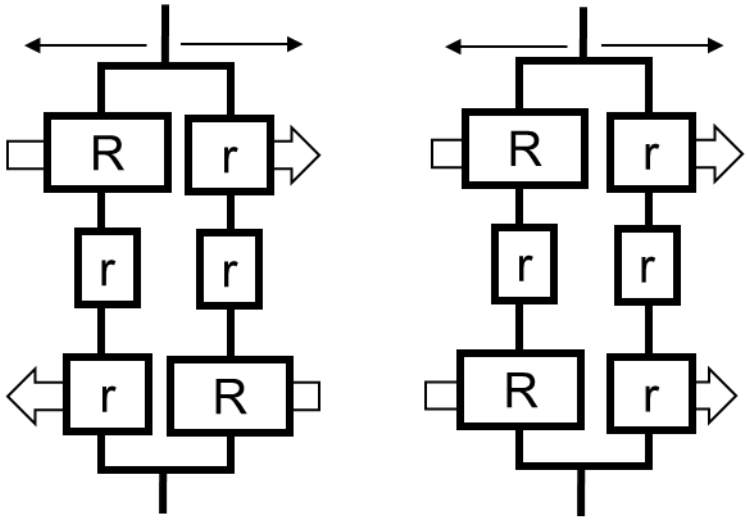

Fig 1.5. Two current series resistor (2CSR) model for CPP-GMR

In the 2CSR model, the spin-dependent scattering process happened in CPP-GMR is represented as high resistance R and low resistance r in the ferromagnetic electrode. Aside from that, the nonmagnetic spacer also contributes for small resistance. Assuming that there is only diffusive transport and no spin-flip, the RA contribution from all metallic layer is the product of layer resistivity ρ and the layer thickness t. While the nonmagnetic (N) layer contribution will be $\rho_N t_N$, the ferromagnetic (F) layer, it is spin-resolved contribution with the form $\rho_F^{\uparrow} t_F$ and $\rho_F^{\downarrow} t_F$, correspond to the resistance at the parallel and antiparallel configuration between spin moment and magnetic layer moment, respectively.

Here we start to introduce the bulk spin scattering asymmetry as $\beta_F = (\rho_F^{\downarrow} - \rho_F^{\uparrow})/(\rho_F^{\downarrow} + \rho_F^{\uparrow})$ and interface spin scattering asymmetry $\gamma_{F/N} = (AR_{F/N}^{\downarrow} - AR_{F/N}^{\uparrow})/(AR_{F/N}^{\downarrow} - AR_{F/N}^{\uparrow})$ with $AR_{F/N}^{\uparrow}$ and $AR_{F/N}^{\downarrow}$ as interface specific resistances behaving like $\rho_F^{\uparrow} t_F$ and $\rho_F^{\downarrow} t_F$. Other modified parameter introduced are also enhanced resistivity $\rho_F^* = \frac{\rho_F^{\downarrow} + \rho_F^{\uparrow}}{4} = \frac{\rho_F}{1-\beta_F^2}$ and enhanced interface specific resistance $AR_{F/N}^* = \frac{AR_{F/N}^{\downarrow} + AR_{F/N}^{\uparrow}}{4} = \frac{AR_{F/N}}{1-\gamma_{F/N}^2}$, where ρ_F is the low temperature resistivity of the F-metal. All of these parameters are basically needed to describe the 2CSR model properly. For the simplicity, derivation for MR ratio using this model will lead to the:

$$\text{MR ratio} \propto (\beta_F \rho_F^* t_F + 2\gamma_{F/N} AR_{F/N}^*)^2 \tag{1-2}$$

Where the MR ratio is strongly depends on finite value of the spin scattering asymmetry β_F and $\gamma_{F/N}$. The 2CSR model is simple yet unrealistic model, due to neglect of the spin-flip process. Valet-Fert model is proposed to overcome the 2CSR model weakness by introducing more parameters such as

spin diffusion length in the N- (l_{sf}^{N}) and F- (l_{sf}^{F}) metal, and also the parameter $\delta_{F/N}$ corresponds to the probability of spin-flip at the F/N interface $p = 1 - \exp(-\delta_{F/N})$. Note that when the spin diffusion length is much longer than metallic layer thicknesses and the spin-flip probability $p = 0$, Valet-Fert model is simply reduced to the 2CSR model. Later, in order to obtain the high MR ratio, search for ferromagnetic material with large β_F and large $\gamma_{F/N}$ due to interface with nonmagnetic spacer were widely conducted. Since then, many of so-called half-metallic materials with fully-spin polarized are proposed as ferromagnetic electrode in CPP-GMR.

1.2.3. Early TMR experiments

In 1975, Julliere observed the first TMR effect on the Fe|oxidized Ge|Co tunnel junctions with 14% MR ratio at low temperature as shown in the Fig 1.6. Separately, tunneling using oxidized Si is investigated by Meservey *et al.* [43], but one FM layer is replaced by superconductor. Later, Gibson *et al.* confirmed the properties of oxidized Si [43] is similar with oxidized Ge in their results [44], but still not observe the spin polarization hence cannot reproduce Julliere results.

At that time, oxide semiconductor is attracted researcher because its low barrier height will reduce criticality of thickness control. Meanwhile, metal oxide such Al_2O_3 were already applied to the tunnel junction with superconducting Al due to its feasibility to be fabricated from Al oxidation [45]. It encourages the usage of alternative metal oxide such NiO. Maekawa *et al.* reported the MR ratio in the Ni/NiO/*TM* with *TM*=Ni, Fe, and Co, accompanied with strong temperature dependence [46]. Nevertheless, the relatively high MR ratio up to 18% was successfully observed using amorphous Al-O tunnel barriers in 1995 [47,48]. Almost a decade later, Parkin *et al.* and Yuasa *et al.* separately reported the giant TMR ratio up to 200%, using MgO barrier [49,50].

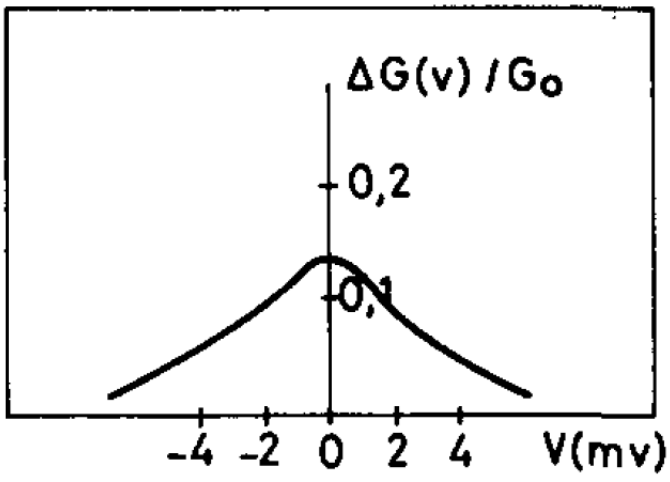

Fig 1.6. First observation of TMR effect on Fe|oxidized Ge|Co by Julliere. The $\Delta G(v)/G_0$ correspond to the MR ratio. Reuse with permission [6].

1.2.4. Theoretical model of TMR

Unlike the origin of GMR which is spin-dependent scattering, the physics behind TMR is spin-dependent tunneling across the nonmagnetic insulator. In order to understand the basic of TMR, we may assume that tunneling resistance is inversely proportional with the product of density of states of ferromagnetic electrode, illustrated in the Fig 1.7:

$$R_P \propto \frac{1}{DOS_{top}^{\uparrow} DOS_{bottom}^{\uparrow} + DOS_{top}^{\downarrow} DOS_{bottom}^{\downarrow}} \tag{1-3}$$

$$R_{AP} \propto \frac{1}{DOS_{top}^{\uparrow} DOS_{bottom}^{\downarrow} + DOS_{top}^{\downarrow} DOS_{bottom}^{\uparrow}} \tag{1-4}$$

And the MR ratio could be simplified as:

$$\text{MR ratio} = \frac{2P_{top}P_{bottom}}{1 - P_{top}P_{bottom}} \tag{1-5}$$

Where the $P_{top(bottom)}$ is the spin polarization of top and bottom electrode.

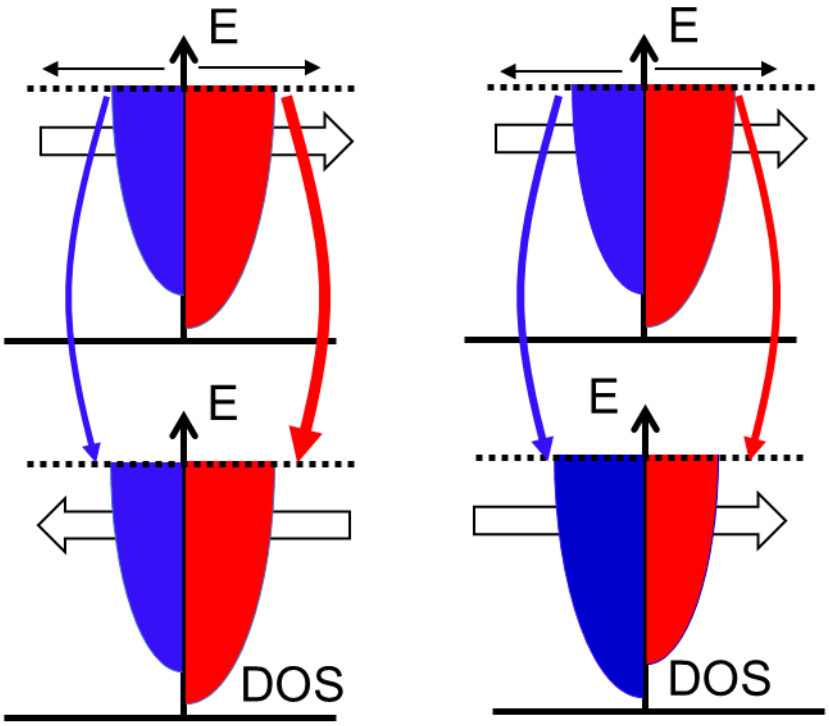

Fig 1.7. Two current model for TMR

In order to understand why replacing amorphous Al-O with crystalline MgO(001) barrier drastically increase the TMR ratio, Butler *et al.* provide the theory of coherent tunneling via crystalline MgO(001) barrier [51]. While Julliere's model simply assumes that all electronic Bloch state have equal tunnel probability (incoherent tunneling) and can be a better approximation for Al-O barrier, the Δ_1 Bloch

state Δ_1 actually has higher tunneling probability and dominate the tunneling process in crystalline MgO barrier. In addition, Δ_1 Bloch states have the symmetry similar with the s, p_z, and d_{z2} orbital, thus we can roughly approximate that MR ratio depends on the spin polarization considering *sp* electrons.

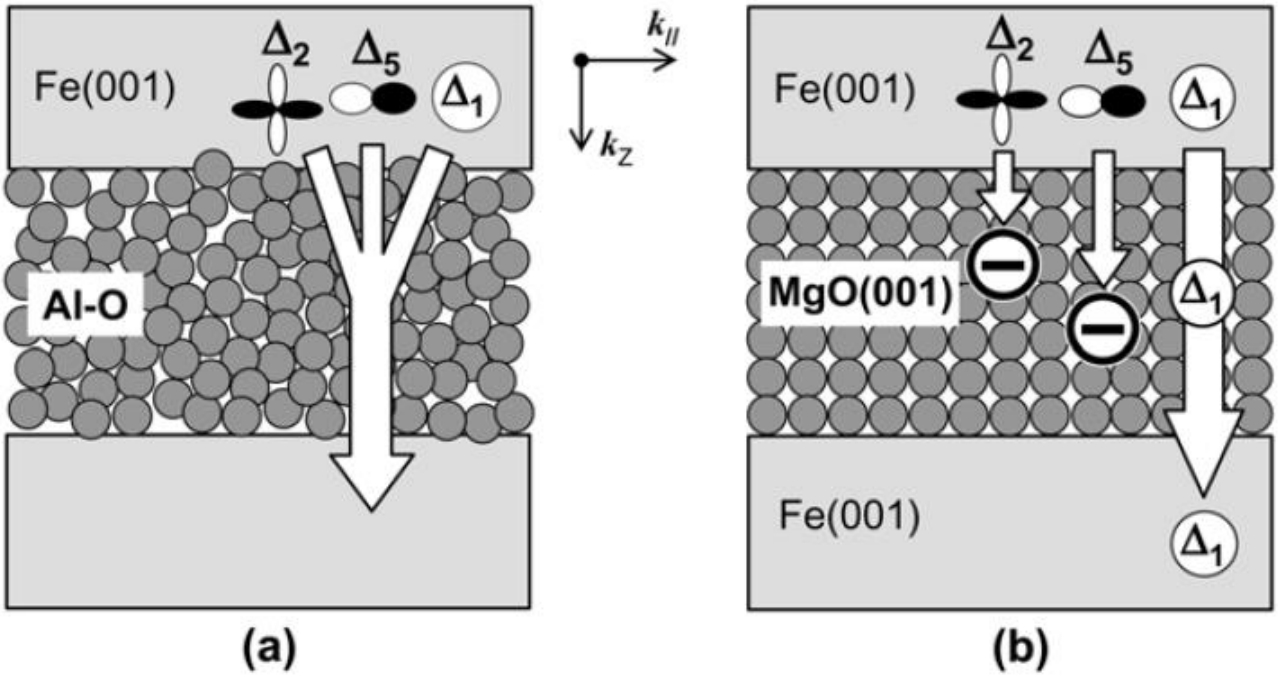

Fig 1.8. Illustration of tunneling process with the (a) amorphous Al-O barrier and (b) crystalline MgO(001) barrier. Reuse with permission [52].

1.3. Spin Polarization

As mentioned in previous part, spin polarization evaluated from electronic structure shown in the Fig 1.9 defined by

$$P = \frac{D^{\uparrow}(E_F) - D^{\downarrow}(E_F)}{D^{\uparrow}(E_F) + D^{\downarrow}(E_F)} \tag{1-6}$$

plays important role to obtain the high MR ratio output in both GMR and TMR effect. Based on the theoretical calculation, it is possible to obtain the material with fully spin-polarized electronic structure. These materials then called as half-metallic ferromagnet. Unfortunately, the 100% spin polarization can exist only at hypothetical ground state and no spin-orbit interaction. When the temperature is raised, the depolarization is expected and spin polarization should reduce. Similarly, spin-orbit interaction (SOI) will mix the majority and minority spin states, hence the same depolarization is also exhibited. Interestingly, at relatively low temperature compared than Curie temperature and small SOI, some of proposed half-metallic ferromagnet materials already

demonstrated remarkable properties which deviates from “normal” ferromagnets. Hence, it is still justified to group these materials as “half-metallic ferromagnetic” although its spin polarization approaching but still less than 100%.

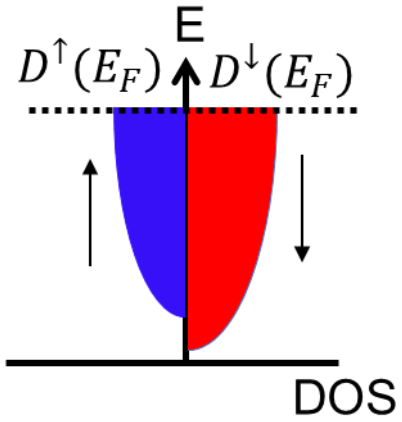

Fig 1.9. Illustration of spin-polarized band structure

Another issue regarding spin polarization is its experimental measurement. In order to confirm the half-metallicity, spin-resolved positron annihilation is the most direct measurement, which successfully prove half-Heusler NiMnSb [53,54] with the accuracy less than one hundredth of electron, but also with its own difficulty and expensive technique. Aside from this, the various measurement method also conducted, using superconducting tunneling spectroscopy (STS) [55], point-contact Andreev reflection (PCAR) [56], non-local spin valve (NLSV) [57], spin-resolved photoelectron spectroscopy [58], and last but not least, TMR and CPP-GMR devices.

The difficulty on experimental measurements lead to the significant role of theoretical study of electronic structure for better understanding of half-metal and fully-spin polarized band structure. However, it is known that theoretical study based on the density functional theory is also show the discrepancy, not only with experiments but also with same theoretical study using different approximation. Anyway, one thing to keep in mind, that all theoretical framework try to picture the origin of half-metallicity, which could be addressed into crystal structure and chemical composition. It is also important to understand that the origin of half-metallicity, we need to differ “strong” and “weak” magnet. In the strong magnet, magnetization is affected by the availability of electronic states, and not the exchange interaction. Contrary to this, magnetization of weak magnet is mainly determined compromise of exchange energy gain and band energy cost. Later, these concepts comprise all the known half-metal compound, which consists of weak magnets with minority spin gap (Heusler alloys), weak magnets with majority spin gap (double perovskites and magnetite), strong

magnets with minority spin gap (chromium dioxides) and strong magnet with majority spin gap (anionogenic ferromagnets) [59].

1.4. Highly spin-polarized material: Heusler alloys

The Heusler alloys is named after Friedrich Heusler due to his discovery of ferromagnetic material formed by nonmagnetic elements such as Cu, Mn, Al [60] at 1903. Interestingly, element can be easily varied to make different combination of alloys with the covalent bonding. However, structure elucidation of Cu_2MnAl took more than 30 years later to be finished by Otto Heusler (Friedrich Heusler's son) [61]. It is found that the Cu_2MnAl structure is the prototype of full-Heusler structure of general composition X_2YZ. Otto also proposed another possible structure when the half of *X* atoms of tetrahedral site is interchanged by the *Y* atoms called as *inverse* Heusler. Later, Castelliz successfully fabricated NiMnSb by reducing Ni content of compositional series of $Ni_{2-x}MnSb$ ($0 \leq x \leq 1$) . The structure of NiMnSb is called as half-Husler since the only half of the *X* atoms of tetrahedral site is occupied.

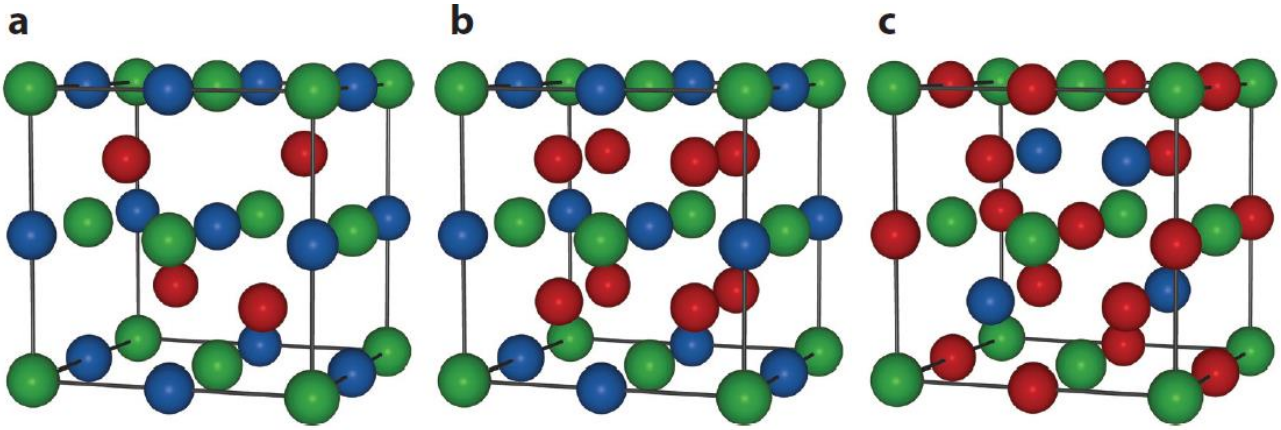

Fig 1.10. The structure of prototype Heusler alloys with *X* (red), *Y* (blue), *Z* (green): (a) Half-Heusler *XYZ*, (b) Full-Heusler X_2YZ, and (c) Inverse-Heusler X_2YZ compound. Reuse with permission [59].

1.4.1. Origin of half-metallic gap

Several full-Heusler compound such as Co_2MnSi and Co_2MnGe are proposed as half-metallic. The insulating gap in the minority spin could be explained as consequence of hybridization between Co and Mn states. As shown in the Fig 1.11, Galanakis *et al.* proposed the mechanism of gap formation in Co_2MnGe by considering the *d* states hybridization at the Γ point [62]. Based on the Fig 1.10, Co atoms in the Co_2YZ compound forms a simple cubic lattice with the octahedral symmetry, and the hybridization between these Co atoms are still important although with second nearest neighbor distance. Due to the octahedral nature, the *d* orbitals of Co are split into twofold degenerate states $d_{x^2-y^2}$, d_{z^2} and threefold degenerate states d_{xy}, d_{xz}, d_{yz}. As shown in Fig 1.11, symmetry only

allows the hybridization between two set of twofold degenerated states to create the e_g (bonding) and e_u (antibonding) orbitals. Similarly, it also happens for two set of threefold degenerated states to create the t_{2g} (bonding) and t_{1u} (antibonding) orbitals. Thus, the Co-Co orbitals are also hybridized with the Mn orbitals following the symmetry to create the set of bonding and antibonding orbitals of e_g and t_{2g}. Since no Mn orbitals have the matched symmetry with the e_u and t_{1u} of Co-Co orbitals, these two sets of degenerated states become non-bonding orbitals, where the e_u orbitals are unoccupied and t_{1u} are occupied, hence Fermi level lies within the gap between the nonbonding states. Despite proposed based on Co_2MnGe, this hybridization model can be used for general half-metal full-Heusler compound composition. In case of all majority spin states is filled, the total seven states ($2e_u$ + $2e_g$ + $3t_{2g}$) remains empty in the minority spin states, giving the maximum magnetic moment of 7 μ_B.

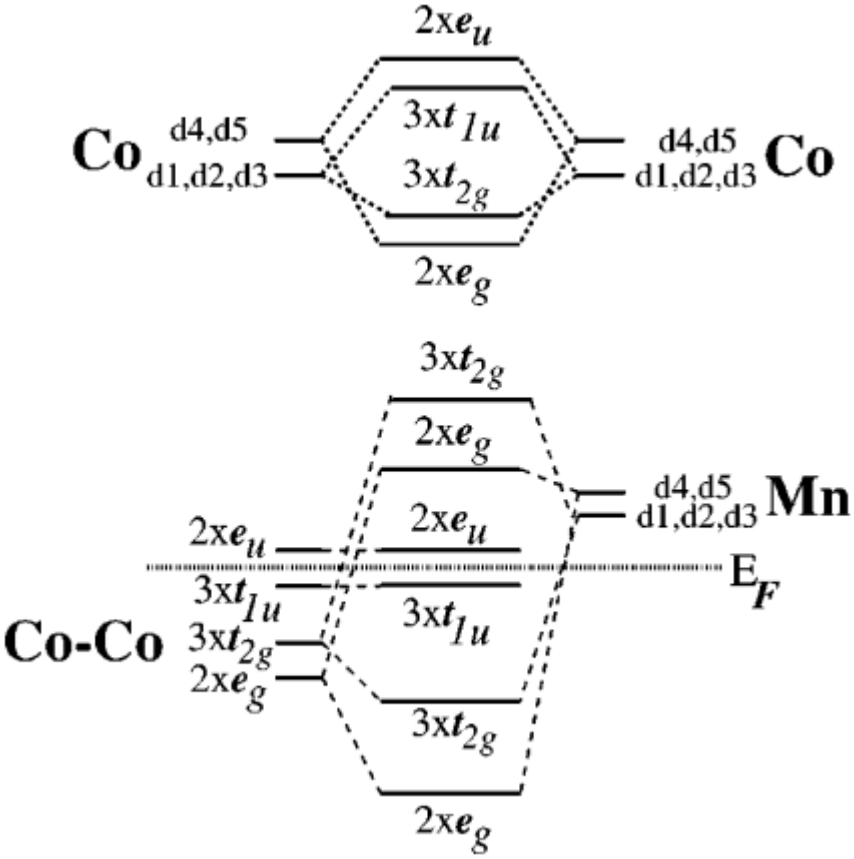

Fig 1.11. Hybridization of Co and Mn minority-spin states as origin of half-metallicity in Co2MnGe. The d1, d2, and d3 correspond to d_{xy}, d_{xz}, d_{yz} orbitals, respectively, and d4, d5 for $d_{x^2-y^2}$, d_{z^2}. Reuse with permission [62].

1.4.2. Slater-Pauling behavior

For half-metallic material, the number of electrons occupying the minority states $N_\downarrow$ should be integer. In a unit cell, there would be 8 electrons (from $2e_g$ + $3t_{2g}$ + $3t_{1u}$ occupied states based on hybridization scheme) and additional 4 electrons from low-energy *sp* bands contributed by *sp* element, resulting in 12 electrons in the minority spin-states. Therefore, the Slater-Pauling rule can be derived as follow:

$$M_t = N_\uparrow - N_\downarrow = Z_t - N_\downarrow - N_\downarrow = Z_t - 2N_\downarrow = Z_t - 24$$

where M_t, $N_\uparrow$, Z_t are total spin moment, number of electrons occupying majority spin states, and total number of valence electrons, respectively. As shown in Fig 1.12, Galanakis *et al.* calculated the total spin moment for various full-Heusler alloys and found that most compound which half-metal will follow the Slater-Pauling behavior properly [62]. However, they also observed that the slight deviation for several Rh- and Co-based compound.

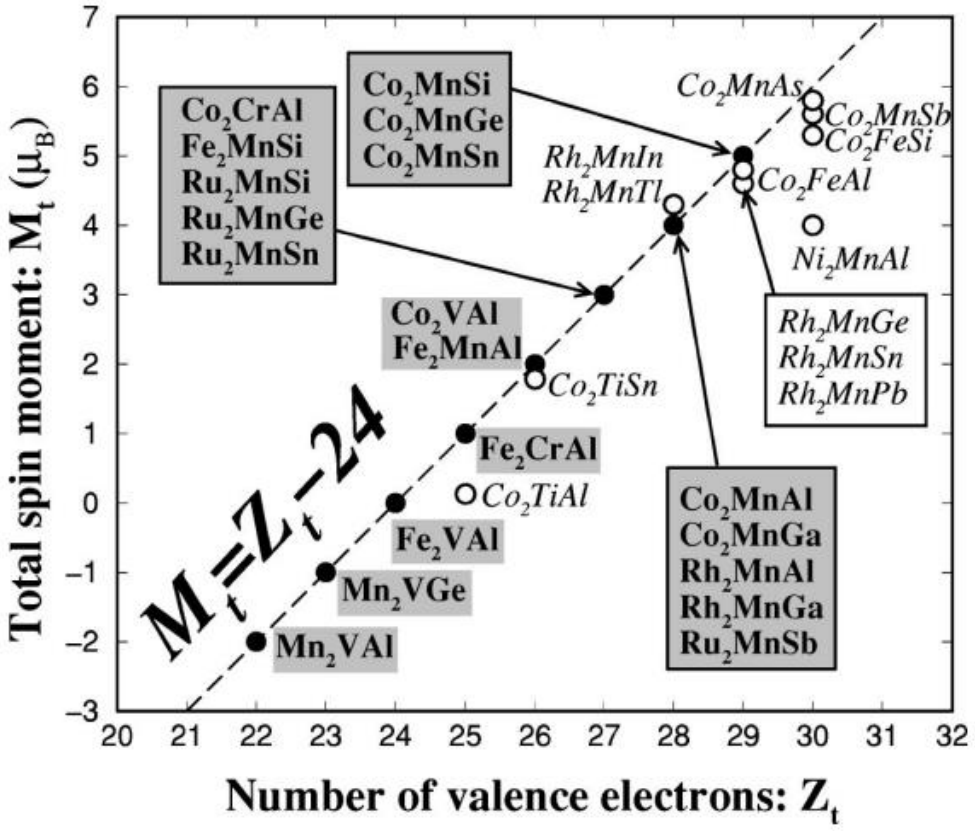

Fig 1.12. Dependence of calculated total spin moment M_t on the total number of valence electrons Z_t. The dashed line denotes the Slater-Pauling behavior. Reuse with permission [62].

1.4.3. Exchange Constants and Curie temperature

In order to implement the highly spin-polarized Heusler alloys to practical applications at room temperature, the materials should have high Curie temperature. Theoretically, Curie temperature depends on the exchange interaction between magnetic atoms. For full-Heusler compound Co_2YZ, it is required to consider the interaction between 3 kinds of magnetic atoms (Co-Co, Co-*Y*, *Y*-*Y*). Previously, conventional way to calculate the Curie temperature is by using mean-field approximation (MFA) or random-phase approximation (RPA) [63]. In the MFA,

$$\langle e^{\mu} \rangle = \frac{2}{3k_B T} \sum_{v} J_0^{\mu v} \langle e^{v} \rangle$$

where $\langle e^{\mu} \rangle$, $\langle e^{v} \rangle$ are the average *z* component of unit vector pointing in the direction of the magnetic moment $\mathbf{e}_{\mathrm{R}}^{\mu}$, $\mathbf{e}_{\mathrm{R}}^{v}$, respectively and $J_0^{\mu v} = \sum_{\mathrm{R}} J_{0\mathbf{R}}^{\mu v}$. The $J_{0\mathbf{R}}^{\mu v}$ is the exchange parameters between sublattices μ and v with the lattice vectors **R**. The equation above can be rearranged as eigenvalue matrix form:

$$(\mathbf{\Theta} - T\mathbf{I})\mathbf{E} = 0$$

where $\Theta_{\mu v} = \frac{2}{3k_B} J_0^{\mu v}$, **I** is a unit matrix, and **E** is the $\langle e^{v} \rangle$ vector. Solving this matrix will give the largest eigenvalue of $\mathbf{\Theta}$ which correspond to the Curie temperature calculated by MFA method T_C^{MFA}

While MFA method is simply the numerical average over the spin waves and mostly overestimate the Curie temperature, the RPA method is taking the harmonic average, hence giving the lower-energy spin waves more contribution and usually accurately determine Curie temperature. For the simplicity, within one magnetic sublattice, the Curie temperature calculated by RPA method T_C^{RPA} is given as:

$$\frac{1}{k_B T_C^{RPA}} = \frac{3}{2} \frac{1}{N} \sum_{q} \frac{1}{J(\mathbf{0}) - J(\mathbf{q})}$$

Using RPA method, Kubler *et al.* found good agreement between calculated Curie temperature and experimental results for various Co-based Heusler alloys [64]. Aside from that, they also observed the linear dependence of Curie temperature $T_C = 23 + 181M_t$. Since the Slater-Pauling behavior uniquely describe that magnetic moment dependence on the total number of valence electrons for half-metal, this result also establishes the linear relation between Curie temperature and total number of valence electrons, as shown in the Fig 1.13.

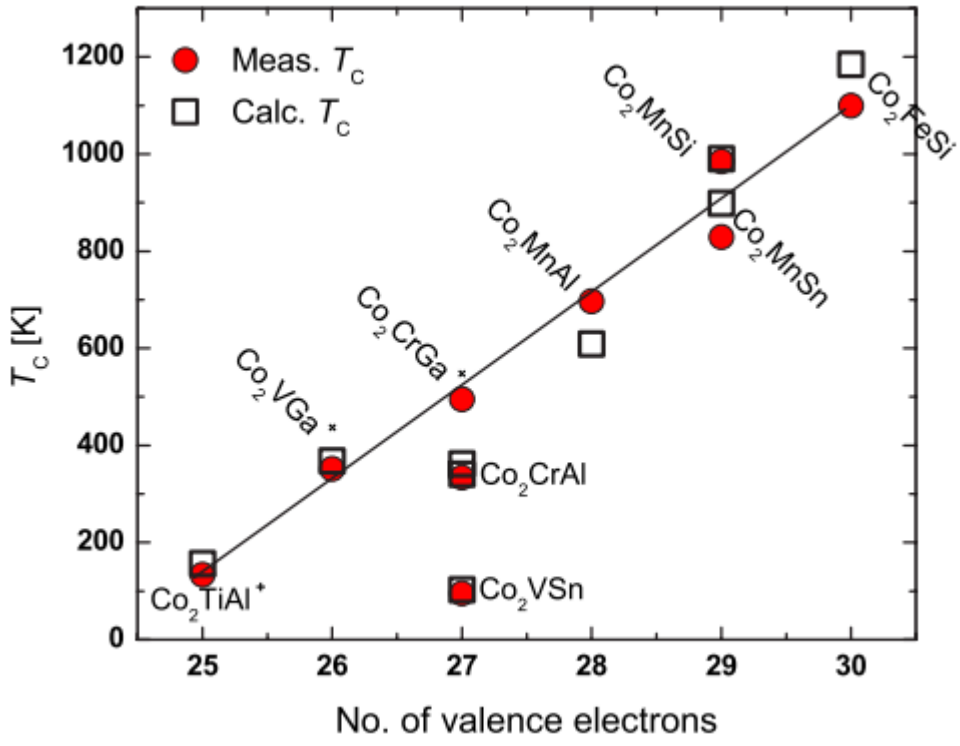

Fig 1.13. Dependence of experimentally measured and theoretically calculated Curie temperature on the total number of valence electrons Z_t. The solid line denotes the Slater-Pauling behavior expected for the Curie temperature. Reuse with permission [64].

1.4.4. Atomic disorder and off-stoichiometry

In reality, perfect $L2_1$-ordered structure of full-Heusler alloys shown in the Fig 1.10(b) is difficult to achieve due to the atomic disorder. There are several kind of atomic disorder that may happen in the full-Heusler Co_2YZ compound: (i) *Y*-*Z* swaps (lead to B2-ordered structure), (ii) Co_Y antisites (*Y* atom is replaced by a Co), (iii) Y_{Co} antisites (Co atom is replaced by a *Y*), (iv) Co-*Y* swaps (lead to $D0_3$ structure), (v) fully random swaps between Co-*Y*-*Z* atoms (lead to A2 structure).

The study of atomic disorder effect on full-Heusler alloys was started after several finding that imply the low value of experimental spin polarization in Co_2MnGe and Co_2MnSi is accompanied by the defects in the sublattices [65–67]. Picozzi *et al.* investigated the various defects type in Co_2MnSi and Co_2MnGe, and found that existence of Co antisites destroy the half-metallicity, while other kind defects basically still preserve the half-metallic gap in the electronic structure [68].

In the same time, Miura *et al.* systematically investigated the $Co_2(Cr_{1-x}Fe_x)Al$ system, and found that fully swapped Cr-Al atoms correspond to B2-ordered structure of Co_2CrAl keep the high spin polarization as shown in the Fig 1.14(a) [69]. On the other hand, Co-Cr disorder is rapidly reduce the spin polarization, consistent with finding by Picozzi *et al.* [68] This effect is due to the additional

states in minority-spin DOS contributed by Co antisites. Fortunately, total energy difference between disordered structure and perfect $L2_1$-ordered structure is significantly increases by disorder level of Co-Cr compared than that of Cr-Al, as shown in the Fig 1.14(b), implying that the harmful Co-Cr disorder is more difficult to happen. In addition, the Co-Cr structural disorder can also be detected by the change of magnetic moment as shown in the Fig 1.14(c), since the Cr antisite can involve in the antiferromagnetic coupling with another Cr atoms.

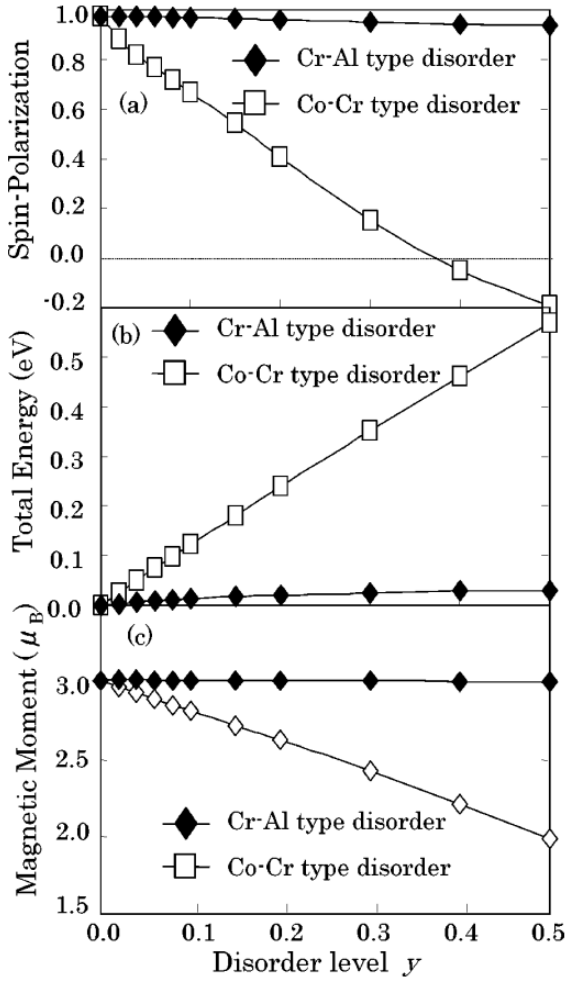

Fig 1.14. Disorder level dependence of (a) spin polarization, (b) total energy relative to that of the ordered structure, and (c) magnetic moment of Co_2CrAl. Reuse with permission from [69].

1.5. Magnetization Dynamics

Magnetization dynamics or spin dynamics is one of essential foundation of spintronics-based devices development. Basically, it refers to the dynamics of spin phase and population in an ensemble of interacting particles. Since the spin dynamics itself comprises many phenomenon in the different timescale, it is important to define the category based on the length and timescale variation.

In the Fig 1.15, the various interaction mechanism is shown with different timescales. Shortest timescale (1 fs) corresponds to coherent spin-photon interaction with mechanism of polarization intraband and interband transitions results in the coherent and decays within the dephasing time T_{2e} of the electronic levels. These processes are responsible for different optical and magneto-optical responses, especially on the spectral dependence. In the order of 10 fs, quantum fluctuation affect the local magnetization changes. Going up to 100 fs, this region represents the thermalization times $\tau_{e,s}$ of electron charge and spin due to the excited electron redistribution in *k*-space. The exchange and correlation interaction takes place in this process. While in the timescale of 1 ps, the phonon will heat the lattice due to the electron-phonon interaction. And finally, in the order of 10 ps-1 ns, the dominant effect on spin dynamics is affected by precession and damping movement.

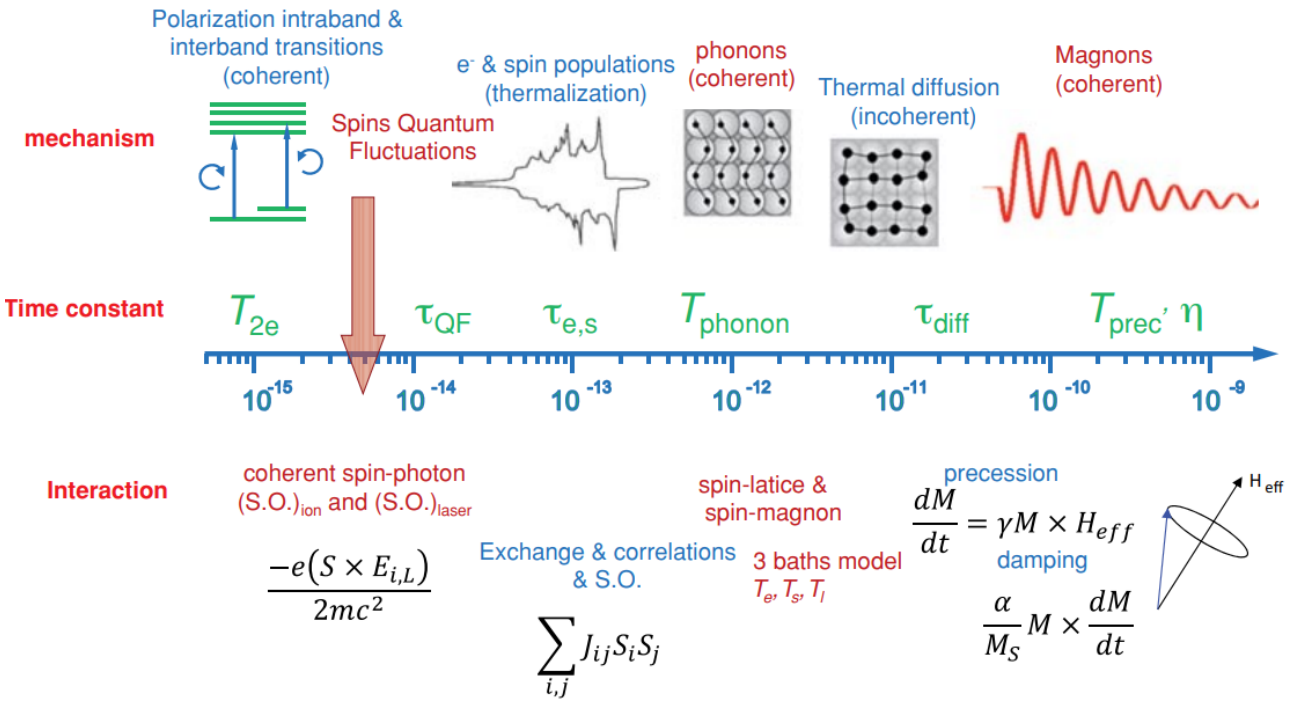

Fig 1.15. Mechanisms and interaction processes of magnetization dynamics based on different timescales. Reuse with permission [70].

Before focus into precession and damping process, there are several physical terms that need to be defined and understood. First, the effective field $\boldsymbol{H}_{eff}$ which is the partial derivative of magnetic free-energy density ϵ with respect to the magnetization at each vector coordinate (M_x, M_y, M_z)

$$\boldsymbol{H}_{eff} = -\frac{\partial \epsilon}{\partial M_x}\hat{x} - \frac{\partial \epsilon}{\partial M_y}\hat{y} - \frac{\partial \epsilon}{\partial M_z}\hat{z} \tag{1-7}$$

And usually, it consists of contribution from magnetic anisotropy, demagnetizing field, and Zeeman energy, etc. When the effective field applied on particular magnetization, the torque $\boldsymbol{\Gamma} = \boldsymbol{M} \times \boldsymbol{H}_{eff}$ is exerted, and the precession movement around the effective field happen.

Precession of the magnetization around the effective field is expressed by the equation of motion below

$$\frac{\partial \boldsymbol{M}}{\partial t} = -\gamma \boldsymbol{M} \times \boldsymbol{H}_{eff} \tag{1-8}$$

where the γ is the gyromagnetic ratio. The gyromagnetic ratio (not to be confused with the dimensionless g-factor g) is the ratio between the magnetic moment $\boldsymbol{m}_{\mathrm{J}}$ with its total spin-orbit angular momentum **J** for an electron

$$\gamma = -\frac{\boldsymbol{m}_{\mathrm{J}}}{\mathbf{J}} = \frac{g\mu_{\mathrm{B}}}{\hbar} \tag{1-9}$$

where μ_{B} is the Bohr magneton, and $\hbar$ is the reduced Planck constant. Note that the both γ and g are positive constants, because the antiparallel orientation between $\boldsymbol{m}_{\mathrm{J}}$ and **J.** The magnitude of **J** depends on the total angular momentum quantum number j via $\mathrm{J} = \hbar\sqrt{j(j+1)}$**.** On the other hand, the g-factor is considered to be related with the spin-orbit interaction strength because the assumption of $g = 2 + 2\left(\frac{m_{\mathrm{L}}}{m_{\mathrm{S}}}\right)$, with m_{L} and m_{S} are orbital- and spin-component of magnetic moment, respectively.

However, in real system, precession movement does not last forever. There are finite dissipation of energy and angular momentum toward to the effective field direction, which end up as alignment of magnetization along the effective field. This dissipation is called as damped precession, and originally defined as phenomenological effect by Landau-Lifshitz equation

$$\frac{\partial \boldsymbol{M}}{\partial t} = -\gamma \boldsymbol{M} \times \boldsymbol{H}_{eff} - \frac{\lambda}{M^2} \boldsymbol{M} \times \boldsymbol{M} \times \boldsymbol{H}_{eff} \tag{1-10}$$

where the λ is the relaxation frequency representing the damping strength. In this case, Gilbert notices that Landau-Lifshitz equation fails to explain the situation when the damping becomes very large, because the solution will give switching time approaches zero. Therefore, Gilbert proposed modified expression:

$$\frac{\partial \boldsymbol{M}}{\partial t} = -\gamma \boldsymbol{M} \times \boldsymbol{H}_{eff} + \frac{\alpha}{M} \boldsymbol{M} \times \frac{\partial \boldsymbol{M}}{\partial t} \tag{1-11}$$

where α is the Gilbert damping constant. In the very large damping ($\alpha > 1$), this modified equation result in the expected slower switching time. Since the most material have $\alpha < 1$, both of the Landau-Lifshitz and Gilbert equation are correct.

1.6. Damping Constant

As mentioned in previous part, dimensionless damping constant represent the strength of "damped" precession. Because it originated in the equation proposed by Gilbert , it is well known to be called as Gilbert damping constant. This damping govern the behavior of magnetization under applied field, especially how quickly the magnetization will finally align to the applied field, as shown in the Fig 1.16. If the damping constant is zero, the magnetization will always precess around the applied field. When the damping constant is finite small value, the precession movement will slowly ended up to align the magnetization along the field direction. On the other hand, increasing the damping constant means the faster process of this alignment. Therefore, for the switching process in the HAMR application, the large damping is required to maintain the fast switching time.

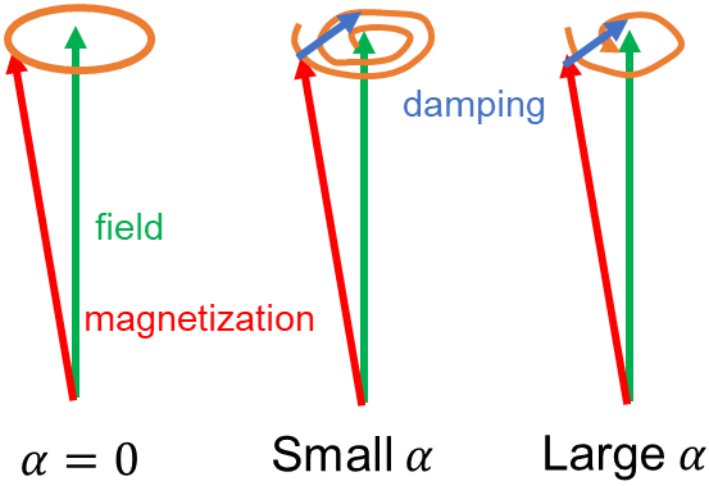

Fig 1.16. Illustration of magnetization dynamics with different value of damping constant α.

Various first principles theoretical model are developed to quantitively evaluated the damping constant, such as breathing Fermi-surface [71], torque correlation [72], and scattering theory [73]. In general, these models show that damping constant will be intrinsically exist as fundamental properties of each material even in the perfect structure. The coupling between the magnetization and other degrees of freedom allows the dissipation of magnetic energy into another systems such lattice or spin waves. Therefore, spin-orbit coupling and electron-phonon scattering plays crucial role as origin of the intrinsic damping constant. In addition, since the intrinsic damping depends on the spin-orbit coupling, heavy-metal containing compound such as FePt is expected to have large damping constant. Based on torque-correlation model [72], the damping constant is contributed from intraband and interband transition, which have conductivitylike and resistivitylike behavior, respectively. This simple model expect the nonmonotonic behavior of temperature dependence of damping, which also experimentally confirmed [74].

Aside from the intrinsic damping constant, there are also extrinsic contributions [75]. This contribution usually observed in all practical samples, and depends on the sample preparation and measurement setup. One of important factor that contribute to extrinsic damping is the sample inhomogeneities. The example of these inhomogeneities can be defects, non-uniform thickness, lattice strains. Because of this, interpretation of experimental results should be carefully clarified to separate the contribution of intrinsic and extrinsic damping.

1.7. Prospective recording media: FePt alloys

Prospective materials for recording media requires to fulfill the quadrillema of magnetic recording as shown in the Fig 1.17 [76]. First, it should allow higher areal density to meet the demand of the growing data capacity. At a glance, this can be easily solved by making the grain smaller. But it is important to keep maintaining the adequate signal to ratio (SNR), which is proportional with the logarithmic of grains per bit. Areal density (AD) itself defined as:

$$AD = \frac{total\ number\ of\ bit}{total\ area} = \frac{bit}{grains} \cdot \frac{grains}{area} = \frac{1}{grains/bit} \cdot \frac{1}{area/grains} \qquad (1\text{-}12)$$

Based on the equation (1-12), in order to keep the same grains per bit, the only way to improve the areal density is the area per grains. This means to reduce the grain size.

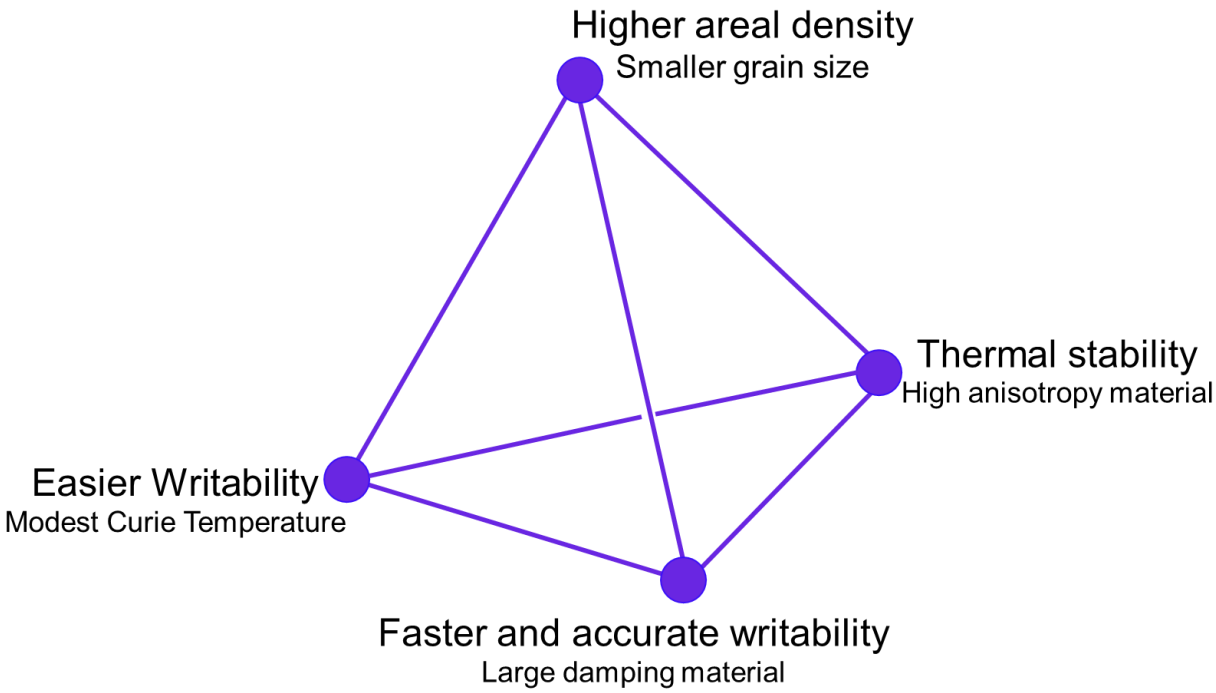

Fig 1.17. Quadrillema of magnetic recording. Figure is redrawn from [76].

However, this lead to the second part of quadrillema, which is the thermal stability. It is known that required thermal stability to retain the bit information at least for 10 years is:

$$\frac{K_U V}{k_B T} > 60 \quad (1\text{-}13)$$

where K_U is the magnetocrystalline anisotropy, k_B is the Boltzmann constant, and T is temperature. The V is the grain volume, which is product from area and height of each grain. Due to the smaller grain size for higher areal density, maintaining the inequality of equation above need the larger K_U material.

There are several candidates for large K_U materials, such as Co-based alloys (CoPtCr, Co, Co_3Pt, etc), rare-earth transition metals (RE-TM) compound ($Nd_2Fe_{14}B$, $SmCo_5$), multilayers (Co/Pt and Co/Pd) and $L1_0$ phases compound (MnAl, CoPt, FePd, and FePt) [8]. In the beginning, CoCr*XY* (*X* = Ta, Pt, and *Y* = Nb, B) alloys are proposed as first option for recording media materials. On the other hand, required phase of RE-TM compound is not easily obtained via sputtering and vulnerable of the corrosion [77]. In case of the multilayers of Co/Pt and Co/Pd, reported anisotropy after being normalized over the total media volume does not offer the significant advantage over the conventional media CoCrPt:oxide. This leads to the $L1_0$ based compound, such as FePt as prospective candidate.

When the K_U is sufficiently large, coercivity is also larger and conventional writing process cannot be done by applying write field to change the grain magnetization anymore. The Slater-Pauling limit is the natural reason behind this drawback. It is defined as upper limit of saturation magnetization of any magnetic material, which is currently held by FeCo alloys with $\mu_0 M_S = 2.45$ T. Since then, alternative writing process considering to incorporate the energy effect. This is the beginning of heat-assisted magnetic recording (HAMR), which apply heat on the recording media up to Curie temperature to reduce its coercivity. Therefore, the third part of quadrillema regarding easier writing process is solved by choosing the recording media with modest Curie temperature.

Since the writing process is carried out around the Curie temperature, *faster and accurate writability* becomes last important issues in the quadrillema of magnetic recording. The switching process at high temperature should be minimize the failure and time, too. Failure in the writing process is represented by the bit error rate (BER) parameter. Kobayashi *et al.* demonstrated that BER parameter and switching time could be minimized when the damping constant is large [78,79]. As mentioned in previous part, damping constant is also originated from SOI, so the large K_U material such as FePt is also expected to have the large damping constant

As summary, prospective material for recording media should have large K_U and damping constant for thermal stability and thermal writability. On the other hand, Curie temperature should be relatively modest to realize the efficient writing. The $L1_0$ FePt fulfill those requirement, with large

magnetocrystalline anisotropy (7×10^7 erg/cc) [80,81], relatively low T_C (750 K) [82], and large damping ($\alpha > 0.05$) [83–86].

1.8. Finite temperature effect

Finite temperature affect the magnetic system with several phenomenon as shown in the Fig 1.18.

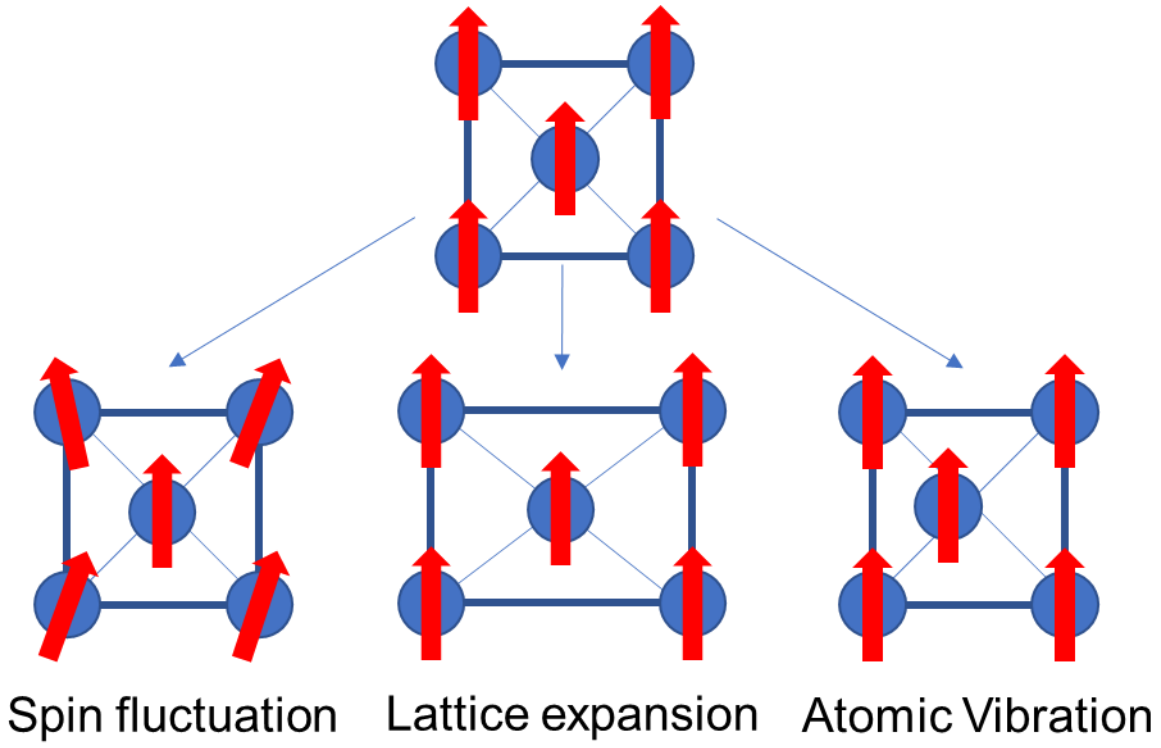

Fig 1.18. Finite temperature effect on the magnetic system.

1.8.1. Spin fluctuation

Magnetic system consisted as perfectly aligned local moment at ground state. The local moment start to fluctuate at finite temperature. This is the origin of reduction of magnetization at finite temperature, which end up to the zero magnetization when all local moments are randomly oriented at Curie temperature. Mean-field approximation can be used to understand this fluctuation in easier way. It is assumed that each local moment experiences a field B proportional with the total magnetization M

$$B = \lambda M \tag{1-14}$$

where λ is the temperature-independent proportionality constant or mean-field constant. In other words, each local moment "feel" the averaged magnetization from surrounding local moments. Complete Brillouin expression for the magnetization with ½ spin is

$$M = N\mu \tanh\left(\frac{\mu B}{k_B T}\right) = N\mu \tanh\left(\frac{\mu \lambda M}{k_B T}\right) \tag{1-15}$$

If the above equation is rewritten by introducing reduced magnetization $m = M/N\mu$ and reduced temperature $t = \frac{k_B T}{N\mu^2\lambda}$, the temperature dependence of magnetization is expressed as

$$m = \tanh\left(\frac{m}{t}\right) \tag{1-16}$$

Note that the critical temperature $t = 1$ is equivalent with $T_C = \frac{N\mu^2\lambda}{k_B}$. However, for the temperature much smaller than T_C, the tanh expression is approximated as

$$\tanh a = 1 - 2\exp(-2a) \ldots \tag{1-17}$$

And the magnetization deviation at finite temperature $\Delta M = M(0) - M(T)$ becomes

$$\Delta M \cong 2N\mu \exp(-2\lambda N\mu^2 / k_B T) \tag{1-18}$$

which give much smaller change of magnetization compared than experimental results on the low temperature.

The spin fluctuation in the magnetic system can be also be understood as spin wave. Imagine the simple one-dimension ferromagnetic system with all parallel *N* spin with magnitude *S* at ground state. The energy of the system is governed by Heisenberg interaction:

$$U = -2J \sum_{p=1}^{N} \boldsymbol{S}_p \cdot \boldsymbol{S}_{p+1} \tag{1-19}$$

where the *J* is the exchange integral, $\boldsymbol{S}_p$ is the spin angular momentum at *p* site. Classical treatment of this equation will give the $\boldsymbol{S}_p \cdot \boldsymbol{S}_{p+1} = S^2$ and ground state exchange energy as $U_0 = -2NJS^2$

There are two possible kind of excited states, first one is the when one spin is reversed. But if reversal is shared with all the spins, lower-energy excited states can be formed as “wave”. This quantized wave of spin orientation is called as magnon, which are analogous with phonons (quantized wave of atomic position). For the n_k magnon with the frequency ω_k, energy is given as

$$\epsilon_k = \left(n_k + \frac{1}{2}\right)\hbar\omega_k \tag{1-20}$$

At the particular temperature, the average number of excited magnon at mode **k** follows the Planck distribution:

$$\langle n_k \rangle = \frac{1}{\exp\left(\frac{\hbar\omega_k}{k_B T}\right) - 1} \tag{1-21}$$

And the total number of excited magnons are

$$\sum_{\mathbf{k}} n_{\mathbf{k}} = \int d\omega \, D(\omega) \, \langle n(\omega) \rangle \tag{1-22}$$

where $D(\omega)$ is the density of modes for magnons

$$D(\omega) = \frac{1}{4\pi^2}\left(\frac{\hbar}{2JSa^2}\right)^{3/2}\omega^{\frac{1}{2}} \tag{1-23}$$

This lead to the total number of magnons

$$\sum_{\mathbf{k}} n_{\mathbf{k}} = \frac{1}{4\pi^2}\left(\frac{\hbar}{2JSa^2}\right)^{3/2}\int_0^\infty d\omega\,\frac{\omega^{\frac{1}{2}}}{e^{\beta\hbar\omega}-1} = \frac{1}{4\pi^2}\left(\frac{k_{\mathrm{B}}T}{2JSa^2}\right)^{3/2}\int_0^\infty dx\,\frac{x^{\frac{1}{2}}}{e^{x}-1} = 0.0587\left(\frac{k_{\mathrm{B}}T}{2JSa^2}\right)^{3/2} \tag{1-24}$$

Since number of N atoms per unit volume is Q/a^3 and Q is the number of atoms in the unit cell. Fractional change of magnetization $\frac{\Delta M}{M(0)}$ is defined as

$$\frac{\Delta M}{M(0)} = \frac{\sum_{\mathbf{k}} n_{\mathbf{k}}}{NS} = \frac{\sum_{\mathbf{k}} n_{\mathbf{k}}}{QS}a^3 = \frac{0.0587}{QS}\left(\frac{k_{\mathrm{B}}T}{2JS}\right)^{3/2} \tag{1-25}$$

which show dependency of magnetization with $T^{\frac{3}{2}}$ terms. This dependency, is also called as Bloch law and successfully explained the experimental results.

1.8.2. Lattice expansion

Lattice expansion is the consequence of anharmonicity in the crystal interactions. Assume a pair of atoms at finite temperature *T*, the potential energy of atoms at particular displacement *x* from the equilibrium position at ground state is defined as:

$$U(x) = ax^2 - bx^3 - cx^4 \tag{1-26}$$

where ax^2 represents the only harmonic terms, bx^3 represents the asymmetric repulsion of atoms, and cx^4 represents the vibration softening at large amplitudes. The existence of anharmonic terms lead to the possibility that global minimum for potential energy is not located at $x = 0$. Therefore, the average displacement calculated by Boltzmann distribution is:

$$\langle x\rangle = \frac{\int_{-\infty}^{\infty} dx\; x\exp[-\beta U(x)]}{\int_{-\infty}^{\infty} dx\;\exp[-\beta U(x)]} \tag{1-27}$$

with $\beta = 1/k_{\mathrm{B}}T$. In case of anharmonic terms are much smaller than $k_{\mathrm{B}}T$, the integrands could be expanded into

$$\int_{-\infty}^{\infty} dx\;\; x\exp[-\beta U(x)] \cong \int dx\,[\exp(-\beta a x^2)](x + \beta b x^4 + \beta c x^5) = \left(\frac{3\pi^{\frac{1}{2}}}{4}\right)\left(\frac{b}{a^{\frac{5}{2}}}\right)\beta^{-\frac{3}{2}} \tag{1-28}$$

$$\int_{-\infty}^{\infty} dx\;\exp[-\beta U(x)] \cong \int dx\,[\exp(-\beta a x^2)] = \left(\frac{\pi}{\beta a}\right)^{\frac{1}{2}} \tag{1-29}$$

and the thermal expansion becomes:

$$\langle x\rangle = \frac{3b}{4a^2}k_{\mathrm{B}}T \tag{1-30}$$

1.8.3. Atomic vibration

In case of the atomic vibration, the similar approach to quantized energy of so-called *phonon* with angular frequency ω and quantum number n is also provided by the equation:

$$\epsilon = \left(n + \frac{1}{2}\right)\hbar\omega$$

where the $\frac{1}{2}\hbar\omega$ terms are required to represent the zero-point energy due to resemblance with the quantum harmonic oscillator. The average of thermal equilibrium occupancy of phonons $\langle n_v(\mathbf{q}, T)\rangle$ at particular phonon mode index v, wave vector $\mathbf{q}$ and temperature T is then given by the Planck distribution.

$$\langle n_v(\mathbf{q}, T)\rangle = \frac{1}{\exp\left(\frac{\hbar\omega_v(\mathbf{q})}{k_B T}\right) - 1}$$

The expected value of squared atomic displacement of becomes as

$$\langle |u_\alpha(jl, t)|^2\rangle = \frac{\hbar}{2Nm_j}\sum_{\boldsymbol{q},v} \omega_v(\boldsymbol{q})^{-1}(1 + 2n_v(\boldsymbol{q}, T))\,|e_v^\alpha(j, \boldsymbol{q})|^2$$

1.9. Status of current research

1.9.1. Magnetoresistance effect and spin polarization

The Valet-Fert model [87] and Julliere model [6] emphasize the importance of highly spin-polarized materials such as full-Heusler alloys to obtain the large MR ratio in the GMR and TMR, respectively. However, there is no satisfactory results obtained until at 2004, when the $L2_1$-ordered $Co_2Cr_{0.6}Fe_{0.4}Al$ (CCFA) demonstrated the MR effect across the insulating phase of grain boundary [88]. This finding is followed by Inomata *et al.* which use B2-CCFA as an electrode in the MTJ and obtained the TMR ratio of 16% at RT and 26.5% at 5 K, respectively [89]. It also triggered the similar research to advance the CPP-GMR performance, which is initiated by Yakushiji *et al.* using $L2_1$ Co_2MnSi (CMS) resulting in the GMR ratio of 2.4% at RT [90]. Since then, the incorporation of highly-spin polarized Heusler alloys for GMR and TMR devices is widely investigated and significantly developed, as shown in the Fig 1.19(a)-(b). Mostly, the Co_2Mn- and Co_2Fe-based compound is used due to their high Curie temperature. Until 2018, the top three materials with largest MR ratio in both TMR and CPP-GMR devices are CMS, CFGG, and CFMS, which are already theoretically predicted as half-metal by different research groups [91–93].

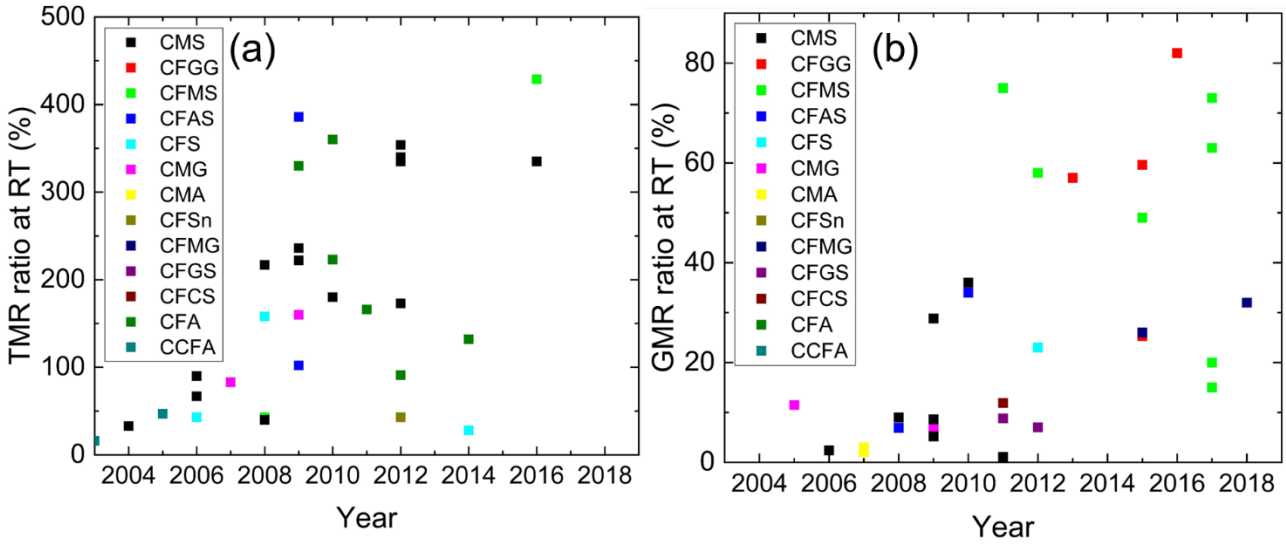

Fig 1.19. (a) GMR ratio and (b) TMR ratio at room temperature using full Heusler alloy electrodes over the years. (CMS: Co_2MnSi, CFGG: $Co_2FeGa_{0.5}Ge_{0.5}$, CFMS: $Co_2Fe_xMn_{1-x}Si$, CFAS: $Co_2FeAl_{0.5}Si_{0.5}$, CFS: Co_2FeSi, CMG: Co_2MnGe, CMA: Co_2MnAl, CFSn: Co_2FeSn, CFMG: $Co_2Fe_{0.4}Mn_{0.6}Ge$, CFGS: $Co_2FeGa_{0.5}Sn_{0.5}$, CFCS: $Co_2Fe_xCr_{1-x}Si$, CFA: Co_2FeAl, CCFA: $Co_2Cr_xFe_{1-x}Al$. Source from [94] and [95].

However, although it is true that MR devices using full-Heusler alloys such CMS, CFGG, and CFMS at room temperature demonstrated highest recorded MR ratio, its value much larger at low temperature as shown in the Fig 1.20(a)-(b). In the Fig 1.20(a), the TMR ratio of CMS/Al-O/CMS at low temperature is much larger than its counterpart CMS/Al-O/CoFe and CoFe/Al-O/CoFe, before getting the similar value with CMS/Al-O/CoFe at room temperature. Similarly, the strong temperature dependence also observed in CPP-GMR devices for CFGG/Ag/CFGG shown in the Fig 1.20(b). There are several proposed explanations behind this reduction. For the TMR, when two ferromagnetic electrode is in antiparallel configuration, thermally excited magnon may cause the spin-flip inelastic tunneling process [96]. This process is enhanced by minority-spin in-gap states in the bulk region and minority-spin interface states at the interface of ferromagnetic/barrier which inevitably exists at finite temperature. It involves two interchangeably steps, which are spin-flip scattering of majority-spin electron into minority spin in-gap or interface states and electrons tunneling from minority spin into majority-spin. Since the number thermally excited magnon is increasing as temperature rises, the spin-flip inelastic tunneling process will increase antiparallel conductance or equivalently decrease antiparallel resistance, hence reduce the MR ratio. Similar picture can be adopted for CPP-GMR, although the interface states is not significant due to metallic conduction in the parallel configuration [97]. Note that MR effect in the CPP-GMR is due to the spin-asymmetric electron scattering, unlike the tunneling in TMR.

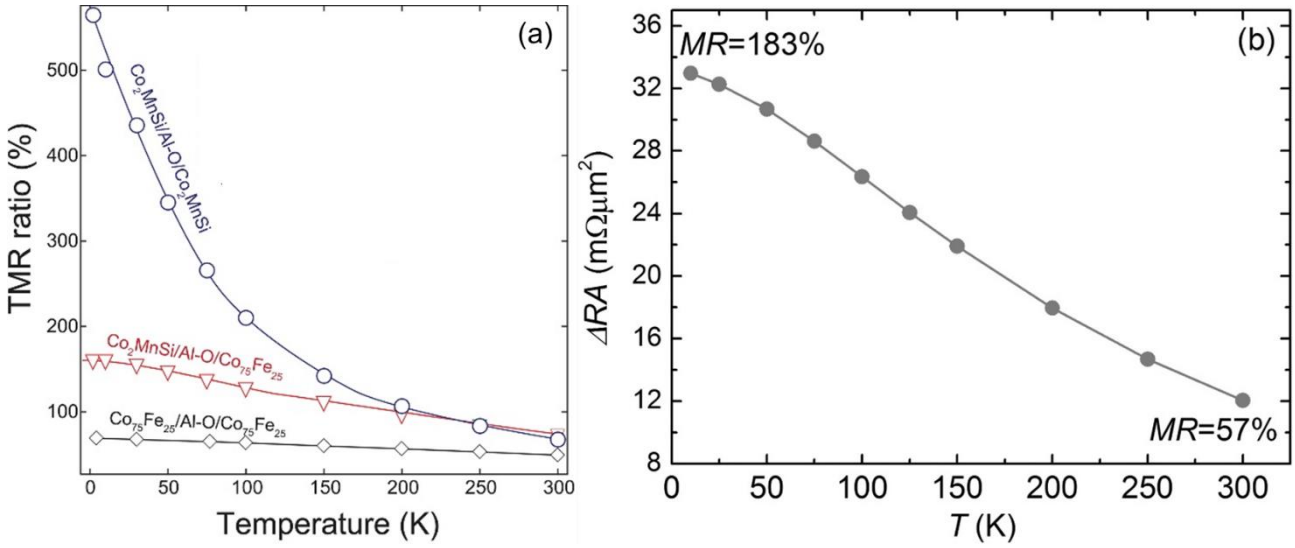

Fig 1.20. Temperature dependence of MR ratio in (a) TMR devices of CMS/Al-O/CMS, CMS/Al-O/CoFe, CoFe/Al-O/CoFe, and (b) CPP-GMR devices of CFGG/Ag/CFGG. Reuse with permission [98,99].

Stacking structures of multilayers that allow the MR effect emphasizes the importance of the interface quality on transport properties. In the TMR devices with MgO crystalline barrier, coherent tunneling from effective coupling between electrode and barrier Δ_1 states are the dominant mechanism behind the giant MR ratio [100], which is very sensitive to the interface structure, unlike the AlOx amorphous barrier. Unfortunately, despite the MnSi terminated Co_2MnSi/MgO interfaces is thermodynamically stable, it is not half-metallic anymore due to nonbonding character of Mn $3d_{yz}$ and $3d_{xz}$ orbitals, which may enhance unwanted tunneling conductance in the antiparallel magnetic configuration [101]. On the other hand, in the CPP-GMR, the interface spin asymmetry γ can be also qualitatively predicted based on the matching of Fermi surface between electrode and spacer layer, leading up the large γ for typical interface of Co_2MnSi/Ag compared to the Co_2MnSi/Cr [102]. However, the value interface spin asymmetry may also reduce at elevated temperature due to the decaying of perfect interface quality, no matter what kind of spacer used.

Another possible explanation is the reduction of bulk spin polarization of ferromagnetic electrode. Since the Valet-Fert model and Julliere model show strong correlation between MR ratio with the bulk spin polarization parameter, if the spin polarization reduces at finite temperature, the MR ratio will also reduce. In order to know the temperature dependence of spin polarization, one should understand how the electronic structure change by temperature. Using dynamical mean-field theory, Chioncel *et al.* demonstrated that nonquasiparticle appear within the minority-spin gap just above Fermi level as shown in Fig 1.21(a) [103]. These nonquasiparticle may exist as superpositions of virtual magnon and excited majority spin electrons, hence dynamical many-body effect should be

taken into account using DMFT. At finite temperature, the nonquasiparticle states is broadened and crossing the Fermi level, hence reducing the spin polarization. However, they also reported the spectral weight redistribution as peak of majority-spin states shift closer toward the Fermi level as increasing temperature. Experimentally, Miyamoto *et al.* observed the photoemission spectra at low and room temperature shown in the Fig 1.21(b) [104]. Due to the energy resolution, they cannot confirm the change in the minority-spin state as predicted by Chioncel *et al.* [103] The obtained spectra also demonstrated the identical results between 30 and 300 K, without any peak-shifting predicted by DMFT calculation. It lead to conclusion that the decay of spin polarization may not be due to the existence of nonquasiparticle states, or strongly correlated electron picture of DMFT is not suitable to describe the magnetism behavior of Heusler alloys.

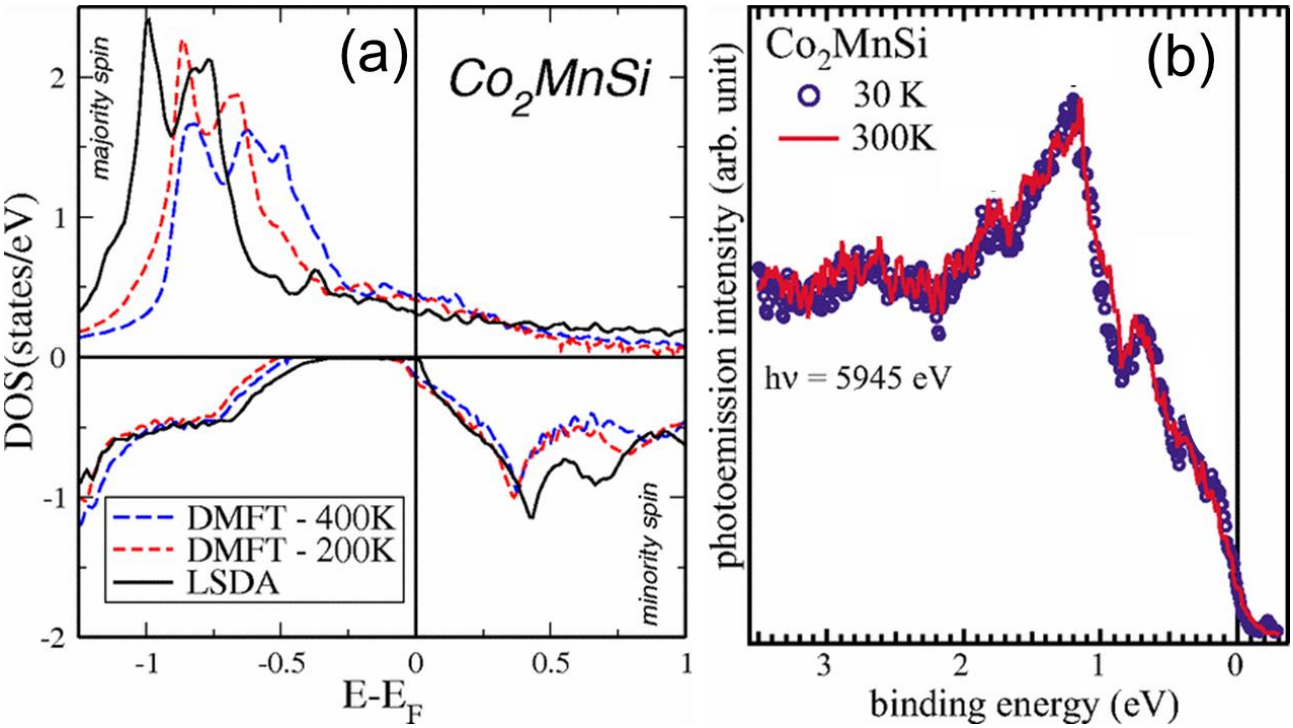

Fig 1.21. Temperature dependence of (a) spin-resolved density of states calculated by DMFT method (b) valence-band photoemission spectra of of Co_2MnSi. Reuse with permission [104,105].

On the other hand, disordered local moment (DLM) method [106] offer the treatment of spin fluctuations as mean-field approximation of local moment, which may be better option to properly describe the Heusler alloys. Using this method, Lezaic *et al.* investigated the decay of spin polarization in half-Heusler NiMnSb [107]. They found that temperature dependence of spin polarization is much stronger than the temperature dependence of magnetization. In the NiMnSb, the decay of spin polarization is originated by change of hybridization strength between *d* states of Ni and Mn, which lead to the shifting of minority spin valence band edge toward Fermi level, hence

destroy the half-metallic gap and reduce the spin polarization. However, they did not report how electronic structure change at finite temperature, therefore the superiority of DLM method over DMFT cannot be confirmed.

Recently, Nawa *et al.* incorporate the DLM method to obtain the electronic structure and spin polarization of CMS at finite temperature [108]. They found that spin polarization is strongly reduced at finite temperature due to contribution from Co *d* minority-spin states. Moreover, the majority-spin valence states also show insignificant peak-shifting which agree with the photoemission spectra reported by Miyamoto *et al.* [104] Their work demonstrated the feasibility of DLM method to explain the significant reduction of spin polarization at finite temperature. They also compare the calculation results with the experimental results of TMR device, and found that the reduction of experimental spin polarization is much stronger than the calculation. This discrepancy can be attributed to the spin-flip inelastic tunneling effect that is not considered from the calculation.

1.9.2. HAMR switching time and damping constant

In the HAMR, magnetization of grains is switched by heat up the recording media to reduce the coercivity near Curie temperature, and followed by applying field to change the magnetic direction [33]. Using the basic assumption for the single magnetic domain, Kikuchi proposed that magnetization switching time τ is given by

$$\tau \propto \frac{1+\alpha^2}{\alpha H}$$

where the α is Gilbert damping constant and H is the applied field [109]. The above equation will give the minimum switching time when $\alpha = 1$. Since the most materials has $\alpha \ll 1$, the switching time will inversely proportional with the damping constant, which imply the large damping constant is preferable for the HAMR application, as illustrated in the Fig 1.22. However, the wide temperature range from storing the information at ambient temperature up to writing the information at near Curie temperature lead to additional requirement, that damping constant behavior should be well understood over those range.

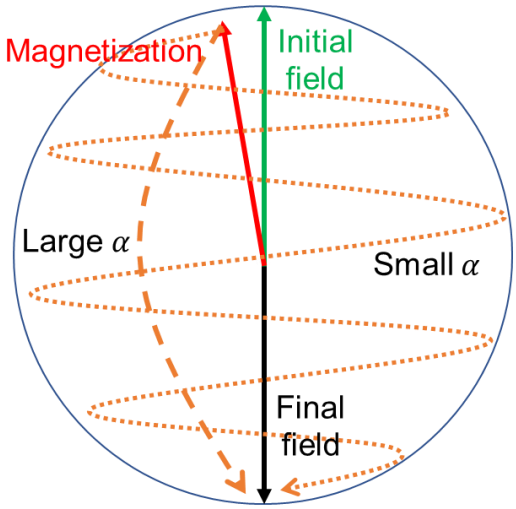

Fig 1.22. Illustration of switching process for large and small damping materials.

There are several way to measure the damping. One of the oldest method is ferromagnetic resonance (FMR) spectroscopy. In this method, oscillating radio-frequency (rf) magnetic field is applied to the sample under the fixed bias field. The rf magnetic field should be set in perpendicular direction relative to the bias field. This rf field will induce the coherent precession motion of spins, hence the magnetization of the materials will also precess. By changing the rf field, the resonance can happen when the angular frequency of rf field is equal to the precession frequency. Since the precession movement at resonance frequency will absorb the rf field power, using Fourier transformation, one may obtain the power spectrum as a function of the frequency. Lorentzian function can be used to fit the spectra curve, and the linewidth of curve corresponds to the effective damping.

Recently, Richardson *et al.* reported the FMR linewidth ΔH of FePt samples is reduced by increasing temperature as shown in the Fig 1.23 [110]. In the FMR experiments, effective damping α_{eff} can be estimated using:

$$\alpha_{\text{eff}} = \frac{\sqrt{3}|\gamma|\Delta H}{4\pi f}$$

where $|\gamma|$ is the absolute gyromagnetic ratio and f is the microwave frequency. The reduction of FMR linewidth imply that the effective damping may reduce near Curie temperature, which will be harmful for the switching time of HAMR.

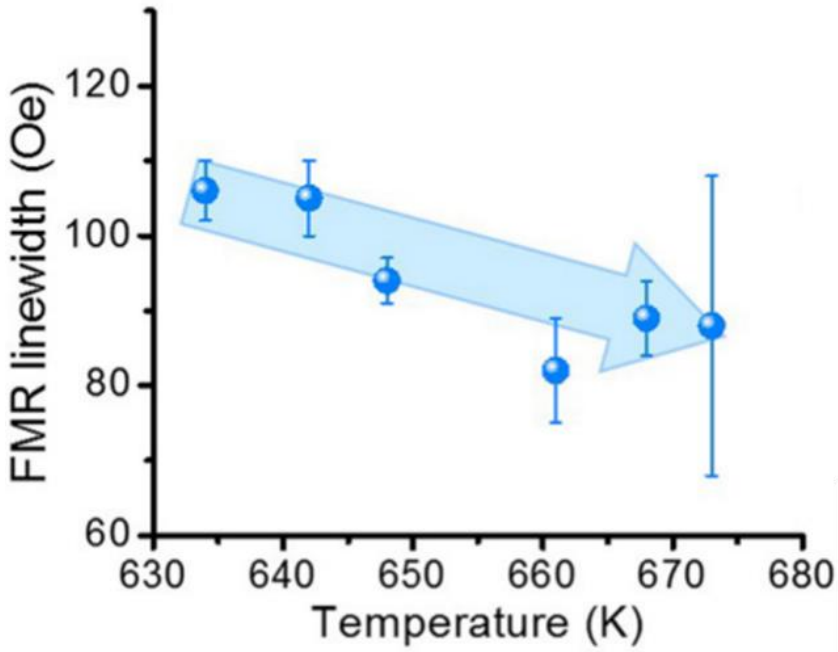

Fig 1.23. Temperature dependence of FMR linewidth reported by Richardson *et al.* Reuse with permission [110].

It is important to note that effective damping consists the total contribution of intrinsic and extrinsic damping. The intrinsic damping is mainly originated from spin-orbit coupling, while the extrinsic contribution is due to the sample inhomogeneities. One of the notable extrinsic contribution is two-magnon scattering mechanism. In the FMR experiment, this mechanism could happen when an uniform precession mode excited by FMR scatters into degenerate states of non-uniform precession mode. Surely, the scattering process is enhanced by increasing scattering centers or inhomogeneities such local defects, non-uniform sample thickness, or any substrate imperfections and also proportional with the square of anisotropy field.

In their work, Richardson *et al.* proposed that the significant reduction of FMR linewidth observed near Curie temperature is due to two-magnon scattering which correspond to the extrinsic contribution of damping [110]. Since the magnetic anisotropy is drastically drop around Curie temperature, the two-magnon scattering contribution is also significantly reduced at finite temperature. Note that they measure granular FePt film with variation of carbon volume fraction for their sample. This motivates Strungaru *et al.* [111] to simulate FMR spectra using atomistic-spin-dynamics (ASD) method. They used ASD simulations because the finite-size effect and magnon scattering become dominant in the granular media can be properly treated within ASD method. It is found that the damping is increasing by increase of temperature, due to the more magnon modes excited, and this effect is more pronounced in the granular systems, where the surface effect is

included. Therefore, the Strungaru *et al.* pointed out that measured FMR linewidth of Richardson *et al.* consists the inhomogeneous line broadening part due to the distribution of grain properties [110,112]. Near the Curie temperature, superparamagnetism is experienced by some grains, hence give less contribution and decrease the FMR linewidth.

Although Strungaru *et al.* demonstrated that the FMR linewidth reduction does not necessarily mean that the damping is also reduced, they extract the damping value using simulation of FMR spectra and attributed the increase of damping due to the extrinsic effect [112]. Meanwhile, the temperature dependence of intrinsic damping is not deeply investigated theoretically. Using Kambersky torque correlation model [72], one may obtain the rough yet intuitive picture of intrinsic damping at the finite temperature. The simplified equation is:

$$\alpha \propto \xi \frac{\mathrm{DOS}(E_F)}{M_s}$$

where ξ is the spin-orbit coupling, $\mathrm{DOS}(E_F)$ is the total density of states at Fermi level, and M_s is the magnetization. Due to the spin fluctuation, M_s will significantly drops to zero near Curie temperature, therefore assuming that ξ and $\mathrm{DOS}(E_F)$ retaining its value, the damping will increase as temperature increases. It is confirmed by recent calculation reported by Hiramatsu *et al.* on FePt [113], which confirm that the damping is significantly increase around Curie temperature as shown in the Fig 1.24. Note that the increase of damping at finite temperature is a simple yet still incomplete picture of the damping based on Kambersky torque correlation model, because there is other competing contribution which decrease the damping by increase of temperature (intraband contribution). On the other hand, atomic vibration is also another important effect at finite temperature aside spin fluctuation. However, the lattice dynamics effect on the temperature dependence of damping is only theoretically investigated in Fe, Co, Ni using the frozen thermal lattice disorder [114].

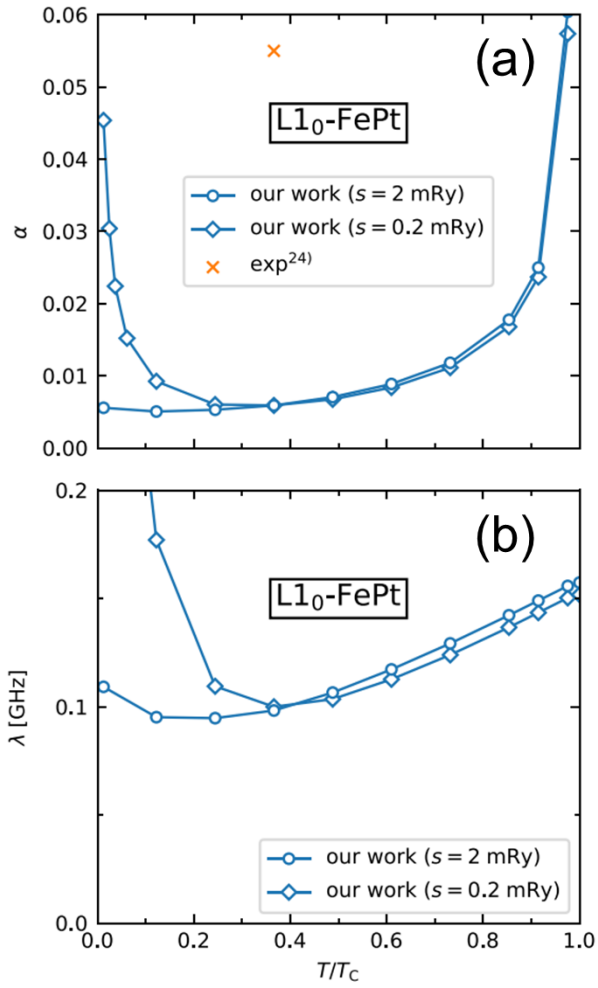

Fig 1.24. Temperature dependence of (a) damping and (b) Landau frequency $\lambda(T) = |\gamma|\alpha(T)M(T)$ using different value of scattering rate correspond to the residual resistivity. Reuse with permission [113].

1.10. The purpose and contents of doctoral thesis

On the basis of previous introductions, understanding of finite temperature effect on spin polarization and damping constant is inevitably significant for prospective materials of read-head sensor and recording media. Therefore, this thesis will focus on three aspects. First, how the spin fluctuation affects the spin polarization of half-metallic Heusler alloys such as $Co_2FeGa_{0.5}Ge_{0.5}$ (CFGG) and Co_2MnSi (CMS) will be clarified. This finding led to the second aspect when the finite temperature first-principles calculation is combined with the machine learning to search other alternative highly-spin polarized Heusler alloys at finite temperature. Lastly, the lattice dynamics effect on the damping constant of FePt is investigated to get an insight on its behavior at high temperature.

The thesis comprises of 6 chapters. Chapter 1 introduces the research background and issues in magnetoresistance devices and magnetization dynamics at finite temperature. Chapter 2 gives theoretical background on the first principles calculation and finite temperature effect. Chapter 3

describes results of temperature dependence of spin polarization of Heusler alloys. Chapter 4 studies the machine learning study of highly spin-polarized Heusler alloys. Chapter 5 studies the temperature dependence of damping constant in FePt. Chapter 6 summarizes the above works, and put forward future perspectives

Chapter 2: Theoretical background

2.1. Density Functional Theory (DFT)

Understanding the electronic structure of materials is the key to explain their interesting macroscopics properties. The electronic structure itself is a consequence of interaction between subatomic particles (electrons and ions) within materials driven by quantum mechanical rule. Schrodinger equation [115] formulates this simply as:

$$H\Phi = E\Phi \tag{2-1}$$

where the Hamiltonian H contains the potential and kinetic terms of all particles, the wave function Φ of all particles in the systems, and E is eigenvalue corresponds to the total energy of the systems. In the hydrogen atom, this equation can be easily solved due to the simple interaction between one electron and one proton. However, for the helium and rest of elements in the periodic table, this equation will become impossible to be solve accurately because more particles complicates the interaction within materials (potential electrons-electrons, electrons-ions, and ions-ions, and kinetic of electrons and ions). This is the origin of the many-body problems terms. In order to simplify this problem, the Born-Oppenheimer approximation [116] is used to neglect the kinetic terms of ions since the ion mass is much larger than electrons. Therefore, the Hamiltonian becomes

$$H = E = V + T + U \tag{2-2}$$

$$V = \sum_i v(r_i) \tag{2-3}$$

$$T = \sum_i -\nabla_i^2 \tag{2-4}$$

$$U = \sum_{i<j} \frac{2}{|r_i - r_j|} \tag{2-5}$$

where V, T, U are the external potential which contains the interaction between electrons and ions, kinetic energy of electrons, and Coulomb energy between electrons, respectively.

If there are *N*-particles, the wave function solution of many-body problems is the function from at least 3*N* spatial degrees of freedom, and added by spin for each electron in the magnetic materials. This means a very complex problem which need suitable approximations to solve. One of the beautiful and clever approximation is density functional theory (DFT) which based on the two Hohenberg-Kohn theorems [117]. The first theorems states that the ground state total energy E for

non-spin polarized system is given uniquely as a function of the ground state electron density $\rho(r)$ as

$$E = E[\rho] \tag{2-6}$$

and by minimization of $E[\rho]$ via variational principle, the second theorem states that the true ground state electron density and other related ground state properties are also functional of the ground state electron density. Electron density itself is depends on the 3 spatial degrees of freedom, which means drastic reduction of problem complexity from 3*N* to 3 by DFT as shown in **Fig 2.1**.

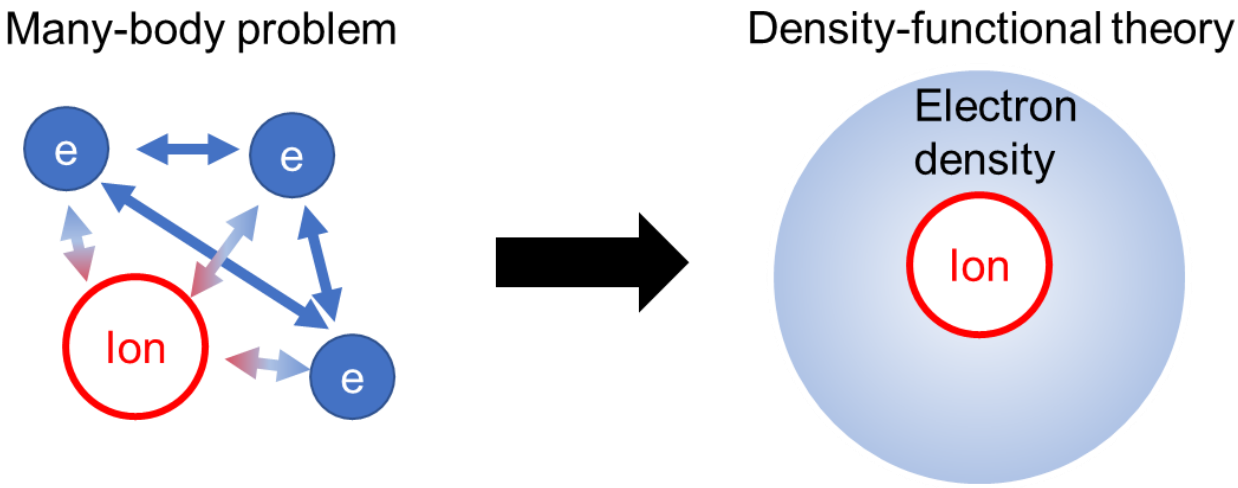

Fig 2.1. Simplification of many-body-problem into density functional theory (DFT)

In the magnetic materials, spin is additional yet crucial degree of freedoms. The treatment of spin in the DFT is quite straightforward by replacing the non-spin polarized electron density ρ with the majority ($\rho^{\uparrow}$) and minority ($\rho^{\downarrow}$) spin densities

$$E = E[\rho^{\uparrow}, \rho^{\downarrow}] \tag{2-7}$$

For simplicity, total energy of non-spin polarized particular systems follows:

$$E[\rho] = V[\rho] + T[\rho] + U[\rho] \tag{2-8}$$

The external potential as a functional of electron density is can also expressed as:

$$V[\rho] = \int d\boldsymbol{r}\, v(\boldsymbol{r})\rho(\boldsymbol{r}) \tag{2-9}$$

where $v(\boldsymbol{r})$ is originated from underlying lattice of atomic nuclei and other external sources aside from the materials itself.

Although the $E[\rho]$ is exact for any quantum mechanical system, but there is no exact form for $T[\rho]$, $U[\rho]$ as functional of $\rho(\boldsymbol{r})$ which make the Hohenberg-Kohn theorems cannot be directly utilized unless the accurate and efficient approximations are provided. One year after Hohenberg-Kohn proposed their theorem, Kohn and Sham solved the problems with representing the electron density of interacting particles with electronic wave function of non-interacting ones [118]. The total energy becomes:

$$E[\rho] = \int d\boldsymbol{r}\, v(\boldsymbol{r})\rho(\boldsymbol{r}) + T_s[\rho] + E_H[\rho] + E_{xc}[\rho] \tag{2-10}$$

where the $T_s[\rho]$ corresponds to the single-particle kinetic energy functional under non-interacting assumptions,

$$T_s[\rho] = \sum_{i=1}^{N} \langle \psi_i(r) | -\nabla_i^2 | \psi_i(r) \rangle \tag{2-11}$$

which depends on the diagonalization of single-particle wave functions $\psi_i(r)$. Since T_s is functional of density and fulfill the Pauli principle, the electron density is given by

$$\rho(\boldsymbol{r}) = \sum_{i=1}^{N} \psi_i(r)\, \psi_i^*(r) \tag{2-12}$$

The $E_H[\rho]$ is the Hartree component of the electron-electron interaction,

$$E_H[\rho] = \iint \frac{\rho(\boldsymbol{r})\rho(\boldsymbol{r}')}{|r'-r|} dr dr' \tag{2-13}$$

The $E_{xc}[\rho]$ is the exchange-correlation energy functional, which contains the difference between $T[\rho]$ and $T_s[\rho]$ and contribution of $U[\rho]$ which go beyond the electrostatic interaction between electron-electron. This is unknown part and must be approximated.

Therefore, total energy expression can be rewritten by replacing every component with the corresponding part as follows:

$$E[\rho] = \int d\boldsymbol{r}\, v(\boldsymbol{r})\rho(\boldsymbol{r}) + T_s[\rho] + \iint \frac{\rho(\boldsymbol{r})\rho(\boldsymbol{r}')}{|r'-r|} dr dr' + E_{xc}[\rho] \tag{2-14}$$

and the one-electron Kohn-Sham equation is derived as follow:

$$\left[-\nabla_i^2 + V_{eff}(r)\right]\psi_i(r) = \varepsilon_i(r)\psi_i(r) \tag{2-15}$$

with an effective Kohn-Sham potential $V_{eff}(r)$ as:

$$V_{eff}(r) = v_{ion}(\boldsymbol{r}) + \int \frac{\rho(\boldsymbol{r})}{|r'-r|} dr + v_{xc}(\boldsymbol{r}) \tag{2-16}$$

Altogether, the complex many-body problems reduced into the one-electron interacting with the effective field. The effective field also depends on the electronic charge density and final solution of eigenvalues ε_i and one-particle wave function ψ_i can be determined by self-consistent field iteration. Different approach to solve the Kohn-Sham equations was proposed, most common are first one which based on the basis sets, and second one which usually called as multiple scattering theory or Green's function method, developed by Korringa, Kohn, and Rostoker (KKR) [119,120].

2.2. Korringa-Kohn-Rostoker (KKR) method

By using Green functions, the KKR method solves the wave equation. This method separates the purely geometric aspects of the crystal lattice from the dynamics correspond with the atoms in the material. Each value of energy and crystal momentum was directly & independently deduced and no need to employ a variational principle or orthogonalization. Using this method is very efficient and able to solve the geometry problem of an impurity in the bulk without replacing it by an ersatz (additional, inferior) geometry such as a finite cluster or a supercell. The availability of the Green functions could be employed into disorder alloys, transport, and spectroscopy problems.

For ordered systems, we start to apply the multiple scattering theory by representing each scattering site (atom or ion) as a potential of a finite range. Then space is divided into distinct sub-volumes so that scattering from a scatterer point stopped before the next scattering event happens. Hence, crystal potential is

$$V(r) = \sum_n V_n(r - R_n) \equiv \sum_n V_n(r_n), \tag{2-17}$$

Which $V_n(r)$ is an individual contribution of an atom on site R_n. Meanwhile $r_n = r - R_n$ show the subtraction of vector r from the origin and the vector R_n of the atomic site n. If the potentials of individual scatterers are isotropic and do not overlap with other potentials, it is called a *muffin-tin approximation* (MTA). Meanwhile, in an anisotropy situation, a cell potential could be expanded in spherical harmonics $Y_L(r)$ to fill the atomic and interstitial space regions.

$$V_n(r_n) = \sum_L V_{nL}(r_n) Y_L(r_n). \tag{2-18}$$

Then we could present the Kohn-Sham equation based on the Green function:

$$[-\Delta_r + V(r) - E]G(r, r'; E) = -\delta(r - r'). \tag{2-19}$$

In order to calculate electronic structure, we need to connect between the Green function $G(r, r'; E)$ of a perturbed system H with the Green function $G^0(r, r'; E)$ of an unperturbed system H^0 by the Dyson equation

$$G(E) = G^0(E) + G^0(E)VG(E) = G^0(E) + G(E)VG^0(E) = G^0(E) + G^0(E)T(E)G^0(E) \tag{2-20}$$

With $V = H - H^0$ as the perturbation potential and T as scattering matrix. By iterating the Equation (4), we will obtain

$$T(E) = V + VG^0(E)T(E) \tag{2-21}$$

Due to the separation of single-site and crystal quantities, we construct the Green function of the crystal potential starting from the Green function of an isolated potential. Using a free-particle Green function $G^0(r, r'; E)$ in the real-space, we obtain the Dyson equation for the single-site Green function

$$G_S(r, r'; E) = G^0(r, r'; E) + \int dr'' \int dr''' G^0(r, r''; E)\, t(r'', r'''; E) G^0(r''', r'; E), \tag{2-22}$$

In the Equation above, t-matrix represents the scattering from a single-site potential, which is diagonal for a spherical potential. Next, the free-particle Green function can be expanded in the angular momentum basis.

$$G_0(r, r'; E) = -ip \sum_L j_l(pr_<) h_l^+(pr_>) Y_L(r) Y_L^*(r'), \tag{2-23}$$

Which $j_l(z)$ and $h_l(z)$ are spherical Bessel and Hankel functions and $p = \sqrt{E}$. Then, matrix elements of the single-scattering t-matrix are defined as

$$t_{LL'}^n(E) = \int dr_n \int dr_n' j_l(pr_n) t(r_n, r_n'; E) j_{l'}(pr_n') Y_L(r_n) Y_L^*(r_n'), \tag{2-24}$$

Single-scattering Green function is expressed below:

$$G_S(r_n, r_n'; E) = \sum_{LL'} Z_L^n(r_n; E) t_{LL'}^n(E) Z_{L'}^{n\times}(r_n'; E) - \sum_L Z_L^n(r_<; E) J_L^{n\times}(r_>; E). \tag{2-25}$$

Meanwhile, the Green function is constructed by regular $Z_L(r; E)$, and irregular $J_L(r; E)$, solutions of the radial Schrödinger equation at the particular complex energy E,

$$Z_L^n(r_n; E) = \sum_{L'} Z_{LL'}^n(r_n; E) Y_{L'}(r_n), \tag{2-26}$$

$$Z_L^{n\times}(r_n; E) = \sum_{L'} Z_{LL'}^n(r_n; E) Y_{L'}^*(r_n), \tag{2-27}$$

$$J_L^n(r_n; E) = \sum_{L'} J_{LL'}^n(r_n; E) Y_{L'}(r_n). \tag{2-28}$$

The radial parts of $Z_L^n(r_n; E)$ and $J_L^n(r_n; E)$ functions are matched to spherical Bessel $j_l(z)$ and Hankel $h_l(z)$ functions outside the potential range ($r \geq S$) :

$$Z_{LL'}^{n}(r_n; E) = j_l(pr_n)t_{LL'}^{n}(E)^{-1} - iph_l^{+}(pr_n)\delta_{LL'}, \quad (2\text{-}29)$$

$$J_{LL'}^{n}(r_n; E) = j_l(pr_n)\delta_{LL'}. \quad (2\text{-}30)$$

From normalization conditions of the wave functions, one could determine t-matrix and corresponding phase shifts. In case of assembly of atoms, the scattering operator is defined as

$$T(E) = \sum_n t^n(E) + \sum_{n\neq m} t^n(E)G^0(E)t^m(E) + \cdots \quad (2\text{-}31)$$

The equation above naturally separates into partial sums which are characterized by fixed-site indices n and m at the leftmost and rightmost single-site t-matrix, respectively. Then, we could define:

$$T(E) = \sum_n \tau^{nm}, \quad (2\text{-}32)$$

Which $\tau^{nm}(E)$ as the scattering path operator which consists of all possible scattering events between the two cells n and m. Then, in case of real-space multiple scattering theory, the Green function for any arrangement of atoms can be expressed in terms of the scattering path operator $\tau^{nm}(E)$:

$$G(r_n, r_m'; E) = \sum_{LL'} Z_L^n(r_n; E)\,\tau_{LL'}^{nm}(E)Z_{L'}^m(r_n'; \varepsilon) - \sum_L Z_L^n(r_<; E)J_L^m(r_>; E)\delta_{nm} \quad (2\text{-}33)$$

For general electronic systems, the τ-matrix is implicitly defined in terms of the t-matrix and the structure constants $g(E)$ represents the free-electron Green function and can be found from the matrix equation as shown below

$$\tau(E)^{nm} = \{[t(E)^{-1} - g(E)]^{-1}\}_{nm}. \quad (2\text{-}34)$$

The equation above is the heart of the KKR Green function method after completing the separation of the potential from the structural aspects of the material.

2.3. Disordered local-moment (DLM) method

The basic assumption of DLM theory is magnetic system consisted by perfectly aligned local magnetic moment at ground state as shown in the **Fig 2.2** [121]. These local moments may be originated from itinerant or localized electrons. Hence, we can designate the direction $\vec{\hat{e}}_i$ and magnitude μ_i for each local moment at the i-th site. Increasing temperature leads to the local moment direction $\vec{\hat{e}}_i$ fluctuation corresponds to the higher-energy DLM microstates. It is important to note that DLM theory assume no change on longitudinal magnitude μ_i. Therefore, this theory only applicable to the system with magnitudes $\mu_i \geq 1\,\mu_B$ due to retained magnetization at elevated temperature.

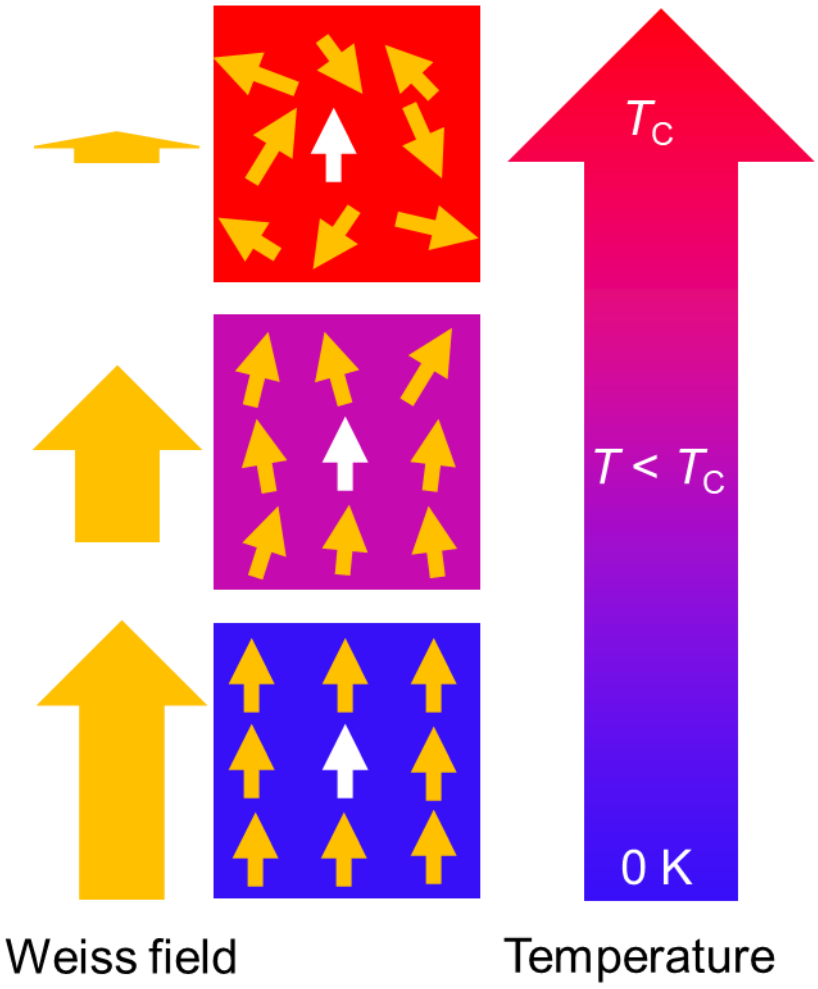

Fig 2.2. Illustration of disordered local moment method

Classical treatment of fluctuation of the local moments are used in DLM theory. Imagining a sphere where direction $\vec{\hat{e}}_i$ may take any orientation, so we can define a microstate using a set of direction vector $\{\vec{\hat{e}}_i\}$, and its energy as grand potential of $\Omega(\{\vec{\hat{e}}_i\})$. The probability to find our system in this microstate is

$$P(\{\vec{\hat{e}}_i\}) = \exp[-\beta\,\Omega(\{\vec{\hat{e}}_i\})]/Z \tag{2-35}$$

Where the partition function $Z = \int d\vec{\hat{e}}_1 d\vec{\hat{e}}_2 \ldots \exp[-\beta\Omega(\{\vec{\hat{e}}_i\})]$ and $\beta = 1/(k_B T)$ with k_B as Boltzmann's constant and T as temperature.

Basically, grand potential $\Omega(\{\vec{\hat{e}}_i\})$ can be calculated via constrained spin-DFT method, imposing constraints on the integrals of magnetization and charge density to the user-defined values. Since $\{\vec{\hat{e}}_i\}$ corresponds to the all of local moment orientations instead of simple unit cell. Hence, integration

over the structure considered in this calculation will be computationally expensive. Instead, we "approximate" the statistical mechanics using auxiliary grand potential Ω_0

$$\Omega_0\left(\{\vec{\hat{e}}_i\}\right) = -\sum_i \vec{h}_i \cdot \vec{\hat{e}}_i \tag{2-36}$$

Where the vector $\{\vec{h}_i\}$ corresponds to the "Weiss fields". Weiss field is the magnetic field felt by each local moment and generated from surrounding local moment. Large Weiss field means high degree of magnetic order implying low temperature condition. For the sake of convenience, the Weiss field and direction unit vector $\vec{n}_i$ is introduced as "beta-h"/lambda $\vec{\lambda}_i = \beta\vec{h}_i$ and $\vec{n}_i = \frac{\vec{\lambda}_i}{\lambda_i}$, respectively. Analytical solution of statistical mechanics lead to the single-site probability factorization

$$P_0\left(\{\vec{\hat{e}}_i\}\right) = \prod_i P_{0i}\left(\vec{\hat{e}}_i\right) \tag{2-37}$$

$$P_{0i}\left(\vec{\hat{e}}_i\right) = \frac{\exp[\vec{\lambda}_i \cdot \vec{e}_i]}{\left(\frac{4\pi}{\lambda_i}\right)\sinh\lambda_i} \tag{2-38}$$

For each local moment $\vec{m}_i$, order parameter is defined as $\langle\vec{\hat{e}}_i\rangle_{0,T}$. The $\langle\ \rangle_{0,T}$ denotes a thermal average, and

$$\vec{m}_i = \int d\vec{\hat{e}}_i\, P_{0i}\left(\vec{\hat{e}}_i\right)\vec{\hat{e}}_i \prod_{j\neq i}\int d\vec{\hat{e}}_j\, P_{0j}\left(\vec{\hat{e}}_j\right) = L(\lambda_i)\vec{n}_i \tag{2-39}$$

Where $L(\lambda_i)$ is the Langevin function, $L(\lambda_i) = \frac{1}{\tanh\lambda_i} - \frac{1}{\lambda_i}$. Equation above indirectly imply the directions and magnitudes of the order parameters are determined by the Weiss fields, and also small "beta- h" is also means to low magnetic order parameter.

There should be thermodynamic inequality between Helmholtz energy of auxiliary $F_0(T)$ and true system $F(T)$, connected by $\mathcal{F}(T)$ which is upper bound of the $F(T)$

$$\mathcal{F}(T) = F_0(T) - \langle\Omega_0\rangle_{0,T} + \langle\Omega\rangle_{0,T} \tag{2-40}$$

In order to minimize $\mathcal{F}(T)$ via $\nabla_{\vec{h}_i}\mathcal{F} = 0$, we can obtain best Weiss fields

$$\vec{h}_i = -\nabla_{\vec{m}_i}\langle\Omega\rangle_{0,T} = -\frac{3}{4\pi}\int d\vec{\hat{e}}_i \langle\Omega\rangle_{0,T}^{\vec{\hat{e}}_i}\vec{\hat{e}}_i \tag{2-41}$$

Where the $\langle\ \rangle_{0,T}^{\vec{\hat{e}}_i}$ denotes the thermal average over all orientations except for the ith moment, which is fixed at the $\vec{\hat{e}}_i$ orientation. Strong correlation between order parameter, grand potential, and temperature is shown. Consequence of these relations are nonzero solutions of Weiss field is only obtained when temperature is smaller that Curie temperature. Interestingly, despite DLM method

solving the fully relativistic Kohn-Sham-Dirac Equation non-self-consistently, the Equation above indirectly implied the self-consistency due to the dependence of thermal average of grand potential $\langle\Omega\rangle_{0,T}^{\vec{\hat{e}}_i}$ on the probability $P_{0i}(\vec{\hat{e}}_i)$ which fixed by the Weiss fields.

2.4. Bayesian Optimization

When the output results cannot be simply understood from the input, corresponding function is called a black-box problem. In order to solve this problem efficiently, Bayesian optimization is widely known to be used to solve this problem by reducing the uncertainty after obtaining new value of black box function at particular candidates as shown in the **Fig 2.4**. As an example, let us define a set of candidates as a part of d-dimensional vectors $\boldsymbol{x}_1, \ldots, \boldsymbol{x}_m \in \Re^d$. For each candidate point $\boldsymbol{x}_i$, the value of black-box function y_i can be evaluated via experiments or theoretical calculation. When n number of candidates points are already evaluated, we have training data set $D = \{\boldsymbol{x}_i, y_i\}_{i=1}^n$, and the next point will be evaluated sequentially until predetermined number of evaluation are done.

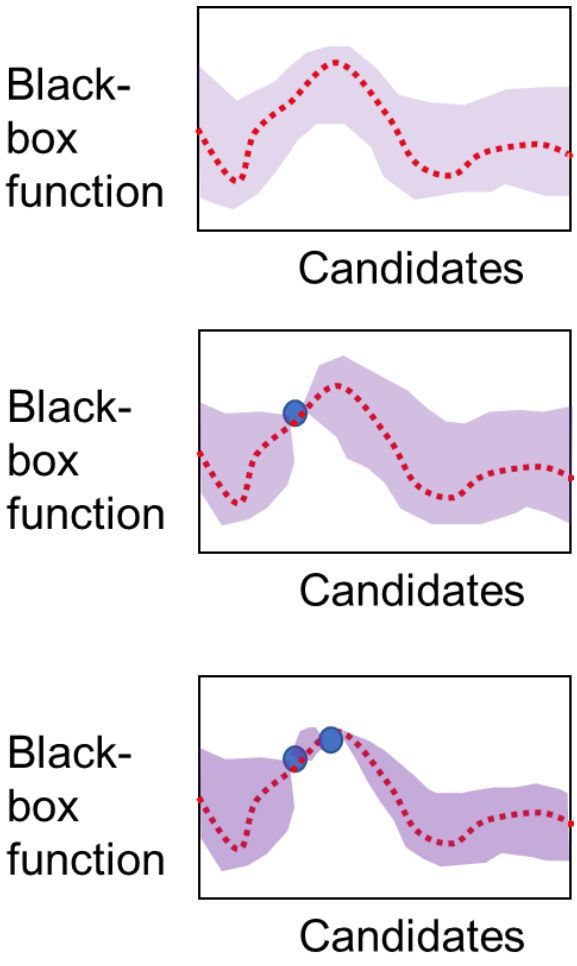

Fig 2.3. Optimization of black box function. Red dashed line correspond to the unknown true function, purple area is uncertainty, and blue point correspond to the evaluated function.

One way to determine which candidate points need to be evaluated is by Thompson sampling algorithm. This algorithm choose the candidate points with the highest probability to be optimal point. Therefore, prediction model is necessary, such as Bayesian linear regression model.

$$y = \boldsymbol{w}^{\mathsf{T}}\boldsymbol{\phi}(\boldsymbol{x}) + \epsilon \tag{2-42}$$

where $\boldsymbol{w}$ represents weight vector, $\boldsymbol{\phi}$ represents feature map, $\boldsymbol{x}$ represents input vector of a candidate point, and ϵ represents noise subject of $\mathcal{N}(0, \sigma^2)$. Posterior distribution which contains information of prior distribution and likelihood function of $\boldsymbol{w}$ for a particular dataset of D is

$$\boldsymbol{w}|D \sim \mathcal{N}(\boldsymbol{\mu}, \Sigma) \tag{2-43}$$

with $\boldsymbol{\mu} = (\boldsymbol{\Phi}\boldsymbol{\Phi}^{\mathsf{T}} + \sigma^2 I)^{-\mathbf{1}}\boldsymbol{\Phi}\boldsymbol{y}$, $\Sigma = \sigma^2(\boldsymbol{\Phi}\boldsymbol{\Phi}^{\mathsf{T}} + \sigma^2 I)^{-\mathbf{1}}$, and $\boldsymbol{\Phi}$ is the $\ell \times n$ matrix where $\boldsymbol{\phi}(\boldsymbol{x}_i)$ is the i-th column. Based on this model, predicted value for candidate point $\boldsymbol{x}_i$ is $\boldsymbol{w}^{\mathsf{T}}\boldsymbol{\phi}(\boldsymbol{x}_i)$. Therefore, optimal area of $\boldsymbol{w}$ with optimal $\boldsymbol{x}_i$ is defined as

$$W_i = \{\boldsymbol{w} \in \Re^{\ell} | \boldsymbol{w}^{\mathsf{T}}\boldsymbol{\phi}(\boldsymbol{x}_i) = \min_j \boldsymbol{w}^{\mathsf{T}}\boldsymbol{\phi}(\boldsymbol{x}_j)\} \tag{2-44}$$

The probability of candidate point $\boldsymbol{x}_i$ to be optimal is $p_i = P(\boldsymbol{w} \in W_{\boldsymbol{i}}|D)$. However, Thompson sampling can choose the next point which has highest probability even without calculating the p_i directly. Instead, a vector $\boldsymbol{s}$ is sampled from posterior distribution $P(\boldsymbol{w} \mid D)$, and candidate point with minimum score is determined:

$$i^* = \underset{i}{\operatorname{argmin}}\, \boldsymbol{s}^{\mathsf{T}}\boldsymbol{x}_i \tag{2-45}$$

The computational cost to evaluate the above equation is much smaller compared than other methods such as maximum probability of improvement and maximum expected improvement.

Let us define the:

$$A = \tfrac{1}{\sigma^2}\boldsymbol{\Phi}\boldsymbol{\Phi}^{\mathsf{T}} + I \tag{2-46}$$

where the posterior distribution is $\boldsymbol{w}|D \sim \mathcal{N}\left(\left(\tfrac{1}{\sigma^2}\right)A^{-1}\boldsymbol{\Phi}\boldsymbol{y}, A^{-1}\right)$. Each step of Thompson sampling will require the triangular decomposition of A^{-1}. Since new training data $(\boldsymbol{x}', y')$ is sequentially added to the existing training data set, the updated matrix A' is:

$$A' = A + \tfrac{1}{\sigma^2}\boldsymbol{\phi}(\boldsymbol{x}')\boldsymbol{\phi}(\boldsymbol{x}')^{\mathsf{T}} \tag{2-47}$$

Saving computational time is preferred, therefore the Cholesky decomposition of L of A is kept by $A = L^{\mathsf{T}}L$, and for every new data, only L is quickly updated without calculating the A from the scratch.

The sampled vector $\boldsymbol{s}$ is represented as $\boldsymbol{\mu} + \boldsymbol{s}_0$ where $\boldsymbol{s}_0$ is a sample from $\mathcal{N}(0, A^{-1})$. Thus, the following equation:

$$L^{\mathsf{T}}L\boldsymbol{\mu} = \frac{1}{\sigma^2}\Phi\boldsymbol{y} \tag{2-48}$$

will have mean vector $\boldsymbol{\mu}$ as the solution. On the other hand, sampling of $\boldsymbol{z}\sim\mathcal{N}(0, l)$ will give us the $\boldsymbol{s}_0$ and $\boldsymbol{z} = L\boldsymbol{s}_0$ is solved.

Important factor in Bayesian optimization performance is the choice of feature map ϕ. Random feature map can be used to approximate the induced mapping by Gaussian kernel of unit width:

$$k(\Delta) = \exp(-\left|\left|\Delta\right|\right|^2/2) \tag{2-49}$$

According to Bochner's theorem, the equation above can be rewritten as

$$k(\boldsymbol{x} - \boldsymbol{x}') = \int \exp\left(j\boldsymbol{\omega}^{\mathsf{T}}(\boldsymbol{x} - \boldsymbol{x}')\right) p(\boldsymbol{\omega}) d\boldsymbol{\omega} \tag{2-50}$$

where the j is the imaginary unit and

$$p(\boldsymbol{\omega}) = (2\pi)^{-\frac{d}{2}} \exp\left(-\frac{\left|\left|\boldsymbol{\omega}\right|\right|^2}{2}\right) \tag{2-51}$$

Here, we introduce the $z_{\omega,b}(\boldsymbol{x}) = \sqrt{2}\cos(\boldsymbol{\omega}^{\mathsf{T}}\boldsymbol{x} + b)$. If the $\boldsymbol{\omega}$ is determined from $p(\boldsymbol{\omega})$ and b is uniformly drawn from $[0, 2\pi]$, then

$$E\left[z_{\boldsymbol{\omega},b}(\boldsymbol{x}) z_{\boldsymbol{\omega},b}(\boldsymbol{x}')\right] = k(\boldsymbol{x} - \boldsymbol{x}') \tag{2-52}$$

The feature map in COMBO is defined in a way the Gaussian kernel of width η is approximated by inner product of $\phi(\boldsymbol{x})^{\mathsf{T}}\phi(\boldsymbol{x}')$ via $\exp\left(-\left(\left(\left|\left|\boldsymbol{x} - \boldsymbol{x}'\right|\right|^2\right)(2\eta^2)\right)\right)$. When ℓ random samples of $\{\boldsymbol{\omega}_i, b_i\}_{i=1}^{\ell}$, the feature map becomes:

$$\phi(\boldsymbol{x}) = (z_{\boldsymbol{\omega}_i,b_i}\left(\frac{\boldsymbol{x}}{\eta}\right), \ldots, z_{\boldsymbol{\omega}_\ell,b_\ell}\left(\frac{\boldsymbol{x}}{\eta}\right))^{\mathsf{T}} \tag{2-53}$$

In case of infinite ℓ, Bayesian linear model will resembles the Gaussian process.

It is important to note that σ and η are hyperparameters that difficult to be manually determined. Hence, in COMBO these parameters can be automatically set by maximizing the type-II likelihood described by $p(D|\sigma,\eta)$. Initialization of the hyperparameters is done by heuristic procedure, while the tuning is repeatedly performed in each sequential step. However, this tuning may take more computational time than the Bayesian optimization itself.

2.5. Projector Augmented Wave (PAW) method

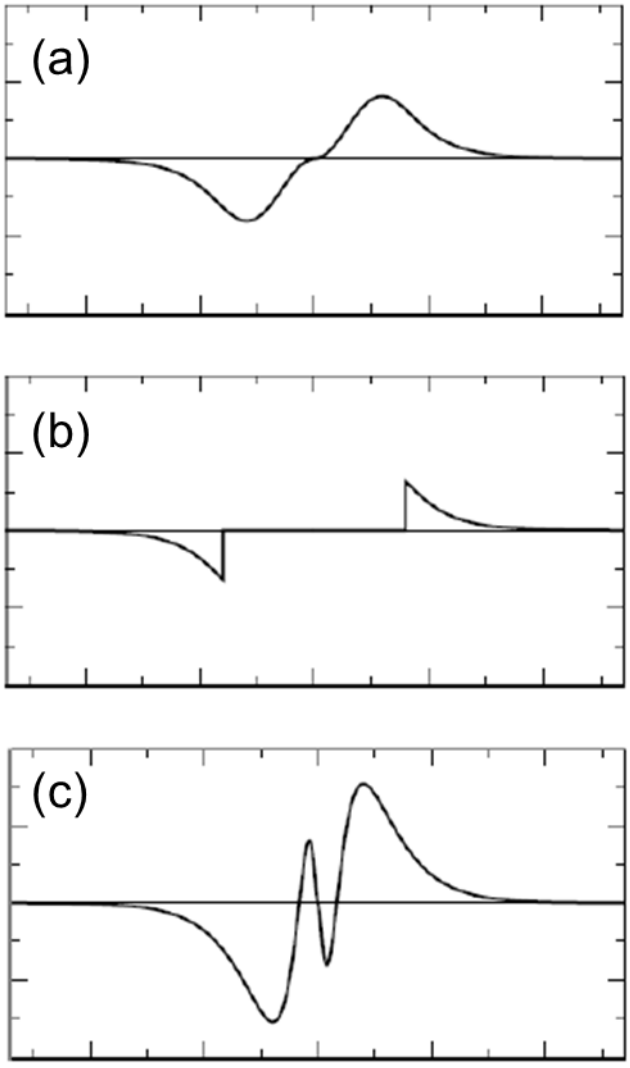

Fig 2.4. The construction of PAW orbitals.

In the projector-augmented wave (PAW) method [122], one electron wavefunction or orbital $\psi_{n\mathbf{k}}$ is defined by linear transformation:

$$|\psi_{n\mathbf{k}}\rangle = |\tilde{\psi}_{n\mathbf{k}}\rangle + \sum_i (|\phi_i\rangle - |\tilde{\phi}_i\rangle)\langle\tilde{p}_i|\tilde{\psi}_{n\mathbf{k}}\rangle \quad (2\text{-}54)$$

where $\tilde{\psi}_{n\mathbf{k}}$ are pseudo orbitals with n, $\mathbf{k}$ are band and k-point index, respectively. Similarly, construction of orbital is illustrated in the **Fig 2.4**(a)-(c). Pseudo orbitals are demonstrated in the **Fig 2.4**(a), followed by the substractions of $|\tilde{\phi}_i\rangle\langle\tilde{p}_i|\tilde{\psi}_{n\mathbf{k}}\rangle$ in the **Fig 2.4**(b), and finally completed by adding the $|\phi_i\rangle\langle\tilde{p}_i|\tilde{\psi}_{n\mathbf{k}}\rangle$ component in the **Fig 2.4**(c)

It is important to note that between the PAW spheres, $\tilde{\psi}_{n\mathbf{k}} = \psi_{n\mathbf{k}}$. However, within the spheres, auxiliary function is required to picture the orbitals accurately. In the reciprocal space, the pseudo orbitals are expanded using plane waves

$$\langle\mathbf{r}|\tilde{\psi}_{n\mathbf{k}}\rangle = \frac{1}{\Omega^{\frac{1}{2}}}\sum_{\mathbf{G}} C_{n\mathbf{k}\mathbf{G}} e^{i(\mathbf{G}+\mathbf{k})\cdot\mathbf{r}} \tag{2-55}$$

Where Ω is the volume of the Wigner-Seitz cell. Then, we can define the all-electron partial waves ϕ_α at the atomic site $\mathbf{R}_\alpha$ as the solutions of Schrodinger equation at the specific energy ε_α and angular momentum l_α

$$\langle\mathbf{r}|\phi_\alpha\rangle = \frac{1}{|\mathbf{r}-\mathbf{R}_\alpha|}u_\alpha(|\mathbf{r}-\mathbf{R}_\alpha|)Y_\alpha(\widehat{\mathbf{r}-\mathbf{R}_\alpha}) = \frac{1}{|\mathbf{r}-\mathbf{R}_\alpha|}u_{l_\alpha\varepsilon_\alpha}(|\mathbf{r}-\mathbf{R}_\alpha|)Y_{l_\alpha m_\alpha}(\widehat{\mathbf{r}-\mathbf{R}_\alpha}) \tag{2-56}$$

Note that $\widehat{\mathbf{r}-\mathbf{R}_\alpha}$ emphasize that spherical harmonics *Y* only depends on the orientation and not on the magnitude of vectors. Therefore, the pseudo partial waves $\tilde{\phi}_\alpha = \phi_\alpha$ in the interstitial region, and continuously suit within core radius.

$$\langle\mathbf{r}|\tilde{\phi}_\alpha\rangle = \frac{1}{|\mathbf{r}-\mathbf{R}_\alpha|}\tilde{u}_\alpha(|\mathbf{r}-\mathbf{R}_\alpha|)Y_\alpha(\widehat{\mathbf{r}-\mathbf{R}_\alpha}) = \frac{1}{|\mathbf{r}-\mathbf{R}_\alpha|}\tilde{u}_{l_\alpha\varepsilon_\alpha}(|\mathbf{r}-\mathbf{R}_\alpha|)Y_{l_\alpha m_\alpha}(\widehat{\mathbf{r}-\mathbf{R}_\alpha}) \tag{2-57}$$

Total charge density is equal with

$$n(\mathbf{r}) = \psi^*_{n\mathbf{k}}(\mathbf{r})\psi_{m\mathbf{k}}(\mathbf{r}) \tag{2-58}$$

2.6. Kambersky Torque Correlation Model

In the Kambersky torque correlation model [72], the precession movement of local moment in the ferromagnet is affected by interaction with conduction electron via spin-orbit torque. This picture is closely related with the Brownian motion of particle in the water as shown in the **Fig 2.5**.

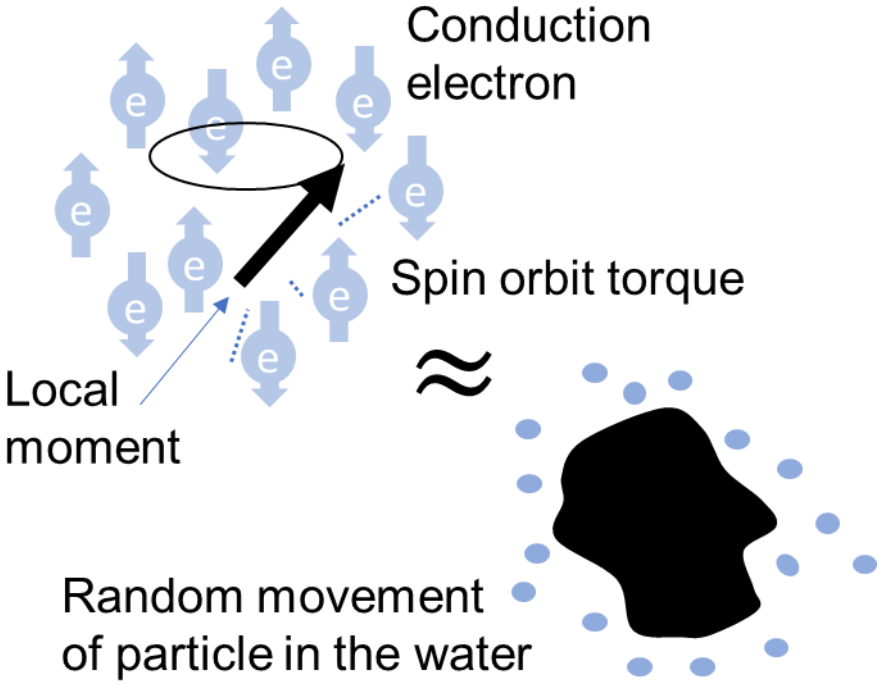

Fig 2.5. Illustration of interaction between local moment and conduction electron in the Kambersky Torque correlation model.

Therefore, Hamiltonian of the ferromagnetic system is described as follows:

$$H = H_{unperturbed} + H_{perturbation} = H_{kinetic} + H_{spin-orbit} + H_{FM\ exchange} + H_{perturbation} = \sum_{ij} t_{ij} c_i^+ c_j + \zeta \vec{L} \cdot \vec{S} + \Delta S_z + \frac{\Delta}{\langle S^z \rangle} (\langle S^+ \rangle S^- + \langle S - \rangle S^+) \quad (2\text{-}59)$$

The magnetization dynamics of spin operator (microscopic picture) can be shown as:

$$\frac{dS^-(t)}{dt} = \frac{i}{\hbar}\left[H_{unperturbed}, S^-(t)\right] \quad (2\text{-}60)$$

$$\frac{dS^-(t)}{dt} = -i\Omega S^-(t) - \left\{\int_0^{t'} dt' \frac{\langle[\varphi(t'), \varphi^+]\rangle_0}{\hbar M} S^-(t - t')\right\} - i\varphi^-(t) \quad (2\text{-}61)$$

$$\frac{dS^-(t)}{dt} = -i\Omega S^-(t) - i\eta^-(t) - \int_0^t P^{-1} \langle[\eta^-(t'), \eta^+]\rangle_0 S^-(t) dt' \quad (2\text{-}62)$$

Where $-i\Omega S^-(t)$ corresponds to the precession term, $i\eta^-(t)$ is spin-torque from SOI term and $\int_0^t P^{-1}\langle[\eta^-(t'), \eta^+]\rangle_0 S^-(t)dt'$ is damping term. Basic derivation of Kambersky torque correlation model is to connect the expression between microscopic and macroscopic susceptibility.

The microscopic susceptibility is expressed

$$\chi^+(\omega) = -\frac{\mu_0 (g\mu_B)^2}{\hbar V} \frac{\hbar M}{\omega + i\varepsilon - (\Omega - \Delta) - (\hbar M)^{-1} F(\omega + i\varepsilon)} \quad (2\text{-}63)$$

While the macroscopic susceptibility is obtained as follows

$$\chi^{+}(\omega) = -\frac{\gamma M_s}{\omega - \gamma H_{eff} + i\alpha\omega} \tag{2-64}$$

Comparing the microscopic and macroscopic susceptibility, we can obtain the expression of damping

$$\alpha = -\lim_{\omega \to 0} \frac{\gamma}{\hbar \mu_0 V M_S} \mathrm{Im}\left[\frac{1}{\omega} F(\omega + i0)\right] \tag{2-65}$$

Where $F(\omega + i0)$ is the green function of torque operator explained as follows

$$F(\omega + i0) = -i \int_{-\infty}^{\infty} \langle [\eta^{-}(t), \eta^{+}] \rangle_0 \theta(t) e^{i(\omega + i0)t}\, dt \tag{2-66}$$

Therefore, the damping expression is

$$\alpha = \frac{g}{\pi M_s} \sum_k W_k \sum_{nn'} \left|\Gamma^{-}_{nn'}(k)\right|^2 \frac{\delta}{(E - E_{nk})^2 + \delta^2} \frac{\delta}{(E - E_{n'k})^2 + \delta^2} \tag{2-67}$$

where g is electron's g-factor, M_s is total magnetization, and $\Gamma^{-}_{nn'}(k) = \langle n, k | [S^{-}, H^{SO}] | n', k \rangle$ is matrix elements measuring wavevector k-conserving-transitions between bands n and n' induced by spin-orbit torque operator $[S^{-}, H^{SO}] = \xi(S^{-}L^{z} - S^{z}L^{-})$ where ξ denote the spin orbit interaction strength, and $S^{-}, S^{z}, L^{-}, L^{z}$ are spin and angular momentum operator, respectively. These transitions are numerically integrated over all wavevector and each band states, weighted by *k*-point weight W_k and electron spectral functions which is Lorentzian centered at the band energy E_{nk} broadened by electron-lattice scattering rate δ. Note that band states $|n, k\rangle$ and E_{nk} are easily obtained from output of ab-initio calculation.

2.7. Frozen thermal lattice disorder

Introducing the finite temperature effect such as atomic vibration into the first-principles calculation can be carried out by randomly shifting the atom with the rigid position from equilibrium coordinate as shown in the **Fig 2.6** [123]. This assumption originated from the fact that experimental FMR frequency together with spin-wave and phonon frequency are much smaller than electronic Fermi velocity frequency. This allows us to separate the motion timescale, because the electrons responsible for transport properties moving around the frozen spins and phonons.

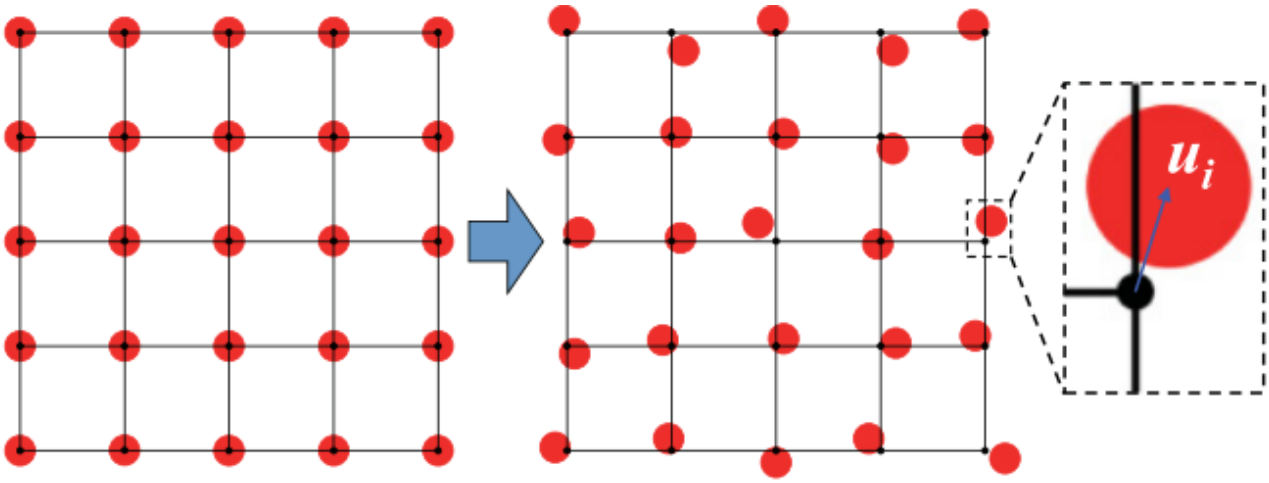

Fig 2.6. Illustration of frozen thermal lattice disorder. Reuse with permission [123].

In order to introduce this effect accurately, phonon dispersion relation is required. The potential energy of phonon system is expressed as follows:

$$V\lfloor \mathbf{r}(j_1 l_1), \ldots \mathbf{r}(j_n l_N) \rfloor \tag{2-68}$$

Where $\mathbf{r}(jl)$ is the position of the j-th atom in the l-th unit cell, n is the number of atoms in a unit cell, and N is number of unit cells. Therefore, force can be defined as:

$$F_\alpha(jl) = -\frac{\partial V}{\partial r_\alpha(jl)} \tag{2-69}$$

and second-order force constant as:

$$\Phi_{\alpha\beta}(jl, j'l') = \frac{\partial^2 V}{\partial r_\alpha(jl)\partial r_\beta(j'l')} = -\frac{\partial F_\beta(j'l')}{\partial r_\alpha(jl)} \tag{2-70}$$

Where j, j', …, are the indices of atoms inside a unit cell, l, l', …, are the indices of unit cells, and α, β, …, are Cartesian coordinate indices. Phonon dispersion itself can be calculated using two method, finite differences approach or density functional perturbation theory. In the finite differences approach, the Equation of force constants is approximated as:

$$\Phi_{\alpha\beta}(jl, j'l') \cong -\frac{F_\beta\left(j'l'; \Delta r_\alpha(jl)\right) - F_\beta(j'l')}{\Delta r_\alpha(jl)} \tag{2-71}$$

Where $F_\beta\left(j'l'; \Delta r_\alpha(jl)\right)$ are the forces when atom is displaced $\Delta r_\alpha(jl)$

Then, we can obtain the dynamical property of atoms after solving the eigenvalue of dynamical matrix $D(\mathbf{q})$ built from the force constants.

$$D(\mathbf{q})\mathbf{e}_{\mathbf{q}v} = [\omega(\mathbf{q}v)]^2\mathbf{e}_{\mathbf{q}v} \text{ and } \sum_{j'\beta} D_{\alpha\beta}(jj', \mathbf{q})\mathbf{e}_{\mathbf{q}v}^{j'\beta} = [\omega(\mathbf{q}v)]^2\mathbf{e}_{\mathbf{q}v}^{j\alpha} \quad (2\text{-}72)$$

$$D_{\alpha\beta}(jj', \mathbf{q}) = \frac{1}{\sqrt{m_j m_{j'}}} \sum_{l'} \Phi_{\alpha\beta}(j0, j'l') \exp(i\mathbf{q} \cdot [\mathbf{r}(j'l') - \mathbf{r}(j0)]) \quad (2\text{-}73)$$

Where $\mathbf{q}$ is the wave vector and m is the atomic mass, v is the band index, $\omega(\mathbf{q}v)$ is the phonon frequency and $\mathbf{e}_{\mathbf{q}v}$ is the polarization vector of the phonon mode. The $\mathbf{e}_{\mathbf{q}v}$ consists of the information of collective atomic motion. Hence the Equation of motion will be:

$$\sum_{j\alpha j'\beta} D_{\alpha\beta}(jj', \mathbf{q}) e_\beta(j', \mathbf{q}v) = [\omega(\mathbf{q}v)]^2 e_\alpha(j, \mathbf{q}v) \quad (2\text{-}74)$$

Where the eigenvector of the band index v at wave vector $\mathbf{q}$ is obtained by the diagonalization of dynamical matrix $D(\mathbf{q})$

$$\sum_{j\alpha j'\beta} e_\alpha(j', \mathbf{q}v)^* D_{\alpha\beta}(jj', \mathbf{q}) e_\beta(j', \mathbf{q}v) = [\omega(\mathbf{q}v)]^2 \delta_{vv'} \quad (2\text{-}75)$$

It is important to note that the eigenvalues $[\omega(\mathbf{q}v)]^2$ is real due to the Hermitian matrix of $D(\mathbf{q})$ with dimension of $3N \times 3N$ where N is the total atoms in the unit cell, and 3 as Cartesian coordinate degree of freedom. Therefore, the atomic displacements can be expressed as below:

$$u_\alpha(jl, t) = \left(\frac{\hbar}{2Nm_j}\right)^{\frac{1}{2}} \sum_{\mathbf{q},v} [\omega(\mathbf{q}v)]^{-\frac{1}{2}} [\hat{a}(\mathbf{q}v) \exp(-i\omega(\mathbf{q}v)t) + \hat{\alpha}^\dagger(-\mathbf{q}v) \exp(i\omega(\mathbf{q}v)t)] \exp(i\mathbf{q} \cdot \mathbf{r}(jl)) e_\alpha(j, \mathbf{q}v) \quad (2\text{-}76)$$

Where the $\hat{a}$ and $\hat{\alpha}^\dagger$ are annihilation and creation operator of phonon, t is the time, and $\hbar$ is the reduced Planck constant. These atomic displacements are explicitly determined since all contribution from all phonon modes occupied at a specified temperature are calculated. At a particular temperature, probability distribution is sampled from canonical ensemble of harmonic phonons, so the expectation value of squared atomic displacement is:

$$\langle |u_\alpha(jl, t)|^2 \rangle = \frac{\hbar}{2Nm_j} \sum_{\mathbf{q},v} \omega_v(\mathbf{q})^{-1} (1 + 2n_v(\mathbf{q}, T)) \, |e_v^\alpha(j, \mathbf{q})|^2 \quad (2\text{-}77)$$

Where the $n_v(\mathbf{q}, T)$ is the phonon population at the particular temperature T and wave vector $\mathbf{q}$, as follows:

$$n_v(\mathbf{q}, T) = \frac{1}{\exp\left(\frac{\hbar\omega_v(\mathbf{q})}{k_B T}\right) - 1} \quad (2\text{-}78)$$

Chapter 3: Temperature dependence of spin polarization in Heusler alloy

3.1. Introduction

As mentioned in Chapter 1, many research groups theoretically predicted that Co-based Heusler alloys such as Co_2MnSi (CMS) and $Co_2FeGa_{0.5}Ge_{0.5}$ (CFGG) as half-metallic material [91,92] and experimentally demonstrated high CPP-GMR or TMR ratio when these materials used for electrodes [99,102,124,125]. However, the high MR ratio was only observed at low temperatures before being strongly reduced at finite temperatures. In this Chapter, I investigated the spin polarization of these materials at finite temperatures since one possibility behind the substantial reduction of MR ratio is the decay of spin polarization due to the spin fluctuation effect. First, I systematically calculated the ground state properties of ternary Co-based Heusler alloys using Korringa-Kohn-Rostoker (KKR) method [119,120]. Afterward, I implemented the finite temperature effect using the disordered local moment (DLM) method, which treats spin fluctuations within a mean-field approximation [106]. The performance and problematic issues of KKR and DLM calculation are addressed, such as too low magnetic moment and too high Curie temperature. Thus, the CMS and CFGG at different structural ordering are used for further study examples. The calculation results are directly compared to the experimental results of CPP-GMR [102,124,126]. In addition, the incorporation of self-interaction correction (SIC) [127] to obtain the experimental reported magnetic moment is also investigated to understand the effect of SIC on the temperature dependence of spin polarization.

3.2. Calculation Details

The model of the $L2_1$ structure of full-Heusler Co_2YZ compound is an fcc lattice that has four atoms consisting of 2 Co (0.25, 0.25, 0.25) and (0.75, 0.75, 0.75), a *Y* (0, 0, 0), and a *Z* (0.5, 0.5, 0.5) as illustrated in Chapter 1. The lattice constant is taken from the experimental value reported by Kandpal *et al*. [128] and Takahashi *et al*. [129] for CMS and CFGG, respectively. For other ternary Heusler alloys, the lattice constant is taken from the Alabama Heusler database [130] and report by Hu *et al.* [131]. For the B2 structure, *Y* and *Z* atoms are randomly swapped, which resembles the CsCl crystal structure. The lattice constant of the B2 structure is assumed as half of the $L2_1$ form. There is no distortion from the cubic system, and the lattice constant is not optimized. For off-stoichiometry system, the composition considered as $Co_2(Fe_{0.9}Co_{0.1})(Ga_{0.5}Ge_{0.5})$ and $(Co_{0.9}Fe_{0.1})_2Fe(Ga_{0.5}Ge_{0.5})$ for Co-rich and Fe-rich system, respectively.

First, spin-polarized ground state electronic structure is calculated by multiple-scattering Green's function formalism of Korringa-Kohn-Rostoker (KKR) method [119,120] implemented into HUTSEPOT code [132]. The local-spin density approximation (LSDA) of Perdew-Wang [133] was used for the exchange correlation. The atomic-sphere approximation (ASA) is used to determine the Kohn-Sham potential. Core and valence electrons are treated within the scalar-relativistic calculation. The maximum value of the orbital angular momentum is three, and B2 disorder is simulated by coherent potential approximation (CPA) [134] between *Y* and *Z* elements. The special k-point mesh of 20 × 20 × 20 for self-consistent field (SCF) calculation is used for numerical integrations in the first Brillouin zone (BZ).

Then, the finite temperature effect is implemented by the DLM method [106], as described in Chapter 2. Ground-state potential obtained from the first step is fed into the DLM framework to solve the fully-relativistic Kohn-Sham-Dirac equation non-self-consistently. Finally, evaluating the spin polarization P is given by

$$P = \frac{D^{\uparrow}(E_F) - D^{\downarrow}(E_F)}{D^{\uparrow}(E_F) + D^{\downarrow}(E_F)} \quad (3\text{-}1)$$

which $D^{\uparrow}(E_F)$ and $D^{\downarrow}(E_F)$ corresponds to the DOS on the Fermi level of majority and minority spin, respectively. The computations were performed on a Numerical Materials Simulator at NIMS.

3.3. Ground State Properties of Heusler alloys at 0 K

3.3.1. Magnetic Properties of Heusler alloys at 0 K

In the Fig 3.1, it is shown that only several Heusler alloys coincides with Slater-Pauling rule, such as Co_2CrZ, Co_2MnZ, and Co_2VIn. It is important to note that strict fulfillment of this rule is only expected for half-metallic ferromagnetic which are fully spin-polarized at ground state. On the other hand, better agreement between calculated spin moment of Heusler with Slater-Pauling rule reported by Galanakis *et al.* [62] and Fecher *et al.* [135] using full-potential method which is accurate, but also computationally expensive. Since the focus of this study is the temperature dependence of spin polarization and not the strict definition of half-metallicity, it is considered that the calculation using atomic sphere approximation is enough to reproduce the general trend of Slater-Pauling rule in the Co-based Heusler alloys.

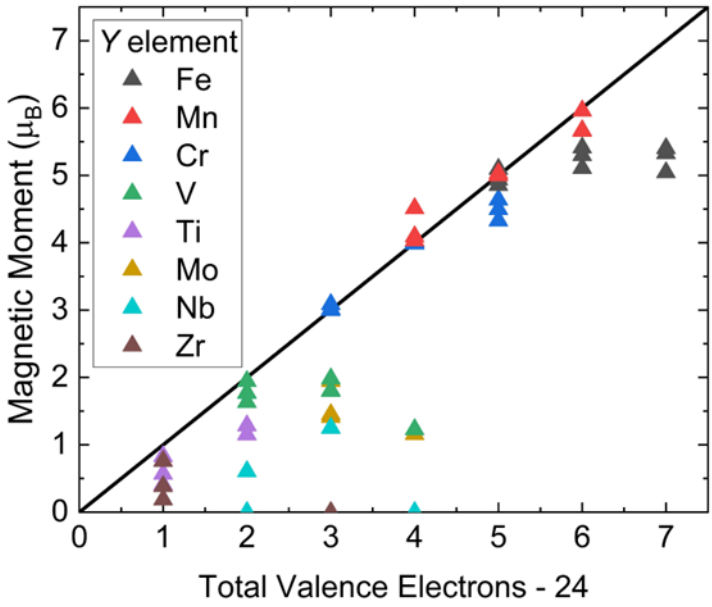

Fig 3.1. The dependence of calculated total spin moments on substracted total valence electrons (TVE) for all ternary Heusler alloys Co2*YZ* with *Y*: Fe, Cr, Mn, V, Ti, Mo, Nb, Zr and *Z*: Al, Ga, In, Si, Ge, Sn, P, As, Sb. The bold line represents the Slater Pauling behavior [62,135].

Similar trend between this calculation with the one reported by Galanakis *et al.* [62] are significant deviation at the upper and lower limit of the Slater-Pauling rule for Co-based Heusler alloys. Minimum contribution of valence electrons of *Y* and *Z* elements are 3 electrons for each, thus total valence electrons cannot be less than 24 in the Co_2YZ. Almost no calculated systems in the lower area ($TVE - 24 < 3$) coincides with the Slater-Pauling rule except Co_2VIn. It can be explained by the difficulty to magnetize the early transition metals element such as Ti, V, Zr, Nb, and Mo which are practically paramagnetic, hence giving the total magnetization less than predicted by Slater-Pauling rule.

In the upper area ($TVE - 24 > 4$), the deviation also started to happen, especially for Co_2FeZ. Based on the simple relation of TVE and magnetic moment, 30 valence electrons in the Co_2FeZ (*Z*: Si, Ge, Sn) should lead to the 6 μ_B magnetic moment, but it is not. This issue also being further investigated by Wurmehl *et al.* [136]. They revisited the Co_2FeSi, which experimentally demonstrated the highest magnetic moment (6 μ_B) and Curie temperature (1100 K) among the Co-based Heusler alloys. Even with full-potential method and varied parametrizations of the exchange-correlation functional, they cannot achieve predicted magnetic moment, implying that the discrepancy is not the consequence of the spherical approximation or variation of exchange-correlation energy functional. In addition, the total energy are already minimum in the experimentally reported lattice constant. If this experimental lattice parameters are enlarged by 8-12 %, the half-metallicity is achieved and magnetic moment is

integer. However, enlargement of the lattice parameters lead to unrealistic volume expansion, because it is much bigger than the error of lattice parameters determination.

First explanation of this discrepancy is due to strong hybridization between two Co atoms and *Y* atom in the Co_2YZ, the moment of *Y* atom will not be larger than 3 μ_B. Despite two empty minority-states e_u of two Co atoms can contribute to the 2 μ_B, the total magnetic moment cannot reach 6 μ_B, let alone 7 μ_B [62]. Second explanation is based on the fact that the magnetic properties Co_2YZ is following the *localized* manner with respect to the Slater-Pauling rule, but *local moment* is contributed by *d* electrons which are *delocalized* in metal. Therefore, *partial localization* of *d* electrons can be properly pictured by including the electron-electron correlation and self-energy correction to *partially localized* states. One scheme that provides this correction is called as LDA+*U* method [137]. Using this method, Kandpal *et al.* successfully regain the integer magnetic moment in the Co_2FeSi [138]. They found the ratio between Co and Fe magnetic moments are also in good agreement with the experimental measurement. Note that while LDA+*U* only corrects the localized states, there is other approach called self-interaction correction (SIC) [127,139,140] which is analog with LDA+*U* where very large *U* is used. Because SIC is already incorporated in the HUTSEPOT code [132], adjustment of magnetic moment of Co_2Fe-based Heusler alloys will be also investigated by SIC and further explained in the Chapter 3.5.

3.3.2. Spin Polarization at 0 K

Real consequence of Slater-Pauling rule is the integer magnetic moment will be expected for the half-metal with integer total valence electron. However, it does not necessarily mean that the material with magnetic moment coincides with the Slater-Pauling behavior is automatically half-metal [135]. The Fig 3.2(a) shows the behavior of spin polarization clearly. One example that demonstrates the irreversibility of Slater-Pauling rule is Co_2VIn. This material has magnetic moment nearly 2 μ_B as predicted by Slater-Pauling rule, but the *spd* spin polarization is very low, less than 40%. It implies the strict definition half-metallicity requires careful examination, not only from Slater-Pauling rule but also from the electronic structure and calculated spin polarization.

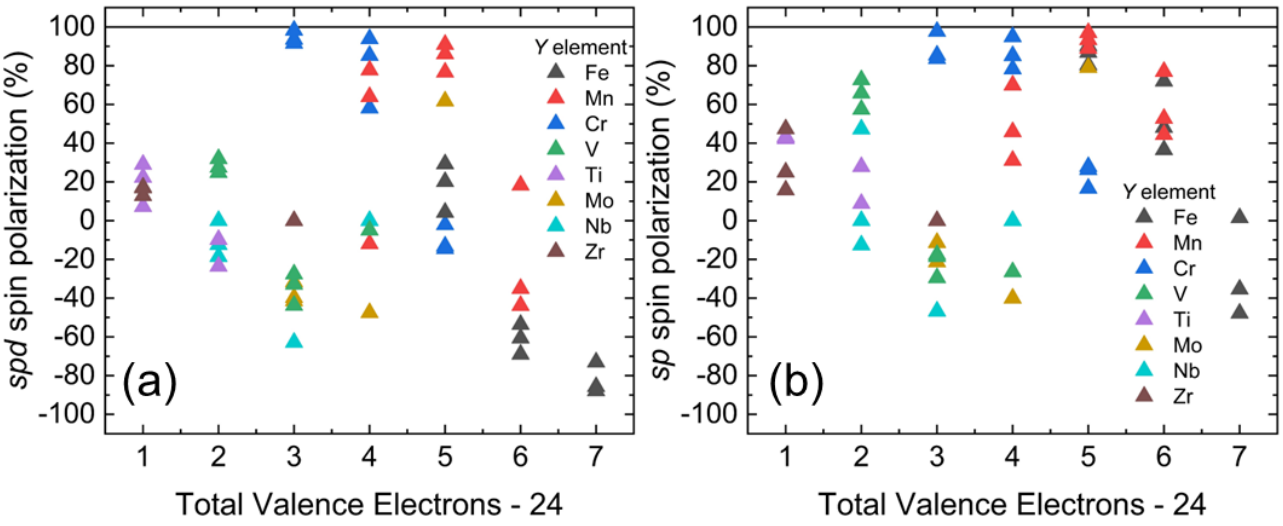

Fig 3.2. The dependence of (a) *spd* spin polarization, and (b) *sp* spin on substracted total valence electrons (TVE) for all ternary Heusler alloys Co_2YZ with *Y*: Fe, Cr, Mn, V, Ti, Mo, Nb, Zr and *Z*: Al, Ga, In, Si, Ge, Sn, P, As, Sb. The bold line represents the full spin-polarization (100%).

Highest *spd* spin polarization is shown by Co_2CrAl (98.29%, virtually half-metal). Other Co_2CrZ and Co_2MnZ compound which coincides with Slater-Pauling behavior demonstrated pretty high spin polarization (>80%) although not fully spin polarized. There are several possible explanations behind this, which one of them is the lattice constant. This study used the lattice constant from The University of Alabama of Heusler Database [130] and previous work by Hu *et al.* [131]. The lattice constant is not optimized again and directly used as it is. Surely, there are discrepancy between theoretical lattice constant and experimental lattice constant, as shown in the Fig 3.3. Majority of compound reported by Webster *et al.* [141] show relatively small deviation between theoretical and experimental lattice constant (<1%), despite for several compound, the deviation can be much larger up to 5% (Co_2NbZ). These deviations, no matter how small or big it is, can affect the spin polarization significantly.

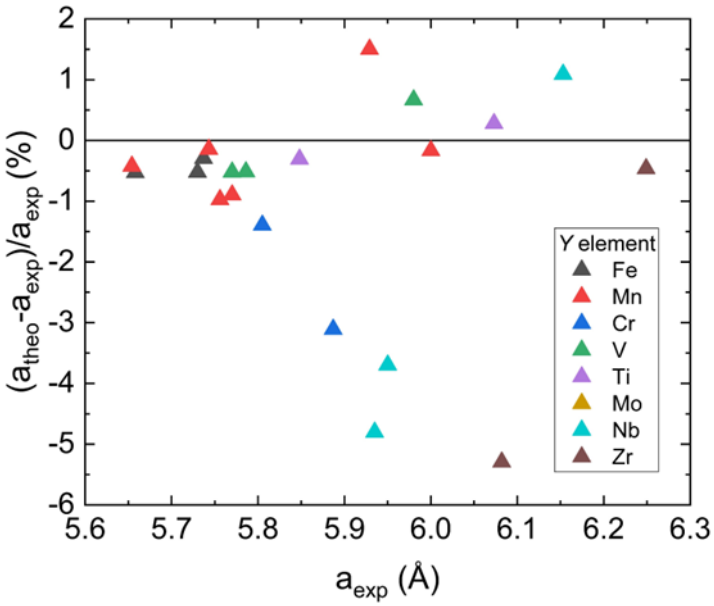

Fig 3.3. The dependence of $(a_{theo}-a_{exp})/a_{exp}$ on experimental lattice constant a_{exp} for ternary Heusler alloys Co_2YZ. The bold line represents zero deviation from a_{exp}. Experimental lattice constant is taken from [141].

How the change of lattice constant affects the spin polarization? As highlighted by Kandpal *et al.* [138] in the Co_2FeSi, the lattice constant strongly related with the interatomic interaction and overlap. Since the half-metallicity in Co-based Heusler alloys Co_2YZ is originated from overlap and hybridization mechanism between orbital of two Co atoms and *Y* atoms, changing the lattice constant can regain the fully spin-polarized band structure.

On the other hand, this is also closely related with the second possible explanation, which is the location of Fermi level. When Fermi level is located in the middle of relatively-wide-gap of minority states, half-metallicity is also expected for relatively-wide variation of lattice constant. However, if the Fermi level is located in the edge of conduction band or valence band on minority spin states, the spin polarization can be very sensitive on the choice of lattice parameters.

Third possible reason, is a bit technical. In the KKR Green's function method, the density of states (DOS) were obtained by inclusion of a small finite imaginary part. If the small value is used, the DOS peaks are sharp. Increase of this imaginary part will broadening the DOS peaks. In order to observe the full spin polarization, the sharper features will be required and also dense *k*-point mesh but the computational cost will be huge.

For the magnetoresistance application, it is known that the itinerant *sp* electrons are responsible for transport properties instead of localized *d* electrons [142,143]. Therefore, the Fig 3.2(b) provides the

information of *sp* spin polarization at 0 K for ternary Heusler alloys. The comparison between *sp* and *spd* spin polarization dependence of substracted TVE is qualitatively similar. However, if one looks closely enough, there are significant difference especially in the Co_2FeZ (TVE $-$ 24 $=$ 5) which show relatively low *spd* spin polarization, but very high *sp* spin polarization (>80%). Aside, there are also notable change of spin polarization value from *spd* to *sp* electrons in the TVE $-$ 24 $>$ 5. In general, the Fig 2.1 show that the *sp* spin polarization is generally larger than *spd* spin polarization for most compounds. The reason why materials demonstrated low *spd* spin polarization but high *sp* spin polarization is may be due to the existence of localized minority spin *d* states around Fermi level.

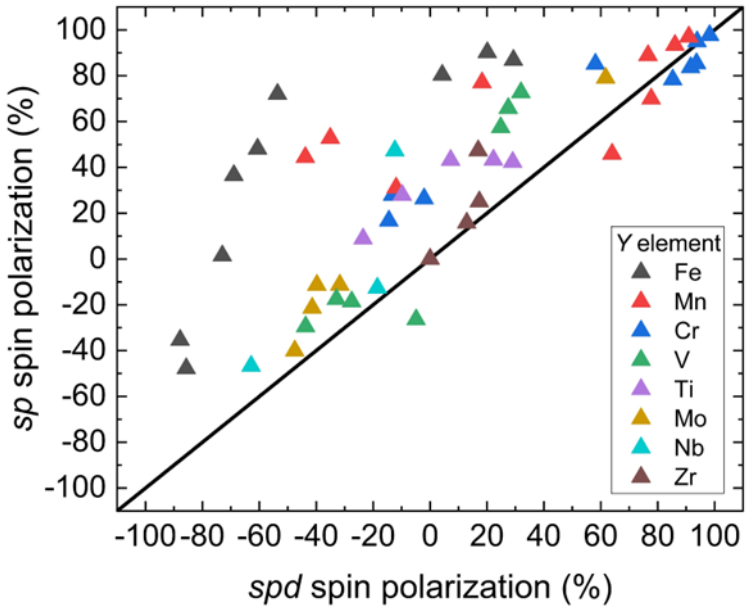

Fig 3.4. The dependence of *sp* spin polarization P_{sp} on *spd* spin polarization P_{spd} of all ternary Heusler alloys Co_2YZ with *Y*: Fe, Cr, Mn, V, Ti, Mo, Nb, Zr and *Z*: Al, Ga, In, Si, Ge, Sn, P, As, Sb. The bold line represents the $P_{spd} = P_{sp}$.

The Fig 2.1 also shows the prospective material that demonstrated the high *sp* spin polarization is dominated by Co_2YZ where the *Z* atoms are Fe, Mn, and Cr. These compositions are also widely investigated by other research groups because relatively high magnetization (>3 μ_B). In the next part, it is revealed the correlation between magnetization of half-metallic Heusler alloys are somewhat related with the Curie temperature, hence the high magnetization imply the high Curie temperature, which are preferable to avoid the negative impact of spin fluctuation at finite temperature.

3.3.3. Formation Energy at 0 K

The formation energy of Heusler alloy in this study is calculated using the following equation:

$$E_{\text{form}}^{\text{calc}} = E_{Co_2YZ}^{\text{total}} - \left(2E_{\text{Co}}^{\text{total}} + E_{Y}^{\text{total}} + E_{Z}^{\text{total}}\right) \quad (3\text{-}2)$$

The total energy of Co_2YZ compound and Co, *Y, Z* elements are obtained from the self-consistent calculation. For simplicity, crystal structure of all elements are based on the Table 3.1.

Table 3.1. The crystal structure of *Y* and *Z* elements assumed in this study

Structure	Elements
Body centered cubic	As, Cr, Fe, Ge, Mn, Mo, Nb, V
Body centered tetragonal	Ga, In
Face centered cubic	Al, P, Rh, Si, Sn
Simple cubic	Sb
Simple hexagonal	Co, Ru, Sc, Ti, Y, Zr

Fig 3.5 shows the relation between calculated formation energy $E_{\text{form}}^{\text{calc}}$ in this study with the reference formation energy $E_{\text{form}}^{\text{ref}}$ by Alabama Database [130]. The reference formation energy is calculated based on the reference states of the elements on Open Quantum Materials Database (OQMD) [144,145] database. It shows good agreement between $E_{\text{form}}^{\text{calc}}$ and $E_{\text{form}}^{\text{ref}}$. Most compounds show the formation energy less than predicted by reference. This is may be due to two possible reasons. First, our simplified assumption for simple crystal structure of some elements which is not the same with the ground state crystal structure based on the OQMD [144,145]. In the OQMD, the Si, Ge, and Sn has diamond structure, meanwhile P, As, Sb, Mn, and Ga adopt more complex crystal structure [144,145]. Second reason is lattice constant. The total energy reached the minimum while the lattice constant is optimized. However, our calculation of total energy for each elements are carried out with the lattice constant reported by Materials Project [146] without any further optimization. Third reason is, in this study, the spherical approximation of potentials is used via ASA [147]. It is widely known that accurate and reliable total energy calculation usually incorporated full-potential method without any shape approximation. Interestingly, even with the simplified structure, unoptimized lattice parameters, and spherical approximation on the real potential, the linear correlation between $E_{\text{form}}^{\text{calc}}$ and $E_{\text{form}}^{\text{ref}}$ is still confirmed, emphasizing that the calculation framework in this study is enough to obtain the general behavior of formation energy.

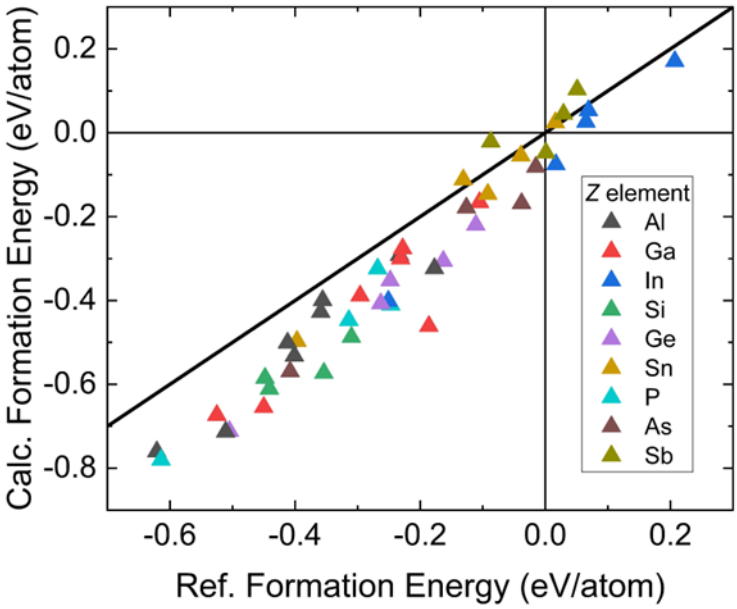

Fig 3.5. The dependence of calculated formation energy $E_{\text{form}}^{\text{calc}}$ on reference formation energy $E_{\text{form}}^{\text{ref}}$ based on [130,131] of ternary Heusler alloys Co_2YZ with *Y*: Fe, Cr, Mn, V, Ti, Zr, Nb, Mo, and *Z*: Al, Ga, In, Si, Ge, Sn, P, As, Sb. The bold line represents the $E_{\text{form}}^{\text{calc}} = E_{\text{form}}^{\text{ref}}$.

Notable feature from the Fig 3.5 is the, for the same valence electrons, increasing of *Z* elements size lead to less negative formation energy. It means the compound will more likely formed using smaller *Z* atoms. When the *Z* atoms become smaller, interatomic distances will also decrease, hence the atomic bindings will be stronger, the total energy is minimized, and formation energy become more negative [148]. Therefore, small positive formation energy for the most ternary Heusler with large *Z* such In, Sb are observed, implying that these materials are more difficult to be fabricated compared with other Heusler compound with the smaller *Z* atoms.

It is important to note that the formation energy is calculated at zero temperature. Negative formation energy means the Heusler compound is more stable than constituent element at the ground state. But it does not necessarily mean that compound with positive formation energy will never be formed. On the other hand, negative formation energy is not only the prerequisite condition for the stability over all possible competing phases. Thermodynamical stability of phases can be confirmed by chemical space, especially when the formation energies of particular phases lies on the *convex hull* of formation energies of all phases. Therefore, the degree of thermodynamic stability depends on the distance of formation energy from the respective *convex hull.* Since such determination is required the accurate calculation of total energy, in this study I only consider the formation energy as measure of thermodynamical stability.

3.4. Finite Temperature Calculation

3.4.1. Convergence of Temperature

In the DLM framework [106], the uniform values of initial beta-*h* parameter is set for all each local-moment site at zeroth round calculation, and the updated value of beta-*h* is used as the input for next iteration round, while keeping the beta-*h* value same for Co site. The convergence is achieved when the iterative temperature difference is less than 1 K. The Fig 3.6 show how the calculated temperature is evolved by iteration round for the prototype of $L2_1$ Co2MnSi. When beta-*h* becomes smaller, it is required more iterative round to reach the convergence (13^{th} round for beta-*h* = 1). However, for larger beta-*h*, the convergence is easily achieved within 5 round or less. The other notable features observed that, zeroth round temperature is always higher than converged temperature except at limit of very large beta-*h*, where temperature is already converged even at the zeroth round, implying that to accurately implement the finite temperature behavior, the computational cost is will increase drastically near the Curie temperature.

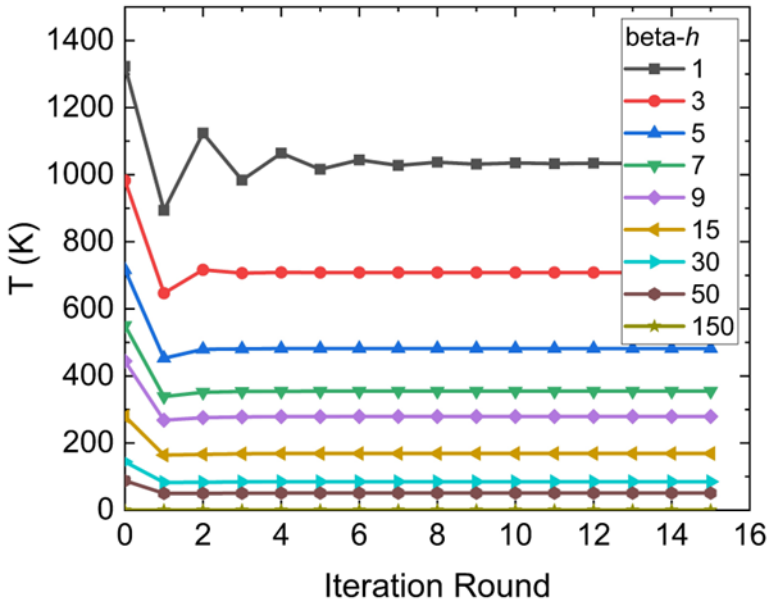

Fig 3.6. The temperature convergence on the number iteration round with varying values of beta-*h* for $L2_1$ Co_2MnSi

By plotting the converged temperature on the initial beta-*h* as shown in Fig 3.7, it is easier to understand physical meaning of the beta-*h* parameter and its implication in the DLM calculation. The beta-*h* corresponds to the Weiss fields or magnetic "mean-field" felt by each local moment. In the ground state or low temperature condition, where the local moments are perfectly aligned and ordered, surely large Weiss field also large. That means beta-*h* is somewhat proportional with the degree of magnetic order, hence inversely proportional with the temperature. Thus, the condition at ground

state and Curie temperature can be simulated at extremely large and small beta-h value, respectively. In general, the beta-h dependence of converged temperature shows two regionswith different behavior. At relatively large beta-h (βh), the linear relation of $\log T = C + m \log(\beta h)$ is expected, where C and m are constants. However, further decrease in βh will lead to the saturation of converged temperature expressed by $\log T = \log T_{\mathrm{C}}$, which T_{C} is Curie temperature.

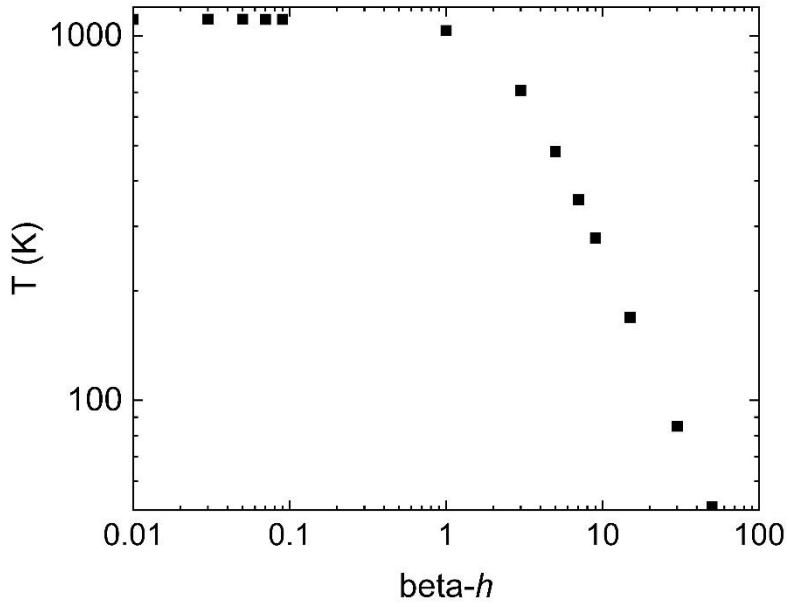

Fig 3.7. The beta-h dependence of converged temperature for $L2_1$ Co_2MnSi

The relation between $\log(\beta h)$ and $\log T$ will also guide us to simulate our system at specified temperature, especially when specified temperature is much lower than Curie temperature. Therefore, to obtain the electronic structure and spin polarization at several temperatures, several calculations is carried out with different set of uniform initial βh value, then extract the C and m to determine what value of βh that converges our system to such temperature. On the other hand, determination of Curie temperature via iterative process seems quite impractical due to many iterative rounds needed to be converged. Thus, in the next part, the alternative way to calculate the T_{C} using exchange constant and expansion potential energy will be introduced.

3.4.2. Curie Temperature Determination

Aside the conventional iterative process with very small initial beta-h value (T_{C}^{I}), alternative way to determine the Curie temperature of Co_2YZ is to expand the potential energy expression into matrix (T_{C}^{M}). Assuming $L2_1$ structure of Co_2YZ, there are two magnetic sublattices, Co and *Y*. Two atoms within the Co sublattices also equivalent due to the symmetry. Since the βh_i is related with the order parameter m_i at the site i as follow:

$$m_i = \coth(\beta h_i) - \frac{1}{\beta h_i} \tag{3-3}$$

At limit of very small βh_i, the equation above is reduced into

$$\lim_{\beta h_i \to 0} m_i = \frac{\beta h_i}{3} \tag{3-4}$$

Meanwhile, the expansion of potential energy for $L2_1$ structure of Co_2YZ is expressed as:

$$\langle \Omega \rangle_{0,T} \approx -\frac{1}{2} J_{\mathrm{Co-Co}} m_{\mathrm{Co}}^2 - J_{\mathrm{Co}-Y} m_{\mathrm{Co}} m_Y - \frac{1}{2} J_{Y-Y} m_Y^2 \tag{3-5}$$

Differentiation of potential energy expansion on the order parameter will give us two expression of Weiss field of Co and *Y* as follow:

$$h_{\mathrm{Co}} = \frac{1}{2} J_{\mathrm{Co-Co}} m_{\mathrm{Co}} + \frac{1}{2} J_{\mathrm{Co}-Y} m_Y \tag{3-6}$$

$$h_Y = J_{\mathrm{Co}-Y} m_{\mathrm{Co}} + J_{Y-Y} m_Y \tag{3-7}$$

Due to the two equivalent sites of Co (Co_1 and Co_2), there is a factor of ½ for h_{Co} expression, which the order parameter of m_{Co} is simply the average between order parameter of site Co_1 and Co_2

$$m_{\mathrm{Co}} = \frac{1}{2}\left(m_{\mathrm{Co}_1} + m_{\mathrm{Co}_2}\right) \tag{3-8}$$

But it is important to note that the differentiation of potential energy takes place as:

$$h_{\mathrm{Co}} = \frac{\partial \Omega}{\partial m_{\mathrm{Co}_i}} \tag{3-9}$$

According the chain rule of differentiation will lead to the ½ multipliers.

In order to calculate the three of exchange constant ($J_{\mathrm{Co-Co}}, J_{\mathrm{Co}-Y}, J_{Y-Y}$), only zeroth round calculation will be required. As example, keeping the same input Co while varying the input *Y* with small value of βh, and vice versa. The output of Weiss field h for Co and *Y* will be somewhat in linear relation with the variation of βh. Gradient of h_{Co} on the βh_{Co} is $\frac{J_{\mathrm{Co-Co}}}{6}$ (1/2 factors from two sublattices and 1/3 factors from limit of small βh_{Co}). Gradient of h_Y on the βh_{Co} is $\frac{J_{\mathrm{Co}-Y}}{3}$, and gradient of h_Y on the βh_Y is $\frac{J_{Y-Y}}{3}$. Therefore, Curie temperature can be determined by rewritten the expression of h_{Co} and h_Y into matrix:

$$\begin{pmatrix} h_{\mathrm{Co}} \\ h_Y \end{pmatrix} = \begin{pmatrix} \frac{1}{2}J_{\mathrm{Co-Co}} & \frac{1}{2}J_{\mathrm{Co}-Y} \\ J_{\mathrm{Co}-Y} & J_{Y-Y} \end{pmatrix} \begin{pmatrix} m_{\mathrm{Co}} \\ m_Y \end{pmatrix} \tag{3-10}$$

Because limit value of βh_i is zero, the $m_i = \frac{\beta h_i}{3}$, and the matrix becomes:

$$\begin{pmatrix} h_{\mathrm{Co}} \\ h_Y \end{pmatrix} = \begin{pmatrix} \frac{1}{2}J_{\mathrm{Co-Co}} & \frac{1}{2}J_{\mathrm{Co}-Y} \\ J_{\mathrm{Co}-Y} & J_{Y-Y} \end{pmatrix} \begin{pmatrix} \frac{\beta h_{\mathrm{Co}}}{3} \\ \frac{\beta h_Y}{3} \end{pmatrix} \tag{3-11}$$

Rewriting the component of matrix above, will give:

$$\begin{pmatrix} \frac{1}{2}J_{\mathrm{Co-Co}} & \frac{1}{2}J_{\mathrm{Co}-Y} \\ J_{\mathrm{Co}-Y} & J_{Y-Y} \end{pmatrix} \begin{pmatrix} h_{\mathrm{Co}} \\ h_Y \end{pmatrix} = 3k_B T \begin{pmatrix} h_{\mathrm{Co}} \\ h_Y \end{pmatrix} \tag{3-12}$$

$$J_{\mathrm{total}} = \frac{1}{2}\left[\frac{1}{2}J_{\mathrm{Co-Co}} + J_{Y-Y} + \sqrt{2J_{\mathrm{Co}-Y}^2 + \left(\frac{1}{2}J_{\mathrm{Co-Co}} + J_{Y-Y}\right)^2}\right] \tag{3-13}$$

$$T_C = \frac{1}{3k_B}J_{\mathrm{total}} \tag{3-14}$$

The largest eigenvalues of exchange constant matrix J_{total} will correspond to the largest value of $k_B T$ where I can still find a solution with vanishing Weiss field. This is Curie temperature.

In *B*2-disordered systems, the modified matrix form becomes

$$\begin{pmatrix} h_{\mathrm{Co}} \\ h_Y \end{pmatrix} = \begin{pmatrix} J_{\mathrm{Co-Co}} & c_Y J_{\mathrm{Co}-Y} \\ J_{\mathrm{Co}-Y} & c_Y J_{Y-Y} \end{pmatrix} \begin{pmatrix} m_{\mathrm{Co}} \\ m_Y \end{pmatrix} \tag{3-15}$$

where the $c_Y = 0.5$ for the fully *B*2-disordered system as I consider in this work.

When the compositionally disordered systems such as Co2(Y_yCo$_{1-y}$)*Z* is considered:

$$\begin{pmatrix} h_{\mathrm{Co}} \\ h_Y \\ h_{\mathrm{Co}_Y} \end{pmatrix} = \begin{pmatrix} \frac{1}{2}J_{\mathrm{Co-Co}} & \frac{1}{2}c_Y J_{\mathrm{Co}-Y} & \frac{1}{2}c_{\mathrm{Co}_Y} J_{\mathrm{Co}-\mathrm{Co}_Y} \\ J_{Y-\mathrm{Co}} & c_Y J_{Y-Y} & c_{\mathrm{Co}_Y} J_{Y-\mathrm{Co}_Y} \\ J_{\mathrm{Co}_Y-\mathrm{Co}} & c_Y J_{\mathrm{Co}_Y-Y} & c_{\mathrm{Co}_Y} J_{Co_Y-Co_Y} \end{pmatrix} \begin{pmatrix} m_{\mathrm{Co}} \\ m_Y \\ m_{\mathrm{Co}_Y} \end{pmatrix} \tag{3-16}$$

with $c_Y = y$ and $c_{\mathrm{Co}_Y} = 1 - y$ which correspond to the composition parameter of *Y* and Co*Y*, respectively.

On the other hand, the (Co$_x$*Y*$_{1-x}$)$_2$*YZ* will have the matrix:

$$\begin{pmatrix} h_{\mathrm{Co}} \\ h_{Y_{\mathrm{Co}}} \\ h_Y \end{pmatrix} = \begin{pmatrix} \frac{1}{2}c_{\mathrm{Co}} J_{\mathrm{Co-Co}} & \frac{1}{2}c_{Y_{\mathrm{Co}}} J_{\mathrm{Co}-Y_{\mathrm{Co}}} & \frac{1}{2}J_{\mathrm{Co}-Y} \\ \frac{1}{2}c_{Co} J_{Y_{\mathrm{Co}}-\mathrm{Co}} & \frac{1}{2}c_{Y_{\mathrm{Co}}} J_{Y_{\mathrm{Co}}-Y_{\mathrm{Co}}} & \frac{1}{2}J_{Y_{\mathrm{Co}}-Y} \\ c_{\mathrm{Co}} J_{Y-\mathrm{Co}} & c_{Y_{\mathrm{Co}}} J_{Y-Y_{\mathrm{Co}}} & J_{Y-Y} \end{pmatrix} \begin{pmatrix} m_{\mathrm{Co}} \\ m_{Y_{\mathrm{Co}}} \\ m_Y \end{pmatrix}, \tag{3-17}$$

where $c_{\mathrm{Co}} = x$ and $c_{Y_{\mathrm{Co}}} = 1 - x$ which correspond to the composition parameter of Co and Co_Y, respectively.

If more than two magnetic sublattices exist, the matrix will be larger than 2×2, and it requires least square fitting to solve and determine the Curie temperature as eigenvalue.

In the Fig 3.8, the calculated Curie temperature using matrix method T_{C}^{M} is plotted on the substracted total valence electron. As comparison, the linear model of experimental Curie temperature is shown together. Linear model of $T_C = 23 + 181m$ was found by Wurmehl *et al.* [136] for Curie temperature of Co-based Heusler alloys on the magnetic moment, which supposed to also linearly related with the total valence electron. Since the DLM framework is based on the mean-field approximation, the overestimation on comparison with experiments is expected. However, using this matrix method, Curie temperature of most compounds are lower than experimental model, which means underestimated value.

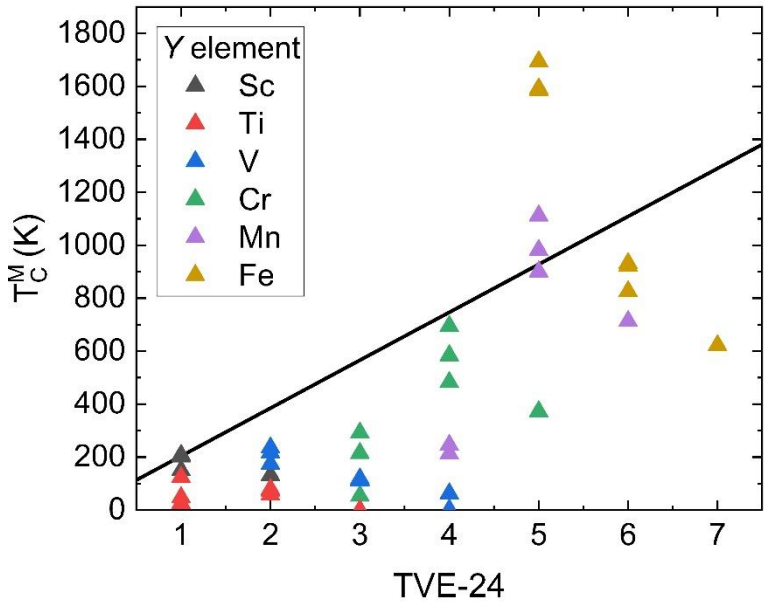

Fig 3.8. The dependence of calculated Curie temperature using matrix method T_{C}^{M} on substracted total valence electron with varying *Y* elements. The bold line is linear model of experimental Curie temperature found by Wurmehl *et al.* [136].

The matrix method allows us to understand the interaction which contributes the most to the eigenvalue J_{total} and Curie temperature, because the matrix is constructed by exchange constant of $J_{\mathrm{Co-Co}}, J_{\mathrm{Co}-Y}, J_{Y-Y}$. The relation between these exchange constants on T_{C}^{M} is shown in the Fig 3.9.

The main contribution to the Curie temperature is $J_{\mathrm{Co}-Y}$, which can be addressed by the approximation of eigenvalue J_{total} where J_{Y-Y} is negligible.

$$J_{\mathrm{total}} = \frac{1}{2}\left[\frac{1}{2}J_{\mathrm{Co}-\mathrm{Co}} + J_{Y-Y} + \sqrt{2J_{\mathrm{Co}-Y}^2 + \left(\frac{1}{2}J_{\mathrm{Co}-\mathrm{Co}} + J_{Y-Y}\right)^2}\right] \tag{3-18}$$

$$J_{\mathrm{total}} = \frac{1}{2}\left[\frac{1}{2}J_{\mathrm{Co}-\mathrm{Co}} + \sqrt{2J_{\mathrm{Co}-Y}^2 + \frac{1}{4}J_{\mathrm{Co}-\mathrm{Co}}^2}\right] \tag{3-19}$$

For the materials with high magnetic moment and Curie temperature, $J_{\mathrm{Co}-Y} \gg J_{\mathrm{Co}-\mathrm{Co}}$, and the equation above will reduce into

$$J_{\mathrm{total}} = \frac{\sqrt{2}}{2}J_{\mathrm{Co}-Y} \tag{3-20}$$

However, in the limit of very low magnetic moment and Curie temperature, $J_{\mathrm{Co}-Y} \ll J_{\mathrm{Co}-\mathrm{Co}}$, and the equation will reduce into

$$J_{\mathrm{total}} = \frac{1}{2}J_{\mathrm{Co}-\mathrm{Co}} \tag{3-21}$$

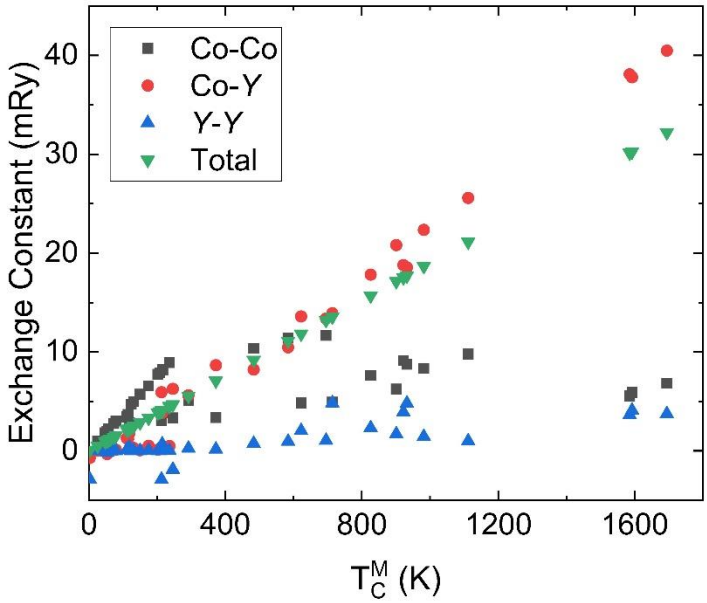

Fig 3.9. The dependence of Co-Co, Co-*Y*, *Y*-*Y*, and total exchange constant on the calculated Curie temperature using matrix method T_{C}^{M}.

On the other hand, as mentioned previously, by setting very small beta-*h*, the temperature can also converged into Curie temperature T_{C}^{I}. This is called as iterative method. The results are shown in the Fig 3.10. Using this method, overestimation of Curie temperature happens for more systems compared than the iterative method. The Fig 3.11 shows the relation more clearly. In general, iterative

method will give the higher Curie temperature than matrix method. However, in terms of computational cost, the iterative method is more expensive since near Curie temperature, it may take ~20 iteration steps to converge. One may notice that only the results for Y = Fe, Mn, and Cr are provided in the graph. This is due to another issues arises using DLM method, which related with the Fermi level adjustment. The adjustments depends on the valence electron and quite problematic for the early transition metal with semi-core states. The further explanation will be addressed later in the next part.

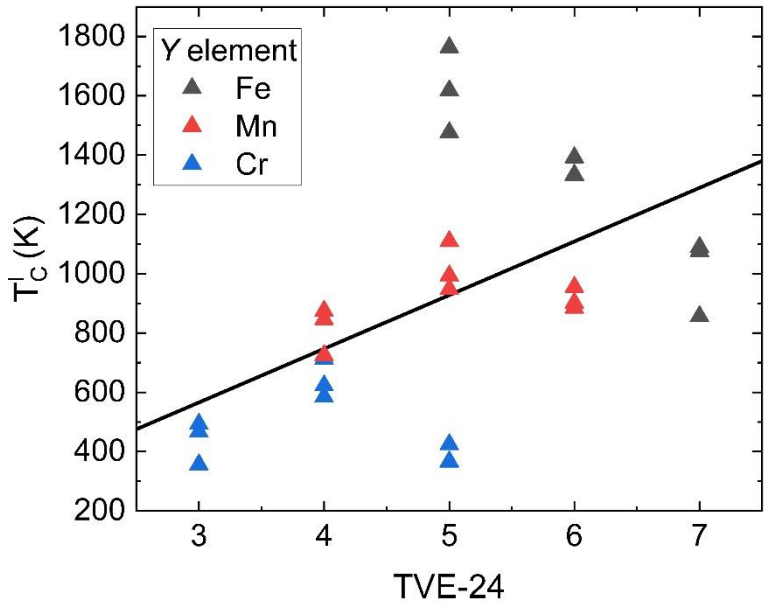

Fig 3.10. The dependence of calculated Curie temperature using iterative method T_C^I on substracted total valence electron with varying Y elements. The bold line is linear model of experimental Curie temperature found by Wurmehl *et al.* [136].

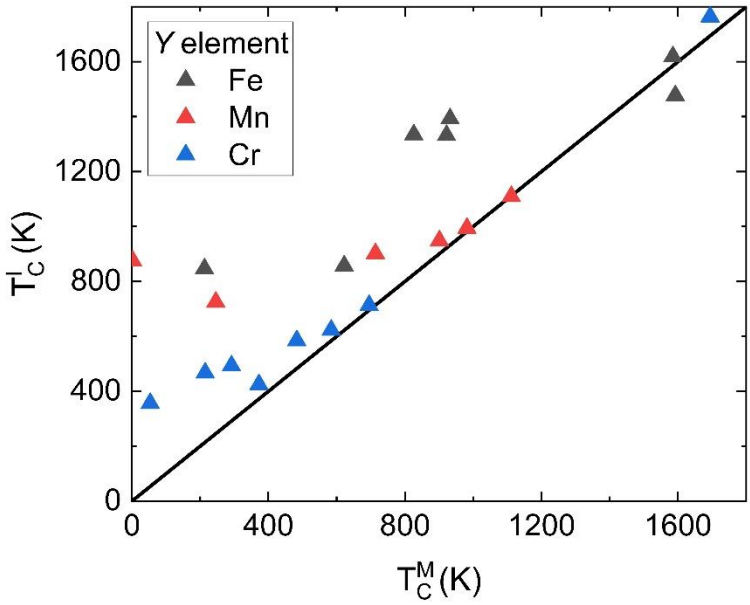

Fig 3.11. The dependence of calculated Curie temperature using iterative method T_C^I on the calculated Curie temperature using matrix method T_C^M with varying *Y* elements. The bold line is where $T_C^I = T_C^M$.

3.4.3. Adjustment of Fermi energy

Due to the treatment of magnetic disorder and spin-orbit interaction, adjustment of Fermi energy is required to match the scalar relativistic ferromagnetic calculation at ground state and fully relativistic DLM calculation at the temperature. By doing this, the integration of density of states yields the correct number of electrons per unit cell. Accurate determination of chemical potential is crucial because the spin polarization is very sensitive with the position of Fermi level. In order to tune the chemical potential, the previous value μ_{prev} is updated with the new value μ_{next} at each iteration step following the Newton's method [149,150],

$$\mu_{next} = \mu_{prev} + \frac{N_{val}^{desired} - N_{val}^{numeric}}{D(E_F)} \tag{3-22}$$

where the $N_{val}^{desired}$ is the desired number of valence electron, $N_{val}^{numeric}$ is the numerically calculated number of valence electrons from the integrated DOS, and $D(E_F)$ is the total DOS at Fermi energy. This iterative process for chemical potential convergence is also carried out simultaneously with the iterative process of temperature convergence. It is important to note that finely-tuned chemical potential also depends on the temperature. In addition, the value at low temperature can be higher or lower than the value at high temperature, which strongly depends on the type of materials. In order to determine the $N_{val}^{desired}$, one may think simply to use the information of total valence electrons.

However, it is found that the in our DLM calculation, the $N_{val}^{desired}$ does not always follow the simple behavior of valence electrons, as shown in the Table 3.2

Table 3.2. The electron contribution to the conventional definition of total valence electrons and calculated $N_{val}^{desired}$ for each element

Elements	Contribution to TVE	Contribution to $N_{val}^{desired}$
Co	9	9
Fe	8	8
Mn	7	7
Cr	6	6
V	5	8
Ti	4	10
Sc	3	9
Al	3	3
Ga	3	13
In	3	13
Si	4	4
Ge	4	14
Sn	4	14
P	5	5
As	5	15
Sb	5	15

3.4.4. Case Study: Co_2MnSi and $Co_2Fe(Ga_{0.5}Ge_{0.5})$

This section is adapted from [151], previously published by Acta Materialia.

In this study, I will take an example of two half-metallic Heusler alloys which demonstrated the high MR output when used as ferromagnetic electrodes in MR devices [102,124,126]. However, as explained in the Chapter 1, the large MR ratio is only observed at low temperature, before it strongly reduced at finite temperature. Here, I will investigate the magnetic properties and electronic structure of these two materials. In the Table 3.3, I show the calculation results for the magnetic moments, spin polarization, and Curie temperature of $L2_1$ and B2-ordered of CMS. At 0 K, the spin magnetic moment of 1.016, 3.042, and -0.073 μ_B for Co, Mn, Si in $L2_1$ structure, respectively. Introducing the B2 structural disorder will reduce the Co magnetic moment into 1.007, where the Mn moment is slightly increase into 3.059, keeping the total magnetic moment 5.000 μ_B. The *sp* spin polarization is pretty high despite not equal to 100%, which imply the almost half-metallic structures. The calculated Curie temperature for $L2_1$ structures is 1103 K, overestimating the experimental reports 985 K. This overestimation nature is well expected for the DLM calculation which incorporate the mean-field treatment.

Table 3.3. The results of spin magnetic moment, *sp* spin polarization at 0 K, and calculated Curie temperature for the $L2_1$ and B2 structures of CMS. Experiment value is taken from [152].

System	Magnetic moment (μ_B)				P_{sp} (%)	T_C (K)
	Co	Mn	Si	Total		
$L2_1$	1.016	3.042	−0.073	5.000	97.1	1103
B2	1.007	3.059	−0.074	5.000	95.6	898
Experiment	5.0					985

In the Table 3.4, the results of spin magnetic moment of $L2_1$ CFGG is 1.229, 2.804, -0.055, -0.032 for Co, Fe, Ga, Ge, respectively. Similar pattern of decrease Co moment and increase *Y* moment in Co_2YZ by introducing B2 disorder also observed. However, the total magnetic moment for both structures is much smaller than experimental reports (5.5 μ_B) [92]. The *sp* spin polarization does not affected that much by the *sp* spin polarization. In case of Curie temperature, the overestimation of experimental Curie temperature is still found.

Table 3.4. The results of spin magnetic moment, *sp* spin polarization at 0 K, and calculated Curie temperature for the $L2_1$ and B2 structures of CFGG. Experiment value is taken from [92].

System	Magnetic moment (μ_B)					P_{sp} (%)	T_C (K)
	Co	Fe	Ga	Ge	Total		
$L2_1$	1.229	2.804	−0.055	−0.032	5.220	89.9	1261
B2	1.184	2.868	−0.070	−0.052	5.176	89.8	1239
Experiment					5.5		1080

In the calculation of magnetic moment, it is found that my results are underestimating the experimental value. The experimental reports is in good agreement with the Slater-Pauling rule, which is assumed valid for the half-metallic materials. Since the magnetic moment of Heusler alloys are governed by *d* electron, there is possibility that *d* electronic structure in CFGG is not half-metal. This hypothesis is confirmed in the temperature-dependent *spd* density of states of CFGG shown in the Fig 3.12. From 0 K to 500 K, there are significant amount of minority spin states at Fermi level, which explicitly destroy the half-metallicity, hence the total magnetic moment does not follow Slater-Pauling rule. On the other hand, there are also interesting features that even with a large change in temperature from 0 K to 500 K, there is no significant peak shifting of majority spin valence band at around 0.9 eV below the Fermi level, which agree with the photoemission spectra [104] and disprove the results of DMFT by Chioncel *et al.* [105]. This result show that our calculation work well for the reproduce the experimental evidence from photoemission spectra results, although the underestimated total magnetic moment is also another important issue that need to be carefully treated, which will later addressed in the Chapter 3.5.

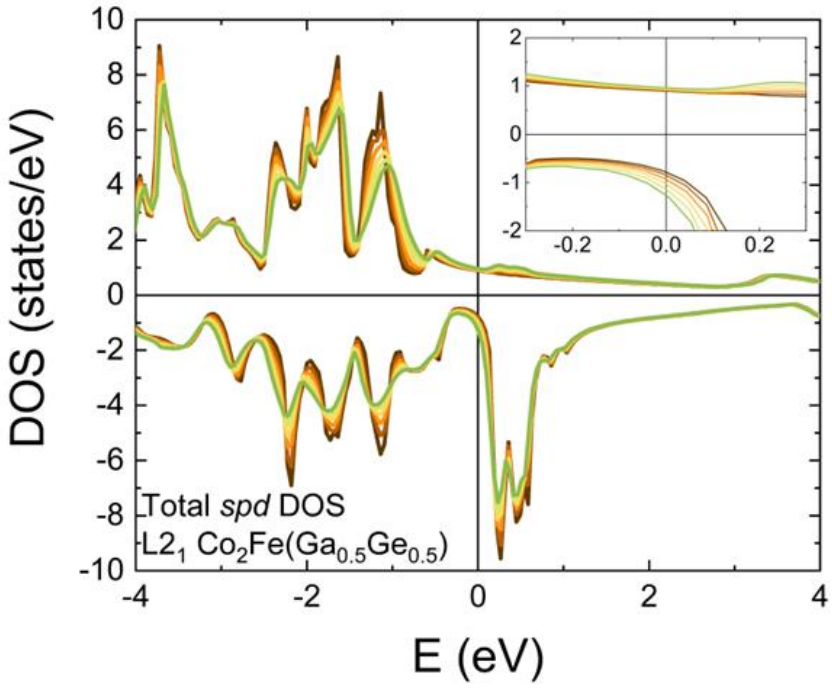

Fig 3.12. Temperature-dependent total *spd* DOS for $L2_1$ CFGG. The positive and negative values on the vertical axis show the majority- and minority-spin states, respectively. The color gradation corresponds to the temperature: Brown (0 K) → Green (500 K).

Fig 3.13(a) and (b) show the calculation results for the *sp* spin polarization (P_{sp}), which is obtained from the density of states (DOS) projected on all the *s* and *p* orbitals, for the CFGG with $L2_1$- and B2-ordered structures together with previously calculated results on CMS. The theoretical value of P_{sp} at 0 K is much larger for CMS (97.1% for $L2_1$ and 95.6% for B2) compared to CFGG (89.9% for $L2_1$ and 89.8% for B2). However, the large spin polarization of CMS is accompanied by strong degradation with increasing temperature: by increasing the temperature to 500 K, P_{sp} decreases to 78.4% and 60.5% in $L2_1$- and B2-ordered CMS. For CFGG, on the other hand, the P_{sp} is only slightly reduced to 77.6% and 75.5% for the $L2_1$ and B2 structures. Therefore, the spin polarization of CFGG at 0 K is lower than that of CMS, but I found the reduction of the spin polarization at finite temperature is rather small compared with that of CMS. In Fig 3.13(a) and (b), I also plot reported experimental value of β from CPP-GMR taken from Refs. [99,102,124]. The first attempt to clarify the bulk spin-asymmetry β value of CFGG by experiment was reported by Goripati *et al.* in B2-ordered CFGG/Ag/CFGG CPP-GMR devices, resulting in values of 90% at 10 K and 73% at RT [124]. Then, by improving the $L2_1$ order, Li *et al.* reported slightly improved β values of 93% at 10 K and 83% at RT for CFGG/Ag/CFGG CPP-GMR devices [99]. The large β value at low temperature implies that a half-metallic character exists in CFGG, although it slightly decreases at finite temperature. The small temperature dependence of β reported in the CFGG-based CPP-GMR devices is consistent with

the present calculation results of P_{sp} for CFGG. In contrast to CFGG, Sakuraba *et al.* reported β values of 72% at 100 K and 50% at 300 K by improving the $L2_1$ order of CMS [102], hence the temperature dependence of β for CMS is much larger than that of CFGG, which shows good agreement with our theoretical results shown in Fig 3.13(a) and (b).

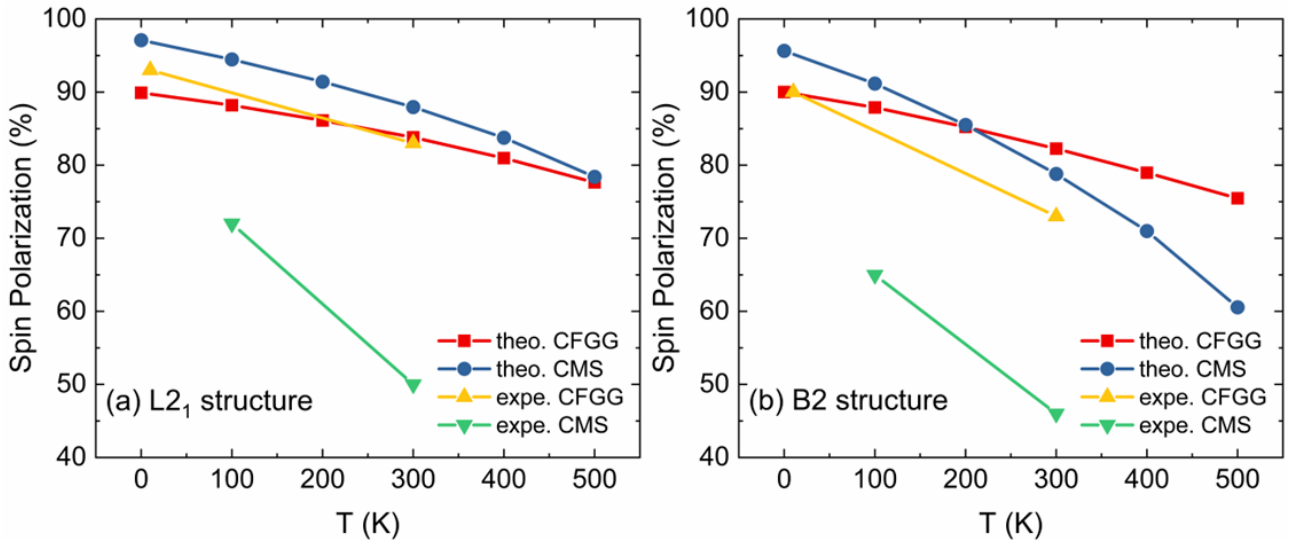

Fig 3.13. Temperature-dependent spin polarization of sp states for (a) $L2_1$-CFGG and CMS, and (b) B2-CFGG and CMS, denoted by "theo." For comparison, the β values deduced from previous experiments are also shown, denoted by "expe." $L2_1$ CFGG [99], B2 CFGG [124], and $L2_1$ and B2 CMS [102].

The previous DLM calculations on CMS successfully clarified the relation between the strong degradation of the spin polarization and the relative position of the Fermi level, which is located at the conduction band edge [108]. The relative position of the Fermi level toward conduction band edge may be one of the possible reasons for differences in the temperature dependence of spin polarization, which I will elaborate further in the next part.

In Fig 3.14(a) and (b), the temperature dependence of the total *sp* DOS for $L2_1$ CFGG and CMS are shown. Note that "total *sp* DOS" means the DOS of *sp* states summed over all atomic sites in CFGG and CMS. Here, "total" is added to "*sp* DOS" in order to distinguish it from the *sp* DOS at each atomic site. When the spin polarization for *sp* states of all atoms (P_{sp}) is considered, which provides the main contribution to the transport properties, the P_{sp} is much larger in value than P_{spd} and corresponds to an almost half-metallic character for the conduction electrons. Note that the bulk spin assymetry β is the spin assymetry of conduction electron, so it should be better described as P_{sp} rather than P_{spd}. In Fig 3.14(a)-(b), the "pseudogap" at the Fermi level for CMS and CFGG are found,

which gives rise to the almost half-metallic value of P_{sp} as shown in Table 3.3. In both the CFGG and CMS cases, the Fermi level is located near the edge of the "pseudogap", indicating that the Fermi level position hardly affects the difference between these systems in the temperature dependence of the spin polarization. Thus, the small temperature dependence of P_{sp} of CFGG as compared to CMS is mainly due to the difference in the Curie temperature. Since the Curie temperature of Co_2YZ can be characterized by the interatomic exchange constants for Co-Co ($J_{\mathrm{Co-Co}}$), Co-Y ($J_{\mathrm{Co-}Y}$), and Y-Y (J_{Y-Y}), these exchange constants $J_{\mathrm{Co-Co}}$, $J_{\mathrm{Co-Fe}}$ and $J_{\mathrm{Fe-Fe}}$ in $L2_1$ CFGG are also calculated. As shown in Table 3.5, the values $J_{\mathrm{Co-Fe}} = 378.1$ meV and $J_{\mathrm{Fe-Fe}} = 53.19$ meV in CFGG are sufficiently larger than those of CMS, which are $J_{\mathrm{Co-Mn}} = 345.6$ meV and $J_{\mathrm{Mn-Mn}} = 14.01$ meV as reported in the previous study for $L2_1$-ordered CMS. On the other hand, $J_{\mathrm{Co-Co}}$ in $L2_1$ CMS is 129.8 meV, very similar to the value in $L2_1$-ordered CFGG, $J_{\mathrm{Co-Co}} = 130.2$ meV. This similarity in $J_{\mathrm{Co-Co}}$ shows that the differences in $J_{\mathrm{Co-}Y}$ and J_{Y-Y} between CFGG and CMS are quite significant for determining not only the Curie temperature but also the temperature dependence of the spin polarization, which is consistent with previous reports. A larger interatomic exchange constant will provide a slower decay of magnetic moments at finite temperature. The magnetic moments in CFGG mainly originate from Fe and Co *d* electrons, not the *sp* electrons making the dominant contribution to the transport properties. However, due to the *s*-*d* and *p*-*d* coupling in the intraatomic orbitals as illustrated in the Fig 3.15, the spin fluctuation in *d*-electrons also affects the DOS of *s*- and *p*-electrons. Thus, a large exchange constant and slow decay of magnetic moments will lead to a small temperature dependence of *sp* spin polarization in Heusler alloys.

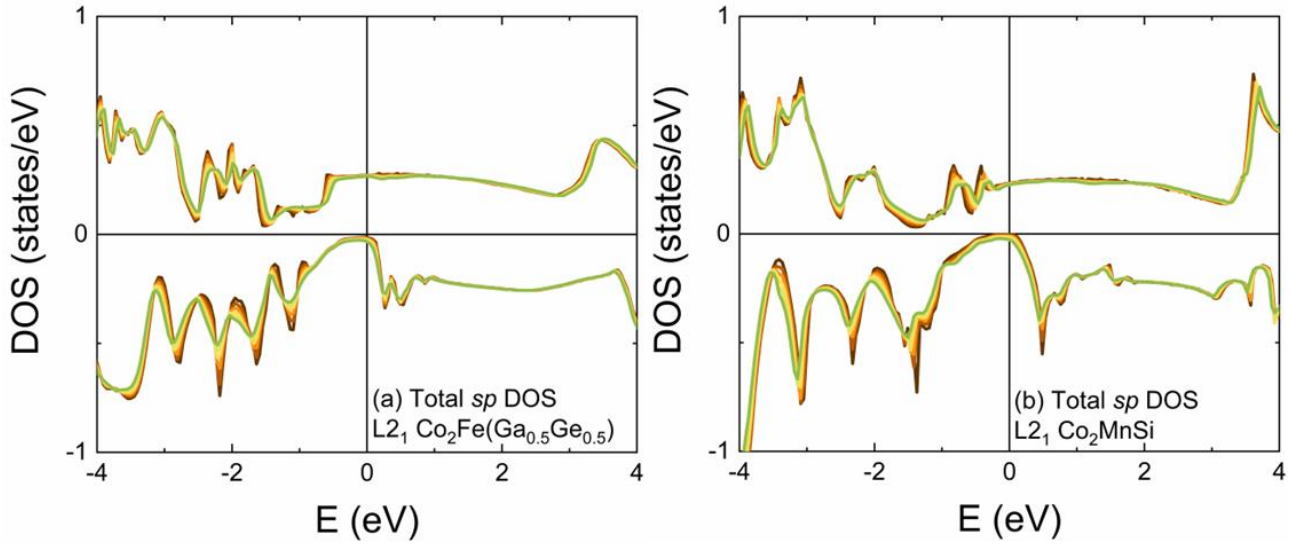

Fig 3.14. Temperature-dependent total *sp* DOS for (a) $L2_1$ CFGG and (b) $L2_1$ CMS. The positive and negative values on the vertical axis show the majority- and minority-spin states, respectively. The color gradation corresponds to the temperature: Brown (0 K) → Green (500 K).

Table 3.5. Exchange constants of Co-Co ($J_{\mathrm{Co-Co}}$), Co-*Y* ($J_{\mathrm{Co-}Y}$), and *Y*-*Y* (J_{Y-Y}) for $L2_1$ CFGG and CMS. The values of CMS are taken from.

System Co_2YZ	Exchange constant *J* (meV)		
	Co-Co	Co-*Y*	*Y*-*Y*
CFGG	129.8	378.1	53.19
CMS	130.2	345.6	14.01

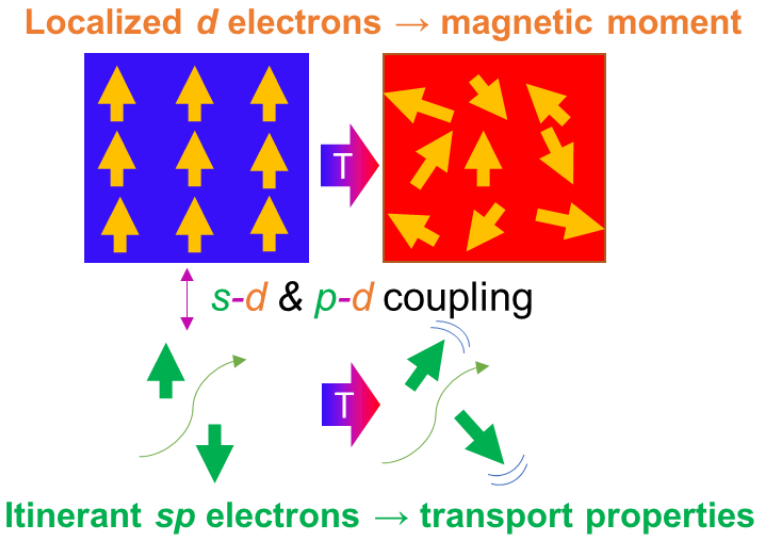

Fig 3.15. Schematic illustrations of how *s*-*d* and *p*-*d* coupling affect the temperature dependence of *sp* spin polarization

In other words, half-metallic Heusler alloys having higher Curie temperature will be appropriate to suppress the reduction of spin polarization at finite temperature. However, there is the fact that among half-metallic Heusler alloys, Co_2Mn- and Co_2Fe-based Heusler alloys have the highest Curie temperature, around 1000 K to 1200 K, and finding new half-metallic Heusler alloys with higher Curie temperature would be difficult. On the other hand, the position of the Fermi level relative to the conduction and valence band edges also affects the temperature dependence of the spin polarization. The temperature dependence of P_{sp} of $L2_1$ CFGG is shown in Fig 3.16(a), where the Fermi level is shifted according to the rigid band model corresponding to the modulation of the number of valence electrons. By intentionally shifting the Fermi level through electron doping (positive $\Delta\mu$), which means going closer to the conduction band edge, a similar large temperature

dependence of total *sp* spin polarization for CFGG to that in CMS is expected. In Fig 3.16(a), it is found that temperature dependence of the spin polarization for electron doping (positive $\Delta\mu$) is larger compared with that of $\Delta\mu = 0$. On the other hand, the shift in the Fermi level due to hole doping (negative $\Delta\mu$) is accompanied by a slight improvement in the temperature dependence of spin polarization, although the spin polarization at 0 K is lower than that of $\Delta\mu = 0$. This improvement in the temperature dependence can be explained on the basis of the Fermi level position relative to the conduction band edge. The significant increase in the minority spin state takes place at the conduction band edge rather than the valence band edge. This suggests the importance of Fermi level tuning to obtain superior properties through compositional tuning as reported previously in CFAS and $Co_2MnAl_{1-x}Si_x$. Similar behavior in B2-ordered CFGG is also confirmed as shown in Fig 3.16(b). In addition, I also observed the high P_{sp} in wider energy range for $L2_1$-ordered CFGG than that of the B2 structure (not shown), which is consistent with previous work.

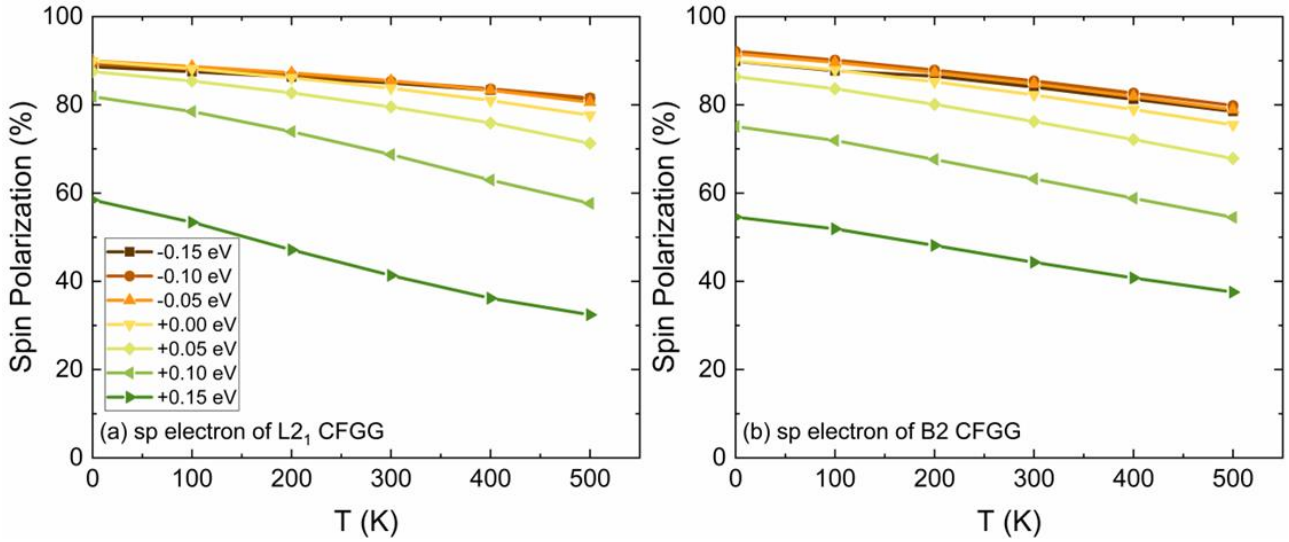

Fig 3.16. Chemical-potential-shift dependence of the total spin polarization for (a) $L2_1$ and (b) B2 CFGG. The shift of chemical potential ($\Delta\mu$) is varied from –0.15 to 0.15 eV.

From an application point of view, it is common to obtain off-stoichiometric compositions during thin-film deposition, so the formation of anti-site lattice defects is inevitable. For Co_2YZ Heusler alloys, a Co_Y anti-site is defined as a Co replacing *Y* sites, and for Y_{Co}, vice versa. Picozzi *et al.* reported that Mn_{Co} in Co_2MnSi is not harmful for the half-metallic character, while Co_Y is detrimental due to the creation of additional minority spin states at the Fermi level [68]. In the following part, I will discuss the detrimental effect of Co_{Fe} and Fe_{Co} anti-sites for 10% substitution. I consider the $Co_2(Fe_{0.9}Co_{0.10})(Ga_{0.5}Ge_{0.5})$ as Co-rich CFGG and $(Co_{0.9}Fe_{0.1})_2Fe(Ga_{0.5}Ge_{0.5})$ as Fe-rich CFGG with the same lattice constant as the stoichiometric one. Furthermore, the Co-rich CFGG and Fe-rich cases

correspond to electron and hole doping to CFGG, respectively. Thus, I can confirm the effects of the modulation of the number of valence electrons on P_{sp} and its temperature dependence by considering Co-rich and Fe-rich CFGG.

The results for total and atomic magnetic moment, spin polarization at 0 K, and Curie temperature are tabulated in Table 3.6. For Co-rich CFGG, Fe moment on the *Y* site is smaller compared to the $L2_1$ case. From the Slater-Pauling prediction ($N_V = 29.6$), a total moment of 5.6 μ_B is expected; however, the calculated result for Co-rich CFGG is 5.082 μ_B, which is much smaller than the prediction. I confirmed that this is also accompanied by very low *spd* spin polarization at 0 K (not shown). In Fig 3.17(a), the total *sp* DOS of Co-rich CFGG are shown. It is found that the Co-rich CFGG has in-gap minority-spin states at the Fermi level arising from the Co_{Fe} anti-site, leading to a smaller magnetic moment and lower spin polarization.

Table 3.6. Same information as Table 1 but for off-stoichiometric CFGG in the $L2_1$ structure. *X* denotes the Co_{Fe} and Fe_{Co} anti-sites for the Co-rich and Fe-rich systems, respectively.

System	Magnetic moment (μ_B)						P_{sp} (%)
	Co	Fe	*X*	Ga	Ge	Total	
Co-rich	1.225	2.798	1.594	−0.056	−0.034	5.082	82.6
Fe-rich	1.154	2.774	1.642	−0.062	−0.044	5.127	86.3

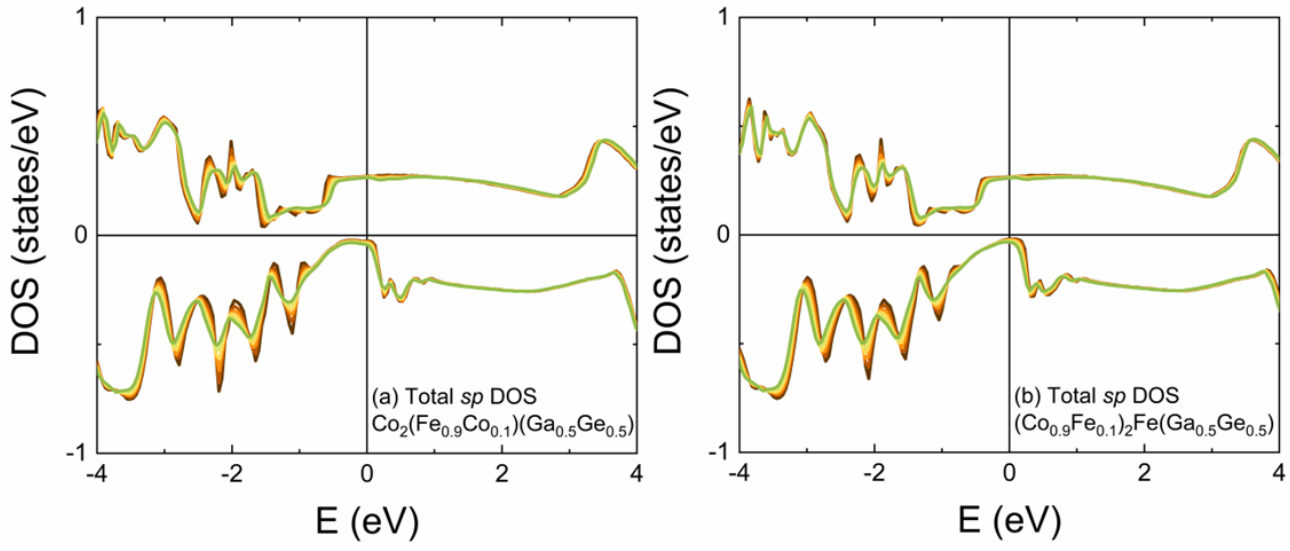

Fig 3.17. Temperature-dependent *sp* DOS for (a) Co-rich CFGG and (b) Fe-rich CFGG.

For Fe-rich CFGG, the magnetic moment of Fe on the *Y* site is also slightly reduced from that in the $L2_1$ structure. Similarly, the $m_{\text{total}} = 5.127\ \mu_B$ is less than the one predicted by the Slater-Pauling rule (($N_V = 29.3$). The total *sp* DOS of Fe-rich CFGG is shown in Fig 3.17(b). The Fe-rich composition simply shifts the Fermi level toward the valence band edge, where the spin polarization P_{sp} will be slightly reduced due to the additional states at the "pseudogap". This shifting is analogous to the effect of hole doping (Fe has one electron less from Co). The *sp* spin polarization at 0 K is quite large, 86.3%, although less than the $L2_1$ counterpart, which is also observed in our previous work in CMS [108].

Finally, the temperature dependence of the total *sp* spin polarization (P_{sp}) for both Co-rich and Fe-rich off-stoichiometric CFGG is shown in Fig 3.18. It is found that relatively small temperature dependence for all cases compared with that of CMS; however, the value of spin polarization is reduced compared to the stoichiometric $L2_1$ structure. I calculated exchange constants and the Curie temperature for the off-stoichiometric CFGG, which were larger than those for CMS. This can be a possible reason for the smaller temperature dependence of P_{sp} in off-stoichiometric CFGG than in CMS. However, due to the degradation of the P_{sp} at 0 K in off-stoichiometric Co-rich and Fe-rich CFGG, the P_{sp} at finite temperature is smaller than that of stoichiometric CFGG. Thus, the modulation of the Fermi level position will be important for stoichiometric Co_2YZ, especially modulation of the composition of the *Y* and *Z* sites, to obtain a large MR ratio for better device performance.

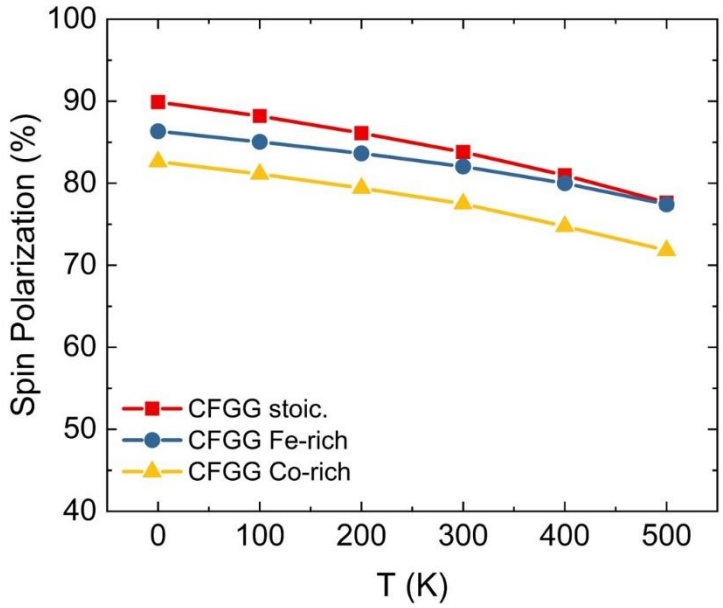

Fig 3.18. Temperature-dependent spin polarization of *sp* states for the stoichiometric, Fe-rich, and Co-rich $L2_1$-CFGG.

3.4.5. Spin polarization of ternary Co-based Heusler alloys

After comparing the calculation results with the experimental spin polarization from CPP-GMR devices of CMS and CFGG and found that Curie temperature plays important role in decay of spin polarization, I investigated the temperature dependence of spin polarization in another ternary Co-based Heusler alloys. The result is shown in the Fig 3.19(a)-(c). Here I only focused on the Co_2YZ with *Y* elements (Cr, Mn, Fe) because it is experimentally demonstrated that these compounds have relatively high Curie temperature larger to allow the application at room temperature [64].

In the Fig 3.19(a), *Z* elements is varied (Al, Ga, In) although contribute to same valence electron number. While Co_2CrAl and Co_2CrGa has very high spin polarization at 0 K (> 90%), it is rapidly decrease at finite temperature, resulting in ~50% spin polarization at room temperature, and finally becomes paramagnetic near 500 K. In contrast to Co_2CrZ compounds, Co_2FeZ show rather constant spin polarization up to 500 K. On the other hand, Co_2MnZ compounds show relatively low spin polarization due to the Fermi level located at the valley of majority spin states and valence band edge of minority spin. One may note that there are no results of Co_2CrIn and Co_2MnIn, because the calculation of these compound does not numerically converge at finite temperature. The difference between temperature dependence of spin polarization in Co_2CrZ and Co_2FeZ compounds can be attributed to the difference of exchange constant parameter $J_{\mathrm{Co}-Y}$ as listed in the Table 3.7. Note that calculated Curie temperature using matrix method mainly depends on the $J_{\mathrm{Co}-Y}$. In the Co_2CrAl and Co_2CrGa, $J_{\mathrm{Co}-\mathrm{Cr}}$ is 76 meV and 52 meV, respectively. While in the Co_2FeAl, Co_2FeGa, and Co_2FeIn, $J_{\mathrm{Co}-\mathrm{Fe}}$ is 551 meV, 518 meV, and 514 meV, respectively. As explained previously, the larger exchange constant lead slower decay of magnetization of *d* electrons, and *sp* spin polarization is also affected via *s-d* and *p-d* coupling, giving the small temperature dependence of *sp* spin polarization.

Table 3.7. The exchange constant of $J_{\mathrm{Co}-Y}$ (in meV unit) for various *Y* and *Z* element of Co_2YZ composition

Y & Z element	Cr	Mn	Fe
Al	76	80	551
Ga	52	85	518
In	-	-	514
Si	182	346	252
Ge	142	304	255
Sn	112	283	242

In the Fig 3.19(b), *Z* elements are Si, Ge, Sn. Calculation of all compounds are numerically converged at finite temperature. Again, the Co_2CrZ show the strongest temperature dependence of spin polarization due to small $J_{\mathrm{Co}-\mathrm{Cr}}$ (Co_2CrSi: 182 meV, Co_2CrGe: 142 meV, Co_2CrSn: 112 meV). On the other hand, Co_2MnZ show the weaker temperature dependence compared to Co_2CrZ due to bigger $J_{\mathrm{Co}-\mathrm{Mn}}$ (Co_2MnSi: 346 meV, Co_2MnGe: 304 meV, Co_2MnSn: 283 meV). The Co_2FeZ compounds shows smaller spin polarization compared to the Co_2MnZ and Co_2CrZ counterpart, despite the similar temperature dependence with Co_2MnSn. This behavior of Co_2FeZ could be attributed to similar $J_{\mathrm{Co}-\mathrm{Fe}}$ (Co_2FeSi: 252 meV, Co_2FeGe: 255 meV, Co_2FeSn: 242 meV) with that of the Co_2MnSn. Note that relatively low $J_{\mathrm{Co}-\mathrm{Fe}}$ in Co_2FeZ is related to the underestimated Curie temperature which also happen in other calculation [64].

On the other hand, Fig 3.19(c) shows rather complex behavior for *Z* elements: P, As, Sb. Only Co_2MnZ shows the relatively high spin polarization at 0 K, which significantly reduced at finite temperature. In case of Co_2CrZ, the spin polarization at 0 K is already less than 50%, which rapidly reduces to zero around room temperature. Moreover, Co_2FeZ compounds demonstrated negative *sp* spin polarization, which slightly become less negative at finite temperature.

Based on these results, I found that compounds with smallest temperature dependence of spin polarization are Co_2FeZ (Z: Al, Ga, In). The superior properties demonstrated by these compounds are attributed due to the large exchange constant of $J_{\mathrm{Co}-\mathrm{Fe}}$. Previously, Co_2FeAl attracted many researchers due its performance on magnetoresistive devices [153], despite only forms in B2-ordered

structure. Meanwhile, Co_2FeGa and Co_2FeIn is not widely investigated. Therefore, these results encourage us to revisit further study on Co_2FeZ. Since in the previous chapter CFGG successfully demonstrated the smaller temperature dependence of spin polarization compared to CMS, it might be worth to consider alloying the Co_2FeZ (Z: Al, Ga, In) with other *Z* elements to improve the structural and electronic properties at finite temperature.

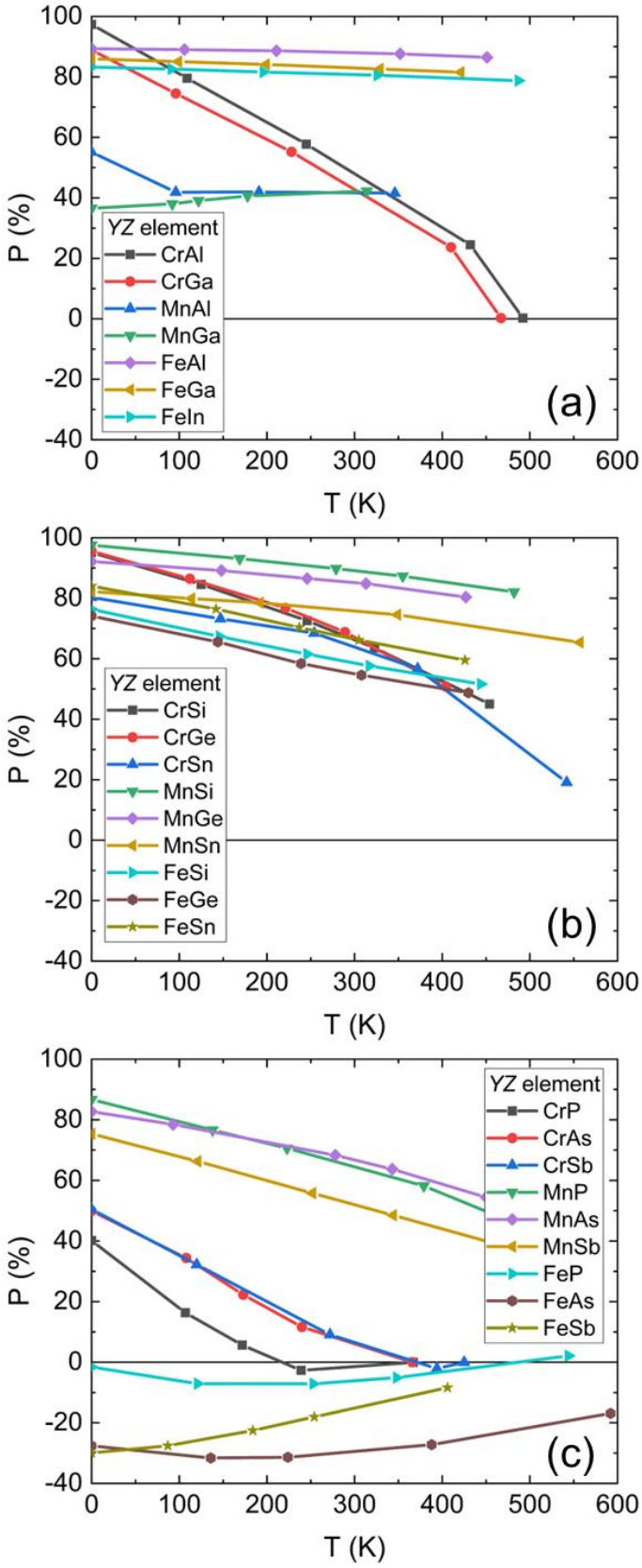

Fig 3.19. Temperature-dependent spin polarization of *sp* states for the ternary $L2_1$-Co_2YZ with combination of *YZ* elements (*Y:* Cr, Mn, Fe) and (a) *Z*: Al, Ga, In, (b) *Z*: Si, Ge, Sn, (c) *Z*: P, As, Sb.

3.5. Effect of Self-interaction correction (SIC)

This section is adapted from [151], previously published by Acta Materialia.

3.5.1. SIC effect on the magnetic properties

It is known that the LSDA fails to describe localized electrons. This is due to non-vanishing unphysical interaction of an electron with itself, i.e., so-called self-interaction. Removing this by using SIC is important to capture the proper electronic structure and magnetic properties. Due to the Slater-Pauling rule of Co-based Heusler alloys, the magnetic moment of CFGG is expected to be 5.5 μ_B per unit cell, which leads to localized electronic structures and spin-density especially around Fe atom in CFGG. Therefore, the LSDA fails to describe the electronic structures and magnetic properties of CFGG. To overcome these problems, I apply the SIC to electronic structure calculations of CFGG. Here, I tested various SIC combinations for the *d* orbitals of Co and Fe to obtain the reliable electronic structures. It is found that the SIC applied to the minority-spin *d* orbitals significantly changes the electronic structures and destroys the gap formation in the minority-spin states around the Fermi level. Thus, I applied the SIC to the majority-spin *d* orbitals only.

Since in the cubic structure of Heusler alloy Co_2YZ, *d* orbitals of Co and *Y* elements are split into two degenerated states: t_{2g} (d_{xy}, d_{yz}, d_{xz}) and e_g ($d_{x^2-y^2}, d_{z^2}$), 16 different combinations were tested with SIC for the majority-spin *d* orbitals of Co and Fe, as shown in Table 3.8 where the combinations are identified by ID = 1~16). Total magnetic moment and atomic spin moments are shown in Fig 3.20. The ID = 4 (SIC to Fe t_{2g}) and 15 (SIC to Fe t_{2g} and e_g) show the total magnetic moment consistent with the predicted value from the Slater-Pauling rule (5.5 μ_B). Interestingly, both configurations treat SIC to the t_{2g} orbital of Fe. On the other hand, once the SIC is included to Co orbitals, the total magnetic moment increases much more than the predicted value from the Slater-Pauling rule. Despite the similar total magnetic moment, very large Fe moment (~3.7 μ_B) in the configuration 15 (SIC to Fe t_{2g} and e_g) seems unphysical to picture the electronic structures of CFGG. Besides that, the SIC with configuration 4 gives a reasonable Curie temperature for CFGG with the $L2_1$ structure (1362 K), which is overestimation compared to the experimental T_C (1080 K) but larger than that of CMS. On the other hand, the SIC with configuration 15 provides relatively smaller T_C (1040 K) than the calculated T_C of CMS (1103 K), which is inconsistent with the experimental observations. Therefore, I consider that only the t_{2g} orbitals of Fe should be corrected by the SIC.

Table 3.8. List of the variations used to incorporate the SIC for the local e_g and t_{2g} orbitals of the Co and Fe atoms in $L2_1$ CFGG. In all the variations, the SIC is introduced in only the majority-spin channel.

ID	Orbital treated by SIC	
	Co	Fe
1	–	–
2	t_{2g}	–
3	e_g	–
4	–	t_{2g}
5	–	e_g
6	t_{2g}	t_{2g}
7	t_{2g}	e_g
8	e_g	t_{2g}
9	e_g	e_g
10	t_{2g}, e_g	t_{2g}
11	t_{2g}, e_g	e_g
12	t_{2g}	t_{2g}, e_g
13	e_g	t_{2g}, e_g
14	t_{2g}, e_g	–
15	–	t_{2g}, e_g
16	t_{2g}, e_g	t_{2g}, e_g

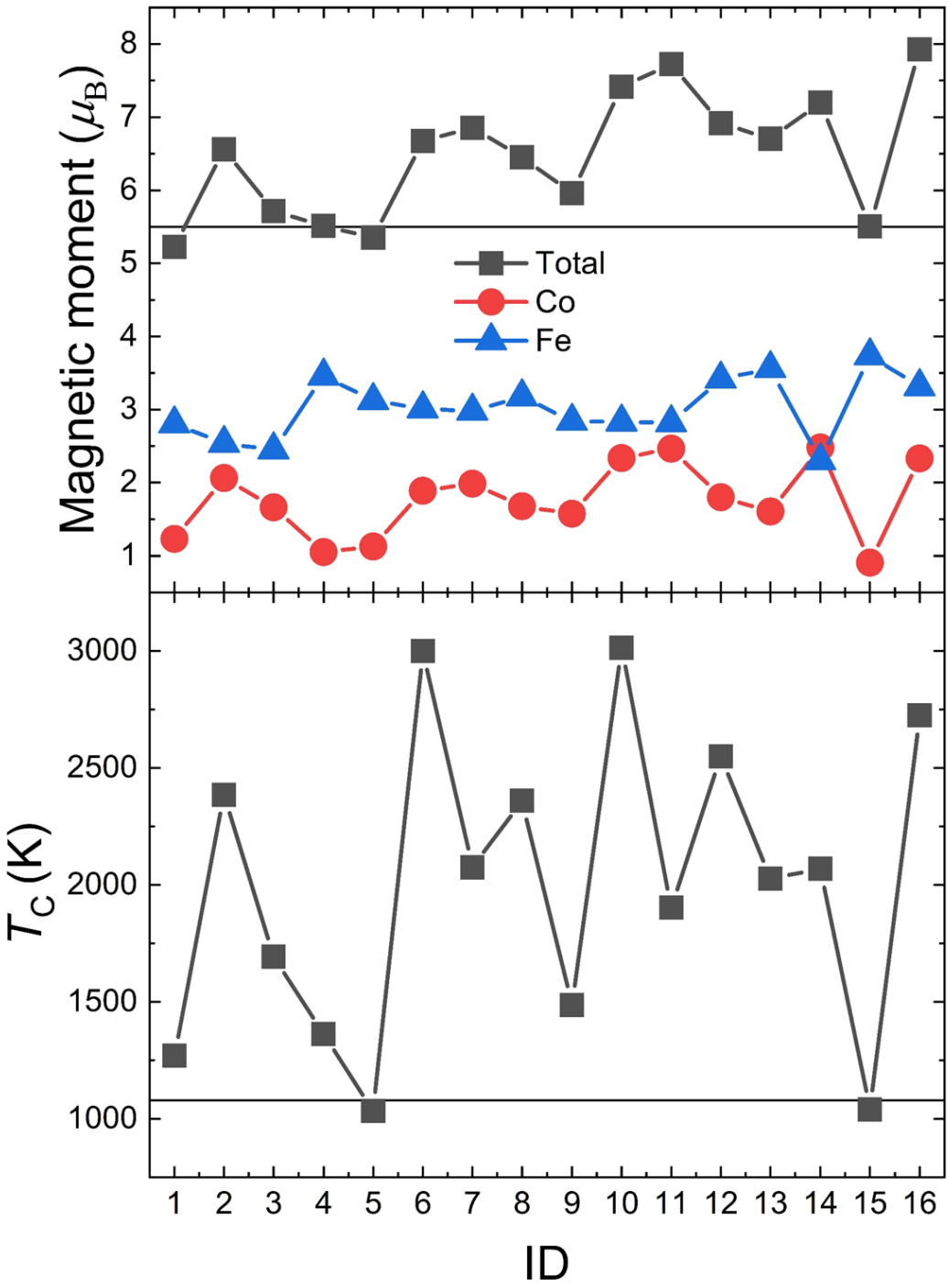

Fig 3.20. Dependence of the SIC effect on total and atomic spin moments (upper panel) and the T_C (lower panel). Experimental results on the total spin magnetic moment and T_C are shown by horizontal lines.

3.5.2. SIC effect on the temperature dependence of electronic structure and spin polarization

After determined orbitals that being corrected by SIC, it is still important to compare the electronic structure and spin polarization before and after SIC implementation to see if our conclusion still holds true. As shown in Fig 3.20, the total magnetic moment with SIC implementation for majority spin of Fe t_{2g} states at 0 K is similar to Slater-Pauling rule prediction for CFGG and experimental value reported by Varaprasad *et al*. [92]. It is also supported from total *spd* DOS shown in Fig 3.21, which explain the improved magnetic moment due to the clearer "pseudogap" at minority spin even at 0 K. Therefore, the total *spd* spin polarization P_{spd} at 0 K is relatively high (>70 %). However, if the *sp* spin polarization of CFGG for LSDA are compared LSDA+SIC implementation, the temperature dependence is still weaker than CMS as shown in Fig 3.22, which is still consistent with the main conclusion. Thus, my conclusion that temperature dependence of *sp* spin polarization of CFGG is weaker than CMS, holds irrespective of the SIC.

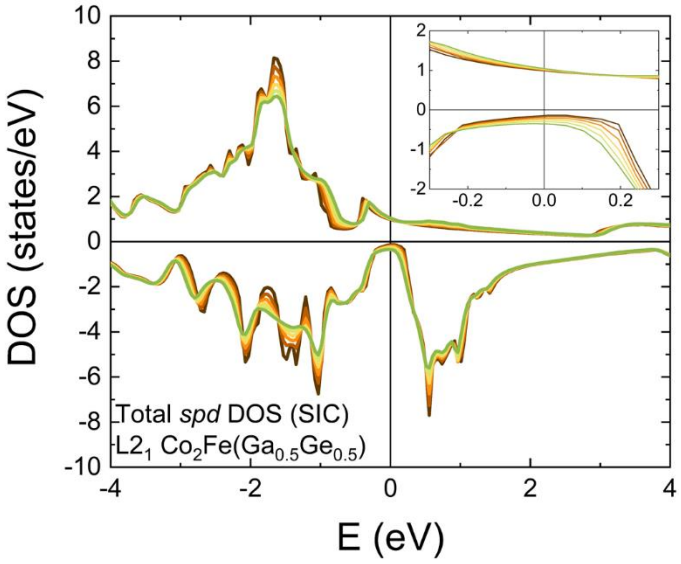

Fig 3.21. Temperature-dependent *spd* density of states for the stoichiometric $L2_1$-CFGG by implementing self-interaction correction on t_{2g} orbitals of Fe.

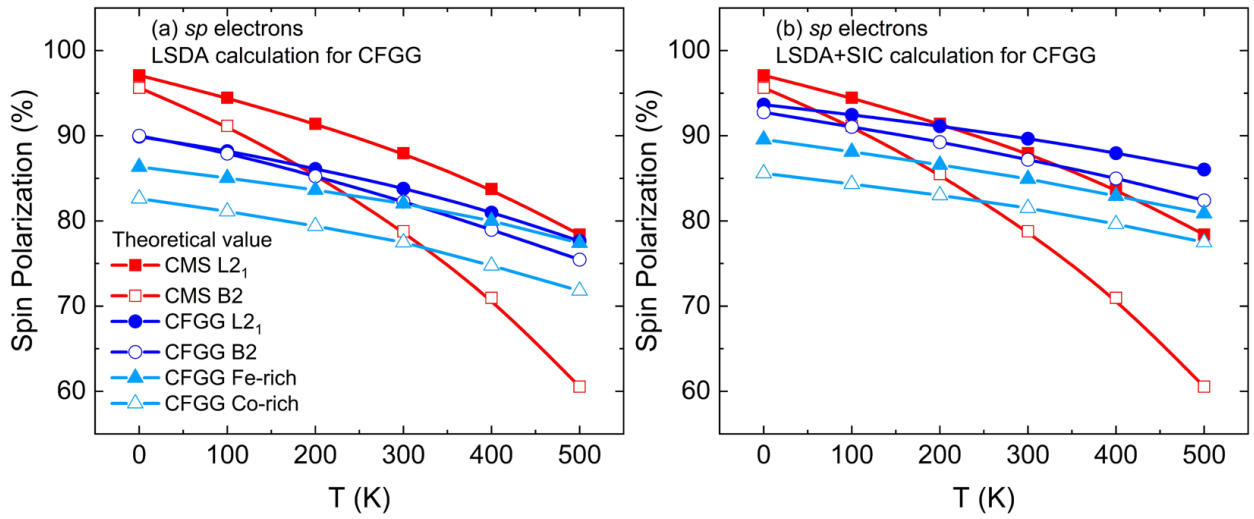

Fig 3.22. Temperature-dependent spin polarization of *sp* states for the stoichiometric, Fe-rich, and Co-rich $L2_1$- and B2-ordered CFGG, compared with the $L2_1$- and B2-ordered CMS (a) without SIC implementation, (b) with SIC implementation.

3.6. Summary

In this Chapter, the magnetic properties and electronic structure of ternary Co-based Heusler alloys at ground state and finite temperature are successfully calculated using the KKR-DLM method. It is found that the temperature dependence of spin polarization for CFGG is smaller than CMS, which is also confirmed in the experimental β values from CPP-GMR. Since both electronic structures show Fermi level located at the edge of the conduction band, the difference of temperature dependence on the spin polarization can be originated from the difference of the Curie temperature between CFGG and CMS. In the DLM model, the Curie temperature of Co_2YZ is strongly related with the interatomic d-d exchange coupling of Co-Y ($J_{\mathrm{Co-}Y}$). Larger interatomic exchange in CFGG ($J_{\mathrm{Co-Fe}}$ = 378 meV) compared to the CMS ($J_{\mathrm{Co-Mn}}$ = 345 meV) will suppress the fluctuation of the magnetic moment at finite temperature. These results provide higher Curie temperature and smaller temperature dependence of *sp* spin polarization for CFGG compared to CMS. Although the magnetic moment is mainly contributed from *d* electrons, the *sp* DOS are affected by the interatomic *d-d* exchange coupling via the intraatomic *s-d* and *p-d* couplings. This is why the material with large Curie temperature such as CFGG will have slower decay of magnetic moment and small temperature dependence of sp spin polarization.

On the other hand, it is also found that the Fermi level position still affects the temperature dependence of sp spin polarization by simulating hole- and electron-doped CFGG. In order to improve temperature dependence of spin polarizations, it is important to keep the Fermi level as far as from the conduction band edge, because the increase of minority spin states from the conduction

band is the origin of spin polarization decay at finite temperature. The increase of Fe composition in the Fe-rich CFGG equivalent to the hole-doped CFGG shows the reduction of spin polarization although slightly improving the temperature dependence. Therefore, this means that there is a possibility to find more superior materials by the modulation of the Fermi level via changing the composition of Y and Z atoms in Co_2YZ Heusler alloys.

Lastly, even with self-interaction correction to obtain the magnetic moment as predicted by Slater-Pauling rule, the temperature dependence of spin polarization of CFGG with or without SIC is still smaller than the CMS, implying my results hold on irrespective of SIC.

Chapter 4: Machine learning study of highly spin-polarized Heusler alloys at finite temperature

4.1. Introduction

In the Chapter 3, it is found that the high spin polarization of CFGG and CMS at low temperature is significantly reduced at finite temperature. This means that simple ground-state calculations of spin-polarization at 0 K are not enough to predict half-metallicity at ambient temperature. In particular, Heusler alloys compound have been actively explored by machine learning and high throughput calculation due to the abundant variety of atomic combinations and the relatively simple fabrication process [131,148,154–156]. However, the machine learning investigation of highly spin-polarized Heusler alloys with the first-principles calculation have been performed only at zero temperature [131]. This made a significant discrepancy between physical properties designed by first principles calculations and experimental results of the predicted material. On the other hand, the inclusion of finite temperature effects in DFT calculations is computationally expensive, and simply implement it in high-throughput manner is just unrealistic. These suggest the importance of machine learning with the finite temperature first-principles calculation to predict novel half-metallic Heusler alloys at room temperature. The alternatives Heusler compound is proposed, and further analysis of Fermi level tuning effect for several composition is provided. General trend of highly-spin polarized Heusler at finite temperature is supported by ground state calculation in high-throughput manner.

4.2. Calculation Details

The schematic framework of machine learning and finite temperature calculation is shown in the Fig 4.1(a)-(c). In short, I started by defining the search space of candidates, then started the Bayesian optimization to do finite temperature calculation. The result of finite temperature calculation is given back into Bayesian optimization model. Thus, the machine learning model will suggest which next candidates that need to be evaluated, and this process is repeatedly done until predetermined number of candidates were evaluated. Since my goal is to find the highly spin-polarized Heusler alloys at finite temperature, all obtained results will be sorted and ranked based on the score. Here, I defined the score as $TP_{sp}(T)$, which is product of temperature T and *sp* spin polarization at particular T. Note that T is the converged temperature after setting the particular initial beta-*h* (Weiss field) parameter. For simplicity, I set the same initial beta-*h* parameter for all systems. The detail of determination set of candidates, parameter of Bayesian optimization, and finite temperature calculation is described as in the following paragraphs.

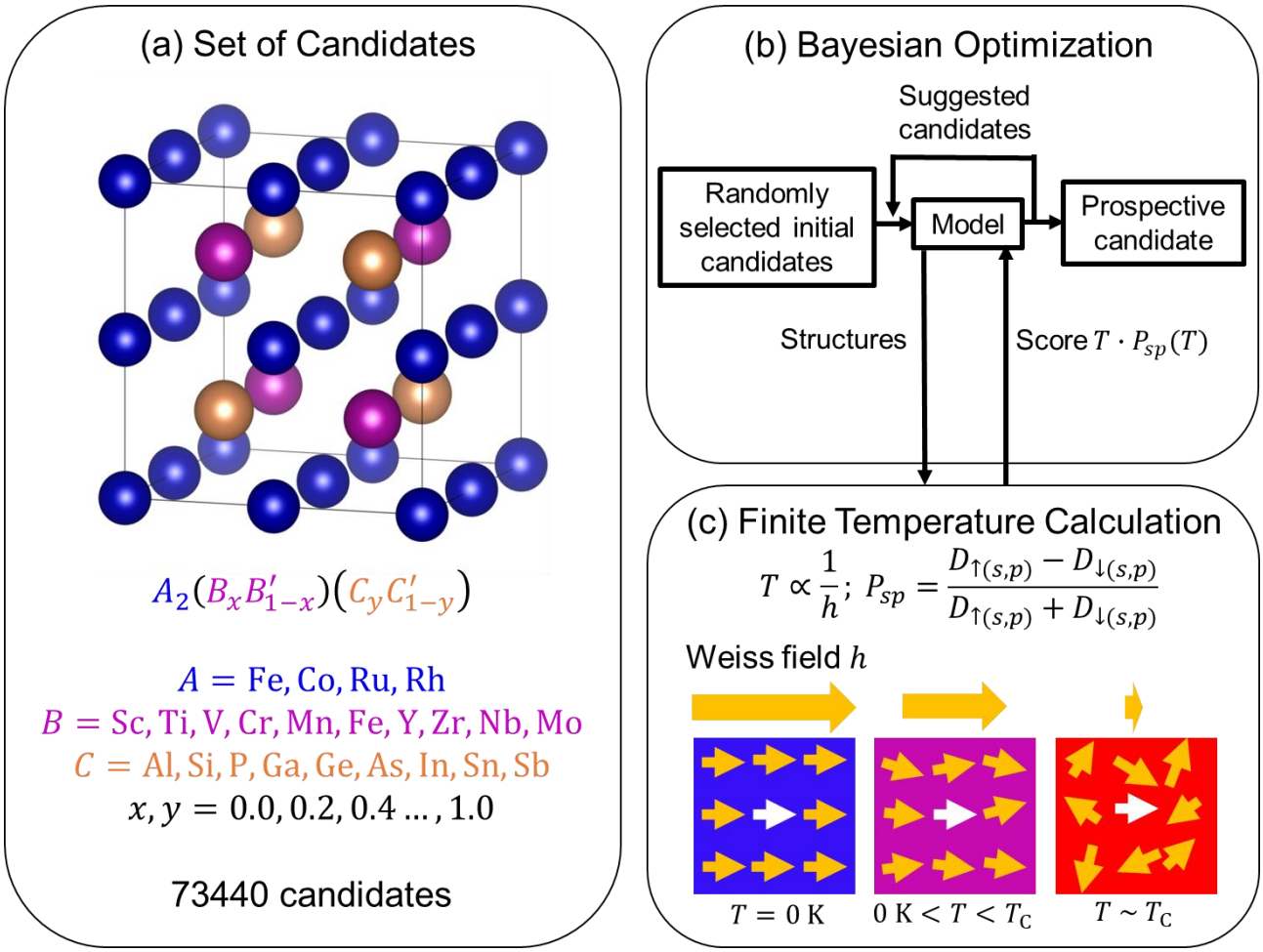

Fig 4.1. The schematic workflow for finding prospective candidates with highly spin-polarized Heusler alloys at finite temperature. (a) Set of candidates to be investigated in this study, (b) implemented Bayesian optimization procedure to find the prospective candidate, and (c) finite-temperature calculation to obtain the *sp* spin polarization at converged temperature T using starting parameter of Weiss field *h*.

Using deep neural network, Hu *et al.* [131] show that the high spin polarization Heusler alloys A_2BC follow the elemental distribution as shown in the Fig 4.2 where A = Fe, Co, Ru, Rh, Mn; B = Sc, Ti, V, Cr, Mn, Fe, Y, Zr, Nb, Mo, La, Lu, Hf, and C = B, Al, Ga, In, Si, Ge, Sn, P, As, Sb, Se, Mg. For simplicity, I ignore some elements and decide to use the distribution as shown in the Fig 4.3: A = Fe, Co, Ru, Rh; B = Sc, Ti, V, Cr, Mn, Fe, Y, Zr, Nb, Mo, and C = Al, Ga, In, Si, Ge, Sn, P, As, Sb. Since the alloying different compounds already demonstrated the improved properties such in the CFGG and CFMS [129,157], I considered general composition $A_2(B_xB'_{1-x})(C_yC'_{1-y})$ with the possibility of nonstoichiometry composition of B, B', C, C' with the coefficient x,y is varied from 0 to 1 with 0.2 interval. Note that $B'(C')$ also follow the elemental distribution of $B(C)$. These combinations lead to 73440 total candidates which consist of 3-, 4-, and 5-elements based compound.

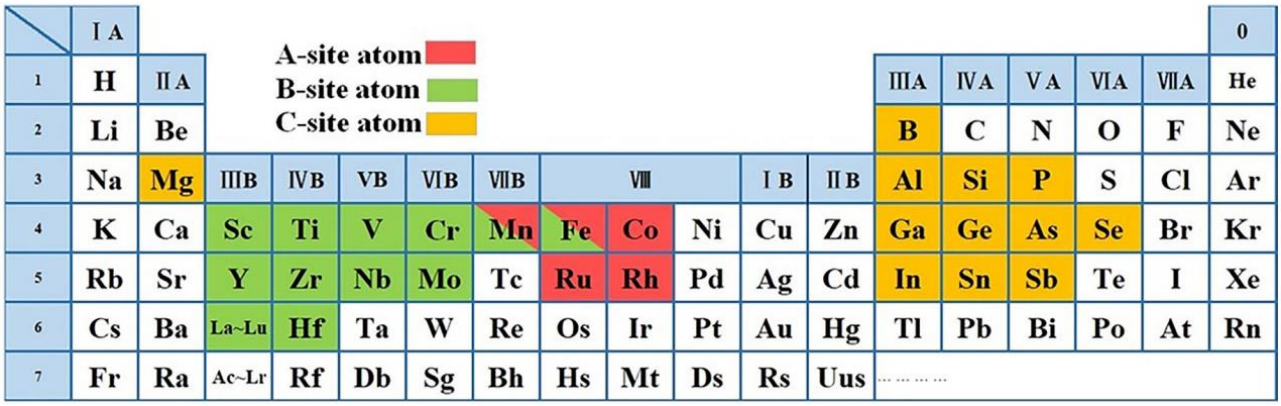

Fig 4.2. The distribution of elements for highly spin-polarized Heusler A_2BC based on Hu *et al.* Reuse with permission [131].

P|G	3	4	5	6	7	8	9	10	11	12	13	14	15
3											Al	Si	P
4	Sc	Ti	V	Cr	Mn	Fe	Co	Ni	Cu	Zn	Ga	Ge	As
5	Y	Zr	Nb	Mo	Tc	Ru	Rh	Pd	Ag	Cd	In	Sn	Sb

Fig 4.3. The elements occupying *A* (blue), *B* and *B'* (purple), *C* and *C'* (brown) considered for machine learning study of $A_2(B_xB'_{1-x})(C_yC'_{1-y})$.

For all candidates, I assume $L2_1$ structure which correspond to fcc lattice having 4 atoms consisted of 2 *A* (0.25, 0.25, 0.25) and (0.75, 0.75, 0.75), a *B*(*B'*) (0, 0, 0), and *C*(*C'*) (0.5, 0.5, 0.5) as illustrated in Fig 4.1. The lattice constant for 3-element compounds are taken from the Alabama Heusler Database [130] and previous report of Hu *et al.* [131]. For 4- and 5-elements compounds, the lattice constant are calculated by assuming linear relation of Vegard's Law [158] on 3- and 4-elements parent compound, respectively.

Before implementation of machine learning, I set the numerical descriptor to identify each composition $A_2(B_xB'_{1-x})(C_yC'_{1-y})$ as a concatenation of integer numbers following the rule,

$$A_2(B_xB'_{1-x})(C_xC'_{1-x}) \rightarrow \mathrm{P|G}_A + \mathrm{P|G}_B + n_x + \mathrm{P|G}_{B'} + n_{1-x} + \mathrm{P|G}_C + n_y + \mathrm{P|G}_{C'} \quad (4\text{-}1)$$

where P|G is a set of the number of period and group in the periodic table as shown in the Fig 4.3 to identify the element (*A, B, B', C, C'*) and *n* indicates the stoichiometry coefficient of *B, B', C,* and *C'*. For examples, Co(Si) is in the 4th (3rd) period and 9th (14th) group, thus I express the $\mathrm{P|G}_{\mathrm{Co}} =$

4|9 ⇒ 49 ($\mathrm{P|G_{Si}} = 3/14 \Rightarrow 314$), respectively. The stoichiometry coefficient of n_x and n_y were described as follow, $x = 0.2 \Rightarrow n_x = 02$, and $y = 1.0 \Rightarrow n_y = 10$, and so on. If there is no $B'(C')$ element, I set $\mathrm{P|G}_{B'} \Rightarrow 00$ ($\mathrm{P|G}_{C'} \Rightarrow 00$) and $n_{1-x} = 00$ ($n_{1-y} = 00$), respectively. By concatenate all of these parameters, each composition will be uniquely described with 20-digit integer descriptor. For example, Heusler alloy, $Ru_2(Mn_{0.6}Fe_{0.4})(P_{0.2}Sb_{0.8})$ can be expressed by "58470648043150251508" due to $\mathrm{P|G_{Ru}} = 58$, $\mathrm{P|G_{Mn}} = 47$, $n_x = 06$, $\mathrm{P|G_{Fe}} = 48$, $n_{1-x} = 04$, $\mathrm{P|G_P} = 315$, $n_y = 02$, $\mathrm{P|G_{Sb}} = 515$, and $n_{1-y} = 08$.

The optimization method used in this study is Bayesian optimization. It is known that Bayesian optimization is suitable to solve the black-box function, which has unknown relation with the input and expensive to calculate. In this study, I employed the open-source Bayesian optimization library COMBO [159]. Training of the Bayesian optimization model are performed by evaluation of the random choice of initial candidates. First 20 compositions were chosen, then information details of composition and structural parameter (lattice constant) is sent to the framework of finite temperature calculation to calculate the score.

In order to calculate the score of each candidate, ground state calculation were performed first using KKR method [119,120] using HUTSEPOT code [132]. The potential ground state calculations become the input of finite temperature calculation using DLM framework [121]. The main idea is to converge the system into particular temperature with initial parameter of beta-*h* (Weiss field) which somehow related to the magnetic order parameter within DLM framework. After convergence of temperature, the density of states calculation is performed and the spin polarization value is obtained. Based on previous investigation on typical Co-based Heusler alloys, it is found that 5-6 iterative rounds are enough to obtain convergence at around room temperature, with total duration ~5-6 hours to obtain the spin polarization at finite temperature. Therefore, I set waiting time 7 hours for each calculation.

Aside the descriptor, the optimization method, the calculator, the fourth and most important component on material informatics are the evaluator [160]. Here, I use the score of $TP_{sp}(T)$ as product of converged temperature T and *sp* spin polarization at converged temperature $P_{sp}(T)$ to evaluate the performance of each composition. Note that I use the *sp* spin polarization because the previous experimental finding show that experimental spin polarization is better explained by *sp* spin polarization than total *spd* spin polarization [142]. Moreover, since this study focus to the highly spin polarized Heusler alloys at finite temperature, it is important to note that high spin polarization is not

only demonstrated at ground state calculation, but also retained at high temperature. That is why I decide to multiply the spin polarization with temperature as score to evaluate each candidate.

4.3. Machine Learning Results and Statistics

The score $TP_{sp}(T)$ is plotted as a function of the number of calculated structures of Heusler alloys in Fig 4.4. The predetermined number of calculated structures is fixed to 2200 structures, which approximately 3% from the total number of candidates in the search space (73 440). This value is considered enough to achieve the convergence of the optimum score, based on Ju *et al.* work on phonon transport with 12 870 total number of candidates [160]. It is important to note that in the relatively small total number of candidates, the convergence may be achieved after as large as 17% of total number candidate are evaluated [161]. It is due to the efficiency of machine learning framework will increase by increasing number of candidates. Since in this study machine learning is employed to tackle "real" and "computationally expensive" black box problem, it is impossible to check the accuracy of this optimization by calculating the score for all candidates, and it is assumed that the convergence will be achieved within this predetermined number of structures.

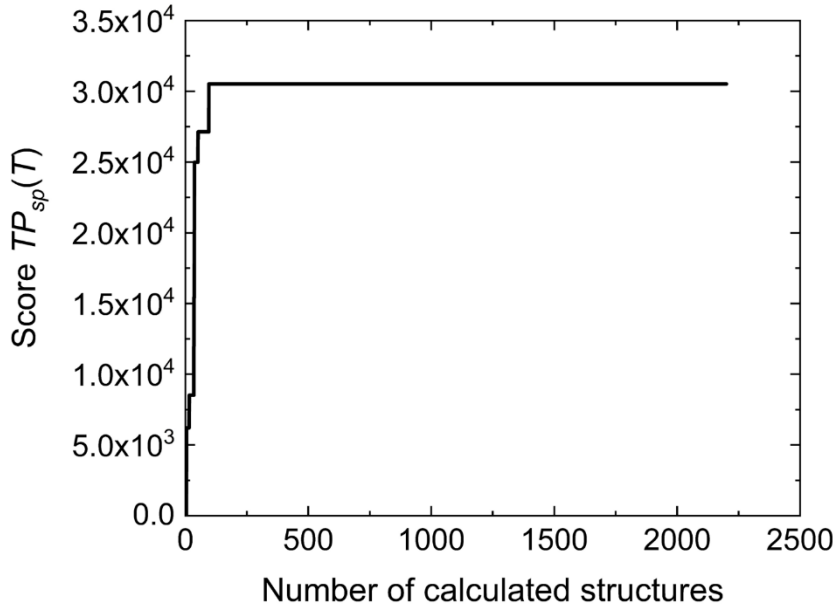

Fig 4.4. The performance of Bayesian optimization for calculated Heusler structures

In this study, the score $TP_{sp}(T)$ is used to characterize the top candidates. Unlike the previous study that only focus the ground state spin polarization [131], here the temperature is also provided to give the context how large the spin polarization is retained after including the finite temperature. The same initial beta-*h* is set for all candidates, based on the value that converge to 300 K in well-known system Co_2MnSi. Intuitively the highest score can be obtained when a structure still retains 100% at around

300 K, which means the $\sim 3.0 \times 10^4$. This is achieved within less than 100 calculations, again emphasizing the superiority of machine learning than the conventional random search method. However, with another different set of initial candidates, this convergence behavior can be different.

Among 2200 number of candidates, only 260 candidates having nonzero score $TP_{sp}(T)$ with distribution shown in Fig 4.5. Note that few candidates occupied the higher score region, indicating the feasibility of Bayesian optimization to find these top candidates. On the other hand, the zero score can be attributed to several different reasons. First, the initial beta-*h* converged to the zero temperature, which imply the initial beta-*h* is too high and simulate the high magnetic ordering corresponding the ground state calculation. Second, despite the initial beta-*h* converged to the finite temperature, the *sp* spin polarization at that particular temperature is zero. Third, the calculation does not converge properly, and it may happen in any step of calculation such ground state self-consistent-field-calculation step, DLM iteration, or process to obtain the density of states and spin polarization. These facts emphasize the huge challenge to properly incorporate lengthy and multistep calculation process such first-principles finite temperature calculation with the machine learning to find alternative highly spin-polarized Heusler alloys at room temperature, which for the first time will be comprehensively presented in this study.

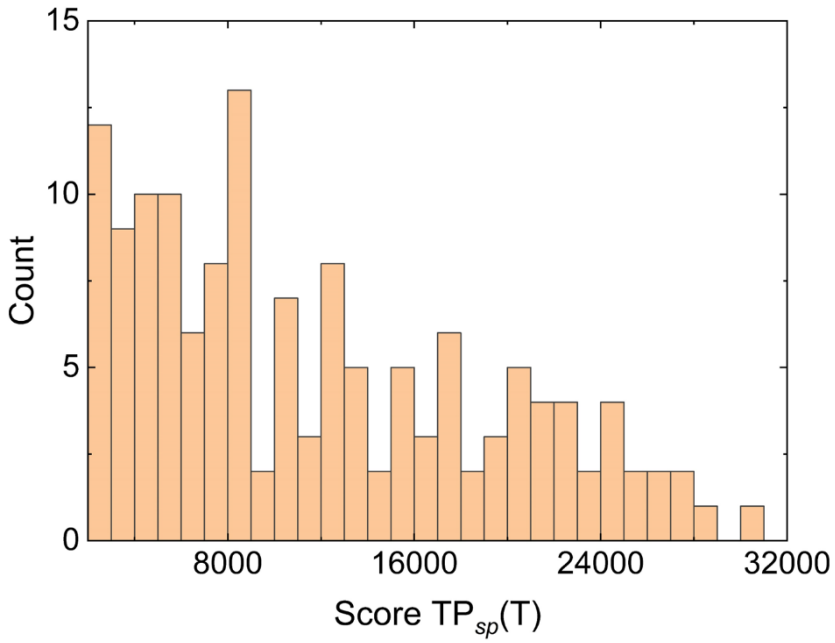

Fig 4.5. The histogram of score $TP_{sp}(T)$

Since for all candidates the same initial beta-*h* is used, the converged temperature can be directly compared as histogram shown in Fig 4.6. The qualitative trend in distribution of converged temperature is similar with the score $TP_{sp}(T)$. There are 378 structures which converged into nonzero

temperature. One may question the justification behind same initial beta-*h*. It is understood that ideal calculation should set specific beta-*h* that converged to the room temperature for *each structure*, however as mentioned in the Chapter 3, such determination of specific beta-*h* for particular temperature will be take much longer time and impossible to be done than the calculation of spin polarization at one temperature. On the other hand, setting the same initial beta-*h* as I did in this study will also give the insight on how the obtained temperature relates with the ground state properties like the magnetic moment at 0 K as shown in the Fig 4.7. It is found that the beta-*h* = 9 is too large to describe the low-magnetic-moment system at room temperature. Therefore, scaling the initial value of beta-*h* with the value of ground state magnetic moment may be a good idea for future improvement of machine learning framework at finite temperature. Note that based the current scheme, most system converged at finite temperature is Co-based Heusler alloys, which may imply two things. First one is further development of the technical method may find another prospective candidate with Fe-, Ru-, and Rh-based compound. Second one is, the only prospective Heusler alloys with high spin polarization at finite temperature can be obtained with Co-based only.

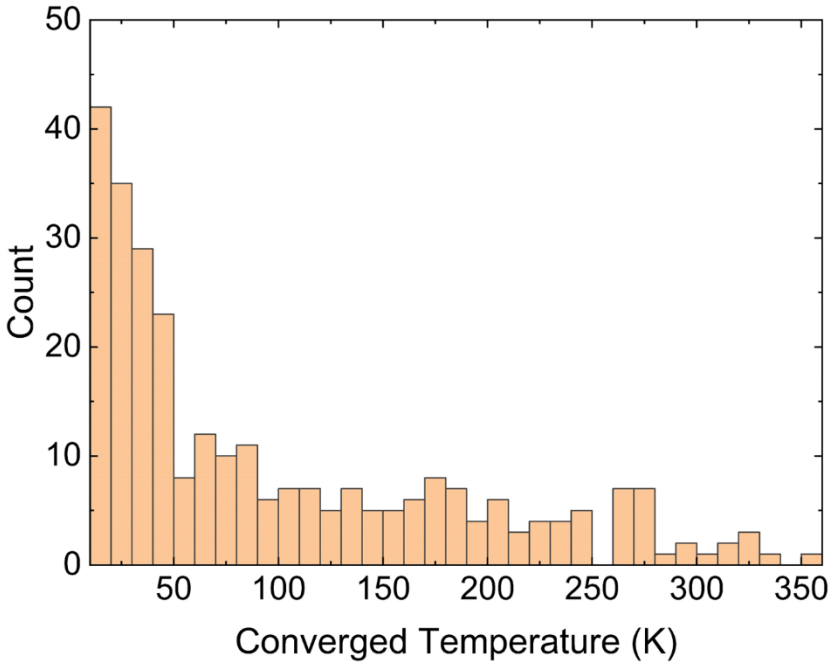

Fig 4.6. The histogram of converged temperature

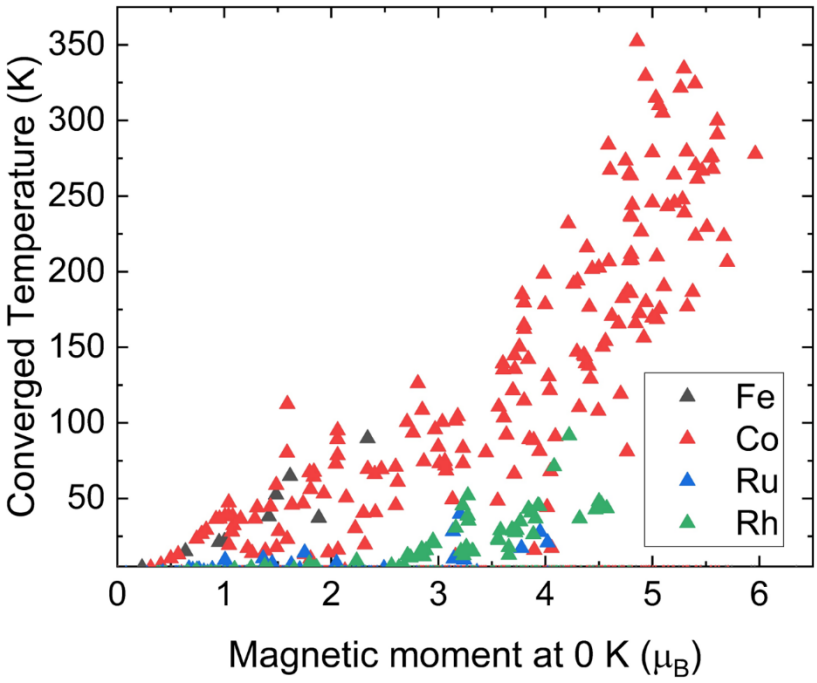

Fig 4.7. The relation between magnetic moment at 0 K with converged temperature with initial beta-*h* = 9.

In the Fig 4.8 the *sp* and *spd* spin polarization are plotted as distribution over converged temperature for investigated system. Most compound converged to the very low temperature or 0 K. When the investigated system converged to the relatively high temperature around room temperature with large *sp* spin polarization, it is found that it does not necessarily mean that the *spd* spin polarization is also large. Because large *sp* spin polarization can be obtained in the very low or even negative value of *spd* spin polarization, the conventional way to focus only on *spd* spin polarization will limiting our search space of prospective candidate. It emphasizes the importance to shift our focus on *sp* spin polarization to find highly spin-polarized Heusler at finite temperature. The Fig 4.9 show the distribution of spin polarization at finite temperature. In general, the distribution of *sp* and *spd* spin polarization of all compound seems evenly spread. Area of high *sp* spin polarization with various *spd* spin polarization are dominated by Co-based Heusler alloys converged to dominate the area of high *sp* spin polarization, where the numerous Rh-based compound converged to dispersive and moderate value of spin polarization. Significant amount of Ru-based Heusler alloys seen to be converged to the high *sp* spin polarization area. However, as I mentioned previously, that score is the product of spin polarization and temperature. Despite the high *sp* spin polarization, if it converges to the low or even zero temperature after DLM iteration, it will lead to the zero score. And in the next part, I will address the crucial factor that may be the origin of problem in the DLM iteration.

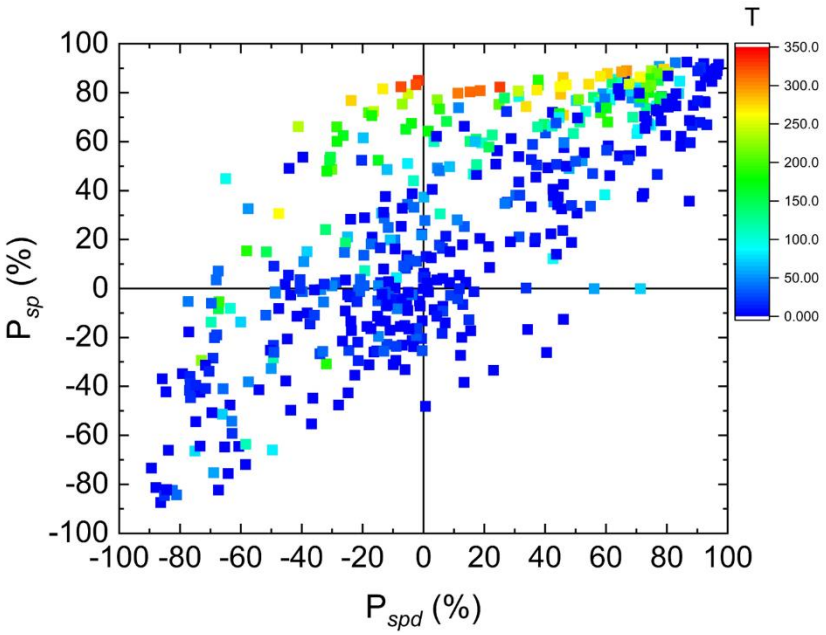

Fig 4.8. The distribution of *sp* and *spd* spin polarization of investigated Heusler structures over converged temperature using Bayesian optimization.

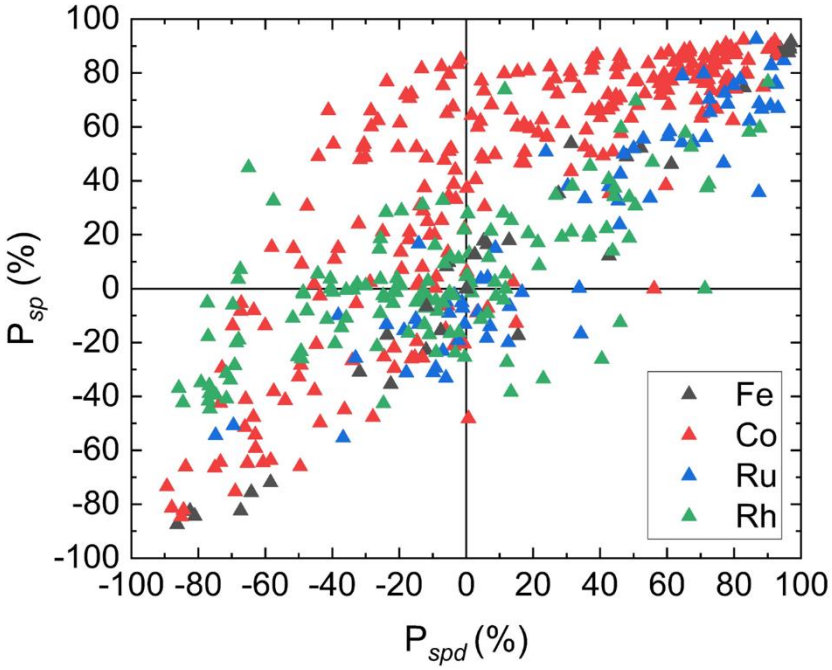

Fig 4.9. The distribution of *sp* and *spd* spin polarization of investigated Heusler structures over *A* element using Bayesian optimization.

In every each DLM iteration step, there are two parameters need to be updated. First, beta-*h* to achieve the convergence in the temperature. Secondly, the Fermi energy to match the result between scalar relativistic ground calculation and fully relativistic DLM calculation at finite temperature. As explained in Chapter 3, this adjustment required the desired number of valence electron. One may

easily suppose that the total valence electron can simply calculated as a sum of valence electron of each atom following its group in the periodic table. However, my comprehensive analysis on the ternary compound of Co-based Heusler alloys reveal that the contribution of electron is not as simply as periodic table predicts. Even after careful consideration of valence electron, Fig 4.10 show that the calculated number of valence electron of zeroth DLM iteration round on predicted number of valence electron is showing rather dispersive behavior. It is expected that for common system such ternary Co-based Heusler alloys, the difference between $N_{val}^{numeric}$ and $N_{val}^{desired}$ will be less than 1 electron. However, there are significant number of cases where $N_{val}^{numeric} < 15$ which dominated by Fe-based compound. This explains the why so few Fe-based compound converged to the finite temperature. Majority of compound considered in this calculation will have $N_{val}^{numeric}$ larger than estimated by $N_{val}^{desired}$, implying that fully relativistic DLM calculation generally overestimates the Fermi energy.

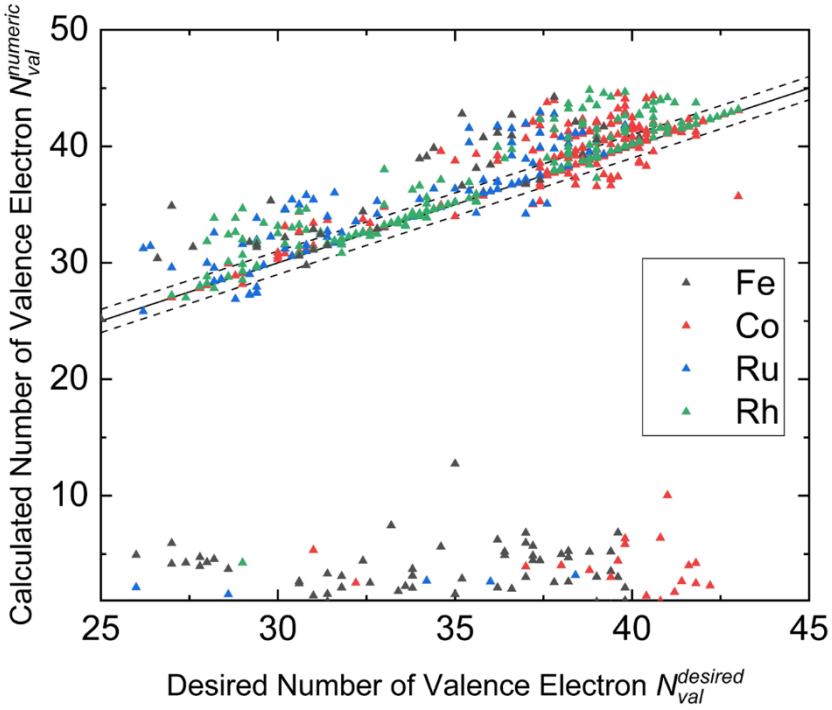

Fig 4.10. The numerically calculated number of valence electron $N_{val}^{numeric}$ of zeroth DLM iteration round on desired number of valence electron $N_{val}^{desired}$. The solid line corresponds to the $N_{val}^{numeric} = N_{val}^{desired}$, and two dashed lines correspond to the $N_{val}^{numeric} = N_{val}^{desired} \pm 1$.

4.4. Prospective Candidates

This section is adapted from [162], previously published by Physical Review Materials.

In Table 3.1, I show the top 30 compounds having highest scores in the Bayesian optimization together with the lattice constant a, the spin moment m_{total}, total and sp spin-polarizations P_{spd} and P_{sp}

at the converged temperature *T*, and also the formation energy E_{form}, which are outputs of the first-principles calculations except for the lattice constants. Note that the lattice constants for the 3-element compounds are taken from Alabama Heusler Database [130] and Hu *et al.* [131], while for the 4- and 5-element are estimated based on the Vegard's law [158]. Scores of $TP_{sp}(T)$ are used in predictions of black box function in Bayesian optimization. The formation energy E_{form} of $A_2(B_xB'_{1-x})(C_yC'_{1-y})$ was calculated by following equation,

$$E_{\text{form}} = E^{\text{total}}_{A_2(B_xB'_{1-x})(C_yC'_{1-y})} - \left(2E^{\text{total}}_{A} + xE^{\text{total}}_{B} + (1-x)E^{\text{total}}_{B'} + yE^{\text{total}}_{C} + (1-y)E^{\text{total}}_{C'}\right) \quad (4\text{-}2)$$

where E^{total} is the total energy for each system for Heusler alloys $A_2(B_xB'_{1-x})(C_yC'_{1-y})$, and single elements *A, B, B', C,* and *C'* calculated using first-principles calculation at zero temperature.

As shown in Table 3.1, I found the general trend of prospective candidate are having Co occupy *A* site, to be specific, Co_2Fe- and Co_2Mn- based Heusler alloys which consisted from 3-, 4-, and 5-element compound. In addition, the *C* elements are varied. These results are summarized in the Fig 4.11, where elemental distribution of highly spin-polarized Heusler alloys are shown with less option compared to the Hu *et al.* [131]. It is important to note that Hu *et al.* only reported the elemental distribution for Heusler alloys with high spin polarization at *ground state* [131]. As demonstrated on my results in the Chapter 3, not all of highly-spin polarized Heusler retain its value at high temperature, because it is strongly related with the exchange constant and Curie temperature. Take Co_2CrAl as an example, where the spin polarization is virtually half metal (~98%) at 0 K based on our calculation, which rapidly decrease at finite temperature, with spin polarization less than 50% at room temperature. It is known that Co_2Fe- and Co_2Mn- based Heusler alloys have high Curie temperature among other full-Heusler based compound, hence basically my result emphasizes the importance of high Curie temperature to have high spin polarization at room temperature.

Among the 3-elements based compound, there are Co_2FeZ with *Z*: Al, Ga, In. In the Chapter 3, I found that these materials have largest exchange constant (> 500 meV) among the investigated ternary Co-based Heusler alloys, as the origin of very weak temperature dependence of spin polarization. Therefore, it is expected to find these compounds as the top candidate suggested by Bayesian optimization. Note that Co_2FeAl also has the highest score among of these candidates. The fact that Bayesian optimization successfully find the Co_2FeZ with *Z*: Al, Ga, In which theoretically predicted to have weak temperature dependence of spin polarization based on simple screening among the ternary Co-based Heusler alloys imply the good efficiency and performance of Bayesian optimization

to find the candidates with optimized properties, despite the Bayesian optimization model does not have any knowledge about physics behind the high spin polarization at finite temperature.

Previously, large magnetoresistance ratio (330% at RT, 700% at 10 K) is reported in the Co2FeAl/MgO/CoFe-MTJ [153]. Even with simple sputtering deposition technique and B2-ordered structure of Co2FeAl, this result was very promising at 2009 [153]. Moreover, the temperature dependence of MR ratio observed from 10 K to room temperature is smaller than Co2MnSi/MgO/CoFe MTJ [163], which can be explained via the difference of exchange constant. However, simple Julliere's model on this MTJ will lead unrealistic spin polarization for B2-Co2FeAl electrode (larger than 100 %) by assuming spin polarization of CoFe is constant 50%, which is attributed to the contribution from the coherent tunneling effect, which is dominant contribution to the tunneling process in the MgO-based MTJ devices [153].

The Co_2FeGa is not predicted as half-metal compound [92,164], where experimental investigation of spin polarization using PCAR method give the comparable value with CoFe [165]. In case of Co_2FeIn, recent theoretical prediction shows this material as half-metal [166], while synthesis attempt were conducted by Galdun *et al.* [167] to obtain nanowires with disordered structure. Similarly, Co_2MnP and Co_2MnAs were only investigated theoretically [168–170]. On the other hand, despite strong temperature dependence of Co_2MnSi, this compound still retains relatively high spin polarization at room temperature, and widely investigated experimentally for TMR and CPP-GMR devices [98,102].

For the 4-elements based compounds, there are several compounds that already previously investigated in the theoretical and experimental manners. Namely, $Co_2Fe_{1.0}Ga_yGe_{1-y}$, $Co_2Mn_{1.0}Al_ySi_{1-y}$, $Co_2Mn_{1.0}Ga_yGe_{1-y}$ [92,171,172]. These compounds are created by mixing two adjacent elements in the periodic table on *C* site, to obtain the optimized properties of two parent ternary Heusler compound. Because the adjacent element allows us to have easier understanding of relation between properties and composition, it becomes widely accepted idea to generate the new composition with better properties. However, my result demonstrated that, in order to obtain top candidates, element mixing does not necessarily to be adjacent each other in the periodic table, such as Al and Sn in $Co_2Fe_{1.0}Al_{0.4}Sn_{0.6}$, Ga and As in $Co_2Mn_{1.0}Ga_{0.2}As_{0.8,}$ or Ga and In in $Co_2Fe_{1.0}Ga_{0.4}In_{0.6}$.

The magnetic moments of these candidates are pretty high, more than 4.5 μ_B, which lead to converged temperature around 200-350 K using same starting parameter Weiss field. Interestingly, these candidates have various value of P_{spd} spanned over the range -20 – 80%, despite the relatively high P_{sp} more than 70%. These results implies conventional approach to find the highly spin-

polarized material based on merely P_{spd} value will exclude many prospective candidates. Note that I also found that almost all potential candidates except $Co_2Fe_{0.8}Mo_{0.2}As_{0.2}Sb_{0.8}$ have negative formation energy, which confirm the thermodynamical stability of most proposed compounds.

Table 4.1. Summary of potential highly spin-polarized Heusler alloys at finite temperature suggested by Bayesian optimization.

System	a (Å)	m_{total} (μ_B)	T (K)	P_{spd} (%)	P_{sp} (%)	TP_{sp}	E_{form} (eV/f.u.)
$Co_2Fe_{1.0}Al_{1.0}$	5.700	4.86	352	39.0	86.7	30521	-1.71
$Co_2Fe_{1.0}Ga_{1.0}$	5.720	4.94	329	25.1	82.4	27134	-3.11
$Co_2Fe_{1.0}In_{1.0}$	5.980	5.10	305	11.4	79.8	24347	-3.38
$Co_2Mn_{1.0}As_{1.0}$	5.796	5.96	278	46.0	70.8	19684	-0.71
$Co_2Mn_{1.0}P_{1.0}$	5.638	5.67	223	4.6	77.1	17230	-1.79
$Co_2Mn_{1.0}Si_{1.0}$	5.630	5.00	299	79.0	88.0	26326	-2.44
$Co_2Fe_{1.0}Al_{0.4}Sn_{0.6}$	5.876	5.29	334	-1.7	85.0	28419	-3.09
$Co_2Fe_{1.0}Ga_{0.2}Ge_{0.8}$	5.736	5.32	280	-23.7	76.9	21485	-1.61
$Co_2Fe_{1.0}Ga_{0.2}In_{0.8}$	5.928	5.06	310	15.3	80.4	24920	-3.18
$Co_2Fe_{1.0}Ga_{0.4}Ge_{0.6}$	5.732	5.26	322	-7.4	82.4	26502	-2.00
$Co_2Fe_{1.0}Ga_{0.4}In_{0.6}$	5.876	5.03	315	18.7	80.9	25476	-3.04
$Co_2Fe_{1.0}In_{0.4}Sn_{0.6}$	5.988	5.40	324	-2.5	83.3	27009	-4.00
$Co_2Mn_{1.0}Al_{0.2}As_{0.8}$	5.777	5.61	300	66.8	89.0	26681	-0.97
$Co_2Mn_{1.0}Al_{0.2}Ge_{0.8}$	5.728	4.80	212	74.8	83.1	17589	-1.48
$Co_2Mn_{1.0}Al_{0.2}Sb_{0.8}$	5.954	5.55	276	60.5	87.8	24250	-0.26
$Co_2Mn_{1.0}Al_{0.2}Si_{0.8}$	5.644	4.80	237	80.5	88.2	20909	-2.29
$Co_2Mn_{1.0}Ga_{0.2}As_{0.8}$	5.781	5.61	291	65.1	88.4	25711	-1.23

$Co_2Mn_{1.0}Ga_{0.2}Ge_{0.8}$	5.731	4.81	208	73.3	82.2	17088	-1.75
$Co_2Mn_{1.0}Ga_{0.2}Sb_{0.8}$	5.958	5.56	268	58.2	86.8	23254	-0.45
$Co_2Mn_{1.0}Ga_{0.4}As_{0.6}$	5.765	5.20	264	71.2	86.4	22836	-1.73
$Co_2Mn_{1.0}Ga_{0.4}Sb_{0.6}$	5.898	5.21	246	67.6	83.6	20525	-0.89
$Co_2Ti_{0.2}Mn_{0.8}Ge_{1.0}$	5.756	4.39	216	66.7	88.0	18998	-1.62
$Co_2Fe_{0.8}Mo_{0.2}As_{0.2}Sb_{0.8}$	5.979	4.60	267	37.4	81.1	21680	0.60
$Co_2Fe_{0.8}Mo_{0.2}In_{0.2}Sb_{0.8}$	6.037	4.80	264	44.9	82.4	21737	-0.13
$Co_2Fe_{0.8}Mo_{0.2}Sn_{0.4}Sb_{0.6}$	6.039	4.78	265	47.0	83.2	22002	-1.27
$Co_2Fe_{0.8}Nb_{0.2}In_{0.6}Sb_{0.4}$	6.032	4.81	244	31.2	80.6	19692	-1.70
$Co_2Mn_{0.8}Fe_{0.2}Ge_{0.4}Sb_{0.6}$	5.902	5.51	230	-7.0	75.4	17302	-0.20
$Co_2Mn_{0.8}Fe_{0.2}In_{0.4}Sb_{0.6}$	6.001	5.40	270	54.4	83.5	22585	-1.40
$Co_2Mn_{0.8}Fe_{0.2}Sn_{0.6}Sb_{0.4}$	6.000	5.54	275	45.9	86.3	23748	-2.79
$Co_2Mn_{0.8}Nb_{0.2}Ge_{0.2}As_{0.8}$	5.773	4.90	226	74.9	89.0	20158	-0.63
$Co_2Mn_{0.8}Nb_{0.2}Ge_{0.4}As_{0.6}$	5.763	4.78	207	76.8	88.0	18251	-0.77
$Co_2Mn_{0.8}Zr_{0.2}P_{0.2}Ge_{0.8}$	5.760	4.50	203	37.8	83.1	16836	-1.22

P|G	3	4	5	6	7	8	9	10	11	12	13	14	15
3											Al	Si	P
4	Sc	Ti	V	Cr	Mn	Fe	Co	Ni	Cu	Zn	Ga	Ge	As
5	Y	Zr	Nb	Mo	Tc	Ru	Rh	Pd	Ag	Cd	In	Sn	Sb

Fig 4.11. The elemental distribution occupying *A* (blue), *B* and *B'* (purple), *C* and *C'* (brown) of highly spin-polarized Heusler alloys $A_2(B_xB'_{1-x})(C_yC'_{1-y})$ at finite temperature.

4.4.1. $Co_2FeAl_ySn_{1-y}$

The Fig 4.12 shows the temperature dependence of P_{spd} for $Co_2FeAl_ySn_{1-y}$, (b) *spd* electronic structure at 0 K, (c) energy dependence of P_{spd} calculated at 0 K, and (d)-(f) its counterpart for P_{sp}

and *sp* electronic structure. As shown in Fig 4.12(a)-(c), the P_{spd} value and *spd* electronic structure of Co_2FeAl over significant temperature range fail to explain the giant tunneling magnetoresistance (TMR) demonstrated especially in the Co_2FeAl/MgO based MTJ [153]. It was widely understood that giant TMR effect in Fe/MgO-based MTJ is due to the spin-filtering effect of single crystalline MgO in which Δ_1 symmetry Bloch states at in-plane k-vector $\vec{k}_{||}$=(0,0) mainly propagates for one spin channel only because of the half-metallic character of the Δ_1 band in bcc-Fe [173]. Due to the fact that s, p_z, d_{z^2} atomic orbitals are compatible to the Δ_1 symmetry, here I can roughly approximate strength of spin filtering effect as spin polarization considering *sp* electron. That explains why TMR effect could be properly described by P_{sp} behavior instead of very low value of P_{spd} [see Fig 4.12(a) and (d)] which consistent with the previous studies on Heusler alloy/MgO based MTJ [142,174]. My calculation shows that P_{sp} exhibits very low temperature dependence but still retain high value of spin polarization for Co_2FeAl which also consistent with estimated spin polarization from Julliere's model of TMR effect of Cr/Co_2FeAl/MgO/CoFe MTJ [175]. The *sp* electronic structure and energy dependence of spin polarization at 0 K shown in the Fig 4.12(e)-(f) indicated that shifting the Fermi level further enough from conduction band edge will lead to lower temperature dependence. Mixing the Al with Sn will shift the Fermi level position toward to the conduction band edge, resulting in lower spin polarization and stronger temperature dependence for high Sn-content composition. However, for $0.4 \leq y \leq 1.0$, the high spin polarization and small temperature dependence is still retained.

The idea of Al-Sn compositional tuning basically resembles the Fermi level tuning of $Co_2FeAl_xSi_{1-x}$. [176]. Moreover, Sn is in the same group with Si in the periodic table. Therefore, one may question the possible drawback of using Sn instead of Si. The comparison between two compound series are shown in the Fig 4.13, where Co_2FeSn and Co_2FeSi basically has similar temperature dependence, but with the higher spin polarization for Co_2FeSn. Replacing Sn(Si) with Al also give similar temperature dependence of spin polarization. These results imply that the performance between these two alloys series may be comparable.

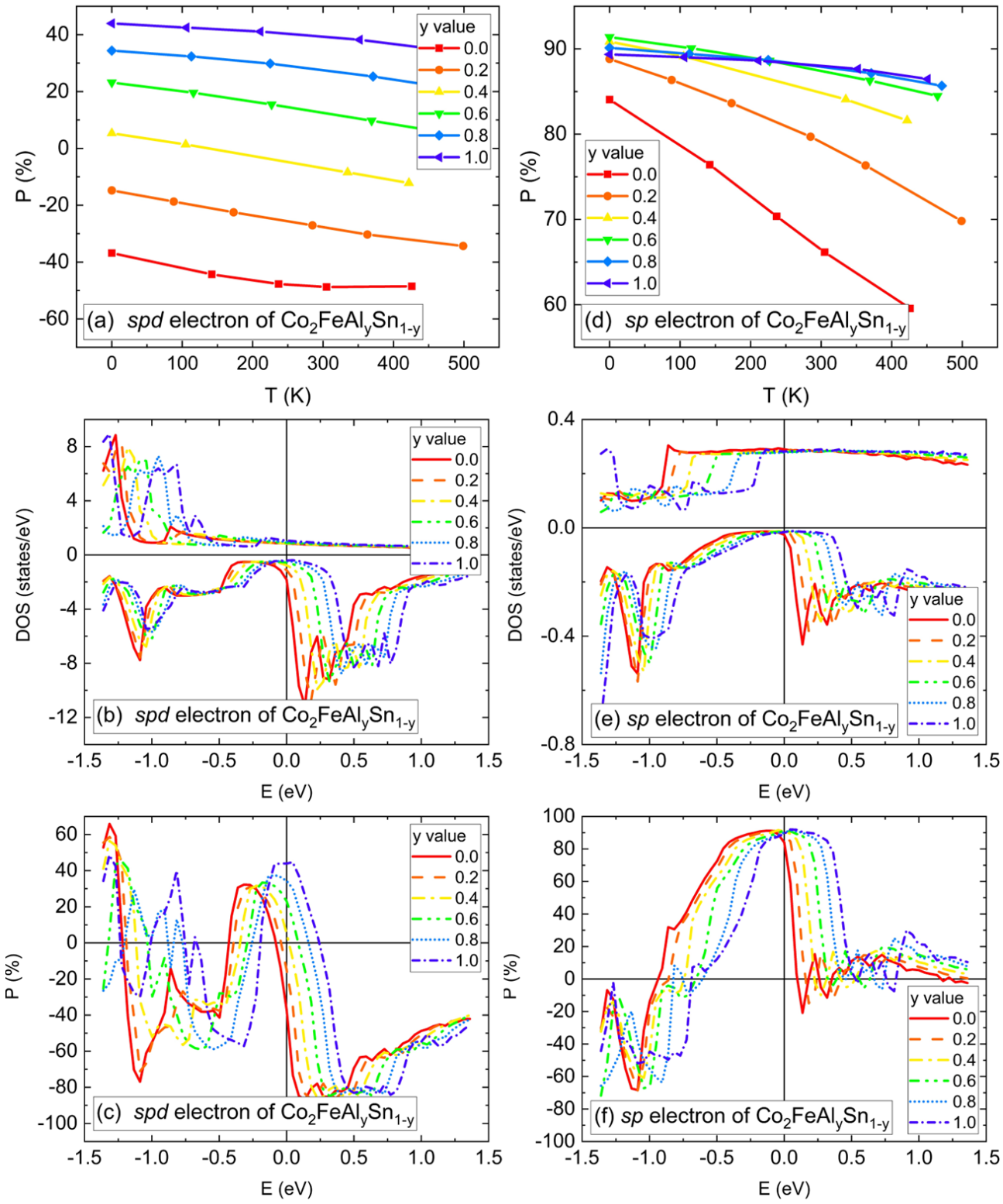

Fig 4.12. The temperature dependence of P_{spd} for $Co_2FeAl_ySn_{1-y}$, (b) *spd* electronic structure at 0 K, (c) energy dependence of P_{spd} calculated at 0 K, and (d)-(f) its counterpart for P_{sp} and *sp* electronic structure. The reference of the energy *E* is the Fermi energy.

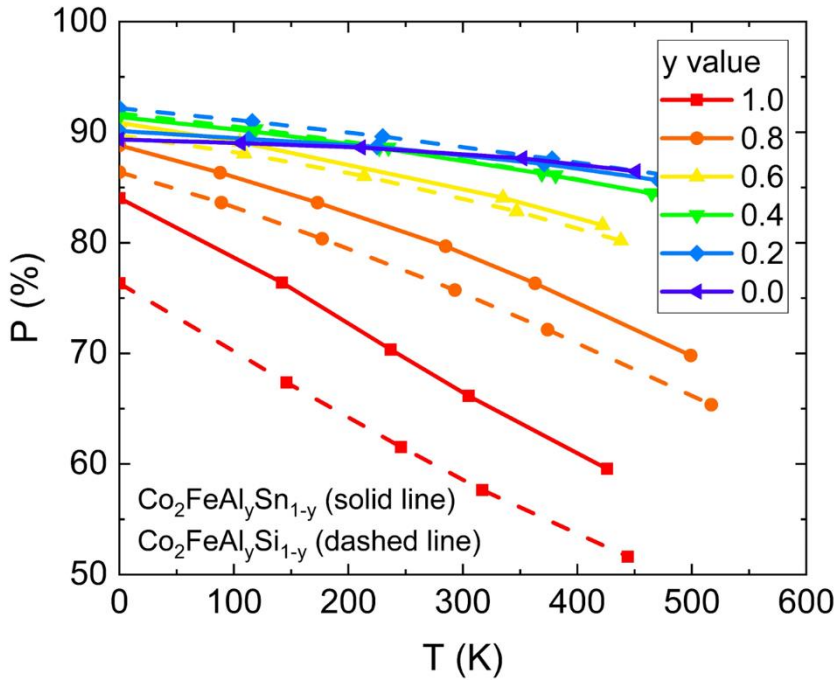

Fig 4.13. The temperature dependence of P_{sp} for $Co_2FeAl_ySn_{1-y}$ (solid line) and $Co_2FeAl_ySi_{1-y}$ (dashed line).

4.4.2. $Co_2FeGa_yIn_{1-y}$

The Fig 4.14(a) shows that *spd* spin polarization for $Co_2FeGa_yIn_{1-y}$ is rather small, with the maximal value at 0 K for Co_2FeGa is ~30% and minimal value for Co_2FeIn (~12%). The spin polarization of these series is linearly changed over the composition, with the strongest and lowest temperature dependence of *spd* spin polarization is found for Co_2FeGa, and Co_2FeIn respectively. The electronic structure at 0 K is provided in the Fig 4.14(b), which demonstrated the in-gap minority states is the origin of the low spin polarization for all compound in the series. This is consistent with the report of Özdogan *et al.* [177] using full-potential non-orthogonal local-orbital minimum-basis band structure scheme (FPLO) and found Fermi level is located in the middle of the pseudogap. In contrast to FPLO calculation, using GGA+U method and varying U value, Varaprasad *et al*. also calculated the electronic structure and found that Co_2FeGa is not fully spin-polarized due to the Fermi level crossed the valence band of minority spin states, although the half-metallic gap remains exist [92]. This type of compound is called as Type III half-metal by Balke *et al.* [164].

It is found at Fig 4.14(a) that the Co_2FeGa has stronger temperature dependence of *spd* spin polarization compared to Co_2FeIn although the 0 K electronic structure at Fig 4.14(b) show that the Fermi level of Co_2FeGa is rather in the middle of the pseudogap and relatively more distant toward the valence band compared to the Co_2FeIn. However, it may be explained better with the energy dependence of *spd* spin polarization in Fig 4.14(c) where the *spd* spin polarization in Co_2FeGa is

quickly drop if the Fermi level is slightly shifted to higher energy. Note that DLM method also take into account of Fermi level adjustment which is temperature-dependent. Therefore, the strong temperature dependence of Co_2FeGa can be addressed to the shifting of the Fermi level to higher energy at finite temperature.

Interestingly, even with very low *spd* spin polarization, the *sp* spin polarization of these series is relatively high, and by changing the composition ratio between Ga and In, almost no change of temperature dependence while the value of *sp* spin polarization is slightly reduced for Co_2FeIn as shown in the Fig 4.14(d). This can be explained due to the very similar electronic structure between Co_2FeGa and Co_2FeIn in the Fig 4.14(e). Note that replacing Ga with In, the valence band of minority spin is getting closer to the Fermi level, resulting to the slightly reduced value of spin polarization. This result indicates that the compositional series of $Co_2FeGa_yIn_{1-y}$ can be promising due to relatively low temperature dependence and high spin polarization over relatively wide range of energy as shown in the Fig 4.14(f)

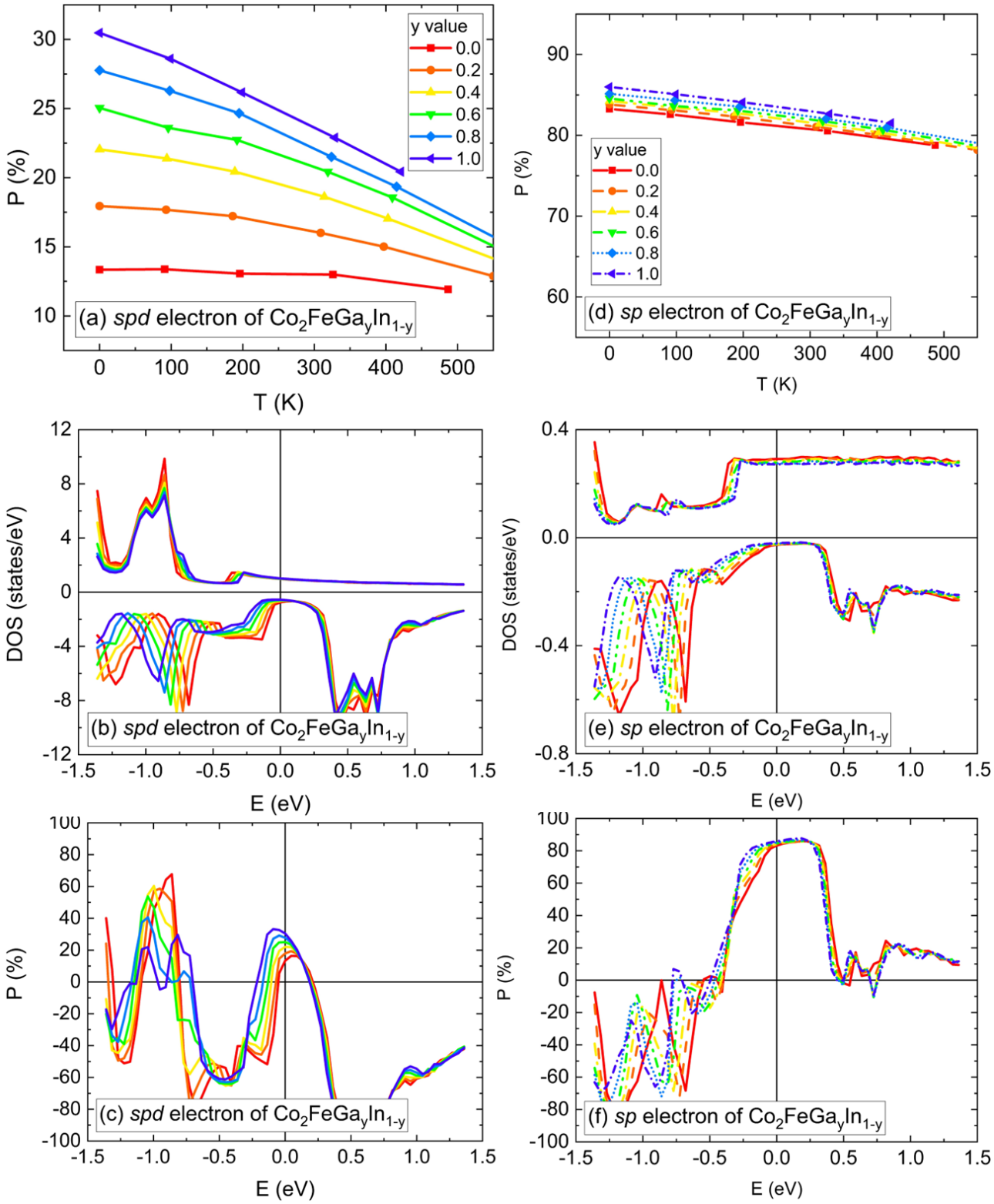

Fig 4.14. The temperature dependence of P_{spd} for $Co_2FeGa_yIn_{1-y}$, (b) *spd* electronic structure at 0 K, (c) energy dependence of P_{spd} calculated at 0 K, and (d)-(f) its counterpart for P_{sp} and *sp* electronic structure. The reference of the energy *E* is the Fermi energy.

4.4.3. $Co_2MnGa_yAs_{1-y}$

Recently, Co_2MnGa was reported to show giant anomalous Nernst effect in the $L2_1$ structure [178]. Meanwhile, theoretical calculations of Co_2MnAs suggest a very large magnetic moment of 6 μ_B [179]. However, both of these compounds and its combinatorial alloy are not widely explored in terms of spin polarization and its application in the magnetoresistance. As shown in the Fig 4.15(a), despite the pretty high value of P_{spd} of Co_2MnAs at 0 K, Ga-doping improves it further. This can be explained by considering the Fermi level tuning from Co_2MnAs (near conduction band edge) to the Co_2MnGa (near valence band edge) [see Fig 4.15(b)-(c)]. Similarly, the effect of Ga-doping is also observed in P_{sp} [see Fig 4.15(d)-(f)], which suggests $Co_2MnGa_{0.2}As_{0.8}$ and $Co_2MnGa_{0.4}As_{0.6}$ have superior spin polarization among the series. Note that despite the significant shift of Fermi level for y from 0.0 to 0.8 for $Co_2MnGa_yAs_{1-y}$, the temperature dependence of P_{sp} does not change depending on y. This is because significant increase of minority spin states happens at the conduction band rather than the valence band edge. For y = 0.0, Fermi level is already quite distant from the conduction band edge, therefore shifting further from the conduction band edge as increasing y does not affect the temperature dependence that much. This phenomenon is also observed experimentally in the $Co_2MnAl_ySi_{1-y}$ with $y < 0.4$ by Sakuraba *et al.* [180].

Since this compound consist of Ga and As, surely this compound is insensitive to the diffusion of Ga and As, especially when established the interface with GaAs compounds. This leads to other prospective applications employing the spin polarization aside from magnetoresistive devices, which is spin injection. There are several attempts to incorporate Heusler alloys Co_2MnGa for spin injection, however the performance is not yet promising [181–183]. This may be related due to low spin polarization predicted for Co_2MnGa by my calculation as shown in the Fig 4.15(a) and (d). By replacing the Ga with As significantly improve the value of spin polarization, it imply the possibility of improvement spin injection efficiency into GaAs semiconductors.

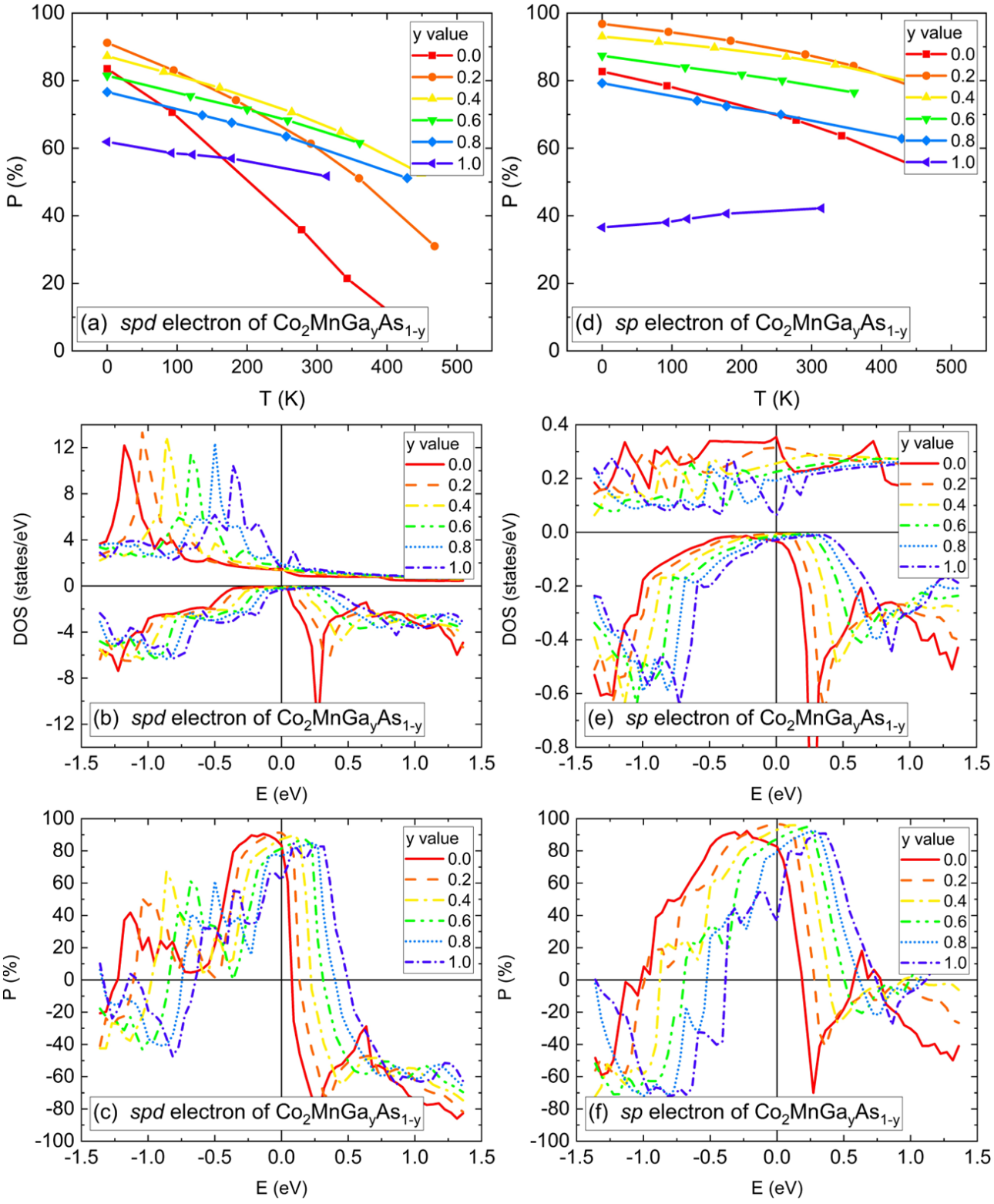

Fig 4.15. The temperature dependence of P_{spd} for $Co_2MnGa_yAs_{1-y}$, (b) *spd* electronic structure at 0 K, (c) energy dependence of P_{spd} calculated at 0 K, and (d)-(f) its counterpart for P_{sp} and *sp* electronic structure. The reference of the energy *E* is the Fermi energy.

4.5. Insight from high-throughput calculation at 0 K

In order to understand why the most prospective highly spin-polarized Heusler alloys suggested by Bayesian optimization are Co-based materials, I also evaluated the ground state properties of all candidates by high-throughput calculations. Note that despite calculations of all candidates (73440 system) were conducted, only 41612 calculations (~56%) converged and obtained the solution. In the Fig 4.16, the number of SCF iteration required to achieve the convergence at ground state calculation is presented as histogram. The distribution resembles the normal distribution, with the majority of compound converge within 40-50 calculation cycles. Smaller number of SCF iteration is expected when dealing with the composition with smaller number of atoms and corresponding size. Since our calculation search space consider the various atomic size especially for *C* elements (Al, Ga, In, Si, Ge, Sn, P, As, and Sb) and the atomic mixing that leads to the ternary, quarternary, and quinary compound, this normal distribution is well expected. In the Fig 4.17, the SCF convergence value is also plotted as histogram. The resulting plot shown like the half of normal distribution graph, where the middle point is 1×10^{-5}, which correspond to the convergence threshold / tolerance used in this calculation. Smaller number of compounds have smaller convergence threshold, and it may simply due to the simple random distribution and have no correlation with the number and type of different atoms.

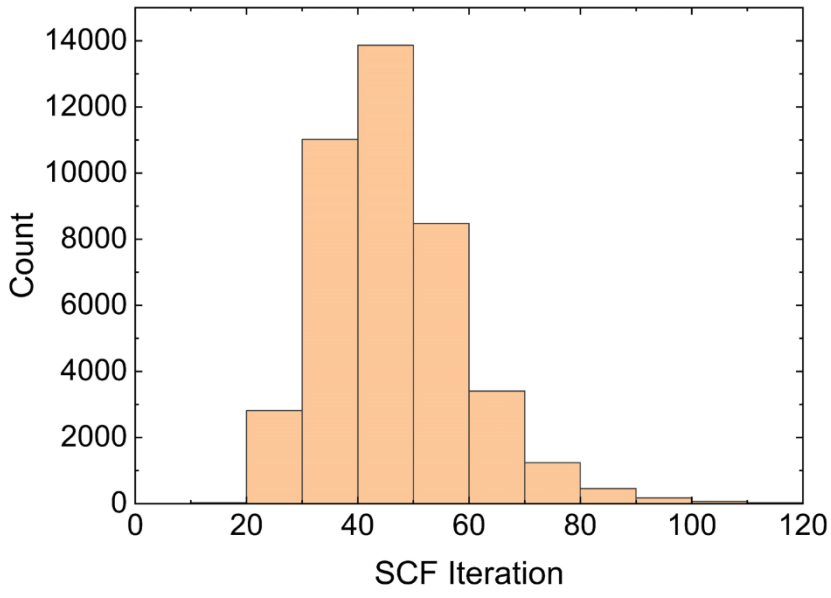

Fig 4.16. The histogram of number of SCF iteration required to obtain the convergence for ground state calculation.

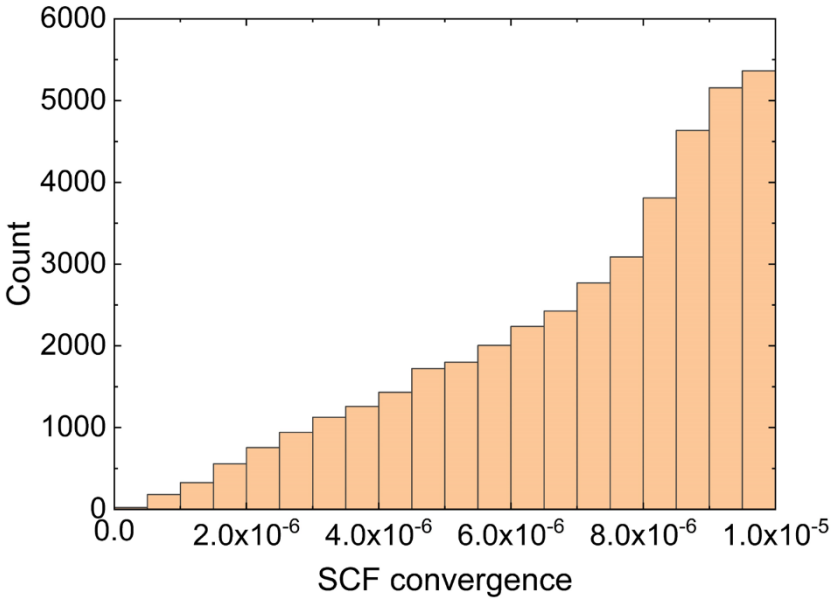

Fig 4.17. The histogram of SCF convergence value

The distribution of obtained magnetic moment at 0 K demonstrated the majority of compounds have very low magnetic moment (0-1 μ_B) as shown in the Fig 4.18. However, if all compounds are assumed as half-metal and follow the Slater-Pauling rule from valence electron, the normal distribution will be expected with the majority compound having magnetic moment 3 μ_B. This imply that the underestimated magnetic moment which obtained in this study will be somewhat related to the low spin-polarization. This is proven by looking on the Fig 4.19, since the distribution of *spd* spin polarization is mostly occupy the low spin polarization region. Moreover, the compound with the negative spin polarization almost equal to the compound with the positive spin polarization. From this result, it is understandable that most of compound having very low magnetic moment compared to the prediction by Slater-Pauling rule, because the rule only followed with half-metal compound, where only 2506 compound found having *spd* spin polarization 90 – 100%.

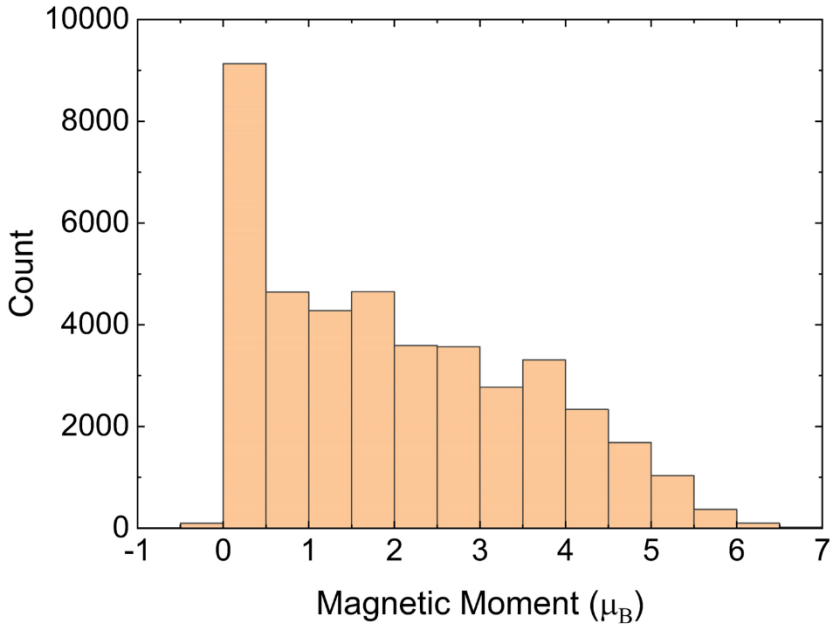

Fig 4.18. The histogram of magnetic moment

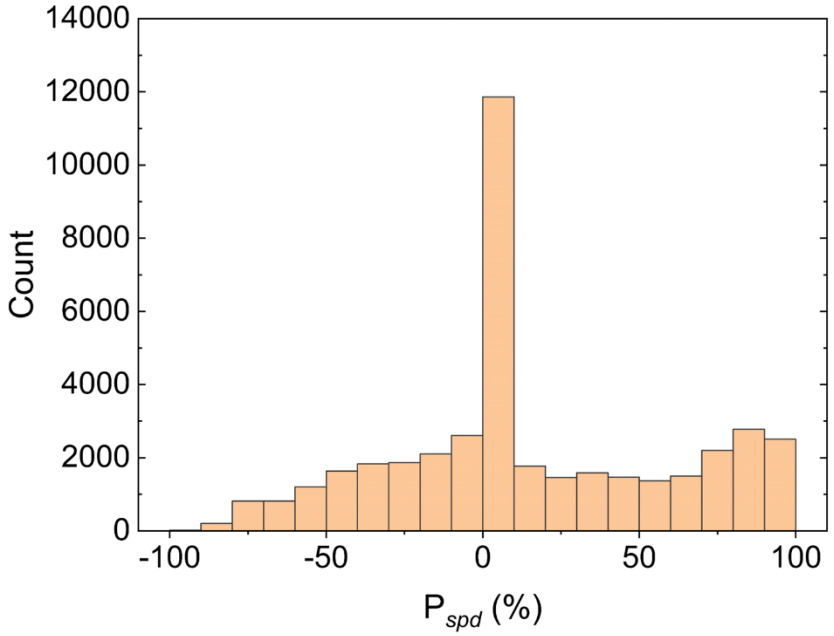

Fig 4.19. The histogram of *spd* spin polarization

In case of the *sp* spin polarization, the histogram in the Fig 4.20 show similar distribution like *spd* spin polarization, especially on the majority compound having very low spin polarization (0 – 10%). Quick glance on these data will give intuitive correlation between *sp* and *spd* spin polarization, which later proven as incorrect because the *sp* and *spd* spin polarization is quite randomly distributed each other. Another feature observed that support the random distribution is the compound having negative spin polarization for *sp* electrons (-50 – -100%) are not as many as for *spd* electrons.

Lastly, the distribution of formation energy is plotted in the Fig 4.21, showing the normal distribution, with the majority of compound having the negative formation energy (-2 – -1 eV/atom). Based on the discussion in the Chapter 3, it is found that the smaller atom leads to the stronger binding, hence minimizing the total energy, and lead to the negative formation energy. On the other hand, the significant number of compounds (> 2000) having relatively small positive formation energy (< 0.5 eV/atom). In the experiments, it is still possible to fabricate these compounds even in the metastable form.

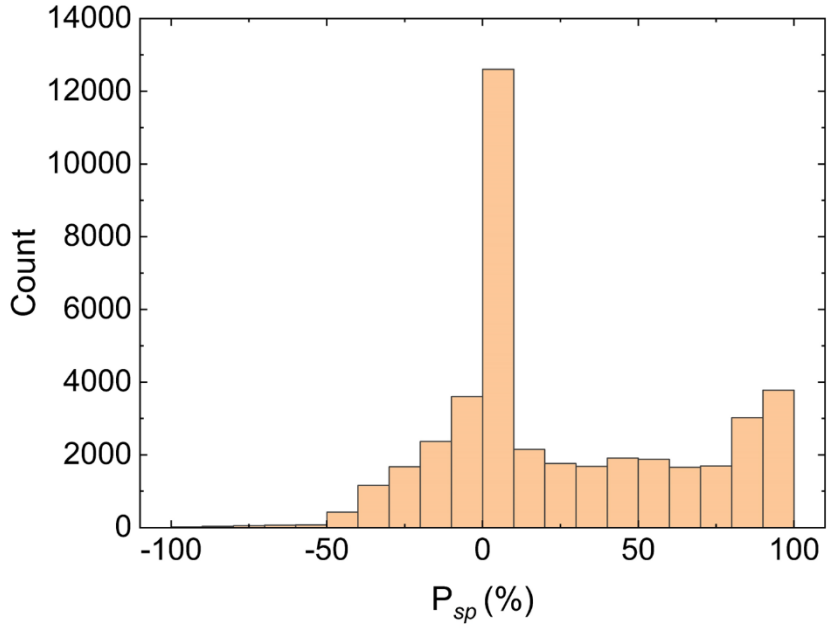

Fig 4.20. The histogram of *sp* spin polarization

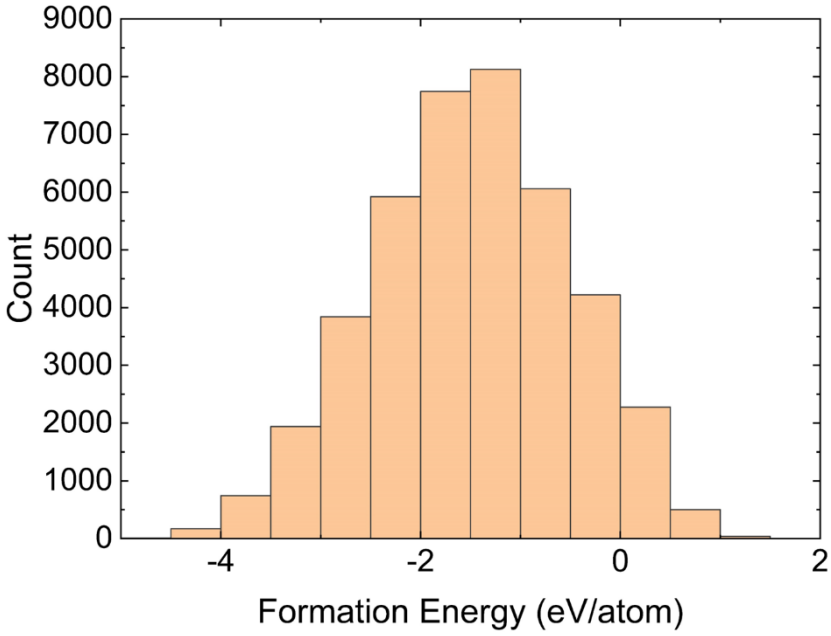

Fig 4.21. The histogram of formation energy

In Fig 4.22(a)-(c), I show the distributions of converged calculation results for ground state P_{spd} and P_{sp} values mapped on two-dimensional plane over A elements, the number of elements and spin moments at 0 K, respectively. Conventional approach of finding highly spin-polarized material were done by "vertically scanning" over the candidates in the high P_{spd} area (specified by sky blue rectangles). However, as mentioned previously that P_{sp} is more suitable to explain the magnetoresistance effect, here I propose to "horizontally scanning" over the high P_{sp} area (specified by red rectangles). Based on the Fig 4.22(a), it is clear that high P_{sp} area is filled by Co-based Heusler alloy. These candidates are mainly consist of quaternary and quinary compound as a consequence of the increase of the number of combinations with increasing the number of elements [see Fig 4.22(b)]. It turned out that the significant portions of these candidates also exhibit the large spin moment (4-6 μ_B) at 0 K [see Fig 4.22(c)] which may imply high Curie temperature and therefore the robustness of spin polarization of Co-based Heusler alloy at finite temperature [184].

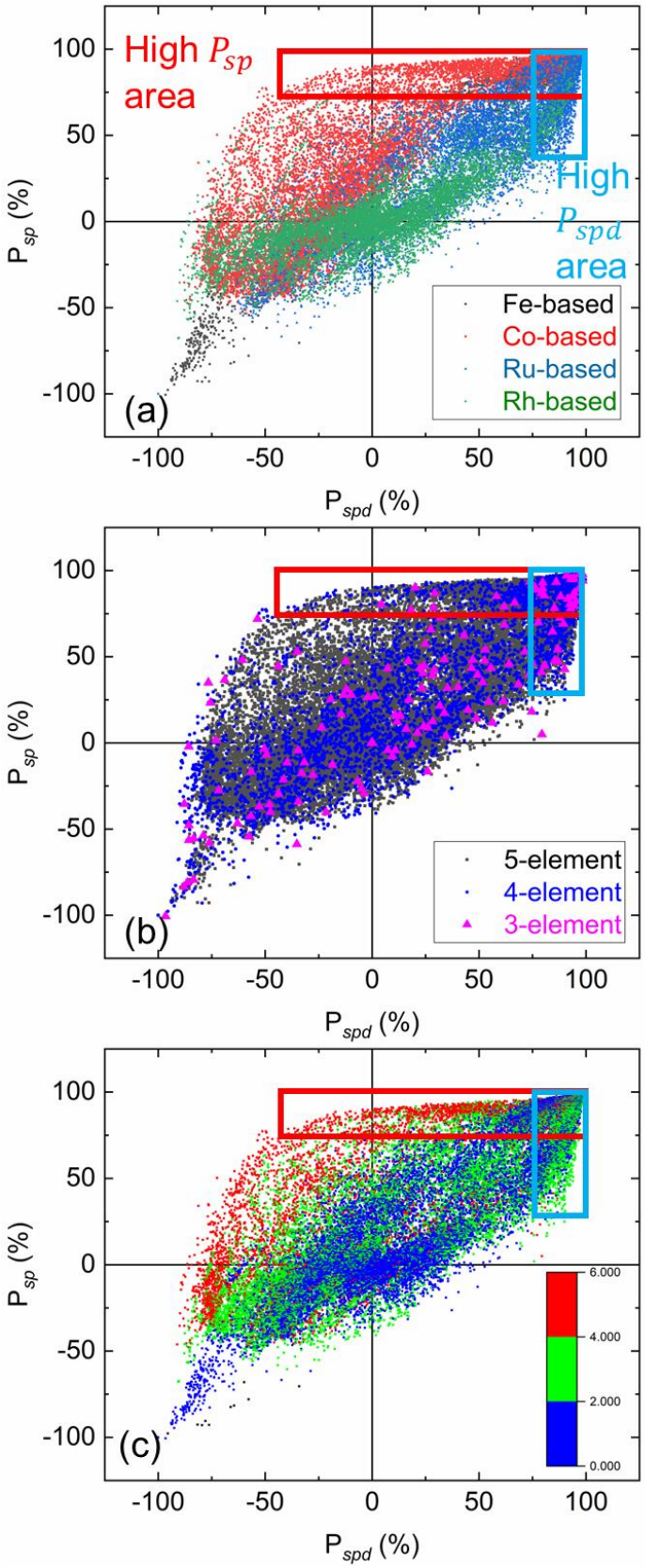

Fig 4.22. The results of high-throughput calculation for ground state *sp* and *spd* spin polarization as (a) distribution over *A* element, (b) distribution over number of elements, and (c) distribution over 0 K moment.

4.6. Summary

In this Chapter, the Bayesian optimization combined with the finite temperature first-principles calculation is successfully performed to find the highly spin-polarized Heusler alloys around room temperature. I found several new compounds such as $Co_2MnGa_{0.2}As_{0.8}$ and $Co_2FeAl_ySn_{1-y}$ ($0.4 \leq y \leq 1.0$) that show high *sp* spin-polarization at around 300 K. The investigation of spin polarization behavior on Co_2FeAl reemphasized the importance of P_{sp} instead of P_{spd} value to explain the magnetoresistance effect, and the alloy mixing to find the more prospective candidate with 4- or 5-element based compound. However, most candidate are Co_2Mn- and Co_2Fe- based Heusler alloys, which is supported by the results from high-throughput screening considering large magnetic moment and high Curie temperature. I also investigated three combinatorial series $Co_2MnGa_yAs_{1-y}$, $Co_2FeAl_ySn_{1-y}$, $Co_2FeGa_yIn_{1-y}$ to understand the effect of alloy mixing on the temperature dependence and importance of distancing Fermi level position from conduction band edge via alloy mixing to further improve the temperature dependence of spin polarization.

Chapter 5: Temperature dependence of damping constant

5.1. Introduction

As mentioned in Chapter 1, damping constant plays important role in the magnetization switching of HAMR process [112]. In the HAMR, $L1_0$-FePt is prospective material for recording media because of its large magneto-crystalline anisotropy and damping [33]. The switching time is inversely proportional to the damping constant [109]. Since the switching process is done at high temperature, the ground state calculation of the damping constant is not enough. Unfortunately, the finite temperature damping behavior of FePt is not fully understood yet. Since experimental measurements of damping mostly includes the extrinsic effects rather than the intrinsic effect, different results were reported by several experimental groups [83–86]. Recently, Richardson *et al.* measured the ferromagnetic resonance (FMR) linewidth of $L1_0$-FePt near Curie temperature which is proportional to the damping constant, and found that the linewidth is strongly reduced near the Curie temperature, implying the possibility of damping reduction [110]. This unexpected decrease of damping will be harmful for the reduction of the switching time in HAMR [112].

In theoretical calculations of intrinsic damping constant of FePt [113,185], the effect of the spin fluctuation at finite temperature was studied using torque correlation model proposed by Kambersky [72]. Hiramatsu *et al*. found that the temperature dependence of damping constant due to the spin fluctuation only is nonmonotonic, and the damping is rapidly increases with increasing temperature near the Curie temperature [113]. On the other hand, effects of the atomic vibration on the damping constant at finite temperature have not been fully understood yet. Therefore, in this Chapter I will investigate the lattice dynamics effect on the temperature dependence of $L1_0$-FePt damping constant and its implication for HAMR applications.

5.2. Calculation Details

In this study, the damping is calculated using Kambersky Torque correlation model [72], and the lattice vibration effect is introduced by creating the “snapshot” of structure with the displaced atoms via phonon dispersion information, which somewhat similar with the frozen thermal lattice disorder approach introduced by Liu *et al.* [123]

5.2.1. Formulation of matrix elements of the spin conserving and spin flip

The damping constant in the Kambersky torque correlation model [72,186] is expressed as

$$\alpha = \frac{g}{\pi M_s}\sum_k W_k \sum_{nn'}\left|\Gamma^-_{nn'}(k)\right|^2 \frac{\delta}{(E_F-\varepsilon_{nk})^2+\delta^2}\frac{\delta}{(E_F-\varepsilon_{n'k})^2+\delta^2}, \quad (5\text{-}1)$$

where the $\Gamma^-_{nn'}(k) = \langle n,k|[S^-, H_{\mathrm{SO}}]|n',k\rangle$ is matrix element for wavevector k between bands n and n' induced by the spin-orbit torque operator $\eta_0^- = [S^-, H_{\mathrm{SO}}] = \sum_I \xi_I(S^-L^z - S^zL^-)$. These matrix elements are numerically integrated over all wavevector k with the weight of W_k and band states together with electron spectral functions, which are Lorentzian centered at the band energy ε_{nk} and broadened by the electron-lattice scattering rate δ. Note that the band states $|n,k\rangle$, Fermi energy E_F and ε_{nk} are easily obtained from the output of the *ab-initio* calculations. Thus, remaining task is determining the matrix elements from spin-orbit torque operator, by separating the contribution of spin conserving $\langle n,k|S^zL^-|n',k\rangle$ and spin flip $\langle n,k|S^-L^z|n',k\rangle$. In order to do that, I will simplify the expression of spin conserving and spin flip into $\langle \mathrm{bra}|L^-|\mathrm{ket}\rangle$, and $\langle \mathrm{bra}|L^z|\mathrm{ket}\rangle$, respectively. Note that bra and ket states already containing the information of allowed spin combination for each spin conserving part ($\langle \mathrm{bra}(\uparrow)|L^-|\mathrm{ket}(\uparrow)\rangle$ and $\langle \mathrm{bra}(\downarrow)|L^-|\mathrm{ket}(\downarrow)\rangle$) and spin flip part ($\langle \mathrm{bra}(\downarrow)|L^-|\mathrm{ket}(\uparrow)\rangle$). Thus, bra and ket can be easily represented as spherical harmonics of each atomic orbital as shown in the Table 3.1.

Table 5.1. The spherical harmonics.

orbital	Spherical harmonics
s	Y_0^0
p_y	$\frac{i}{\sqrt{2}}(Y_1^{-1}+Y_1^1)$
p_z	Y_1^0
p_x	$\frac{1}{\sqrt{2}}(Y_1^{-1}-Y_1^1)$
d_{xy}	$\frac{i}{\sqrt{2}}(Y_2^{-2}-Y_2^2)$
d_{yz}	$\frac{i}{\sqrt{2}}(Y_2^{-1}+Y_2^1)$
d_{z^2}	Y_2^0
d_{xz}	$\frac{1}{\sqrt{2}}(Y_2^{-1}-Y_2^1)$
$d_{x^2-y^2}$	$\frac{1}{\sqrt{2}}(Y_2^{-2}+Y_2^2)$

For 9×9 orbital combination of spin conserving $\langle \text{bra}|L^-|\text{ket}\rangle$, 16 nonzero elements are given as:

$$\langle p_y|L^-|p_z\rangle = \langle -\tfrac{i}{\sqrt{2}}(Y_1^{-1}+Y_1^1)|L^-|Y_1^0\rangle = -\tfrac{i}{\sqrt{2}}\langle Y_1^{-1}|L^-|Y_1^0\rangle = -\tfrac{i}{\sqrt{2}}\sqrt{1(1+1)-0(-1)} = -i \quad (5\text{-}2)$$

$$\langle p_z|L^-|p_y\rangle = \langle Y_1^0|L^-|\tfrac{i}{\sqrt{2}}(Y_1^{-1}+Y_1^1)\rangle = \tfrac{i}{\sqrt{2}}\langle Y_1^0|L^-|Y_1^1\rangle = \tfrac{i}{\sqrt{2}}\sqrt{1(1+1)-1(0)} = i \quad (5\text{-}3)$$

$$\langle p_x|L^-|p_z\rangle = \langle \tfrac{1}{\sqrt{2}}(Y_1^{-1}-Y_1^1)|L^-|Y_1^0\rangle = \tfrac{1}{\sqrt{2}}\langle Y_1^{-1}|L^-|Y_1^0\rangle = \tfrac{1}{\sqrt{2}}\sqrt{1(1+1)-0(-1)} = 1 \quad (5\text{-}4)$$

$$\langle p_z|L^-|p_x\rangle = \langle Y_1^0|L^-|\tfrac{1}{\sqrt{2}}(Y_1^{-1}-Y_1^1)\rangle = -\tfrac{1}{\sqrt{2}}\langle Y_1^0|L^-|Y_1^1\rangle = -\tfrac{1}{\sqrt{2}}\sqrt{1(1+1)-1(0)} = -1 \quad (5\text{-}5)$$

$$\langle d_{xy}|L^-|d_{yz}\rangle = \langle -\tfrac{i}{\sqrt{2}}(Y_2^{-2}-Y_2^2)|L^-|\tfrac{i}{\sqrt{2}}(Y_2^{-1}+Y_2^1)\rangle = \tfrac{1}{2}\langle Y_2^{-2}|L^-|Y_2^{-1}\rangle =$$

$$\tfrac{1}{2}\sqrt{2(2+1)-(-1)(-2)} = 1 \quad (5\text{-}6)$$

$$\langle d_{xy}|L^-|d_{xz}\rangle = \langle -\tfrac{i}{\sqrt{2}}(Y_2^{-2}-Y_2^2)|L^-|\tfrac{1}{\sqrt{2}}(Y_2^{-1}-Y_2^1)\rangle = -\tfrac{i}{2}\langle Y_2^{-2}|L^-|Y_2^{-1}\rangle =$$

$$-\tfrac{i}{2}\sqrt{2(2+1)-(-1)(-2)} = -i \quad (5\text{-}7)$$

$$\langle d_{yz}|L^-|d_{xy}\rangle = \langle -\frac{i}{\sqrt{2}}(Y_2^{-1}+Y_2^1)|L^-|\frac{i}{\sqrt{2}}(Y_2^{-2}-Y_2^2)\rangle = -\frac{1}{2}\langle Y_2^1|L^-|Y_2^2\rangle =$$
$$-\frac{1}{2}\sqrt{2(2+1)-(2)(1)} = -1 \quad (5\text{-}8)$$

$$\langle d_{yz}|L^-|d_{z^2}\rangle = \langle -\frac{i}{\sqrt{2}}(Y_2^{-1}+Y_2^1)|L^-|Y_2^0\rangle = -\frac{i}{\sqrt{2}}\langle Y_2^{-1}|L^-|Y_2^0\rangle = -\frac{i}{\sqrt{2}}\sqrt{2(2+1)-(0)(-1)} =$$
$$-i\sqrt{3} \quad (5\text{-}9)$$

$$\langle d_{yz}|L^-|d_{x^2-y^2}\rangle = \langle -\frac{i}{\sqrt{2}}(Y_2^{-1}+Y_2^1)|L^-|\frac{1}{\sqrt{2}}(Y_2^{-2}+Y_2^2)\rangle = -\frac{i}{2}\langle Y_2^1|L^-|Y_2^2\rangle =$$
$$-\frac{i}{2}\sqrt{2(2+1)-(2)(1)} = -i \quad (5\text{-}10)$$

$$\langle d_{z^2}|L^-|d_{yz}\rangle = \left\langle Y_2^0\middle|L^-\middle|\frac{i}{\sqrt{2}}(Y_2^{-1}+Y_2^1)\right\rangle = \frac{i}{\sqrt{2}}\langle Y_2^0|L^-|Y_2^1\rangle = \frac{i}{\sqrt{2}}\sqrt{2(2+1)-(1)(0)} = i\sqrt{3} \quad (5\text{-}11)$$

$$\langle d_{z^2}|L^-|d_{xz}\rangle = \left\langle Y_2^0\middle|L^-\middle|\frac{1}{\sqrt{2}}(Y_2^{-1}-Y_2^1)\right\rangle = -\frac{1}{\sqrt{2}}\langle Y_2^0|L^-|Y_2^1\rangle = -\frac{1}{\sqrt{2}}\sqrt{2(2+1)-(1)(0)} = -\sqrt{3}$$
(5-12)

$$\langle d_{xz}|L^-|d_{xy}\rangle = \langle \frac{1}{\sqrt{2}}(Y_2^{-1}-Y_2^1)|L^-|\frac{i}{\sqrt{2}}(Y_2^{-2}-Y_2^2)\rangle = \frac{i}{2}\langle Y_2^1|L^-|Y_2^2\rangle = \frac{i}{2}\sqrt{2(2+1)-(2)(1)} = i$$
(5-13)

$$\langle d_{xz}|L^-|d_{z^2}\rangle = \langle \frac{1}{\sqrt{2}}(Y_2^{-1}-Y_2^1)|L^-|Y_2^0\rangle = \frac{1}{2}\langle Y_2^{-1}|L^-|Y_2^0\rangle = \frac{1}{2}\sqrt{2(2+1)-(0)(-1)} = \sqrt{3} \quad (5\text{-}14)$$

$$\langle d_{xz}|L^-|d_{x^2-y^2}\rangle = \langle \frac{1}{\sqrt{2}}(Y_2^{-1}-Y_2^1)|L^-|\frac{1}{\sqrt{2}}(Y_2^{-2}+Y_2^2)\rangle = -\frac{1}{2}\langle Y_2^1|L^-|Y_2^2\rangle =$$
$$-\frac{1}{2}\sqrt{2(2+1)-(2)(1)} = -1 \quad (5\text{-}15)$$

$$\langle d_{x^2-y^2}|L^-|d_{yz}\rangle = \langle \frac{1}{\sqrt{2}}(Y_2^{-2}+Y_2^2)|L^z|\frac{i}{\sqrt{2}}(Y_2^{-1}+Y_2^1)\rangle = \frac{i}{2}\langle Y_2^{-2}|L^-|Y_2^{-1}\rangle =$$
$$\frac{i}{2}\sqrt{2(2+1)-(-1)(-2)} = i \quad (5\text{-}16)$$

$$\langle d_{x^2-y^2}|L^-|d_{xz}\rangle = \langle \frac{1}{\sqrt{2}}(Y_2^{-2}+Y_2^2)|L^z|\frac{1}{\sqrt{2}}(Y_2^{-1}-Y_2^1)\rangle = \frac{1}{2}\langle Y_2^{-2}|L^-|Y_2^{-1}\rangle =$$
$$\frac{1}{2}\sqrt{2(2+1)-(-1)(-2)} = 1 \quad (5\text{-}17)$$

While for 9 × 9 orbital combination of spin flip ⟨bra|L^z|ket⟩, 6 nonzero elements are given as:

$$\langle p_x|L^z|p_y\rangle = \langle \frac{1}{\sqrt{2}}(Y_1^{-1}-Y_1^1)|L^z|\frac{i}{\sqrt{2}}(Y_1^{-1}+Y_1^1)\rangle = \frac{i}{2}(\langle Y_1^{-1}|L^z|Y_1^{-1}\rangle - \langle Y_1^1|L^z|Y_1^1\rangle) = \frac{i}{2}(-1-1) =$$
$$-i \quad (5\text{-}18)$$

$$\langle p_y|L^z|p_x\rangle = \langle -\frac{i}{\sqrt{2}}(Y_1^{-1}+Y_1^1)|L^z|\frac{1}{\sqrt{2}}(Y_1^{-1}-Y_1^1)\rangle = -\frac{i}{2}(\langle Y_1^{-1}|L^z|Y_1^{-1}\rangle - \langle Y_1^1|L^z|Y_1^1\rangle) =$$
$$-\frac{i}{2}(-1-1) = i \quad (5\text{-}19)$$

$$\langle d_{xy}|L^z|d_{x^2-y^2}\rangle = \langle -\frac{i}{\sqrt{2}}(Y_2^{-2}-Y_2^2)|L^z|\frac{1}{\sqrt{2}}(Y_2^{-2}+Y_2^2)\rangle = -\frac{i}{2}(\langle Y_2^{-2}|L^z|Y_2^{-2}\rangle - \langle Y_2^2|L^z|Y_2^2\rangle) =$$
$$-\frac{i}{2}(-2-2) = 2i \quad (5\text{-}20)$$

$$\langle d_{yz}|L^z|d_{xz}\rangle = \langle -\frac{i}{\sqrt{2}}(Y_2^{-1}+Y_2^1)|L^z|\frac{1}{\sqrt{2}}(Y_2^{-1}-Y_2^1)\rangle = -\frac{i}{2}(\langle Y_2^{-1}|L^z|Y_2^{-1}\rangle - \langle Y_2^1|L^z|Y_2^1\rangle) =$$

$$-\frac{i}{2}(-1-1) = i \tag{5-21}$$

$$\langle d_{xz}|L^z|d_{yz}\rangle = \langle \frac{1}{\sqrt{2}}(Y_2^{-1}-Y_2^1)|L^z|\frac{i}{\sqrt{2}}(Y_2^{-1}+Y_2^1)\rangle = \frac{i}{2}(\langle Y_2^{-1}|L^z|Y_2^{-1}\rangle - \langle Y_2^1|L^z|Y_2^1\rangle) = \frac{i}{2}(-1-$$

$$1) = -i \tag{5-22}$$

$$\langle d_{x^2-y^2}|L^z|d_{xy}\rangle = \langle \frac{1}{\sqrt{2}}(Y_2^{-2}+Y_2^2)|L^z|\frac{i}{\sqrt{2}}(Y_2^{-2}-Y_2^2)\rangle = \frac{i}{2}(\langle Y_2^{-2}|L^z|Y_2^{-2}\rangle - \langle Y_2^2|L^z|Y_2^2\rangle) = \frac{i}{2}(-2-$$

$$2) = -2i \tag{5-23}$$

Therefore, the matrix operation of orbital combination for spin conserving $\langle \text{bra}|L^-|\text{ket}\rangle$ and spin flip $\langle \text{bra}|L^z|\text{ket}\rangle$ contribution can be expressed as shown in the Table 5.2 and Table 5.3, respectively.

Table 5.2. The results of operation $\langle \text{bra}|L^z|\text{ket}\rangle$

Bra / Ket	s	p_y	p_z	p_x	d_{xy}	d_{yz}	d_{z^2}	d_{xz}	$d_{x^2-y^2}$
s	0	0	0	0	0	0	0	0	0
p_y	0	0	0	i	0	0	0	0	0
p_z	0	0	0	0	0	0	0	0	0
p_x	0	$-i$	0	0	0	0	0	0	0
d_{xy}	0	0	0	0	0	0	0	0	$2i$
d_{yz}	0	0	0	0	0	0	0	i	0
d_{z^2}	0	0	0	0	0	0	0	0	0
d_{xz}	0	0	0	0	0	$-i$	0	0	0
$d_{x^2-y^2}$	0	0	0	0	$-2i$	0	0	0	0

Table 5.3. The results of operation $\langle \text{bra}|L^{-}|\text{ket}\rangle$

Bra \ Ket	s	p_y	p_z	p_x	d_{xy}	d_{yz}	d_{z^2}	d_{xz}	$d_{x^2-y^2}$
s	0	0	0	0	0	0	0	0	0
p_y	0	0	$-i$	0	0	0	0	0	0
p_z	0	i	0	-1	0	0	0	0	0
p_x	0	0	1	0	0	0	0	0	0
d_{xy}	0	0	0	0	0	1	0	$-i$	0
d_{yz}	0	0	0	0	-1	0	$-i\sqrt{3}$	0	$-i$
d_{z^2}	0	0	0	0	0	$i\sqrt{3}$	0	$-\sqrt{3}$	0
d_{xz}	0	0	0	0	i	0	$\sqrt{3}$	0	-1
$d_{x^2-y^2}$	0	0	0	0	0	i	0	1	0

5.2.2. Ab-initio calculation

I performed first-principles density-functional calculations using the Vienna *ab initio* simulation package (VASP) [187] to obtain electronic structures and phonon dispersions of $L1_0$-FePt together with the projection onto local atomic orbitals. The projector augmented-wave (PAW) potential was used to describe the behavior of core electrons [122]. Generalized gradient approximation (GGA) proposed by Perdew, Burke, and Ernzerhof was adopted for the exchange and correlation energies [188]. The 2 × 2 × 2 supercell containing 8 Fe and 8 Pt atoms was constructed using the tetragonal unit cell with a = 5.4563 Å and c = 7.5579 Å for phonon and damping calculations. I used the plane-wave cut-off energy of 335 eV for the wavefunction expansion and 10 × 10 × 10 k-points mesh for wave-vector integration in the first Brillouin zone. Note that the rather sparse k-points mesh was used, since the purpose of this study is to offer an insight into the temperature dependence of damping due to the atomic vibrations. I confirm that the qualitative feature of the temperature dependence of the damping constant has been converged by the present k-point density.

5.2.3. Creating the snapshots

Although I neglected the spin-phonon coupling in the correlation function of the spin torque, I incorporate the atomic vibration effect via phonon dispersion as "modified frozen thermal lattice disorder" [123], where the atomic displacement is explicitly determined from the phonon dispersion information. First, I confirmed that there is no negative phonon mode for FePt structure calculated by PHONOPY [189], which implies the ground state is dynamically stable. The atomic displacements $u_{\kappa\ell}^{\alpha}$ in the supercell can be obtained from the normal mode coordinates ($Q_{q\nu}$) in the reciprocal space as

$$u_{\kappa\ell}^{\alpha} = \frac{1}{\sqrt{M_{\kappa}N}} \sum_{q\nu} Q_{q\nu} e_{\alpha}(\kappa; q\nu) \mathrm{e}^{\mathrm{i}q\cdot r(\ell)} \tag{5-24}$$

where α is the Cartesian coordinate index, $M_{\kappa}$is the mass of the κ-th atom in the unit cell, ℓ is the unit cell index in the supercell, and N is the number of q points commensurate with the supercell. The polarization vector $e_{\alpha}(\kappa; q\nu)$ gives the direction in which each atom moves with the wavevector q and the mode index ν. To generate structural snapshots relevant at each temperature, I randomly sample $Q_{q\nu}$ from the Gaussian (normal) distribution with the deviation $\sigma_{q\nu}$, which is given as [190]:

$$\sigma_{q\nu}^2 = \langle Q_{q\nu} Q_{q\nu}^{*} \rangle = \frac{\hbar}{2\omega_{q\nu}} \left(2n_{q\nu} + 1\right) \tag{5-25}$$

where $\omega_{q\nu}$is the harmonic phonon frequency, and $n_{q\nu}(\omega, T) = (\mathrm{e}^{\hbar\omega/k_{\mathrm{B}}T} - 1)^{-1}$ being the Bose-Einstein occupation function.

Therefore, I calculate the damping value of each "snapshot" using the Kambersky model [72] and do averaging to obtain the damping value over hundreds of "snapshots" at each temperature. I confirmed that the averaging over 100 "snapshots" is enough to obtain the converged magnetic damping at finite temperatures up to 900 K.

5.2.4. Estimation of scattering rate

The scattering rate δ in Eq. (5-1) was estimated from the imaginary part of the Fan-Migdal (FM) self-energy defined as [191]

$$\Gamma_{nk} = \mathrm{Im}\Sigma_{nk}^{\mathrm{FM}}(\epsilon_{nk}) = \frac{\pi}{N_q} \sum_{mq\nu} |g_{nm\nu}(k,q)|^2 \times \left[\left(1 - f_{mk+q} + n_{q\nu}\right)\delta\left(\varepsilon_{nk} - \hbar\omega_{q\nu} - \varepsilon_{mk+q}\right) + \left(f_{mk+q} + n_{q\nu}\right)\delta\left(\varepsilon_{nk} + \hbar\omega_{q\nu} - \varepsilon_{mk+q}\right)\right], \tag{5-26}$$

where $g_{nm\nu}(k,q)$ is the electron-phonon coupling constant and $f_{nk} = \left(e^{(\varepsilon_{nk}-\mu)/k_{\mathrm{B}}T} + 1\right)^{-1}$is the Fermi-Dirac distribution function. The dense 100 × 100 × 100 k- and q-point grids are used for the

summation of imaginary part of the FM self-energy. To that end, the electron-phonon coupling constants were first computed based on density functional perturbation theory (DFPT) for the $2 \times 2 \times 2$ q points along with the $12 \times 12 \times 12$ k points and subsequently interpolated to the dense grids using the Wannier interpolation. The DFT and DFPT calculations were performed under a collinear magnetic state using the Quantum ESPRESSO package [192], where the GBRV ultrasoft pseudopotentials [193] were used with the kinetic energy cutoffs of 90 Ry and 1080 Ry, respectively, for the wavefunction and charge density. The maximally localized Wannier functions were constructed using the Wannier90 code [194], where the outer energy window of [-10:8] eV relative to the Fermi level was used. The calculation of Γ_{nk} was performed using the Perturbo code [195].

5.3. Damping at Ground States

5.3.1. Damping dependence of k-point

In the Fig 4.1, the scattering rate dependence of damping is shown for varied number of k-points in the one dimension of Fe, Co, and Ni. The torque correlation model predicts the decrease behavior for intraband damping, while the interband contribution is enhanced by increasing scattering rate. These two competing behaviors resulting in nonmonotonic trend of the total damping. In my calculation, these patterns were observed in the sufficiently large number of one-dimension k-points (>40). Since Lorentzian part of damping equation depends on the eigenenergies of each band at each k-points, too low k-points may not reproduce the sharpness of spectral functions which yields the significant deviation from prediction. This is also observed for Fe by Qu *et al.* [196] when one-dimension k-point is less than 64 for Fe. On the other hand, Gilmore *et al.* used 160, 100, and 120 k-points in one-dimension for convergence in Fe, Co, Ni, respectively [186].

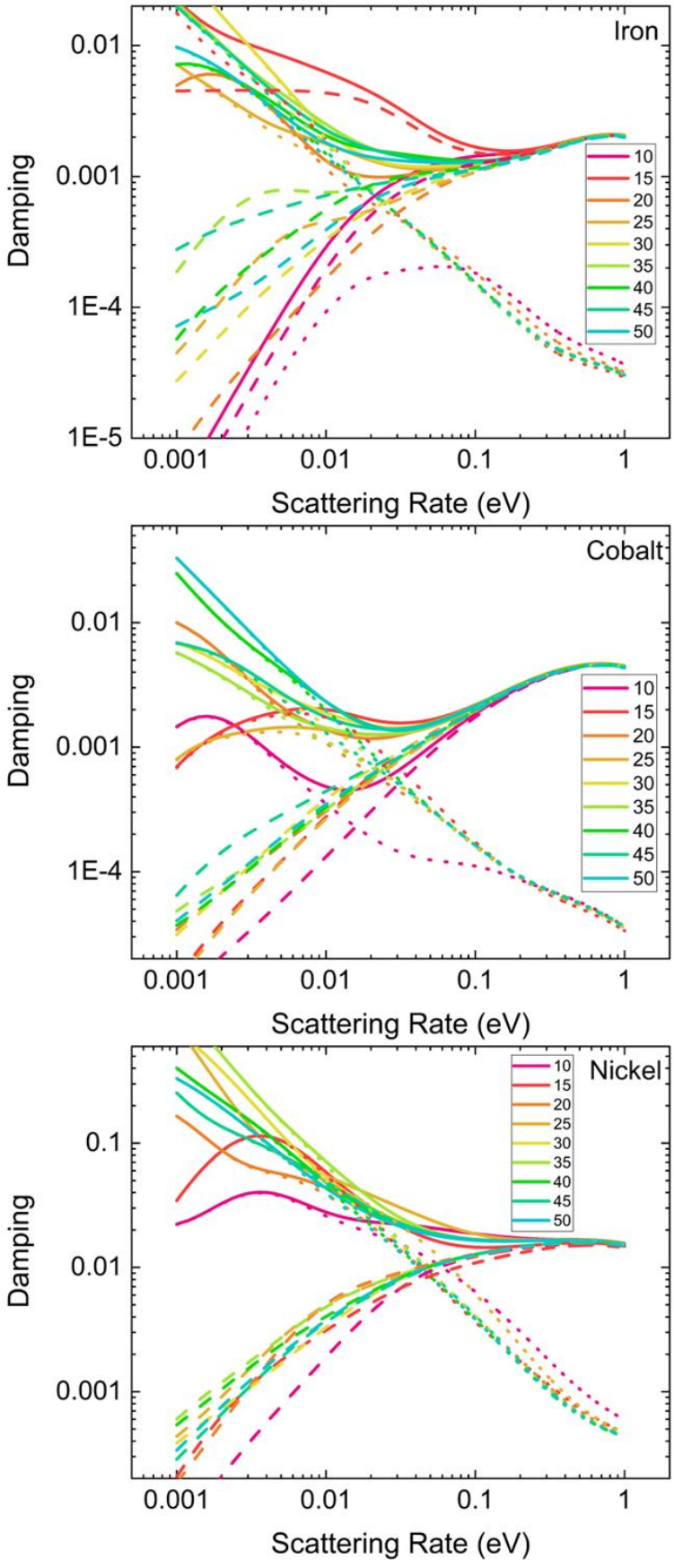

Fig 5.1. The scattering rate dependence of total (solid lines), intraband (dotted lines), and interband (dashed lines) damping for Fe, Co, Ni metals with various k-points in one dimension.

The damping behavior at low scattering rate is also more difficult to converge over varied k-points. In contrast, at the upper limit of considered scattering rate (1 eV), the damping is already converged even at very low k-points. This is can also be explained due to the scattering rate contribution into Lorentzian of spectral functions. At the high scattering rate, $\delta \gg (E_F - \varepsilon_{nk})$ and $\delta \gg (E_F - \varepsilon_{n'k})$ so the damping equation may reduce into:

$$\alpha = \frac{g}{\pi M_s}\frac{1}{\delta^2}\sum_k W_k \sum_{nn'} \left|\Gamma^{-}_{nn'}(k)\right|^2 \tag{5-27}$$

which does not strongly depend on number of k-points. These results are also qualitatively in good agreement with the Barati *et al.* [197] which found that one-dimension k-point needed for convergence at δ = 0.01 eV and 0.001 eV are 300 and 600, respectively.

The similar result for primitive cell FePt is shown in the Fig 5.2. The qualitative trend is easier to converge at around 20 k-point. Although previous works demonstrates the quantitative convergence is achieved at much larger k-points [186,196,197], as this work focuses only on temperature dependence of damping, I chose the rather sparse k-point mesh as long as it reproduces general qualitative trend predicted by torque correlation model [72]. When the finite temperature is included in the latter part, the $2 \times 2 \times 2$ supercell were constructed and the k-point mesh can be constructed as half of its value for primitive cell. Therefore, when supercell is used, $10 \times 10 \times 10$ k-point mesh is considered enough for my calculation.

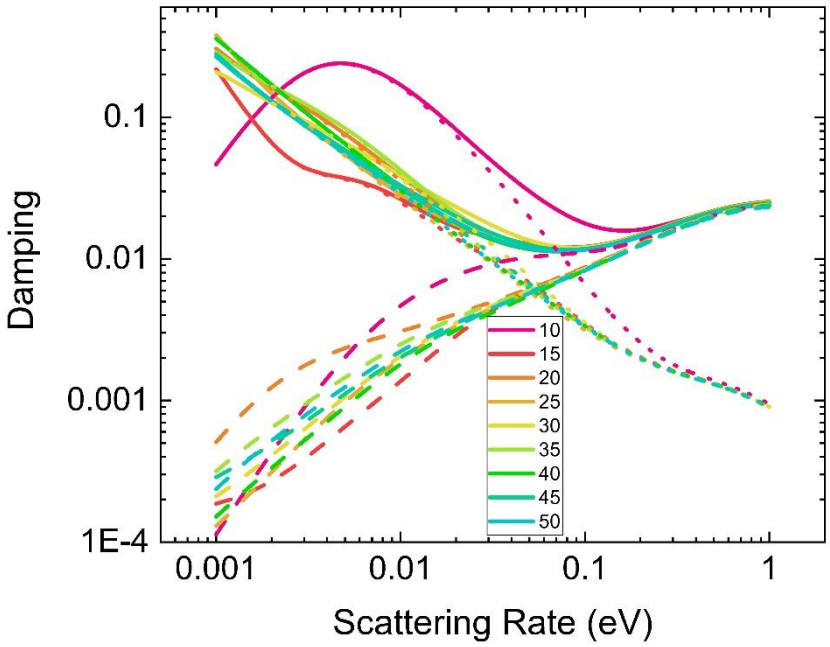

Fig 5.2. The scattering rate dependence of total (solid lines), intraband (dotted lines), and interband (dashed lines) damping for FePt metals with various k-points in one dimension.

5.3.2. Damping dependence of number of bands

After determine how many k-points to be used in the supercell calculation, the next part is to determine the number of bands for qualitative convergence. Since the damping calculation is computationally expensive, one may decide the sufficient required number of combination k-point and bands which suitable with the purpose of the study. By constructing $2 \times 2 \times 2$ supercell, I found in the Fig 5.3 that 192 bands are enough for the reproducing the trend. It is important to note that the unoccupied bands should be sufficiently included in the calculation, so not only the magnetic moment can be calculated accurately, but also the damping. The damping is affected predominantly by states close to the Fermi level E_F. It also explicitly represented as denominator in the Lorentzian, where the maximum value of Lorentzian were obtained in $E_F \approx E_{nk}$.

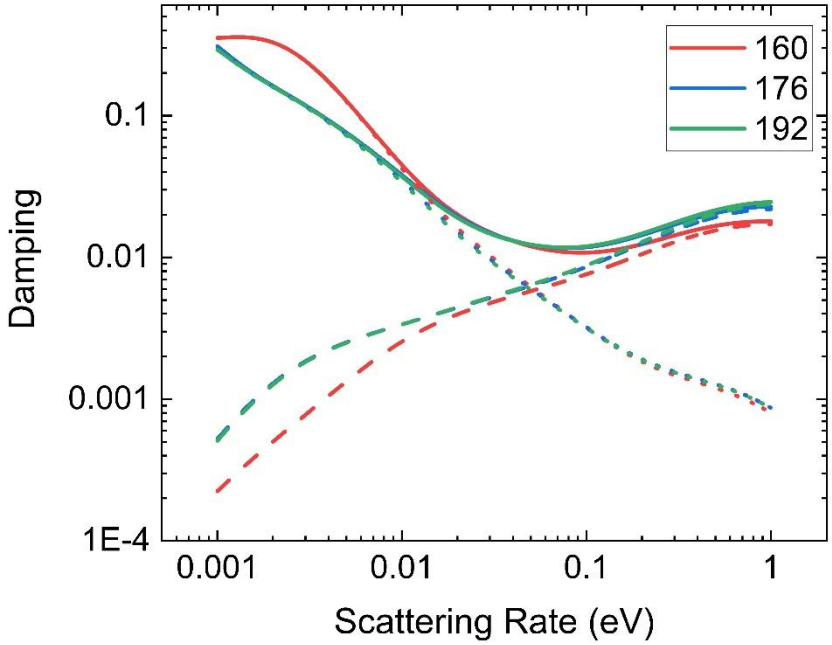

Fig 5.3. The scattering rate dependence of damping for $2 \times 2 \times 2$ supercell FePt with varied number of total bands

5.3.3. Comparison of the calculated ground state damping with previous work

In order to validate my damping calculation code, the results of calculated damping with previous work by Gilmore *et al.* [186] are shown for Fe, Co, and Ni in the Fig 5.4. Similar behavior were obtained, not only qualitatively but also quantitatively. Although the eigenenergies and band states in the Gilmore *et al.* were calculated using linearized-augmented-plane-wave (LAPW) [186] which is slightly different with our projector-augmented-wave (PAW) calculation, these agreements are still quite surprising because the k-point mesh used for my calculation is much smaller than Gilmore's. Aside from that, the difference of lattice constant and spin-orbit coupling energy may also contribute

to the small discrepancy between two calculations. For the results of Cobalt, my result seems overestimate the Gilmore's result for all range of scattering rate [186]. This is may due to my calculation does not differ the treatment of basal plane and along *c* axis as Gilmore did for the k-point mesh [186].

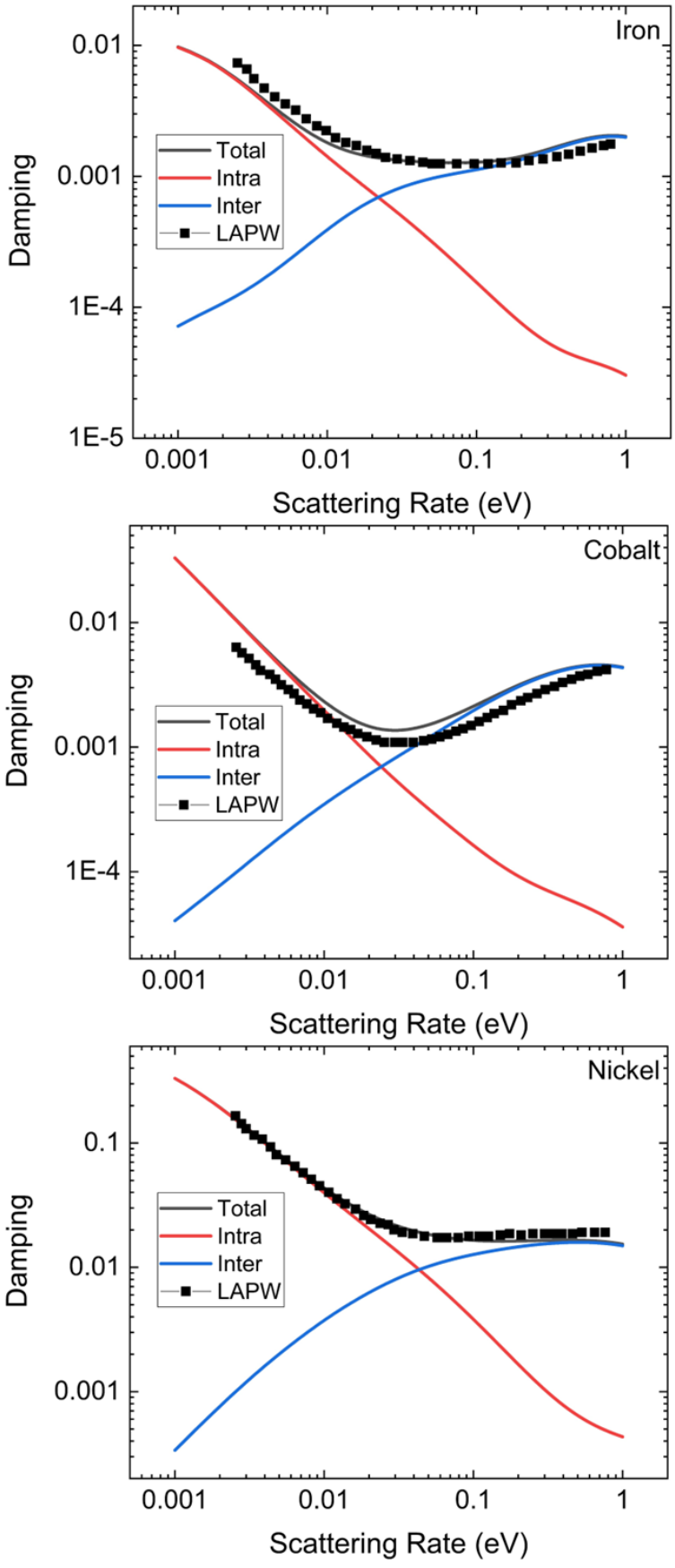

Fig 5.4. The scattering rate dependence of damping for Fe, Co, Ni metals at $50 \times 50 \times 50$ k-point mesh compared with LAPW calculation by Gilmore *et al.* [186].

Both of my calculation and results of Gilmore's show that the damping value of Ni is much higher, while the Co and Fe value is pretty similar [186]. Aside of much higher spin orbit interaction, sharp peak of Ni DOS at Fermi level also contributes to the large damping [198], which will be further explained in the next part. Other interesting features are scattering rate where the intraband and interband damping become equal follow the Fe < Co < Ni, which related with the strength of spin-orbit interaction. This information can be helpful to determine when the intraband or interband dominates the damping [199].

On the other hand, comparison between my calculation on FePt are underestimates the results of Qu *et al.* [200] as shown in the Fig 5.5. It is important to note that Qu *et al.* calculate the damping using tight-binding (TB) model [200], where the electronic states are obtained within the static Hamiltonian. This static Hamiltonian consists of contribution from spin-independent paramagnetic Hamiltonian, ferromagnetic exchange Hamiltonian, and spin orbit interaction Hamiltonian. These Hamiltonian is self-consistently solved by exchange interaction parameters and enhanced spin orbit interaction to match experimentally observed spin and orbital moment. Consequently, their TB result demonstrated the enhanced damping in all range of scattering rate when compared with the LAPW results of Gilmore *et al.* for Fe [196]. Because my calculation is in very good agreement with the Gilmore's, the underestimation compared than Qu's can be accepted.

By enhanced spin-orbit interaction using by Qu *et al.*, the intraband damping become equal to interband damping at the scattering rate 0.07 eV [200], where my calculation give the value of 0.05 eV. It reiterates the finding that scattering rate where minima damping is found due to equivalent contribution between intraband and interband damping is related with the spin-orbit interaction. Assuming that scattering rate is proportional with the temperature, it implies that when the spin-orbit interaction is stronger, minima damping will be observed at much higher temperature, hence the nonmonotonic behavior may be less pronounced and disappear, leaving the only decrease behavior of damping at finite temperature.

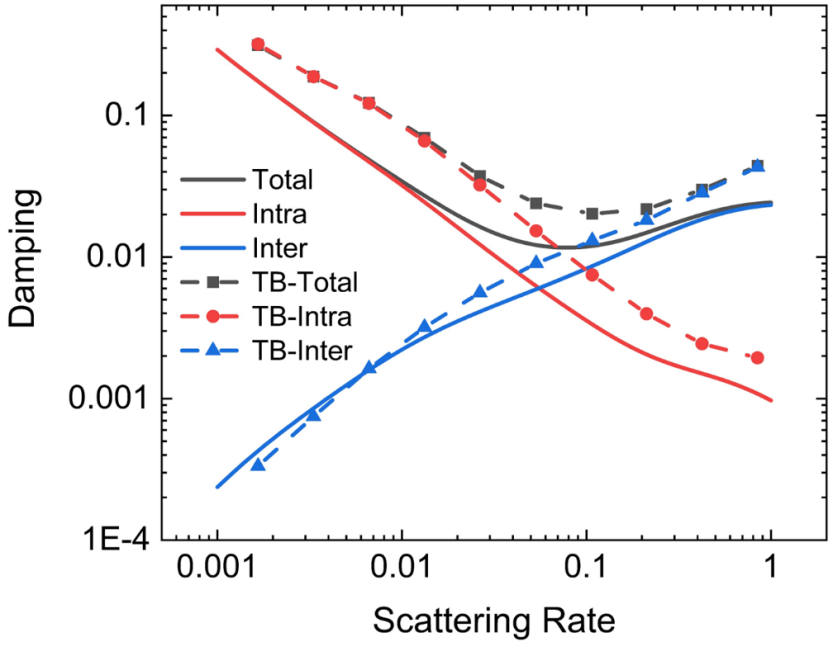

Fig 5.5. The scattering rate dependence of damping for $2 \times 2 \times 2$ supercell FePt with $10 \times 10 \times 10$ k-point mesh compared with calculation using TB method by Qu *et al.* [200].

5.3.4. Damping dependence of spectral energy

As demonstrated in the previous part, the damping calculation is very sensitive to the band calculation method and various parameters, in addition to validate the obtained results using the scattering rate dependence, another useful way to judge the adequacy is to compare the spectral energy dependence of damping with the density of states [198]. This is shown for FePt in the Fig 5.6. The damping pattern follow the behavior of the density of states in quite good agreement. This can be explained by breakdown the contribution of total damping into intraband and interband damping.

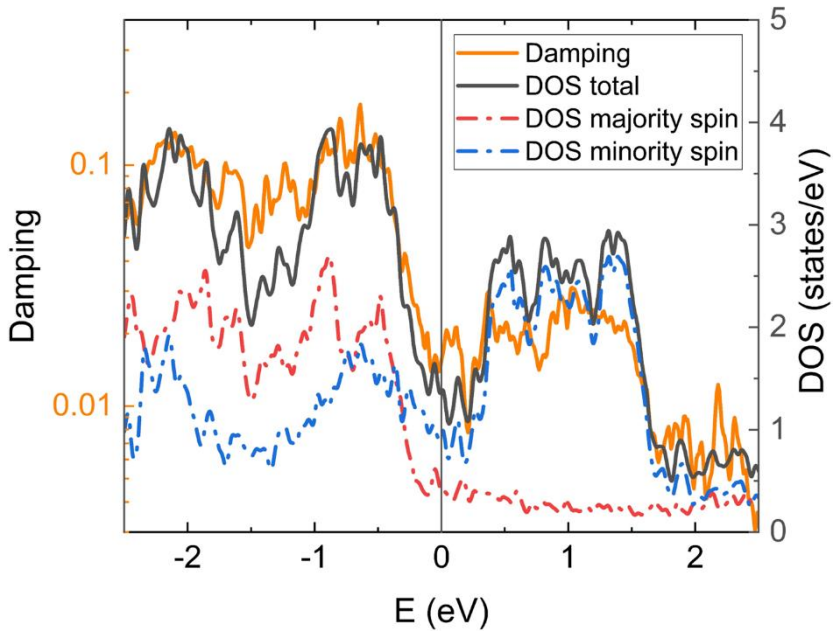

Fig 5.6. The spectral energy dependence of damping for $2 \times 2 \times 2$ supercell FePt with $10 \times 10 \times 10$ k-point mesh compared the density of states (total, majority spin, and minority spin).

The intraband damping corresponds to the transition within the same bands or $n = n'$

$$\alpha = \frac{g}{\pi M_s} \sum_k W_k \sum_{nn'} \left| \Gamma^-_{nn'}(k) \right|^2 \left[\frac{\delta}{(E - E_{nk})^2 + \delta^2} \right]^2 \tag{5-28}$$

On the other hand, density of states (DOS) can be expressed as delta function δ (not to be confused with scattering rate δ in damping equation) smeared by Lorentzian function:

$$\mathrm{DOS} = \sum_k \sum_n \delta(E - E_{nk}) = \frac{1}{\pi} \sum_k \sum_n \frac{\epsilon}{(E - E_{nk})^2 + \epsilon^2} \tag{5-29}$$

where ϵ play important role as small finite electronic broadening parameter. Direct comparison give the relation between

$$\log \alpha \propto \mathrm{DOS} \tag{5-30}$$

While spectral energy dependence of interband damping terms is rather complicated [201]. Since the interband terms corresponds to the transition between different bands or $n \neq n'$, the spectral overlap depends on the relation between scattering rate δ and energy spacing $|E_{nk} - E_{n'k}|$. The interband terms can be proportional to the δ especially when $\delta \ll |E_{nk} - E_{n'k}|$, however it also means that interband contribution is much smaller than intraband contribution. When $\delta \sim |E_{nk} - E_{n'k}|$, the damping will reach the stagnant value with respect to the scattering rate. Due to the complex behavior of interband damping, it is not easy to simply describe its spectral dependence. However, strong relation between intraband damping and DOS is still reflected even in the total damping, showing this simple relation can be generalized for the total damping.

5.4. Lattice dynamics on temperature dependence of damping constant

5.4.1. Convergence on the number of snapshot structures

Aside from the convergence on number of k-point and bands, it is important to also check the convergence on number of the snapshot structures. Since the structural snapshots is randomly sampled from the Gaussian distribution, more snapshots would be better in accuracy. On the other hand, more snapshots also means more burden on computational cost, so it is needed to be just sufficiently chosen. In the Fig 5.7(a), it is shown that for the lower limit of scattering rate 0.001 eV, around 100 snapshots or more is required to obtain convergence. By increasing the scattering rate into 0.05 eV as shown in the Fig 5.7(b), it may only require ~70 averaged snapshots. Further increase of scattering rate up to 1 eV, only 30 averaged snapshots required to achieve the convergence as

shown in the Fig 5.7(c). The general trend that demonstrate the damping with smaller scattering rate is more difficult to converge than the larger scattering rate is also found by Barati *et al.* [197] when investigating convergence of damping value on the number of k-points. However, they also found the inclusion of finite temperature effect via Fermi-Dirac distribution function may improve the numerical efficiency, which does not observed in my calculation. This can be attributed to the different way to implement the finite temperature effect in my study.

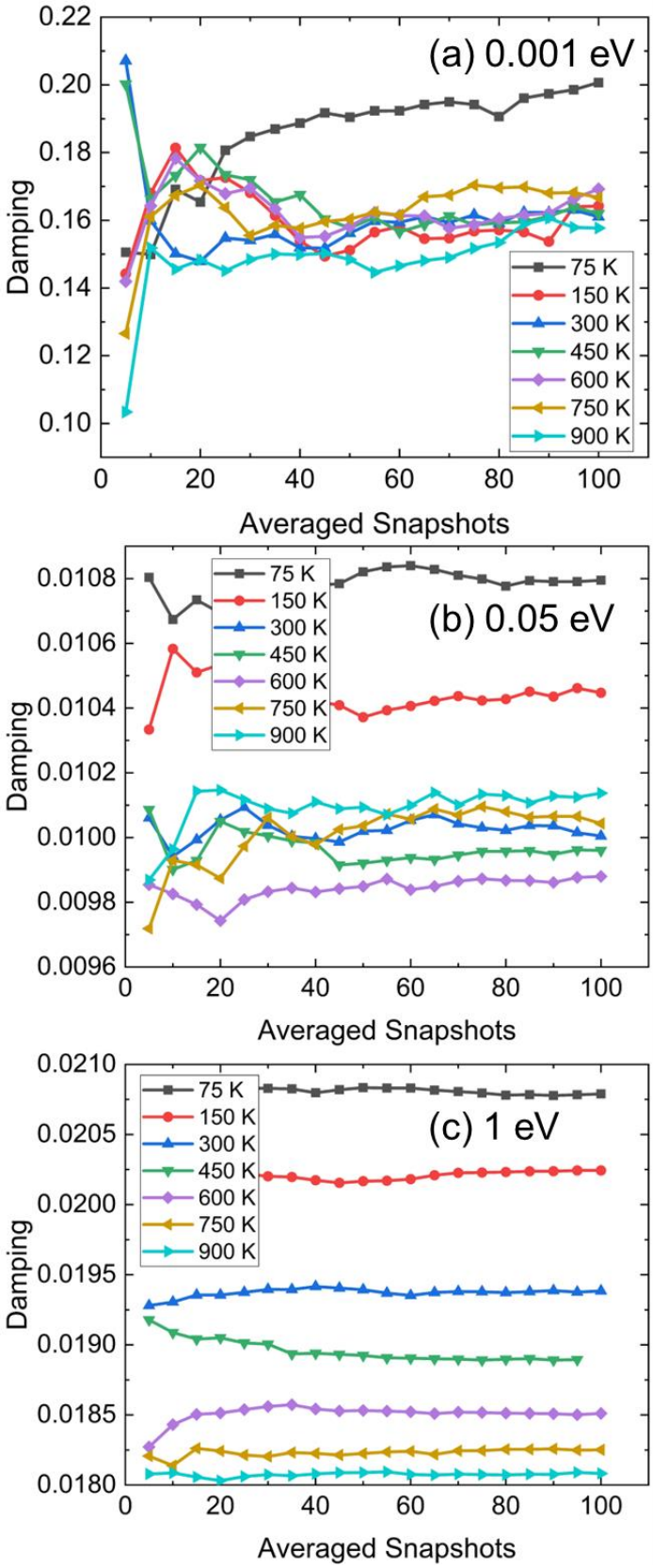

Fig 5.7. The convergence of damping value on number of averaged snapshots with different scattering rate value: (a) 0.001 eV, (b) 0.05 eV, (c) 1 eV.

5.4.2. Scattering rate dependence of damping at different temperature

In Fig 5.8(a), I show the total damping computed with various scattering rates after averaging over 100 "snapshots" for each temperature. The intra-band and inter-band contributions are still dominantly contribute in the low and high scattering regions, respectively. However, the nearly-overlapped curve shown at the elevated temperature (300-900 K) may imply that the effects of atomic vibration on the magnetic damping are not significant, especially at high temperatures. The Fig 5.8(b) contains the same information as Fig 5.8(a) but shows the temperature dependence of damping using a constant scattering rate δ for better visualization. The range of the scattering rate δ was chosen based on the values considered in the previous reports (0.03-0.10 eV) [113,200]. When a relatively low scattering rate δ=0.03-0.04 eV is used, the temperature dependence of the damping value shows an approximately monotonic decrease followed by saturation of damping at high temperatures. However, the use of scattering rates δ=0.05-0.10 eV increases damping at high temperatures; hence a nonmonotonic behavior is clearly demonstrated.

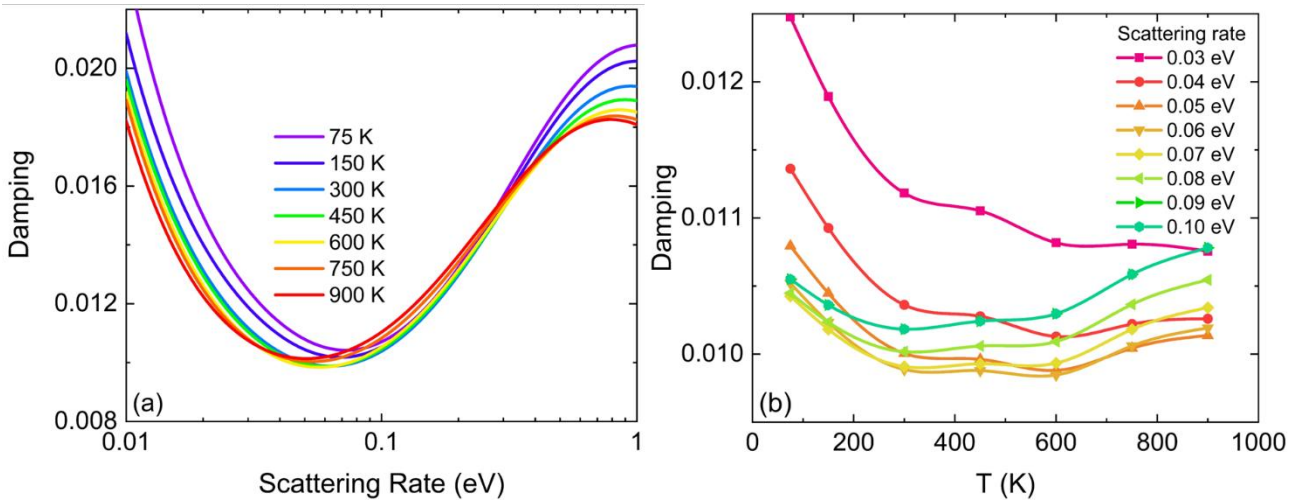

Fig 5.8. (a) The scattering rate dependence of total damping with varying temperature (b) The temperature dependence of total damping with varying scattering rate of $L1_0$-FePt.

5.4.3. Comparison between theoretical and experimental results

In Fig 5.9, I also plot the reported experimental results of FePt damping taken from Refs [110,202] by the blue and green line-points. In the experiment, they measure the FMR linewidth, which is directly proportional to the damping under the assumption of a negligible contribution of inhomogeneity line broadening. Thus, the damping value can be extracted from FMR linewidth and plotted together with the calculated temperature dependence of damping. Previously, Richardson *et al.* reported the reduction of FMR linewidth in the $L1_0$-FePt granular sample, which correspond to the strong reduction of damping (blue dashed line) [110]. Since I and Hiramatsu *et al.* separately

reported that the intrinsic damping of FePt will increase at high temperatures due to the atomic vibration and spin fluctuation [113], respectively, intrinsic damping can be ruled out the as an origin of the experimental reduction of FMR linewidth (damping) observed by Richardson *et al* [110]. In addition, recently published work by Liu *et al.* reported that the FMR linewidth of continuous thin films of cubic A1-FePt significantly increases near the Curie temperature (green dashed line) [202]. This qualitative behavior in cubic A1-FePt shows good agreement with the spin fluctuation effect on damping of tetragonal $L1_0$-FePt reported by Hiramatsu *et al* [113] due to the small extrinsic contribution. Note that the rapid increase of damping of A1-FePt reported by Liu *et al.* happens at a lower temperature than that predicted by Hiramatsu *et al.* for $L1_0$-FePt due to lower experimental T_C of A1-FePt (575 K) [202] compared to the calculated T_C of $L1_0$-FePt (820 K) [113]. While the continuous A1-FePt thin films have fewer defects and smaller extrinsic contribution, the granular structure of $L1_0$-FePt media investigated by Richardson *et al.* has more defects due to the grain boundary, resulting in the stronger extrinsic contribution to the damping [110,202]. Hence, the comparison of these results leads to the two major findings: (1) the temperature dependence of intrinsic damping due to the atomic vibration and also the spin fluctuation is nonmonotonic, and the damping always increases with increasing the temperature near the Curie temperature, (2) the extrinsic contribution will play an important role behind the possible reduction of FePt damping in the experiment.

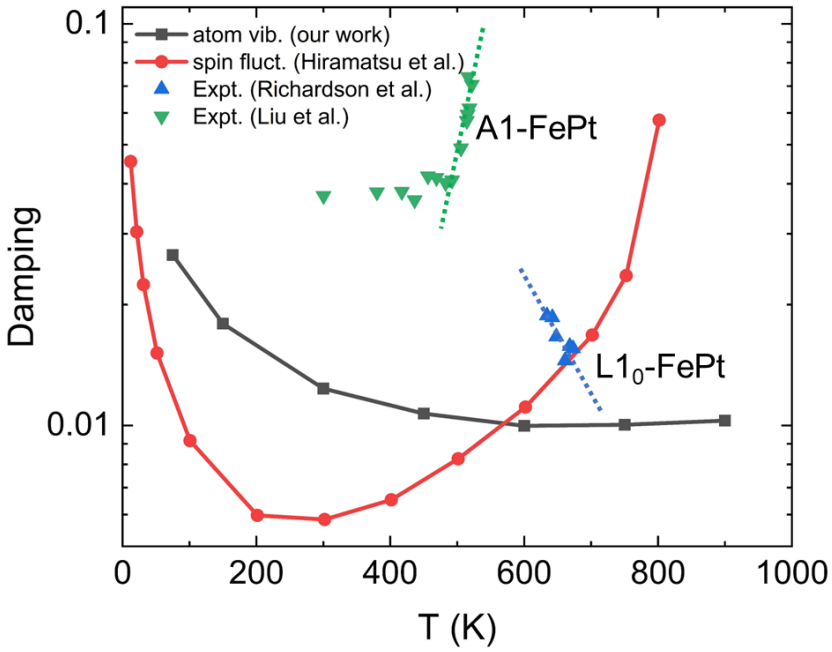

Fig 5.9. Atomic vibration effect on the temperature dependence of the damping of $L1_0$-FePt calculated using the imaginary part of FM self-energy as temperature-dependent scattering rate. For comparison, the spin fluctuation effect on the temperature dependence of damping constant of $L1_0$-FePt calculated by Hiramatsu *et al.* [113], experimental damping constant extracted from FMR

linewidth of $L1_0$-FePt granular media by Richardson *et al.* [110] and A1-FePt continuous thin films by Liu *et al.* [202] are plotted together. Dashed line corresponds to the trend of the temperature dependence of experimental damping constant near Curie temperature.

5.4.4. Spin-flip and spin-conserving contribution

Then, I divide the spin-orbit torque operator $\eta_0^- = [S^-, H_{SO}] = \sum_I \xi_I (S^- L^z - S^z L^-)$ into two parts, one is the spin-conserving term $S^z L^-$ and the other is the spin-flip term $S^- L^z$. In the Fig 5.10, I show separated contributions of scattering rate dependence of damping into spin-conserving transitions and spin-flip transition. I found that the spin-conserving ($S^z L^-$) contribution is always larger than the spin-flip ($S^- L^z$) contribution over range of scattering rate considered in this study. This can be attributed to two possible reasons. First, the small majority-spin DOS compared to the minority-spin DOS at the Fermi level due to the exchange splitting of FePt (See Fig 5.6) will lead to the small contribution of spin-flip transition from occupied majority-spin states to unoccupied minority-spin states. Second, the matrix elements of spin flip $\langle n, k | S^- L^z | n', k \rangle$ only allows the nonzero value for the 6 combinations of atomic orbitals with same magnetic quantum number, where the spin conserving $\langle n, k | S^z L^- | n', k \rangle$ give the nonzero value for the 16 combinations of atomic orbitals with different magnetic quantum number as expected from the calculation of matrix elements shown in the Table 5.2 and Table 5.3 [203].

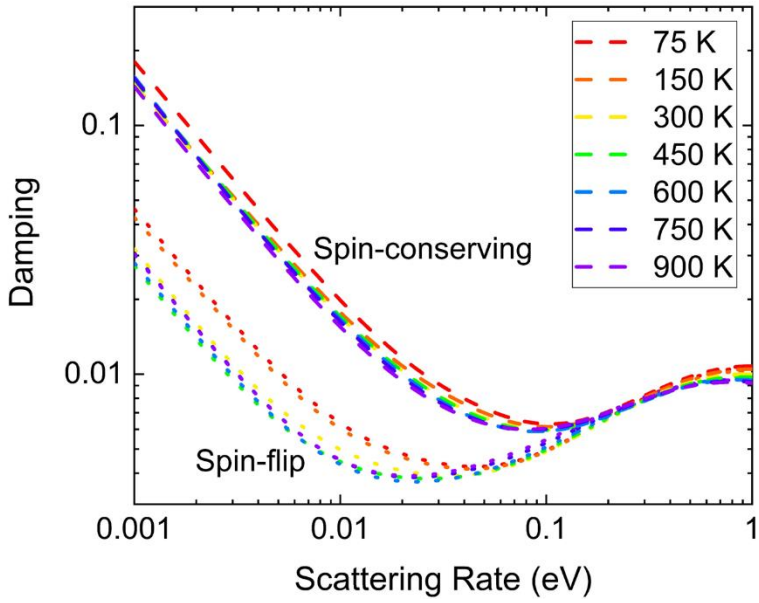

Fig 5.10. The scattering rate dependence of separated contribution of spin conserving and spin flip damping for FePt.

When I use the imaginary part of FM self energy as temperature dependent scattering rate, the temperature dependence between two contributions is also different as shown in the Fig 5.11. The spin-conserving part of damping shows rather monotonic decrease. On the other hand, the spin-flip

part shows nonmonotonic behavior, which is similar with the total damping in Fig 5.9. Previously, it is understood that nonmonotonic behavior of damping is attributed to the competition between the intra-band (conductivity-like) and inter-band (resistivity-like) contribution. While the spin-flip term in the intra-band contribution is almost negligible due to assumption of a pure spin state, the strong spin-flip contribution from the inter-band transition may be origin of enhancement of damping at high temperature.

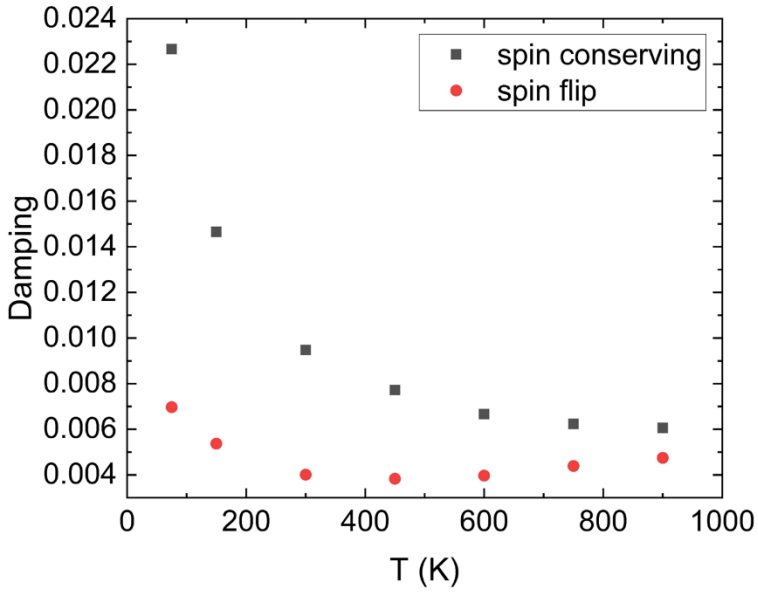

Fig 5.11. The temperature dependence of the spin-conserving and spin flip contribution to damping calculated using the imaginary part of FM self-energy as temperature-dependent scattering rate

In the experiments, it is common to fabricate sample with imperfect quality due to the impurity, disorder, etc. Assuming that relatively small amounts of impurities does not affect the electronic structure and magnetic properties significantly, I can approximate the impurities amount is proportional to the temperature-independent part of scattering rate Λ_{imp}. In the Fig 5.12, I show the spin-conserving and spin-flip damping as a function of temperature for different value of impurity scattering rates Λ_{imp}. I found that the enhancement of the spin-flip damping at high-temperature is more pronounced with increasing Λ_{imp}. On the other hand, the spin-conserving damping hardly increases at high temperature with increasing Λ_{imp}.This result implies that adding impurities in FePt is more beneficial for the preventing the unexpected reduction in damping at high temperature. However, this contribution can be less significant than spin fluctuation because the damping is explicitly dependent on the magnetization. Experimentally, this impurity can be introduced by doping of small atoms (C or B) or magnetic atoms which have similar properties with the Fe and Pt (like Ni).

It is also important to note that introducing doping may have risk to affect another properties of FePt, such as anisotropy, Curie temperature, and etc.

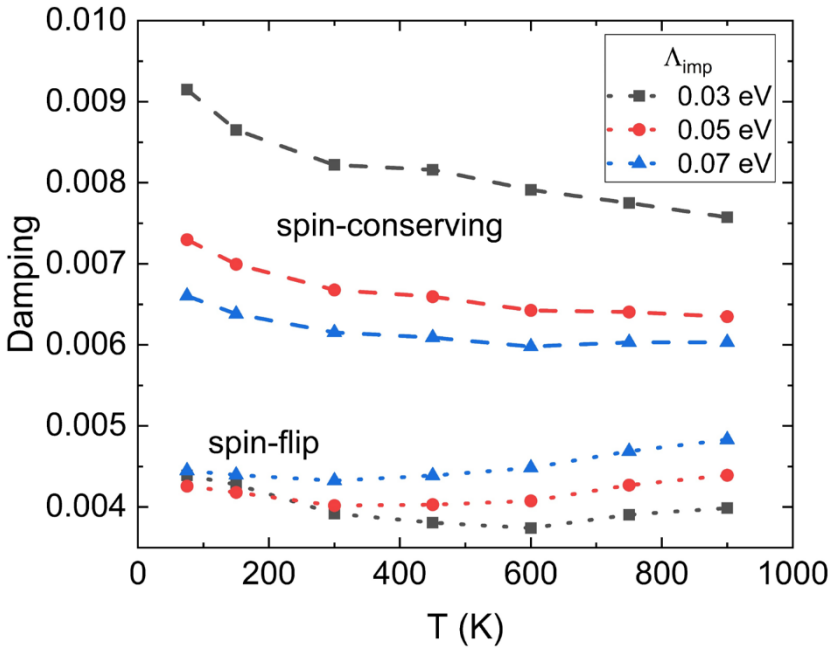

Fig 5.12. The amplitude dependence of damping for FePt compared at different commensurate at 0.1 eV

5.4.5. Phonon-mode analysis of damping

Finally, to understand how each phonon mode affects the damping behavior, I created modulated structures with displacing the atoms along the specified normal modes with different amplitudes at the commensurate q-points. The κ-th atom displacements in the defined supercell with total N atoms are defined as:

$$\frac{A}{\sqrt{NM_\kappa}}\mathrm{Re}[\exp(i\phi)\, e_\alpha(\kappa; qv)\exp(iq\cdot r_{\kappa\ell})], \tag{5-31}$$

where A is the amplitude in the unit of $u^{1/2}$Å, M_κ is the atomic mass of the κ-th atom in the unit of u (atomic mass unit/amu), ϕ is the phase, e_α is the polarization vector of the κ-th atom along α direction, q is the q-point, and $r_{\kappa l}$ is the κ-th atom position in the l-th unit cell. I created supercells with displacements due to the phonon mode for each commensurate q-point. In the primitive $L1_0$ FePt unit cell, there are 2 atoms, yielding 6 phonon modes at each q point. Since the $2 \times 2 \times 2$ supercell is used, there are 8 different commensurate q points labeled as follows: Γ (0,0,0), Z (0,0,-0.5), X (0,-0.5,0), R (0,-0.5,-0.5), X' (-0.5,0,0), R' (-0.5,0,-0.5), M (-0.5,-0.5,0), and A (-0.5,-0.5,-0.5). Note that X(X') and R(R') are equivalent points in the phonon dispersion calculation.

In the Fig 5.13(a)-(c), I showed how each phonon mode affects the ratio of the damping in the modulated structure α_{mod} to the damping in the unmodulated (perfect supercell) structure α_{unmod} ($\alpha_{\mathrm{mod}}/\alpha_{\mathrm{unmod}}$) with changing the amplitude of atomic displacements. The constant scattering rate of 0.05 eV was used. Red (blue) points correspond to the phonon mode that enhances (weakens) the damping value compared to the unmodulated structure. The presence of both red and blue phonon modes indicates two competing contributions to the temperature dependence of damping, which explains its nonmonotonic behavior.

At higher temperatures, a larger amplitude of displacements is expected, and higher-frequency phonon modes will be more occupied. I show in Fig 5.14(a)-(h) the amplitude dependence of the normalized damping $\alpha_{\mathrm{mod}}/\alpha_{\mathrm{unmod}}$ of $L1_0$ FePt due to phonon modes at various commensurate q-points. Larger amplitude and higher-frequency phonon mode generally result in the larger change in the magnitude of $\alpha_{\mathrm{mod}}/\alpha_{\mathrm{unmod}}$. In particular, the high-frequency phonon mode at Γ point has always enhanced the damping, which may be a dominant contribution to the increase of damping at high temperatures in the Fig 5.8.

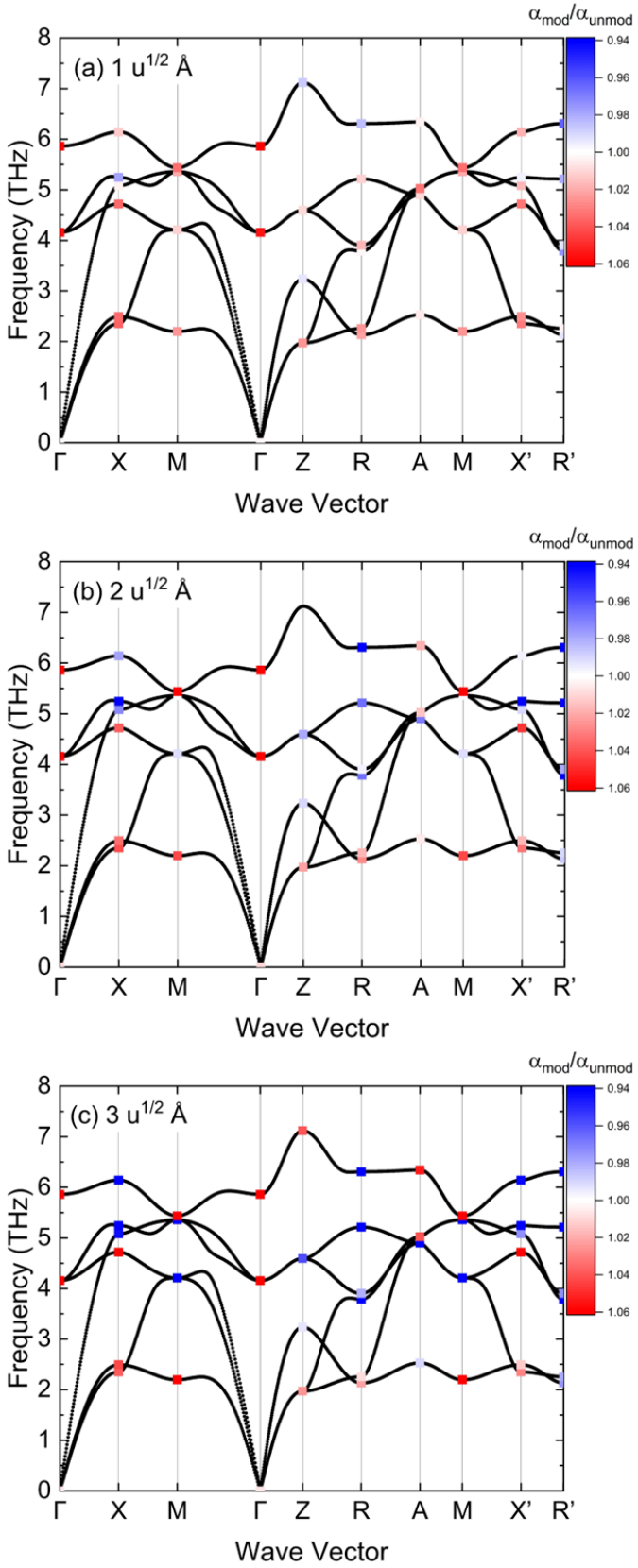

Fig 5.13. The amplitude dependence of damping for FePt compared at different commensurate at 0.05 eV

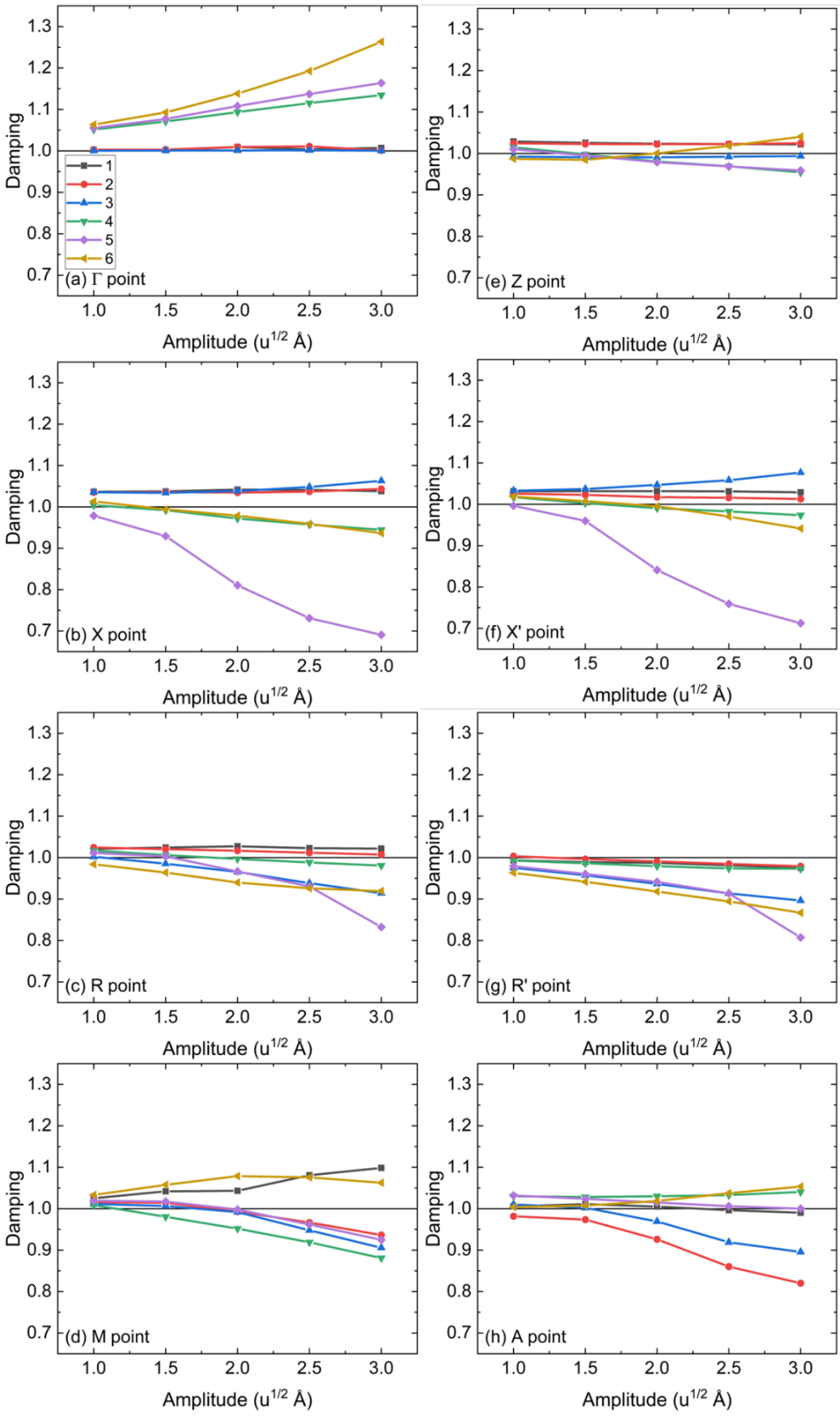

Fig 5.14. The amplitude dependence of damping for FePt compared at different commensurate at 0.05 eV

5.5. Summary

I carried out a theoretical study of lattice dynamics effects on damping constants of $L1_0$-FePt at finite temperatures based on the Kambersky torque correlation model and the improved frozen thermal lattice disorder approach. Using the imaginary part of Fan-Migdal self-energy as the temperature-dependent scattering rate, I showed the weak nonmonotonic behavior of temperature dependence of damping. As a result, the damping slightly increased at high temperatures due to the effect of atomic vibrations, although the magnitude is not as large as that of the spin fluctuation effect. Hence, our results rule out lattice dynamics as an exclusive origin of the observed temperature-induced reduction in the damping constant. Comparison with the reported experimental results emphasized the importance of extrinsic contribution on possible reduction of damping in $L1_0$-FePt granular media for HAMR application. Furthermore, I found that increase of the damping at high temperatures is due to the spin-flip ($S^- L^z$) contribution, which can be enhanced by the larger impurity scattering rate. These results suggest that in practical applications the inclusion of impurities such as carbon and boron may suppress the observed reduction of the damping from extrinsic contribution at high temperature.

Chapter 6: Summary and Future Perspective

Spin polarization and damping constant are considered to be two important properties to realize the better performance of read sensor and writing process in ultrahigh density magnetic recording. Since the application of recording devices are done in the finite temperature, understanding the temperature dependence behavior of these two properties are crucial. This thesis work was conducted to clarify the finite temperature effect on spin polarization and damping constant of prospective magnetic materials for MR devices and HAMR media, respectively. The results are summarized as follow:

1. The temperature dependence of *sp* spin polarization Heusler alloys due to spin fluctuation depends on Curie temperature and location of Fermi level of the material. High Curie temperature is originated from interatomic exchange constant which provide slower decay of magnetic moments at finite temperature. Although magnetic moment is dominantly contributed by *d* electrons and reduces to zero at Curie temperature, the *sp* electrons can be affected via *s-d* and *p-d* coupling in the intraatomic orbitals. Therefore, large exchange constant will lead to slow decay of magnetic moments and small temperature dependence of *sp* spin polarization in Heusler alloys. On the other hand, temperature dependence can also be improved by the tuning stoichiometry ratio to shift the Fermi level position. However, this effect can be negligible if the Fermi level position is already quite distant from valence band or conduction band.
2. Machine learning combined with finite temperature first principles calculation is successfully conducted. Based on the Bayesian optimization, general composition for the highly spin-polarized Heusler alloys at finite temperature is $Co_2Mn(Z_yZ'_{1-y})$ and $Co_2Fe(Z_yZ'_{1-y})$ with *Z* site can be occupied by varied elements. This could be explained by large exchange constant and superiority of Curie temperature of these Co_2Mn- and Co_2Fe- based compound, which experimentally demonstrated the Curie temperature as high as 1000 K based on Slater-Pauling rule. Machine learning also suggests several new compounds with high spin polarization at finite temperature such as $Co_2FeAl_ySn_{1-y}$, $Co_2MnGa_yAs_{1-y}$, and $Co_2FeGa_yIn_{1-y}$ for various applications.
3. The temperature dependence of intrinsic damping constant of $L1_0$ FePt due the lattice dynamics is nonmonotonic behavior with slight increase at high temperature, unlike rapid increase demonstrated by spin fluctuation effect. Therefore, possible reduction of damping of $L1_0$ FePt observed in recently reported experiment is due to the extrinsic effect. In addition, increase of the damping at high temperature is attributed to spin-flip contribution, which can be enhanced by the larger impurity scattering rate. Phonon mode analysis also reveal the existence of two kind phonon mode that enhance or weaken the damping as origin of nonmonotonic behavior of damping.

Lastly, I would like to mention several important suggestions for future perspectives on experimental and theoretical work.

Since the large exchange constant are crucial to obtain small temperature dependence of *sp* spin polarization, the highly spin-polarized Co_2MnZ and Co_2FeZ based Heusler composition are optimal choice for ferromagnetic electrode in the magnetoresistive devices due to their high Curie temperature (> 1000 K). While it is unlikely to find other Heusler alloys with higher Curie temperature, Fermi level tuning by mixing two different atoms for *Z* site can be another way to improve the temperature dependence of *sp* spin polarization. Although Fermi level tuning are thoroughly investigated and experimentally confirmed, the focus of atom combination is mostly on adjacent elements at periodic table. On the other hand, machine learning results show that combination with *Z* elements such as P, As, Sb, Sn, In, open the unexplored area to obtain the new materials with superior properties. These results also encouraged the further systematic investigation on effect mixing various *Z* elements.

On the other hand, the intrinsic damping constant of $L1_0$ FePt is found to be slightly increasing at finite temperature due to lattice vibration. Since the damping also inversely proportional with magnetization, it is also expected to increase near Curie temperature. These results imply that intrinsic damping constant of $L1_0$ FePt always increase at high temperature. Therefore, the remaining problem is to minimize the extrinsic contribution as possible reason behind the rapid reduction of damping constant. Since the spin-flip contribution to damping high temperature can be enhanced by impurity scattering rate, adding impurities into $L1_0$ FePt might be useful to suppress the reduction of damping due to extrinsic damping. This could be done via doping of atoms into $L1_0$ FePt recording media. Small atoms such carbon and boron can be considered as options for this doping.

In terms of theoretical framework, I successfully combined machine learning with the finite temperature first principles calculation. This attempt prove that machine learning can be incorporated to optimize the real example of expensive black box function such as evaluating spin polarization at finite temperature. One may consider to implement this framework to obtain the magnetic materials with another superior properties at finite temperature for broader applications. On the other hand, due to the computational cost, the finite temperature effect (spin fluctuation and lattice vibration) is separately considered in this study for spin polarization and damping constant, respectively. In reality, those effects simultaneously happen on the magnetic materials at room temperature, therefore further study to efficiently combine these effects are needed. Moreover, in some cases, the lattice expansion cannot be neglected. Coupling between spin and phonon degrees of freedom would be considered as better approach to picture the magnetic system at finite temperature.

References

[1] D. R.-J. G.-J. Rydning, J. Reinsel, and J. Gantz, Fram. Int. Data Corp. 16 (2018).

[2] A. Hirohata, K. Yamada, Y. Nakatani, L. Prejbeanu, B. Diény, P. Pirro, and B. Hillebrands, J. Magn. Magn. Mater. **509**, (2020).

[3] M. M. Waldrop, Nature **530**, 144 (2016).

[4] M. N. Baibich, J. M. Broto, A. Fert, F. N. Van Dau, F. Petroff, P. Etienne, G. Creuzet, A. Friederich, and J. Chazelas, Phys. Rev. Lett. **61**, 2472 (1988).

[5] G. Binasch, P. Grünberg, F. Saurenbach, and W. Zinn, Phys. Rev. B **39**, 4828 (1989).

[6] M. Julliere, Phys. Lett. A **54**, 225 (1975).

[7] http://asrc.idema.org/documents-roadmap/.

[8] D. Weller, A. Moser, L. Folks, M. E. Best, Wen Lee, M. F. Toney, M. Schwickert, J.-U. Thiele, and M. F. Doerner, IEEE Trans. Magn. **36**, 10 (2000).

[9] E. N. Abarra, I. Okamoto, and Y. Mizoshita, in *INTERMAG 2000 Digest of Technical Papers. 2000 IEEE International Magnetics Conference*, Vol. 2581 (IEEE, 2000), pp. 6–6.

[10] D. Weller and A. Moser, IEEE Trans. Magn. **35**, 4423 (1999).

[11] S. H. Charap, Pu-Ling Lu, and Yanjun He, IEEE Trans. Magn. **33**, 978 (1997).

[12] K. R. Coffey, M. A. Parker, and J. K. Howard, IEEE Trans. Magn. **31**, 2737 (1995).

[13] E. E. Fullerton, D. T. Margulies, M. E. Schabes, M. Carey, B. Gurney, A. Moser, M. Best, G. Zeltzer, K. Rubin, H. Rosen, and M. Doerner, Appl. Phys. Lett. **77**, 3806 (2000).

[14] D. Weller and M. F. Doerner, Annu. Rev. Mater. Sci. **30**, 611 (2000).

[15] J. J. M. Ruigrok, R. Coehoorn, S. R. Cumpson, and H. W. Kesteren, J. Appl. Phys. **87**, 5398 (2000).

[16] S. I. Iwasaki and K. Takemura, IEEE Trans. Magn. **11**, 1173 (1975).

[17] S. Iwasaki, Y. Nakamura, and K. Ouchi, IEEE Trans. Magn. **15**, 1456 (1979).

[18] R. H. Victora and X. Shen, IEEE Trans. Magn. **41**, 2828 (2005).

[19] R. H. Victora and Xiao Shen, IEEE Trans. Magn. **41**, 537 (2005).

[20] R. Wood, IEEE Trans. Magn. **36**, 36 (2000).

[21] S. N. Piramanayagam, J. Appl. Phys. **102**, 011301 (2007).

[22] D. Suess, T. Schrefl, S. Fähler, M. Kirschner, G. Hrkac, F. Dorfbauer, and J. Fidler, Appl. Phys. Lett. **87**, 2003 (2005).

[23] M. Mallary, A. Torabi, and M. Benakli, IEEE Trans. Magn. **38**, 1719 (2002).

[24] S. Iwasaki, IEEE Trans. Magn. **16**, 71 (1980).

[25] R. H. Victora, S. M. Morgan, K. Momsen, E. Cho, and M. F. Erden, IEEE Trans. Magn. **48**, 1697 (2012).

[26] A. Amer, J. Holliday, D. D. E. Long, E. L. Miller, J. F. Pâris, and T. Schwarz, IEEE Trans. Magn. **47**, 3691 (2011).

[27] Y. Kanai, Y. Jinbo, T. Tsukamoto, S. J. Greaves, K. Yoshida, and H. Muraoka, IEEE Trans. Magn. **46**, 715 (2010).

[28] K. S. Chan, J. J. Miles, E. Hwang, B. V. K. Vijayakumar, J. G. Zhu, W. C. Lin, and R. Negi, IEEE Trans. Magn. **45**, 3837 (2009).

[29] Y. Shiroishi, K. Fukuda, I. Tagawa, H. Iwasaki, S. Takenoiri, H. Tanaka, H. Mutoh, and N. Yoshikawa, IEEE Trans. Magn. **45**, 3816 (2009).

[30] R. Wood, M. Williams, A. Kavcic, and J. Miles, IEEE Trans. Magn. **45**, 917 (2009).

[31] G. Scheunert, O. Heinonen, R. Hardeman, A. Lapicki, M. Gubbins, and R. M. Bowman, Appl. Phys. Rev. **3**, 011301 (2016).

[32] M. Alex, T. Valet, T. McDaniel, and C. Brucker, J. Magn. Soc. Japan **25**, 328 (2001).

[33] D. Weller, G. Parker, O. Mosendz, A. Lyberatos, D. Mitin, N. Y. Safonova, and M. Albrecht, J. Vac. Sci. Technol. B, Nanotechnol. Microelectron. Mater. Process. Meas. Phenom. **34**, 060801 (2016).

[34] D. Weller, G. Parker, O. Mosendz, E. Champion, B. Stipe, X. Wang, T. Klemmer, G. Ju, and A. Ajan, IEEE Trans. Magn. **50**, 1 (2014).

[35] D. Weller, O. Mosendz, G. Parker, S. Pisana, and T. S. Santos, Phys. Status Solidi Appl. Mater. Sci. **210**, 1245 (2013).

[36] R. E. Rottmayer, S. Batra, D. Buechel, W. A. Challener, J. Hohlfeld, Y. Kubota, L. Li, B. Lu, C. Mihalcea, K. Mountfield, K. Pelhos, C. Peng, T. Rausch, M. A. Seigler, D. Weller, and X. Yang, **42**, 2417 (2006).

[37] W. A. Challener, C. Peng, A. V. Itagi, D. Karns, W. Peng, Y. Peng, X. Yang, X. Zhu, N. J. Gokemeijer, Y. T. Hsia, G. Ju, R. E. Rottmayer, M. A. Seigler, and E. C. Gage, Nat. Photonics **3**, 220 (2009).

[38] W. P. Pratt, S. F. Lee, J. M. Slaughter, R. Loloee, P. A. Schroeder, and J. Bass, Phys. Rev. Lett. **66**, 3060 (1991).

[39] M. A. M. Gijs, S. K. J. Lenczowski, and J. B. Giesbers, Phys. Rev. Lett. **70**, 3343 (1993).

[40] M. A. M. Gijs, J. B. Giesbers, M. T. Johnson, J. B. F. aan de Stegge, H. H. J. M. Janssen, S. K. J. Lenczowski, R. J. M. van de Veerdonk, and W. J. M. de Jonge, J. Appl. Phys. **75**, 6709 (1994).

[41] M. A. M. Gijs, S. K. J. Lenczowski, J. B. Giesbers, R. J. M. van de Veerdonk, M. T. Johnson, and J. B. F. aan de Stegge, Mater. Sci. Eng. B **31**, 85 (1995).

[42] S. Zhang and P. M. Levy, J. Appl. Phys. **69**, 4786 (1991).

[43] R. Meservey, P. M. Tedrow, and J. S. Brooks, J. Appl. Phys. **53**, 1563 (1982).

[44] G. A. Gibson and R. Meservey, J. Appl. Phys. **58**, 1584 (1985).

[45] J. S. Moodera, R. Meservey, and P. M. Tedrow, Appl. Phys. Lett. **41**, 488 (1982).

[46] S. Maekawa and U. Gafvert, IEEE Trans. Magn. **18**, 707 (1982).

[47] T. Miyazaki, T. Yaoi, and S. Ishio, J. Magn. Magn. Mater. **98**, L7 (1991).

[48] J. S. Moodera, L. R. Kinder, T. M. Wong, and R. Meservey, Phys. Rev. Lett. **74**, 3273 (1995).

[49] S. S. P. Parkin, C. Kaiser, A. Panchula, P. M. Rice, B. Hughes, M. Samant, and S. H. Yang, Nat. Mater. **3**, 862 (2004).

[50] S. Yuasa, T. Nagahama, A. Fukushima, Y. Suzuki, and K. Ando, Nat. Mater. **3**, 868 (2004).

[51] W. H. Butler, Sci. Technol. Adv. Mater. **9**, (2008).

[52] S. Yuasa and D. D. Djayaprawira, J. Phys. D. Appl. Phys. **40**, R337 (2007).

[53] K. E. H. M. Hanssen and P. E. Mijnarends, Phys. Rev. B **34**, 5009 (1986).

[54] K. E. H. M. Hanssen, P. E. Mijnarends, L. P. L. M. Rabou, and K. H. J. Buschow, Phys. Rev. B **42**, 1533 (1990).

[55] R. Meservey, P. M. Tedrow, and P. Fulde, Phys. Rev. Lett. **25**, 1270 (1970).

[56] R. J. Soulen, J. M. Byers, M. S. Osofsky, B. Nadgorny, T. Ambrose, S. F. Cheng, P. R. Broussard, C. T. Tanaka, J. Nowak, J. S. Moodera, A. Barry, and J. M. D. Coey, Science (80-.). **282**, 85 (1998).

[57] N. Tombros, C. Jozsa, M. Popinciuc, H. T. Jonkman, and B. J. Van Wees, Nature **448**, 571 (2007).

[58] Y. S. Dedkov, U. Rüdiger, and G. Güntherodt, Phys. Rev. B **65**, 064417 (2002).

[59] L. Wollmann, A. K. Nayak, S. S. P. Parkin, and C. Felser, Annu. Rev. Mater. Res. **47**, 247 (2017).

[60] F. Heusler, Verh. Dtsch. Phys. Ges. **5**, 219 (1903).

[61] O. Heusler, Ann. Phys. **411**, 155 (1934).

[62] I. Galanakis, P. H. Dederichs, and N. Papanikolaou, Phys. Rev. B **66**, 174429 (2002).

[63] E. Şaşıoğlu, L. M. Sandratskii, P. Bruno, and I. Galanakis, Phys. Rev. B **72**, 184415 (2005).

[64] J. Kübler, G. H. Fecher, and C. Felser, Phys. Rev. B **76**, 024414 (2007).

[65] M. P. Raphael, B. Ravel, M. A. Willard, S. F. Cheng, B. N. Das, R. M. Stroud, K. M. Bussmann, J. H. Claassen, and V. G. Harris, Appl. Phys. Lett. **79**, 4396 (2001).

[66] B. Ravel, J. O. Cross, M. P. Raphael, V. G. Harris, R. Ramesh, and L. V. Saraf, Appl. Phys. Lett. **81**, 2812 (2002).

[67] M. P. Raphael, B. Ravel, Q. Huang, M. A. Willard, S. F. Cheng, B. N. Das, R. M. Stroud, K. M. Bussmann, J. H. Claassen, and V. G. Harris, Phys. Rev. B **66**, 104429 (2002).

[68] S. Picozzi, A. Continenza, and A. J. Freeman, Phys. Rev. B **69**, 094423 (2004).

[69] Y. Miura, K. Nagao, and M. Shirai, Phys. Rev. B **69**, 144413 (2004).

[70] J.-Y. Bigot and M. Vomir, Ann. Phys. **525**, 2 (2013).

[71] V. Kamberský, Can. J. Phys. **48**, 2906 (1970).

[72] V. Kamberský, Czechoslov. J. Phys. **26**, 1366 (1976).

[73] H. Ebert, S. Mankovsky, K. Chadova, S. Polesya, J. Minár, and D. Ködderitzsch, Phys. Rev. B **91**, 165132 (2015).

[74] S. M. Bhagat and P. Lubitz, Phys. Rev. B **10**, 179 (1974).

[75] Z. Xu, K. Zhang, and J. Li, Phys. Rev. B **104**, 224404 (2021).

[76] R. F. L. Evans, R. W. Chantrell, U. Nowak, A. Lyberatos, and H.-J. Richter, Appl. Phys. Lett. **100**, 102402 (2012).

[77] M. H. Kryder, E. C. Gage, T. W. Mcdaniel, W. A. Challener, R. E. Rottmayer, G. Ju, Y. T. Hsia, and M. F. Erden, Proc. IEEE **96**, 1810 (2008).

[78] T. Kobayashi, Y. Nakatani, and Y. Fujiwara, J. Magn. Soc. Japan **42**, 110 (2018).

[79] T. Kobayashi, Y. Nakatani, and Y. Fujiwara, J. Magn. Soc. Japan **43**, 70 (2019).

[80] T. Shima, K. Takanashi, Y. K. Takahashi, and K. Hono, Appl. Phys. Lett. **81**, 1050 (2002).

[81] L. Zhang, Y. K. Takahashi, A. Perumal, and K. Hono, J. Magn. Magn. Mater. **322**, 2658 (2010).

[82] A. Kußmann and G. G. v. Rittberg, Int. J. Mater. Res. **41**, 470 (1950).

[83] S. Mizukami, S. Iihama, N. Inami, T. Hiratsuka, G. Kim, H. Naganuma, M. Oogane, and Y. Ando, Appl. Phys. Lett. **98**, 052501 (2011).

[84] J. Becker, O. Mosendz, D. Weller, A. Kirilyuk, J. C. Maan, P. C. M. Christianen, T. Rasing, and A. Kimel, Appl. Phys. Lett. **104**, 152412 (2014).

[85] K. D. Lee, H. S. Song, J. W. Kim, H. S. Ko, J. W. Sohn, B. G. Park, and S. C. Shin, Appl. Phys. Express **7**, 113004 (2014).

[86] J. W. Kim, H. S. Song, J. W. Jeong, K. D. Lee, J. W. Sohn, T. Shima, and S. C. Shin, Appl. Phys. Lett. **98**, 092509 (2011).

[87] T. Valet and A. Fert, Phys. Rev. B **48**, 7099 (1993).

[88] T. Block, C. Felser, G. Jakob, J. Ensling, B. Mühling, P. Gütlich, and R. J. Cava, J. Solid State Chem. **176**, 646 (2003).

[89] K. Inomata, S. Okamura, R. Goto, and N. Tezuka, Jpn. J. Appl. Phys. **42**, L419 (2003).

[90] K. Yakushiji, K. Saito, S. Mitani, K. Takanashi, Y. K. Takahashi, and K. Hono, Appl. Phys. Lett. **88**, 222504 (2006).

[91] S. Ishida, S. Fujii, S. Kashiwagi, and S. Asano, J. Phys. Soc. Japan **64**, 2152 (1995).

[92] B. S. D. C. S. Varaprasad, A. Srinivasan, Y. K. Takahashi, M. Hayashi, A. Rajanikanth, and K. Hono, Acta Mater. **60**, 6257 (2012).

[93] B. Balke, G. H. Fecher, H. C. Kandpal, C. Felser, K. Kobayashi, E. Ikenaga, J.-J. Kim, and S. Ueda, Phys. Rev. B **74**, 104405 (2006).

[94] T. Kubota, Z. Wen, and K. Takanashi, J. Magn. Magn. Mater. **492**, 165667 (2019).

[95] S. Mitani, *Magnetic Tunnel Junctions Using Heusler Alloys* (2016), pp. 401–412.

[96] Y. Sakuraba, K. Izumi, S. Bosu, K. Saito, and K. Takanashi, J. Phys. D. Appl. Phys. **44**, 064009 (2011).

[97] P. Mavropoulos, M. Ležaić, and S. Blügel, Phys. Rev. B **72**, 174428 (2005).

[98] Y. Sakuraba, M. Hattori, M. Oogane, Y. Ando, H. Kato, A. Sakuma, T. Miyazaki, and H. Kubota, Appl. Phys. Lett. **88**, 192508 (2006).

[99] S. Li, Y. K. Takahashi, T. Furubayashi, and K. Hono, Appl. Phys. Lett. **103**, 042405 (2013).

[100] S. Yuasa and D. D. Djayaprawira, J. Phys. D. Appl. Phys. **40**, R337 (2007).

[101] Y. Miura, H. Uchida, Y. Oba, K. Abe, and M. Shirai, Phys. Rev. B **78**, 064416 (2008).

[102] Y. Sakuraba, K. Izumi, T. Iwase, S. Bosu, K. Saito, K. Takanashi, Y. Miura, K. Futatsukawa, K. Abe, and M. Shirai, Phys. Rev. B - Condens. Matter Mater. Phys. **82**, 094444 (2010).

[103] L. Chioncel, Y. Sakuraba, E. Arrigoni, M. I. Katsnelson, M. Oogane, Y. Ando, T. Miyazaki, E. Burzo, and A. I. Lichtenstein, Phys. Rev. Lett. **100**, 086402 (2008).

[104] K. Miyamoto, A. Kimura, Y. Miura, M. Shirai, M. Ye, Y. Cui, K. Shimada, H. Namatame, M.

Taniguchi, Y. Takeda, Y. Saitoh, E. Ikenaga, S. Ueda, K. Kobayashi, and T. Kanomata, Phys. Rev. B - Condens. Matter Mater. Phys. **79**, 100405 (2009).

[105] L. Chioncel, Y. Sakuraba, E. Arrigoni, M. I. Katsnelson, M. Oogane, Y. Ando, T. Miyazaki, E. Burzo, and A. I. Lichtenstein, Phys. Rev. Lett. **100**, 086402 (2008).

[106] B. L. Gyorffy, A. J. Pindor, J. Staunton, G. M. Stocks, and H. Winter, J. Phys. F Met. Phys. **15**, 1337 (1985).

[107] M. Ležaić, P. Mavropoulos, J. Enkovaara, G. Bihlmayer, and S. Blügel, Phys. Rev. Lett. **97**, 026404 (2006).

[108] K. Nawa, I. Kurniawan, K. Masuda, Y. Miura, C. E. Patrick, and J. B. Staunton, Phys. Rev. B **102**, 1 (2020).

[109] R. Kikuchi, J. Appl. Phys. **27**, 1352 (1956).

[110] D. Richardson, S. Katz, J. Wang, Y. K. Takahashi, K. Srinivasan, A. Kalitsov, K. Hono, A. Ajan, and M. Mingzhong, Phys. Rev. Appl. **10**, 054046 (2018).

[111] M. Strungaru, S. Ruta, R. F. L. Evans, and R. W. Chantrell, Phys. Rev. Appl. **14**, 014077 (2020).

[112] M. Strungaru, S. Ruta, R. F. L. Evans, and R. W. Chantrell, Phys. Rev. Appl. **14**, 014077 (2020).

[113] R. Hiramatsu, D. Miura, and A. Sakuma, Appl. Phys. Express **15**, 013003 (2021).

[114] Y. Liu, A. A. Starikov, Z. Yuan, and P. J. Kelly, Phys. Rev. B - Condens. Matter Mater. Phys. **84**, 014412 (2011).

[115] E. Schrödinger, Ann. Phys. **384**, 361 (1926).

[116] M. Born and R. Oppenheimer, Ann. Phys. **389**, 457 (1927).

[117] P. Hohenberg and W. Kohn, Phys. Rev. **136**, B864 (1964).

[118] W. Kohn and L. J. Sham, Phys. Rev. **140**, A1133 (1965).

[119] W. Kohn and N. Rostoker, Phys. Rev. **94**, 1111 (1954).

[120] J. Korringa, Physica **13**, 392 (1947).

[121] B. L. Gyorffy, A. J. Pindor, J. Staunton, G. M. Stocks, and H. Winter, J. Phys. F Met. Phys. **15**, 1337 (1985).

[122] P. E. Blöchl, Phys. Rev. B **50**, 17953 (1994).

[123] Y. Liu, A. A. Starikov, Z. Yuan, and P. J. Kelly, Phys. Rev. B **84**, 014412 (2011).

[124] H. S. Goripati, T. Furubayashi, Y. K. Takahashi, and K. Hono, J. Appl. Phys. **113**, 043901 (2013).

[125] J. W. Jung, Y. Sakuraba, T. T. Sasaki, Y. Miura, and K. Hono, Appl. Phys. Lett. **108**, 102408 (2016).

[126] S. Li, Y. K. Takahashi, T. Furubayashi, and K. Hono, Appl. Phys. Lett. **103**, 1 (2013).

[127] M. Lüders, A. Ernst, M. Däne, Z. Szotek, A. Svane, D. Ködderitzsch, W. Hergert, B. L. Györffy, and W. M. Temmerman, Phys. Rev. B **71**, 205109 (2005).

[128] H. C. Kandpal, G. H. Fecher, and C. Felser, J. Phys. D. Appl. Phys. **40**, 1507 (2007).

[129] Y. K. Takahashi, A. Srinivasan, B. Varaprasad, A. Rajanikanth, N. Hase, T. M. Nakatani, S. Kasai, T. Furubayashi, and K. Hono, Appl. Phys. Lett. **98**, 152501 (2011).

[130] 2015.

[131] X. Hu, Y. Zhang, S. Fan, X. Li, Z. Zhao, C. He, Y. Zhao, Y. Liu, and W. Xie, J. Phys. Condens. Matter **32**, 205901 (2020).

[132] M. Hoffmann, A. Ernst, W. Hergert, V. N. Antonov, W. A. Adeagbo, R. M. Geilhufe, and H. Ben Hamed, Phys. Status Solidi **257**, 1900671 (2020).

[133] J. P. Perdew and Y. Wang, Phys. Rev. B **45**, 13244 (1992).

[134] P. Soven, Phys. Rev. **156**, 809 (1967).

[135] G. H. Fecher, H. C. Kandpal, S. Wurmehl, C. Felser, and G. Schönhense, J. Appl. Phys. **99**, 1 (2006).

[136] S. Wurmehl, G. H. Fecher, H. C. Kandpal, V. Ksenofontov, C. Felser, H.-J. Lin, and J. Morais, Phys. Rev. B **72**, 184434 (2005).

[137] V. I. Anisimov, F. Aryasetiawan, and A. I. Lichtenstein, J. Phys. Condens. Matter **9**, 767

(1997).

[138] H. C. Kandpal, G. H. Fecher, C. Felser, and G. Schönhense, Phys. Rev. B **73**, 094422 (2006).

[139] J. P. Perdew and A. Zunger, Phys. Rev. B **23**, 5048 (1981).

[140] M. Däne, M. Lüders, A. Ernst, D. Ködderitzsch, W. M. Temmerman, Z. Szotek, and W. Hergert, J. Phys. Condens. Matter **21**, 045604 (2009).

[141] K. R. A. ZIEBECK and K.-U. NEUMANN, *Alloys and Compounds of D-Elements with Main Group Elements. Part 2*, Vol. 32C (Springer-Verlag, Berlin/Heidelberg, 2001).

[142] K. Moges, Y. Honda, H. X. Liu, T. Uemura, M. Yamamoto, Y. Miura, and M. Shirai, Phys. Rev. B **93**, 134403 (2016).

[143] S. Li, T. Nakatani, K. Masuda, Y. Sakuraba, X. D. Xu, T. T. Sasaki, H. Tajiri, Y. Miura, T. Furubayashi, and K. Hono, Acta Mater. **142**, 49 (2018).

[144] S. Kirklin, J. E. Saal, B. Meredig, A. Thompson, J. W. Doak, M. Aykol, S. Rühl, and C. Wolverton, Npj Comput. Mater. **1**, 15010 (2015).

[145] J. E. Saal, S. Kirklin, M. Aykol, B. Meredig, and C. Wolverton, Jom **65**, 1501 (2013).

[146] A. Jain, S. P. Ong, G. Hautier, W. Chen, W. D. Richards, S. Dacek, S. Cholia, D. Gunter, D. Skinner, G. Ceder, and K. A. Persson, APL Mater. **1**, 011002 (2013).

[147] W. M. Temmerman, B. L. Gyorffy, and G. M. Stocks, J. Phys. F Met. Phys. **8**, 2461 (1978).

[148] J. Ma, V. I. Hegde, K. Munira, Y. Xie, S. Keshavarz, D. T. Mildebrath, C. Wolverton, A. W. Ghosh, and W. H. Butler, Phys. Rev. B **95**, 024411 (2017).

[149] M. Matsumoto, R. Banerjee, and J. B. Staunton, Phys. Rev. B **90**, 054421 (2014).

[150] G. A. Marchant, C. E. Patrick, and J. B. Staunton, Phys. Rev. B **99**, 054415 (2019).

[151] I. Kurniawan, K. Nawa, K. Masuda, Y. Miura, and K. Hono, Acta Mater. **218**, 117218 (2021).

[152] C. C. M. Campbell, J. Phys. F Met. Phys. **5**, 1931 (1975).

[153] W. Wang, H. Sukegawa, R. Shan, S. Mitani, and K. Inomata, Appl. Phys. Lett. **95**, 182502 (2009).

[154] J. Ma, J. He, D. Mazumdar, K. Munira, S. Keshavarz, T. Lovorn, C. Wolverton, A. W. Ghosh,

and W. H. Butler, Phys. Rev. B **98**, 094410 (2018).

[155] S. Sanvito, C. Oses, J. Xue, A. Tiwari, M. Zic, T. Archer, P. Tozman, M. Venkatesan, M. Coey, and S. Curtarolo, Sci. Adv. **3**, (2017).

[156] S. V. Faleev, Y. Ferrante, J. Jeong, M. G. Samant, B. Jones, and S. S. P. Parkin, Phys. Rev. Mater. **1**, 024402 (2017).

[157] M. Kallmayer, H. J. Elmers, B. Balke, S. Wurmehl, F. Emmerling, G. H. Fecher, and C. Felser, J. Phys. D. Appl. Phys. **39**, 786 (2006).

[158] A. R. Denton and N. W. Ashcroft, Phys. Rev. A **43**, 3161 (1991).

[159] T. Ueno, T. D. Rhone, Z. Hou, T. Mizoguchi, and K. Tsuda, Mater. Discov. **4**, 18 (2016).

[160] S. Ju, T. Shiga, L. Feng, Z. Hou, K. Tsuda, and J. Shiomi, Phys. Rev. X **7**, 021024 (2017).

[161] S. Ju, Y. Miura, K. Yamamoto, K. Masuda, K. Uchida, and J. Shiomi, Phys. Rev. Res. **2**, 023187 (2020).

[162] I. Kurniawan, Y. Miura, and K. Hono, Phys. Rev. Mater. **6**, L091402 (2022).

[163] S. Tsunegi, Y. Sakuraba, M. Oogane, K. Takanashi, and Y. Ando, Appl. Phys. Lett. **93**, 112506 (2008).

[164] B. Balke, S. Wurmehl, G. H. Fecher, C. Felser, and J. Kübler, Sci. Technol. Adv. Mater. **9**, 014102 (2008).

[165] M. Zhang, E. Brück, F. R. de Boer, Z. Li, and G. Wu, J. Phys. D. Appl. Phys. **37**, 2049 (2004).

[166] M. El Amine Monir, R. Khenata, H. Baltache, G. Murtaza, M. S. Abu-Jafar, A. Bouhemadou, S. Bin Omran, and D. Rached, J. Magn. Magn. Mater. **394**, 404 (2015).

[167] L. Galdun, V. Vega, Z. Vargová, E. D. Barriga-Castro, C. Luna, R. Varga, and V. M. Prida, ACS Appl. Nano Mater. **1**, 7066 (2018).

[168] A. Bakhshayeshi, M. M. Sarmazdeh, R. T. Mendi, and A. Boochani, J. Electron. Mater. **46**, 2196 (2017).

[169] S. A. Sofi, S. Yousuf, T. M. Bhat, M. Nabi, S. Singh, Z. Saleem, S. A. Mir, S. A. Khandy, A. Q. Seh, and D. C. Gupta, in *AIP Conference Proceedings*, Vol. 2115 (2019), p. 030349.

[170] Z. Yao, S. Gong, J. Fu, Y.-S. Zhang, and K.-L. Yao, Solid State Commun. **150**, 2239 (2010).

[171] Y. Sakuraba, K. Takanashi, Y. Kota, T. Kubota, M. Oogane, A. Sakuma, and Y. Ando, Phys. Rev. B **81**, 144422 (2010).

[172] Y. K. Takahashi, N. Hase, M. Kodzuka, A. Itoh, T. Koganezawa, T. Furubayashi, S. Li, B. S. D. C. S. Varaprasad, T. Ohkubo, and K. Hono, J. Appl. Phys. **113**, 223901 (2013).

[173] W. H. Butler, X. G. Zhang, T. C. Schulthess, and J. M. MacLaren, Phys. Rev. B - Condens. Matter Mater. Phys. **63**, 544161 (2001).

[174] G. F. Li, Y. Honda, H. X. Liu, K. I. Matsuda, M. Arita, T. Uemura, M. Yamamoto, Y. Miura, M. Shirai, T. Saito, F. Shi, and P. M. Voyles, Phys. Rev. B - Condens. Matter Mater. Phys. **89**, 014428 (2014).

[175] W. Wang, H. Sukegawa, and K. Inomata, Phys. Rev. B - Condens. Matter Mater. Phys. **82**, 092402 (2010).

[176] R. Shan, H. Sukegawa, W. H. Wang, M. Kodzuka, T. Furubayashi, T. Ohkubo, S. Mitani, K. Inomata, and K. Hono, Phys. Rev. Lett. **102**, 246601 (2009).

[177] K. Özdoğan, B. Aktaş, I. Galanakis, and E. Şaşioğlu, J. Appl. Phys. **101**, (2007).

[178] A. Sakai, Y. P. Mizuta, A. A. Nugroho, R. Sihombing, T. Koretsune, M. T. Suzuki, N. Takemori, R. Ishii, D. Nishio-Hamane, R. Arita, P. Goswami, and S. Nakatsuji, Nature Physics.

[179] A. Bakhshayeshi, M. M. Sarmazdeh, R. T. Mendi, and A. Boochani, J. Electron. Mater. **46**, 2196 (2017).

[180] Y. Sakuraba, K. Takanashi, Y. Kota, T. Kubota, M. Oogane, A. Sakuma, and Y. Ando, Phys. Rev. B - Condens. Matter Mater. Phys. **81**, 144422 (2010).

[181] S. N. Holmes and M. Pepper, J. Supercond. Nov. Magn. **16**, 191 (2003).

[182] C. D. Damsgaard, M. C. Hickey, S. N. Holmes, R. Feidenhans'l, S. O. Mariager, C. S. Jacobsen, and J. B. Hansen, J. Appl. Phys. **105**, 124502 (2009).

[183] S. N. Holmes and M. Pepper, Appl. Phys. Lett. **81**, 1651 (2002).

[184] S. Wurmehl, G. H. Fecher, H. C. Kandpal, V. Ksenofontov, C. Felser, H. J. Lin, and J. Morais, Phys. Rev. B - Condens. Matter Mater. Phys. **72**, 184434 (2005).

[185] D. Ozaki, D. Miura, and A. Sakuma, IEEE Trans. Magn. **53**, (2017).

[186] K. Gilmore, Y. U. Idzerda, and M. D. Stiles, Phys. Rev. Lett. **99**, 027204 (2007).

[187] G. Kresse and J. Furthmüller, Phys. Rev. B **54**, 11169 (1996).

[188] J. P. Perdew, K. Burke, and M. Ernzerhof, Phys. Rev. Lett. **77**, 3865 (1996).

[189] A. Togo and I. Tanaka, Scr. Mater. **108**, 1 (2015).

[190] Y. N. Wu, W. A. Saidi, J. K. Wuenschell, T. Tadano, P. Ohodnicki, B. Chorpening, and Y. Duan, J. Phys. Chem. Lett. **11**, 2518 (2020).

[191] F. Giustino, Rev. Mod. Phys. **89**, 015003 (2017).

[192] P. Giannozzi, O. Andreussi, T. Brumme, O. Bunau, M. B. Nardelli, M. Calandra, R. Car, C. Cavazzoni, D. Ceresoli, M. Cococcioni, and others, J. Phys. Condens. Matter **29**, 465901 (2017).

[193] K. F. Garrity, J. W. Bennett, K. M. Rabe, and D. Vanderbilt, Comput. Mater. Sci. **81**, 446 (2014).

[194] G. Pizzi, V. Vitale, R. Arita, S. Blügel, F. Freimuth, G. Géranton, M. Gibertini, D. Gresch, C. Johnson, T. Koretsune, J. Ibañez-Azpiroz, H. Lee, J.-M. Lihm, D. Marchand, A. Marrazzo, Y. Mokrousov, J. I. Mustafa, Y. Nohara, Y. Nomura, L. Paulatto, S. Poncé, T. Ponweiser, J. Qiao, F. Thöle, S. S. Tsirkin, M. Wierzbowska, N. Marzari, D. Vanderbilt, I. Souza, A. A. Mostofi, and J. R. Yates, J. Phys. Condens. Matter **32**, 165902 (2020).

[195] J.-J. Zhou, J. Park, I.-T. Lu, I. Maliyov, X. Tong, and M. Bernardi, Comput. Phys. Commun. **264**, 107970 (2021).

[196] T. Qu and R. H. Victora, J. Appl. Phys. **115**, 17C506 (2014).

[197] E. Barati, M. Cinal, D. M. Edwards, and A. Umerski, Phys. Rev. B **90**, 014420 (2014).

[198] A. Sakuma, J. Phys. Soc. Japan **81**, 084701 (2012).

[199] F. S. M. Guimarães, J. R. Suckert, J. Chico, J. Bouaziz, M. dos Santos Dias, and S. Lounis, J. Phys. Condens. Matter **31**, 255802 (2019).

[200] T. Qu and R. H. Victora, Appl. Phys. Lett. **106**, 072404 (2015).

[201] K. Gilmore, Y. U. Idzerda, and M. D. Stiles, J. Appl. Phys. **103**, 07D303 (2008).

[202] C. Liu, K. Srinivasan, A. Ajan, E. McCollum, A. Kalitsov, V. Kalappattil, and M. Wu, J. Magn. Magn. Mater. **563**, 169988 (2022).

[203] C. Liu, C. K. A. Mewes, M. Chshiev, T. Mewes, and W. H. Butler, Appl. Phys. Lett. **95**, 022509 (2009).

List of Publications and Presentations

Publications and presentations related to this thesis

1. I. Kurniawan, K. Nawa, K. Masuda, Y. Miura, and K. Hono
   First-principles disordered local-moment study on temperature dependence of spin polarization in $Co_2Fe(Ga_{0.5}Ge_{0.5})$ Heusler alloy
   Acta Mater. 218, 117218 (2021)

2. I. Kurniawan, Y. Miura, and K. Hono
   Machine learning study of highly spin-polarized Heusler alloys at finite temperature
   Phys. Rev. Materials 6, L091402 (2022)

3. I. Kurniawan, Y. Miura, G. Xing, T. Tadano, and K. Hono
   Theoretical Study of Lattice Dynamics Effect on Damping Constant of FePt at Finite Temperature
   Phys. Rev. B (submitted)

4. I. Kurniawan, Y. Miura, K. Hono
   Machine learning study of highly spin-polarized Heusler alloys at finite temperature
   第 83 回 応用物理学会秋季学術講演会 The 83th JSAP Autumn Meeting 2022
   English Presentation Encouragement Award from Spintronics Research Group of the JSAP

5. I. Kurniawan, K. Nawa, K. Masuda, Y. Miura, and K. Hono
   First-Principles Disordered Local-Moment Study on Temperature Dependence of Spin Polarization in Co2Fe($Ga_{0.5}Ge_{0.5}$) Heusler Alloy
   第 82 回 応用物理学会秋季学術講演会 The 82th JSAP Autumn Meeting 2021

Other co-authored publications and presentations

1. K. Goto, L. S. R. Kumara, Y. Sakuraba, Y. Miura, I. Kurniawan, A. Yasui, H. Tajiri, Y. Fujita, Z. Chen, and K. Hono
   Effects of the atomic order on the half-metallic electronic structure in the $Co_2Fe(Ga_{0.5}Ge_{0.5})$ Heusler alloy thin film
   Phys. Rev. Materials 4, 114406 (2020)

2. X. Tang, H. Sepehri-Amin, N. Terada, A. Martin-Cid, I. Kurniawan, S. Kobayashi, Y. Kotani, H. Takeya, J. Lai, Y. Matsushita, T. Ohkubo, Y. Miura, T. Nakamura & K. Hono
   Magnetic refrigeration material operating at a full temperature range required for hydrogen liquefaction
   Nat. Commun. 13, 1817 (2022)

3. R. Mandal, I. Kurniawan, I. Suzuki, Z. Wen, Y. Miura, T. Kubota, K. Takanashi, T. Ohkubo, K. Hono, and Y. K. Takahashi
   Nanoscale-Thick Ni-Based Half-Heusler Alloys with Structural Ordering-Dependent Ultralow Magnetic Damping: Implications for Spintronic Applications
   ACS Applied Nano Materials 2022 5 (1), 569-577

4. R. Mandal, Y. Sasaki, I. Kurniawan, J. Jung, Y. Miura, Y. Sakuraba, K. Hono, and Y. K. Takahashi
   Estimation of Magnetic Gilbert Damping at High Temperature: An Approach of Ferromagnetic Resonance Study
   ACS Applied Electronic Materials 2022 4 (9), 4741-4747

5. V. K. Kushwaha, Y. Sakuraba, T. Nakatani, T. Sasaki, I. Kurniawan, Y. Miura, H. Tajiri, K. Hono
   High $L2_1$-atomic ordering and spin-polarization in Co_2MnZ (Z = Ge, Sn) Heusler thin films with low-temperature annealing process
   APL Materials 10, 091119 (2022)

6. V. K. Kushwaha, Y. Sakuraba, T. Nakatani, T. Sasaki, I. Kurniawan, K. Hono
   Enhancement of L21-atomic order and spin-polarization in Co2MnZ (Z = Ge, Sn) Heusler thin films by low-temperature annealing process
   INTERMAG2021